Utah State University

DigitalCommons@USU

All Graduate Theses and Dissertations

Graduate Studies

8-2017

Facilitation of Nanoscale Thermal Transport by Hydrogen Bonds

Lin Zhang

Utah State University

Follow this and additional works at: https://digitalcommons.usu.edu/etd

Part of the Mechanical Engineering Commons

Recommended Citation

Zhang, Lin, "Facilitation of Nanoscale Thermal Transport by Hydrogen Bonds" (2017). *All Graduate Theses and Dissertations*. 6638.
https://digitalcommons.usu.edu/etd/6638

This Dissertation is brought to you for free and open access by the Graduate Studies at DigitalCommons@USU. It has been accepted for inclusion in All Graduate Theses and Dissertations by an authorized administrator of DigitalCommons@USU. For more information, please contact digitalcommons@usu.edu.

UtahStateUniversity
MERRILL-CAZIER LIBRARY

FACILITATION OF NANOSCALE THERMAL TRANSPORT BY HYDROGEN BONDS

by

Lin Zhang

A dissertation submitted in partial fulfillment
of the requirements for the degree
of

DOCTOR OF PHILOSOPHY

in

Mechanical Engineering

Approved:

Ling Liu, Ph.D. Major Professor	Heng Ban, Ph.D. Committee Member
Nick Roberts, Ph.D. Committee Member	Thomas H. Fronk, Ph.D. Committee Member
Steve Scheiner, Ph.D. Committee Member	Mark R. McLellan, Ph.D. Vice President for Research and Dean of the School of Graduate Studies

UTAH STATE UNIVERSITY
Logan, Utah

2017

Copyright © Lin Zhang 2017

All Rights Reserved

ABSTRACT

Facilitation of Nanoscale Thermal Transport by Hydrogen Bonds

by

Lin Zhang, Doctor of Philosophy

Utah State University, 2017

Major Professor: Dr. Ling Liu
Department: Mechanical and Aerospace Engineering

Advances in nanotechnology and biotechnology bring new challenges in thermal management and heat removal due to the effects of ultra-small sizes and dimensions, complicated nature of materials, and various interfacial phenomena, etc. Different from thermal transport processes at micro/macro scales, nanoscale thermal transport is significantly subject to boundary and interfacial scattering and highly dependent on molecular morphology and atomic bonding, which can be controlled by chemical engineering at interfaces. As a result, rational approaches are required to guide material design for desirable thermal properties.

Hydrogen bonds are ubiquitous in organic materials. In this study, the role of hydrogen bonding in thermal transport is studied in three representative material systems by molecular dynamics simulations. First, beta sheet nanocrystals of spider silk, silkworm silk, and synthetic silk are investigated with native inter-strand hydrogen bonds. Results show that thermal transport along beta strands are substantially improved by hydrogen bonds, in association with other effects including primary sequence and geometry size. Second, the concept of using hydrogen bonds to improve thermal transport is further extended to nanocrystalline polymer nanofibers. Hydrogen bonds are found to restrict the torsion of polymer chains, stiffen polymer nanofibers, and increase the group velocity of acoustic phonons, all of which contribute to enhanced thermal transport. Third, the effect of hydrogen bonds on interfacial thermal transport is investigated between graphene and polymers by introducing hydrogen-bond-capable functional groups on graphene. Analyses show that hydrogen bonds provide an efficient channel to conduct heat across the interface. Based on these understandings, a hierarchical heat spreader of polymer monolayer is designed to further enhance interfacial thermal conductance. The physical insights obtained from these studies are expected to enrich the nanoscale thermal transport theory and provide rational design guidelines to improve thermal transport properties of various nanomaterials and structures towards many applications.

(257 pages)

PUBLIC ABSTRACT

Facilitation of Nanoscale Thermal Transport by Hydrogen Bonds

Lin Zhang

Thermal transport performance at the nanoscale and/or of biomaterials is essential to the success of many new technologies including nanoelectronics, biomedical devices, and various nanocomposites. Due to complicated microstructures and chemical bonding, thermal transport process in these materials has not been well understood yet. In terms of chemical bonding, it is well known that the strength of atomic bonding can significantly affect thermal transport across materials or across interfaces between materials. Given the intrinsic high strength of hydrogen bonds, this dissertation explores the role of hydrogen bonds in nanoscale thermal transport in various materials, and investigates novel material designs incorporating hydrogen bonds for drastically enhanced thermal conduction.

Molecular dynamics simulation is employed to study thermal transport processes in three representative hydrogen-bonded materials: (1) crystalline motifs of the spider silk, silkworm silk and synthetic silk, (2) crystalline polymer nanofibers, and (3) polymer nanocomposites incorporating graphene or functionalized graphene. Computational and theoretical investigations demonstrate that hydrogen bonds significantly facilitate thermal transport in all three material systems. The underlying molecular mechanisms are systematically investigated. The results will not only contribute new physical insights, but also provide novel concepts of materials design to improve thermal properties towards a wide range of applications.

ACKNOWLEDGMENTS

First, I am grateful to my major advisor, Professor Ling Liu, for his continual support, insightful guidance, and the commitment to my training. His open mind, high expectation, and stimulation direct me to delve into a new field beyond my original aspiration. As a result, I learned to build up a global vision, independent thinking, and critical thinking. He is not only my advisor but also my friend, providing endless suggestions and help in my life.

I am also indebted to Professor Heng Ban for his support and insightful discussions. My gratitude also goes out to Professor Steve Scheiner. He generously allowed me to audit three courses lectured by him. His patient instruction and clear teaching enable me to drink from his well of vast knowledge. I would like to thank Professor Nick Roberts and Thomas Fronk for their enthusiastic impartment of knowledge. I am also greatly appreciative of the support and endorsements of Professor Robert E. Spall for my grant and fellowship application.

I would like to thank all the past and present lab colleagues, Heng Zhang, Zhitong Bai, and Jinlong He for my life they filled, the cooperation, and the excellent traits I learned from them. I appreciate the help from Fang Jiang and Jinlu Han in my life.

Finally, I give special thanks to my parents, parents-in-law, my wife, and my daughters for their support, patience, and unconditional love. I thank all those people who helped me reach this point.

Lin Zhang

CONTENTS

Page

ABSTRACT iii

PUBLIC ABSTRACT v

ACKNOWLEDGMENTS vi

LIST OF TABLES xi

LIST OF FIGURES xii

CHAPTER

1 INTRODUCTION 1
  1.1 Motivations and Problem Statement 1
    1.1.1 Challenges of Thermal Management at the Nanoscale 1
    1.1.2 Importance of Material Interfaces in Nanoscale Thermal Transport 2
    1.1.3 Importance of Interfacial Bonding Strength in Nanoscale Thermal Transport 2
    1.1.4 Potentials of Hydrogen Bonds to Enhance Nanoscale Thermal Transport 5
  1.2 Material Systems Studied in This Dissertation 6
    1.2.1 Nanocrystals of Silk Materials 7
    1.2.2 Crystalline Polymer Nanofibers 10
    1.2.3 Carbon/Polymer Nanocomposites 13
  1.3 Outline of Dissertation 15
  REFERENCES 17

2 HYDROGEN BONDING-ASSISTED THERMAL CONDUCTION IN β-SHEET CRYSTALS OF SPIDER SILK PROTEIN 25
  2.1 Abstract 25
  2.2 Introduction 25
  2.3 Models 28
  2.4 Results and Discussion 29
  2.5 Conclusions 37
  2.6 Methods 38
    2.6.1 Calculation of Thermal Conductivity 38
    2.6.2 Phonon Density of States Analysis 39
    2.6.3 Simulation Details 39
  2.7 Acknowledgment 40
  NOTES AND REFERENCES 41

3 EFFECTS OF AMINO ACID SEQUENCE ON THERMAL CONDUCTION THROUGH β-SHEET CRYSTALS OF NATURAL SILK PROTEIN 44
- 3.1 Abstract 44
- 3.2 Introduction 44
- 3.3 Models and Methods 49
- 3.4 Results and Discussions 53
- 3.5 Conclusions 62
- 3.6 Acknowledgments 63
- REFERENCES 64

4 TUNING THERMAL CONDUCTIVITY OF CRYSTALLINE POLYMER NANOFIBERS BY INTERCHAIN HYDROGEN BONDING 67
- 4.1 Abstract 67
- 4.2 Introduction 67
- 4.3 Models and Methods 70
  - 4.3.1 Models 70
  - 4.3.2 Structural Relaxation 71
  - 4.3.3 Non-Equilibrium Molecular Dynamics 72
  - 4.3.4 Calculation of Thermal Conductivity 73
  - 4.3.5 Phonon Dispersion Curves 73
- 4.4 Results and Discussion 74
  - 4.4.1 Hydrogen Bonding-Enhanced Thermal Conductivity 74
  - 4.4.2 Hydrogen Bonding Increases Phonon Group Velocity 77
  - 4.4.3 Hydrogen Bonding Improves Inter-Chain Lattice Ordering 79
  - 4.4.4 Coupled Effects of Inter-Sheet VdW Interaction and Intra-Sheet Hydrogen Bonding 82
- 4.5 Conclusions 84
- 4.6 Acknowledgments 84
- NOTES AND REFERENCES 85

5 EXCEPTIONAL THERMAL CONDUCTANCE ACROSS HYDROGEN-BONDED GRAPHENE/POLYMER INTERFACES 87
- 5.1 Abstract 87
- 5.2 Introduction 88
- 5.3 Results and Discussion 90
- 5.4 Conclusion 105
- 5.5 Experimental Section 106
  - 5.5.1 Interfacial Thermal Conductivity Calculations 106
  - 5.5.2 Molecular Dynamics 107
  - 5.5.3 Vibrational Density of States (VDOS) 109
  - 5.5.4 Cumulative Correlation Factor 110
  - 5.5.5 Integrated Autocorrelation of Interfacial Heat Power 111
  - 5.5.6 Identification of Hydrogen Bonds 112
- REFERENCES 113

6 POLYMERIC SELF-ASSEMBLED MONOLAYERS ANOMALOUSLY IMPROVE THERMAL TRANSPORT ACROSS GRAPHENE/POLYMER INTERFACES 117
6.1 Abstract 117
6.2 Keywords 118
6.3 Introduction 118
6.4 Computational Methods 123
6.4.1 Models 123
6.4.2 Equilibration 125
6.4.3 Interfacial Thermal Conductance. 125
6.4.4 Temperature Contour and Atomic Number Density 127
6.4.5 Herman’s Orientation Factor 127
6.4.6 Vibrational Density of States (VDOS) 128
6.4.7 Cumulative Correlation Factor 129
6.4.8 Integrated Autocorrelation of Interfacial Heat Power 129
6.4.9 Interfacial Adhesion 130
6.5 Results and Discussion 131
6.5.1 Validation of Computation 131
6.5.2 Effect of Grafting Density on Interfacial Thermal Conductance 131
6.5.3 Temperature Field 133
6.5.4 Chain Conformation 134
6.5.5 Herman’s Orientation Factor 136
6.5.6 Vibrational Coupling 138
6.5.7 Integrated Autocorrelation of Interfacial Heat Power 140
6.5.8 Interfacial Adhesion 142
6.6 Conclusions 142
6.7 Associated Content 144
6.7.1 Supporting Information 144
6.8 Acknowledgments 144
REFERENCES 145

7 ENHANCED INTERFACIAL THERMAL TRANSPORT OF GRAPHENE/POLYMER NANOCOMPOSITES VIA A HIERARCHICALLY HYDROGEN-BONDED MOLECULAR HEAT SPREADER 152
7.1 Abstract 152
7.2 Introduction 153
7.3 Modeling and Simulations 156
7.3.1 Modeling 156
7.3.2 Simulations 157
7.4 Results and Discussion 161
7.4.1 Validation 161
7.4.2 Effect of Grafting Density on Interfacial Thermal Conductance 162
7.4.3 Effect of Grafting Density on Interfacial Morphology 163
7.4.4 Role of Polymer Monolayer 170

7.4.5 Dependence on Interfacial Adhesion ... 174
7.4.6 Effect of Hydrogen Bonding Density ... 176
7.5 Conclusion ... 177
7.6 Acknowledgments ... 179
REFERENCES ... 180

8 CONCLUSIONS AND FUTURE WORK ... 184

APPENDIX

A SUPPLEMENTAL MATERIAL OF CHAPTER 2 ... 189
A.1 Structure ... 189
A.2 Determination of Unit Cell Size ... 191
A.3 Determination of Area ... 192
A.4 Representative Temperature Profile and Determination of d*T*/d*x* ... 194
A.5 Phonon Density of States (DOS) and Partial DOS Profiles for Representative β-Sheet Structures ... 195
REFERENCES ... 197

B SUPPLEMENTAL MATERIAL OF CHAPTER 3 ... 199
B.1 Structure ... 199
B.2 Identification of Hydrogen Bonds ... 200
B.3 Calculation of Thermal Conductivity ... 202
REFERENCES ... 203

C SUPPLEMENTAL MATERIAL OF CHAPTER 4 ... 204
C.1 OPLSAA Force Field ... 204
C.2 Effects of Torsional Disorder on Thermal Conduction ... 206
C.3 Normalized Distributions of 12 Types of Dihedrals in Nylon2-20-*m*-1 ... 208
C.4 Time Histories of 12 Types of Dihedrals in Nylon2-20-*m*-1 ... 210
REFERENCES ... 214

D SUPPORTING INFORMATION OF CHAPTER 5 ... 215

E SUPPORTING INFORMATION OF CHAPTER 6 ... 222

F SUPPORTING INFORMATION OF CHAPTER 7 ... 226

CURRICULUM VITAE ... 231

LIST OF TABLES

Table Page

3.1 Computed thermal conductivities of three standalone β-strands (κ_{single}), and the interior and edge β-strands in the corresponding β-sheets (κ_{int} and κ_{edge})..........54

4.1 Length and thermal conductivity of four fully extended nylon chains. Each of them has 20 repeat units along the chain direction. 75

C.1 Non-bonded potential parameters for all atom types of nylon..........204

C.2 Bond stretching potential parameters for all bond types of nylon..........205

C.3 Angle bending potential parameters for all angle types of nylon..........205

C.4 Torsional potential parameters for all dihedral types of nylon..........206

LIST OF FIGURES

Figure Page

1.1 Material interfaces. 3

1.2 Schematic representation of a hydrogen bond....................5

1.3 Thermal conductivities of several biomaterials. 7

1.4 The hierarchical structures of (a) spider silk and (b) silkworm cocoon silk. Each dragline spider silk has (c) a skin-core structure at the macroscopic level. In each thread of the *B. mori* silkworm cocoon, (d) twin filaments are coated by glue-like sericins. Both of the spidroin and fibroin fibrils have similar (e) microscopic structures, where (f) numerous β-sheet nanocrystals are embedded in a semi-amorphous matrix. 8

1.5 Thermal conductivities of several polymers....................10

1.6 Schematic representation of (a) amorphous polymer, (b) aligned polymer nanofiber, and (c) single extended polymer chain....................11

1.7 Thermal conductivities of amorphous polymers, carbon-based nanomaterials, and their composites....................14

1.8 Schematics of (a) a polymer/pristine graphene interface, (b) a polymer/polymer-grafted graphene interface, and (c) a polymer/functionalized graphene interface (with hydrogen bonds). (d) Heat flux without hydrogen bonds. (e) Hypothesized heat flux with hydrogen bonds providing additional thermal pathways. (f) A hierarchical heat spreader combining (b) and (c). 14

2.1 Dragline from the (a) *Nephila clavipes* orb web comprises numerous (b) β-sheet crystal units embedded in an amorphous matrix. (c) Each β-sheet unit consists of β-strands interlocked by hydrogen bonding. (d) For calculating thermal conductivity in β-sheets, a non-equilibrium MD system was employed in which heat flow was generated from the heat source (red region) to the heat sink (blue regions).. 27

2.2 (a) Two configurations of hydrogen bonding (red lines) in β-sheet protein where each R represents a side chain. (b) Thermal conductivity versus the number of β-strands. (c) Phonon DOS profiles of two anti-parallel β-sheet structures. (d) Partial phonon DOS projected on H atoms (hydrogen atoms bonded to nitrogen atoms) and HA atoms (hydrogen atoms bonded to α-carbon atoms) for A16-1-1. (e) Partial phonon DOS projected on backbone atoms for two anti-parallel β-sheets. (f) Phonon DOS profiles for edge and interior β-strands. (g) Phonon DOS profiles for parallel and anti-parallel A16-5-1 β-sheets. 30

2.3 Thermal conductivities of anti-parallel 16-alanine β-sheets predicted by a thermal resistance model (black curve) and extracted from MD simulation (red squares).. 33

2.4 Thermal conductivity versus length for individual poly-A β-strands.. 35

3.1 Natural silk from (a) the *Nephila clavipes* spider and (b) the *Bombyx mori* silkworm has a similar hierarchical structure in which the (c) β-sheet protein structure serves as an essential building block. (d) poly-A motifs, while those in the *Bombyx mori* silkworm silk are formed by repeated (e) poly-(GA) motifs. (f) To compute the thermal conductivity of a β-sheet, heat flow is generated from the "heat source" (red region) to the "heat sink" (blue region) by a velocity swapping algorism. (g) The β-sheet is analogous to a network of thermal resistors.. 46

3.2 (a) Thermal conductivity and (b) thermal conductance versus the number of β-strands (n) for the poly-A, poly-G, and poly-(GA) β-sheets. 52

3.3 Evaluation of the cross-sectional area of a poly-A β-strand based on the equilibrium positions of the interior β-strands in a β-sheet................................ 57

3.4 Partial phonon DOS projected on the glycine and alanine residues of (a) a GA8-5-1 β-sheet and (b) a standalone GA8-1-1 β-strand. 58

3.5 Thermal conductivity versus the number of layers in β-sheet structures with the poly-A and poly-(GA) sequences. 62

4.1 (a) Illustration of hydrogen bonds in crystalline polymers. (b) Molecular structure of an extended polymer chain of nylon 4. (c) Multiple such chains are interlocked by hydrogen bonds to form a crystalline nanosheet. (d) Multiple such nanosheets stack to form a nylon crystal. (e) A computational model of a crystalline nylon nanofiber. (f) An example temperature profile (solid spheres) along the direction of heat flux (x-direction).. 70

4.2 (a) Normalized thermal conductivity of 20 nylon nanosheets with different types and different widths (characterized by *m*). (b) Normalized thermal conductivity versus the number density of hydrogen bonds in the nanosheet. 75

4.3 (a) Phonon dispersion curves of nylon2-2-1-1 (left) and nylon2-2-2-1(right). (b) Acoustic phonon branches are compared between nylon2-2-1-1 (black), nylon2-2-2-1 (blue), and nylon2-2-3-1 (red).. 78

4.4 (a) Normalized distribution of all dihedrals in the nylon2-20-*m*-1 nanosheets where *m* is 1, 2, and 3, respectively. (b) The H-N-CT-C dihedral. (c) The mean of all H-N-CT-C dihedrals versus time. (d) The standard deviation of all H-N-CT-C dihedrals versus time...............................80

4.5 (a) Thermal conductivity of multilayer nylon 2 nanofibers, nylon2-20-*m*-*m*, where *m* is 1, 2, 3, 5, and 7. (b) Normalized dihedral distribution of the nylon2-20-2-2 nanofiber and the nylon2-20-1-1 single chain............................83

5.1 (a) A molecular dynamics simulation system to calculate interfacial thermal conductance. (b) The interface between graphene (cyan) and PMMA (grey) is dominated by van der Waals interactions. (c) The interface between hydroxyl-functionalized graphene (cyan) and PMMA (grey) involves numerous hydrogen bonds (red dashed lines). Temperature profiles generated in the systems incorporating (d) graphene/PMMA interfaces and (e) hydroxyl-functionalized graphene/PMMA interfaces. 91

5.2 (a) Interfacial thermal conductance at graphene/PMMA (MLG), methyl-functionalized graphene/PMMA (MLG-CH_3), and hydroxyl-functionalized graphene/PMMA (MLG-OH) interfaces. (b) Temperature distributions near the MLG (top panel) and MLG-OH (bottom panel) interfaces...92

5.3 Atomic number density of PMMA in the vicinity of graphene in the MLG, MLG-CH_3, and MLG-OH systems..95

5.4 Vibrational density of states (VDOS) of different components of (a) MLG, (b) MLG-CH_3, and (c) MLG-OH. 96

5.5 Cumulative correlation factor calculated between the graphene and PMMA in MLG, between the hydroxyl groups and PMMA in MLG-OH, and between the methyl groups and PMMA in MLG-CH_3. 99

5.6 The integrated autocorrelation of interfacial heat power (a) between the graphene and PMMA in MLG, (b) between three components of the functionalized graphene and PMMA in MLG-CH_3, and (c) between three components of the functionalized graphene and PMMA in MLG-OH. 100

5.7 Interfacial thermal conductance versus the degrees of functionalization in MLG-OH and MLG-CH_3.. 101

5.8 (a) Number of hydrogen bonds versus time at a hydroxyl-functionalized graphene/PMMA interface. (b) Converged integrated autocorrelation of interfacial heat power between PMMA and three components of the hydroxyl-functionalized graphene at three degrees of functionalization. 103

5.9 (a) Atomic number density of PMMA in MLG-CH_3 with different degrees of functionalization. (b) Converged integrated autocorrelation of interfacial heat power between PMMA and three components of the methyl-functionalized graphene at three degrees of functionalization....104

6.1 (a) Atomistic model of the graphene/polymer interface. (b) A 3D view of the PE-functionalized graphene. (c) A representative temperature profile generated by reverse non-equilibrium molecular dynamics simulation. (d) An example computational system for RNEMD simulation with periodic boundary conditions applied along all directions. 123

6.2 Atomistic model for pullout simulation. 130

6.3 Interfacial thermal conductance in G*X*PE8 versus *X*, the number of PE chains grafted to each side of graphene. 132

6.4 Temperature profiles for (a) G32PE8 and (b) G1PE8. The matching temperature contours are also plotted for (c) G32PE8 and (d) G1PE8. 134

6.5 Atomic number density distributions of graphene and selected PE chains for (a) G32PE8 and (b) G1PE8. Temperature contours are also plotted for (c) G32PE8 and (d) G1PE8. 136

6.6 Distributions of the local Herman's orientation factor for PE chains (a,c,e,g) and PMMA chains (b,d,f,h) in G32PE8, G16PE8, G8PE8, and G1PE8, respectively 137

6.7 The vibrational density of states (VDOS) of PE, PMMA, and graphene in (a) G32PE8 and (b) G1PE8. (c) The cumulative correlation factor between PMMA and graphene (solid lines) and between PMMA and PE (dashed lines) in both G32PE8 (red) and G1PE8 (black) systems. 139

6.8 The integrated autocorrelation of interfacial heat power exchange (a) between graphene (sp^2 carbons) and PMMA and (b) between PE and PMMA for four systems with increasing *X*. 141

6.9 Pullout force versus interfacial separation for five systems with increasing *X*. 141

7.1 (a) A representative system for nonequilibrium molecular dynamics simulation. (b) A snapshot of the interfacial structure between PVA functionalized graphene and PMMA. (c) Temperature profile of G32PVA generated by RNEMD simulation. (d) Interfacial thermal conductance versus the number of functional molecules grafted on graphene (*X*) for G*X*PVA and G*X*OH, respectively..159

7.2 An atomistic model for the molecular dynamics simulation of the pull-out process. 160

7.3 Temperature profiles of (a) G1PVA and (b) G32PVA from nonequilibrium molecular dynamics simulation. Temperature contours of (c) G1PVA and (d) G32PVA. 161

7.4 Contour plots of atomic number density (a) and (b), plots of hydrogen bonds (c) and (d), and contour plots of temperature (e) and (f) for graphene and a pair of PVA chains in G1PVA and G32PVA, respectively. 164

7.5 Atomic number density distributions of (a) PVA and (b) PMMA versus the distance to the surface of graphene...167

7.6 Averaged number of hydrogen bonds per PVA chain......................................168

7.7 Local Herman’s orientation factor of main chains of PMMA and PVA in G*X*PVA with $X = 1$ (a), 8 (b), 16 (c), and 32 (d). 168

7.8 Partial vibrational density of states (VDOS) of (a) G1PVA and (b) G32PVA. (c) Cumulative correlation factor. 171

7.9 Integrated autocorrelation of interfacial heat power (a) between PVA and PMMA and (b) between graphene (sp^2 carbons) and PMMA. 173

7.10 Pull-out force versus interfacial separation. 175

7.11 Interfacial thermal conductance versus the proportion of vinyl alcohol (VA) units in the copolymer of ethylene and vinyl alcohol (EVOH). 176

A.1 (a) The protein sequence of MaSp1 and MaSp2 *N. Clavipes* spider silk [3]. (b) A snapshot of the simulation model from VMD. (c) Percentage of hydrogen bond formation versus simulation time. (d) Structural comparison for a β-sheet before and after energy exchange. 189

A.2 Variations of (a) system potential energy and (b) number of hydrogen bonds with respect to unit cell size along the length direction..........................191

A.3 Determination of the area associated with each β-strand. 193

A.4 Determination of d*T*/d*x*...194

A.5 (a) Phonon DOS profiles of three antiparallel β-sheet structures (A16-1-1, A16-3-1, and A16-5-1). Partial phonon DOS projected on (b) backbone atoms, (c) H atoms (hydrogen atoms bonded to nitrogen atoms), (d) HA atoms (hydrogen atoms bonded to α-carbon atoms), (e) HB atoms (hydrogen atoms of methyl groups), and (f) nitrogen atoms (denoted by N). 195

B.1 (a) A snapshot of the simulation model from VMD. (b) Percentage of hydrogen bond formation versus simulation time. (c) Structural comparison for a β-sheet before and after velocity swapping..........................200

B.2 Temperature profile along the length of a β-sheet 201

C.1 (a) Dihedral distributions of nylon4-20-1-1 computed with and without considering the dihedral potential in the force field. (b) Thermal conductivities of nylon4-20-1-1 and nylon4-20-2-1 computed with and without the dihedral potential. 207

C.2 Normalized distribution of dihedrals. 209

C.3 Mean value of dihedral angles versus time. 211

C.4 Standard deviation of dihedral angles versus time. 213

D.1 Atomic number density of the atoms of different types in the functional groups in MLG-OH and MLG-CH_3. The graphene is positioned at $z = 0$. 215

D.2 (a) Interfacial normal stress versus the displacement of the filler material with respect to PMMA in MLG, MLG-OH, and MLG-CH3. (b) Schematic illustration of the interfacial strength simulation setup. 216

D.3 In-plane and out-of-plane vibrational density of states (VDOS) of different components in three material systems. 217

D.4 In-plane and out-of-plane cumulative correlation factors between PMMA and different components of the filler materials...218

D.5 The integrated autocorrelation of interfacial heat power between PMMA and the sp^2 and sp^3 carbon atoms of the functionalized graphene in MLG-OH (left) and MLG-CH_3 (right). 218

D.6 The integrated autocorrelation of interfacial heat power between three components of the hydroxyl-functionalized graphene and PMMA in MLG-OH at three degrees of functionalization (*S*): (a) 6.25%, (b) 12.5%, and (c) 25%....219

D.7 The integrated autocorrelation of interfacial heat power between three components of the methyl-functionalized graphene and PMMA in MLG-CH_3 at three degrees of functionalization (*S*): (a) 6.25%, (b) 12.5%, and (c) 25%. 219

D.8 Atomic number density of PMMA in MLG, and MLG-CH_3 and MLG-OH with different degrees of functionalization (*S*). 220

D.9 Illustration of how the converged integrated autocorrelation of interfacial heat power is calculated....220

D.10 Schematic representation of a hydrogen bond....221

E.1 A molecular dynamics simulation system to evaluate interfacial thermal conductance by nonequilibrium molecular dynamics method. 222

E.2 Atomic number density distributions of graphene and two functional polyethylene chains for G32PE8. 223

E.3 Normalized end-to-end length and height of PE chains versus the number of PE chains in GXPE8 (8 repeat units). 224

E.4 Temperature contours of graphene and two functional polyethylene chains for G32PE8. 224

E.5 Local Herman's orientation factors of main chains of polyethylene molecules and PMMA matrix for (a) G32PE8, (b) G16PE8, (c) G8PE8, and (d) G1PE8, respectively. 225

F.1 A system setup for nonequilibrium molecular dynamics simulations (NEMD). 226

F.2 Heat energy added to the heat source by the Langevin thermostat versus time in NEMD. 226

F.3 Contour plots of the atomic number density of graphene and a pair of PVA chains chosen from G32PVA. 227

F.4 Geometric criterion to identify a hydrogen bond. 227

F.5 Plots of hydrogen bonds formed with a pair of PVA chains of G32PVA.........228

F.6 Temperature profiles of G1PVA from NEMD. 228

F.7 Temperature contours of graphene and a pair of PVA chains of G32PVA. 229

F.8 Hydrogen bonds of G*X*PVA (a) between PVA and PMMA and (b) within PVA. 229

F.9 Local Herman's orientation factor of main chains in G*X*PVA. 230

CHAPTER 1

INTRODUCTION

1.1 Motivations and Problem Statement

1.1.1 Challenges of Thermal Management at the Nanoscale

Nanotechnology has advanced many technologies such as nanoelectronics, nanocomposites, and biomedical therapies, which have significantly impacted the industry and the society. These technologies usually require effective and efficient thermal transport in materials for heat dissipation [1-4]. Due to the recent progress in synthesis, processing, and characterization techniques, the size of engineering devices and structures continually decreases down to the nanometer level, and the size of structures is comparable to the mean free path of phonons. Therefore, many factors that are negligible at larger length scales emerge to dictate thermal transport processes at the nanoscale. In the past decades, numerous studies have been carried out to understand the mechanisms of nanoscale thermal transport and enhance thermal transport by engineering new materials with novel microstructures and chemistry [5-7]. Despite the significant progress, gaps still exist between experimental findings and theoretical understanding as well as between the demand by application and the performance achievable by current techniques. For instance, thermal transport in biological macromolecular systems including proteins is underexplored, which is known to affect allosteric communication pathways [8-10]. Another example is the great challenges for heat removal and thermal management in nanoelectronics due to the constant increase in power and decrease in size. All these challenges call for advancements in materials science to improve the understanding of fundamental physics and to create new concepts of materials design.

1.1.2 Importance of Material Interfaces in Nanoscale Thermal Transport

Heat conduction in solids results from the random motions of energy carriers from one position of the system to another. These carriers include phonons, electrons, and photons [11]. In particular, phonons represent quantized energy waves associated with vibrations of atoms. When the structural size is much larger than the phonon mean free path (i.e. the average distance that a carrier travels between two successive collisions), the primary resistance to heat flow results from the scattering of heat carriers, which is defined as diffusive thermal transport. At the nanoscale, phonon mean free path may be longer than the size of structural features including interfaces and boundaries. Therefore, scattering between phonons at material interfaces or boundaries becomes a critical factor that significantly affects the thermal transport processes [5, 6, 12].

1.1.3 Importance of Interfacial Bonding Strength in Nanoscale Thermal Transport

This dissertation involves interfaces of the same materials and between dissimilar materials, all of which dictate nanoscale thermal transport by scattering phonons [5, 6]. The strength of the interfacial bonding plays an important role in determining thermal transport both parallel to (Fig. 1.1(a)) and perpendicular to (Fig. 1.1(b)) the material interface.

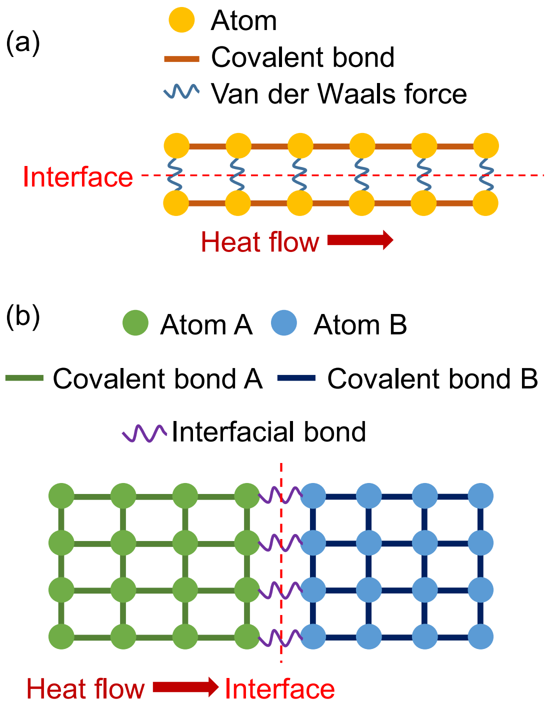
(a)
Atom
Covalent bond
Van der Waals force
Interface
Heat flow
(b)
Atom A
Atom B
Covalent bond A
Covalent bond B
Interfacial bond
Heat flow
Interface

Fig. 1.1 Material interfaces. (a) An interface between two molecular chains of the same material, and (b) an interface between two dissimilar materials.

In the case where heat flow is parallel to the interface (Fig. 1.1(a)), one-dimensional Frenkel-Kontorova lattice models have been developed to theoretically study the effects of intrachain and interchain interactions on the thermal conductivities of materials consisting of multiple identical chains [13-16]. The interchain covalent bonding and nonbonded interactions are modeled by harmonic springs and on-site potentials, respectively. The interchain interactions are described by either harmonic springs or the van der Waals interactions. For the former, the thermal conductivity of a double-chain lattice increases with the strength of the interchain covalent bonding when the on-site potential is above 10.0 and decreases when the on-site potential is below 5.0 [15]. For the latter, thermal conductivity increases with the intensity of the interchain van der Waals interactions when the dimensionless temperature is below 0.11 [14]. Furthermore, computational and experimental results have demonstrated that weak van der Waals interactions typically reduce the thermal conductivity of bundled or layered materials with increased constituting units. Examples include bundled carbon nanotubes (CNTs) [17], multi-walled CNTs [18], and few-layer graphene [19, 20]. Moreover, the thermal conductivity of multilayer boron nanoribbons is found to increase with the number of layers owing to the strong van der Waals interactions [21]. All these results suggest that stronger interchain or interlayer interactions can improve thermal conductivities.

In the case where heat flow is perpendicular to the interface (Fig. 1.1(b)), the effect of interfacial bonding on thermal conductance has been extensively studied by molecular dynamics simulations, theoretical models, and experiments. These studies range from gas/solid crystal interfaces [22], liquid/surfactant interfaces [23], solid crystal/solid crystal interfaces [24], and solid crystal/amorphous polymer interfaces [25], to solid crystal/self-assembled monolayer/solid crystal interfaces [26, 27]. Interfacial thermal conductance is found to be approximately linear with the interfacial bonding, which is in agreement with the findings by experiments [28]. An analytical model with van der Waals interactions shows that interfacial thermal conductance is proportional to the square of interfacial van der Waals forces when the strength is weak [29]. As the strength increases further, interfacial thermal conductance reaches a plateau. All of these simulations and theoretical studies have demonstrated that stronger interfacial bonding facilitates thermal transport across the interfaces between dissimilar materials.

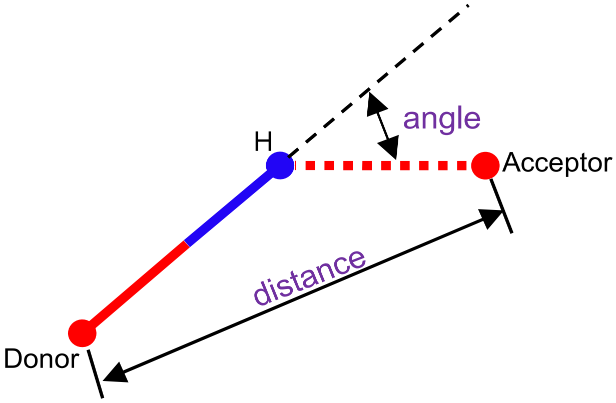

Fig. 1.2 Schematic representation of a hydrogen bond (red dashed line).

Studies in both areas indicate that enhancing the strength of molecular interactions may enhance thermal transport parallel to the interface in bundled materials and across the interface between dissimilar materials.

1.1.4 Potentials of Hydrogen Bonds to Enhance Nanoscale Thermal Transport

A hydrogen bond is a secondary bond between polar groups resulting from electrostatic attraction, as shown in Fig. 1.2. It forms between a hydrogen atom (H) which is bonded to a more electronegative atom, the donor (D), and another nearby highly electronegative atom, the acceptor (A) [30-32]. A hydrogen bond can be denoted by D–H…A, where the hyphen represents a covalent bond and the three dots indicates the hydrogen bond. D and A can be nitrogen (N), oxygen (O), or fluorine (F). The strength of hydrogen bonds varies from 10 to 100 kJ mol^{-1}, 1~2 orders of magnitude stronger than that of van der Waals interaction [30, 31, 33].

Hydrogen bonds are a ubiquitous and fundamental element of many materials including proteins, hydrogels, organic electronics and photovoltaic materials, and DNA

[34]. In proteins, hydrogen bonds are essential to the formation of secondary structures including β-sheets and α-helices, without which proteins cannot exist [35]. In hydrogels, polar groups in the polymer strongly bind water through hydrogen bonds, leading to tough hydrogels [36]. Hydrogen bonds are also responsible for many other excellent physical properties of materials. For instance, hydrogen bonds have been shown to play a key role in determining the extraordinary mechanical properties of spider silk [37].

Hydrogen bonds have the potentials to enhance the existing thermal pathways and create new ones to conduct heat more efficiently. For example, the thermal conductivity of a polymer blend of poly(N-acryloyl piperidine) and poly(acrylic acid) was measured to be 1.5 W m^{-1} K^{-1}, an order of magnitude higher than that of the constituting polymers [38]. Another example is that α-helices of more hydrogen bonds have higher thermal diffusivity [39, 40]. Since hydrogen bonds are stronger than the van der Waals interactions, we hypothesized that properly engineered hydrogen bonds can drastically improve thermal transport both parallel to and perpendicular to interfaces.

1.2 Material Systems Studied in This Dissertation

Three representative material systems are studied in this dissertation to verify whether or not hydrogen bonds facilitate thermal transport in nanostructures and across material interface and to quantitatively reveal the role of hydrogen bonds in nanoscale thermal transport. These materials are crystalline units in silk proteins, nanocrystalline polymer nanofibers, and graphene/polymer nanocomposites. In the first two cases, materials are crystalline and composed of bundles of individual strands or chains, and thermal energy transports parallel to the interfaces (boundaries). The last one consists of mechanically dissimilar materials, where heat conducts across the interfaces.

1.2.1 Nanocrystals of Silk Materials

Spider silk, an ancient fibrous biomaterial over several million years of evolution, has attracted substantial attention in the past decade due to its extraordinary mechanical properties including large extensibility and high stiffness, strength, and toughness [41-44]. These properties, along with the inherent biocompatibility, have made spider silk a versatile material with enormous potential for aerospace, biological, and medical applications [45]. For thermal conductivity, dragline silk of *Nephila clavipes* was first measured up to 151~416 W m^{-1} K^{-1}, comparable to that of copper [46]. However, the value was measured to be 1.23 W m^{-1} K^{-1} with the same experimental setup except for an improved heat transfer model and a higher vacuum level [47]. Despite the discrepancy, the measured thermal conductivities of the spider silk are at least more than four times that of other proteins including myoglobin and the green fluorescent protein [48] (Fig. 1.3), making it promising for various applications.

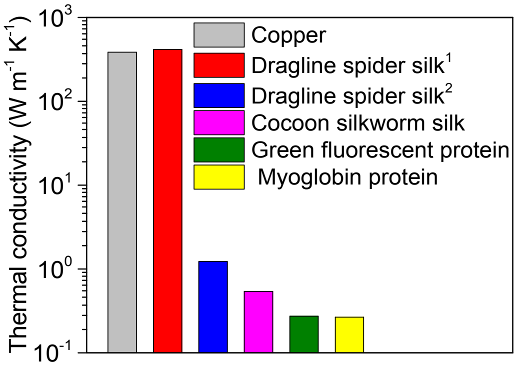

Fig. 1.3 Thermal conductivities of several biomaterials [46, 47, 49, 51]. The data of Dragline^{1} is from [46], and that of Dragline^{2} from [47].

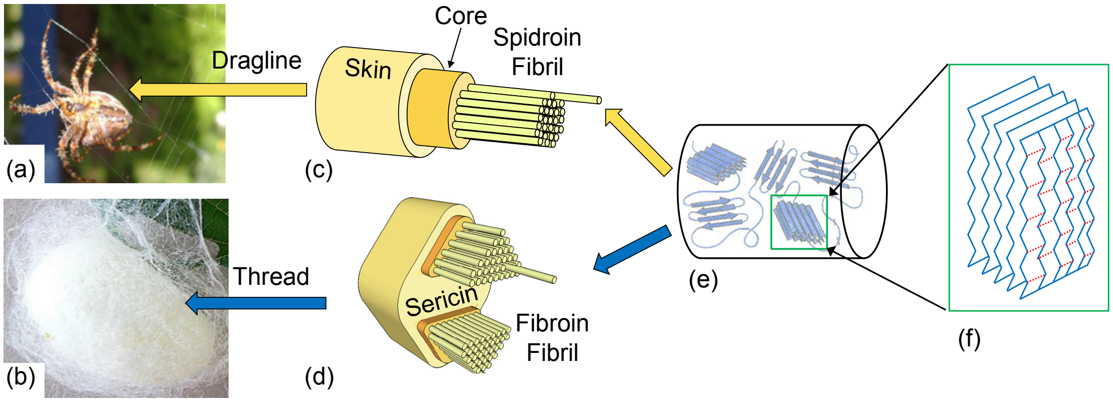

Fig. 1.4 The hierarchical structures of (a) spider silk and (b) silkworm cocoon silk. Each dragline spider silk has (c) a skin-core structure at the macroscopic level. In each thread of the *B. mori* silkworm cocoon, (d) twin filaments are coated by glue-like sericins. Both of the spidroin and fibroin fibrils have similar (e) microscopic structures, where (f) numerous β-sheet nanocrystals are embedded in a semi-amorphous matrix.

In contrast, thermal conduction in silkworm silk is less efficient and as low as 0.54 W m^{-1} K^{-1} [49], and silkworm silk-based textiles have been used as a thermal insulator for thousands of years [50]. It is striking that spider and silkworm silks (shown in Fig. 1.3), both spun by arthropods, have such different thermal conducting capabilities which must be attributable to the distinctions in microstructures.

Fig. 1.4 shows that the proteins of spider and silkworm silks have similar hierarchical structures, where β-sheets are embedded in a semi-amorphous matrix of helices and β-turns [52, 53]. The β-sheets are composed of multiple aligned polypeptide strands, interlocked by hydrogen bonds, and are believed to underpin the silk's exceptional mechanical properties [37, 42, 54] including large extensibility and high stiffness, strength, and toughness [41-44]. Compared with β-sheets, the amorphous phase is characterized by more phonon scattering and shorter mean free path of phonons, which are expected to reduce thermal conductivities significantly [55]. Furthermore, according to the relationship between thermal conductivity and elasticity (i.e. $k \sim \sqrt{E}$ where E is the Young's modulus, and k is the thermal conductivity) [46], it is straightforward to expect that β-sheet crystals are good thermal conductors in view of their high elastic moduli. As a result, this study focuses on the β-sheets nanocrystals, and amorphous phase are not studied in this dissertation.

Regarding the protein sequence of β-sheets, the dragline silk of the *Nephila clavipes* spider has abundant poly-Alanine repeats while the cocoon silk from the *Bombyx mori* silkworm features poly-(Glycine-Alanine) repeats [52, 53]. Such a difference in the protein sequence has been found responsible for the distinct mechanical properties of different β-sheets [56]. Nevertheless, how thermal conduction is affected by the protein sequence remains unknown.

Many techniques have been developed to produce silk materials with desirable primary sequences. With genetic recombination, synthetic fibers were produced with the recombinant spider silk proteins extracted from *E. coli*, yeast, tobacco, and even goat's milk [57, 58]. Manipulation of protein sequences enables the control of the proportion of secondary structures and hence material properties. However, it is unknown how heat flow in the β-sheets of silk proteins is affected by the side groups of different types of amino acids. Understanding the underlying mechanisms will not only provide insights into the thermal behavior of natural spider silk and other biomaterials but also may guide a rational design of synthetic silk [59-61] to achieve tunable thermal properties for a wide range of applications.

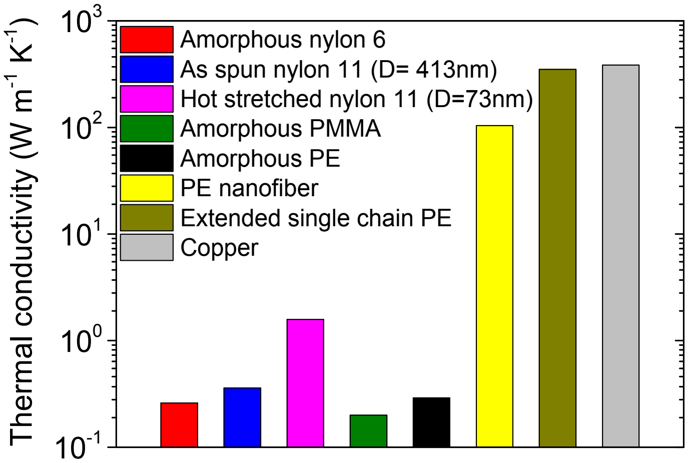

Fig. 1.5 Thermal conductivities of several polymers [64-68]. *D* is the diameter. The draw ratio of hot stretched nylon 11 and PE nanofiber is 1.5 and 410, respectively [67, 68].

1.2.2 Crystalline Polymer Nanofibers

Polymers are key materials in many engineering technologies for their low mass density, high corrosion resistance, excellent manufacturability, and low costs [62]. Despite many advantages, the material suffers from an apparent bottleneck. Bulk polymers are thermal insulators and have low thermal conductivities on the order of 0.1-0.5 W m^{-1} K^{-1} [63] (Fig. 1.5). The low thermal conductivity makes polymers inferior to metals and ceramics for applications where fast heat dissipation is essential.

The morphology of polymers significantly affects their thermal transport properties. Polymers can be amorphous (Fig. 1.6a), crystalline (Fig. 1.6b), or semi-crystalline, depending on the nature of polymer and process. As the molecular weight and type of monomers increase, bulk polymers are usually semi-crystalline where the crystalline units are embedded in the amorphous regions. Molecular chains in the amorphous region are randomly oriented and entangled, while those of crystalline region are well aligned.

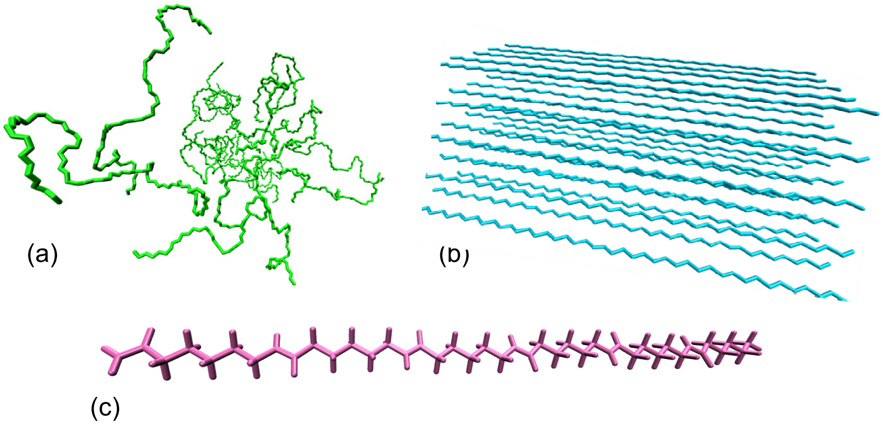

Fig. 1.6 Schematic representation of (a) amorphous polymer, (b) aligned polymer nanofiber, and (c) single extended polymer chain.

Moreover, bulk polymers feature plenty of defects including the ends of molecular chains, vacancies, branched chains, and impurities. The random coils, molecular entanglement, and defects significantly scatter phonons in the bulk polymers and shorten the mean free path of heat carrier, phonons, resulting in low thermal conductivities.

Contrary to common wisdom, the thermal conductivity of single polyethylene chains can be larger than 350 W m^{-1} K^{-1} [66]. This drastic difference underscores the significance of molecular morphology on the thermal conductivities. For single polymer chains, non-straight morphology including waviness and torsion is known to affect the conduction along the chain negatively [69]. The scattering caused by the waviness and torsion can be significantly suppressed in single extended polymer chains (Fig. 1.6c). Therefore, aligning polymer chains by mechanical stretching becomes a promising method to improve the thermal conductivity of polymers. For hot-stretched nanofibers [67] or the crystalline nanofibers formed by other processing techniques [68], the amorphous regions and defects are reduced drastically. An ultra-drawn polyethylene nanofiber can have a high thermal conductivity of 104 W m^{-1} K^{-1}, mainly due to the enhanced phonon transport in mechanically aligned polymer chains [70]. With the draw ratio of 1.5, the thermal conductivity of nylon 11 nanofibers can be 4.4 times that of the as-spun counterpart [67]. Molecular dynamics simulations demonstrated that the thermal conductivity of an amorphous polymer could be increased by ~500% with a tensile strain of 100% [55]. The ultimate solution to generate aligned polymer chains is to produce single-crystal polymers. Novel topochemical polymerization reaction has been developed to produce high-quality, large-size polymer single crystals [71]. The advancements have made it compelling to design single-crystal polymers.

When multiple aligned chains form a nanofiber or bulk material, the strength of the interchain interaction becomes a critical factor. A three-dimensional polyethylene nanofiber has a thermal conductivity of 50 W m^{-1} K^{-1} [72], much lower than that of single extended polymer chains, mainly due to the weak van der Waals interactions between the aligned polymer chains. Stronger than van der Waals interaction, hydrogen bonds are advantageous to improve the thermal conductivity of an amorphous polymer blend up to 1.5 W m^{-1} K^{-1}, an order of magnitude higher than that of its constituting polymers, 0.19 and 0.22 W m^{-1} K^{-1} [38].

Hydrogen bonds are promising to improve the thermal conductivity of aligned polymer fibers. Polymer molecules must possess enormous hydrogen bond donors and acceptors for a lot of interchain hydrogen bonds. Despite this, the design is flexible since hydrogen bond-capable moieties (donors or acceptors) exist in many synthetic polymers such as nylons, PMMA, and the poly-(acrylic acid). However, it deserves noting that, changes in the molecular monomers for hydrogen bonding by introducing other atoms into the polymers may induce new mechanisms scattering the heat conducting phonons. The competition between hydrogen-bond-enabled enhancement and the increased phonon scattering must be well understood and balanced to maximize the thermal transport properties. The optimal designs involve the selection of hydrogen bond-capable moieties at controlled densities to systematically study the effects of the type and density of hydrogen bonds in the thermal transport processes.

1.2.3 Carbon/Polymer Nanocomposites

Another way to improve the thermal conductivity of polymers is introducing materials of high thermal conductivities such as graphene [73] and carbon nanotube [3] to make nanocomposites. However, the enhancement of thermal conductivity including the carbon materials is not as expected, lower than the prediction by the effective medium theory [74, 75] (Fig. 1.7). Despite the high thermal conductivities of graphene (~5000 W m^{-1} K^{-1}) and nanotubes (2000~6600 W m^{-1} K^{-1}) [76, 77], the graphene/polymer and nanotube/polymer interfaces feature low thermal conductance of 60 and 12 MW m^{-2} K^{-1} [74, 78]. At the interfaces, heat flow is inhibited due to the weak interfacial interactions. To this end, enormous efforts have been made on grafting graphene with polymer chains [79] and tailoring phonon modes with functionalization [80].

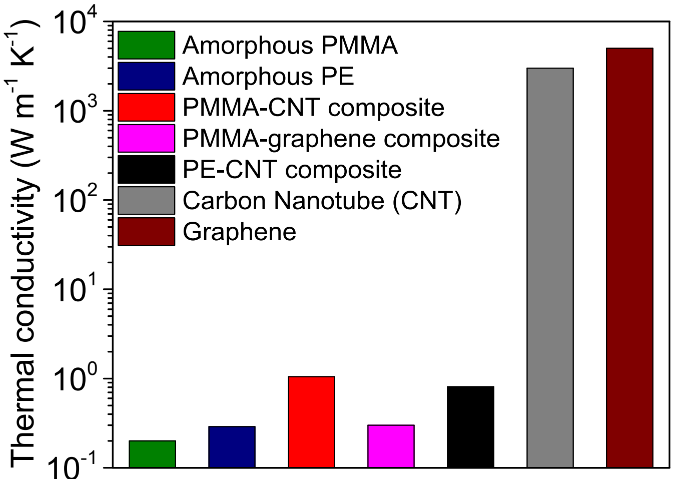

Fig. 1.7 Thermal conductivities of amorphous polymers, carbon-based nanomaterials, and their composites [51, 64, 76, 77, 81-86].

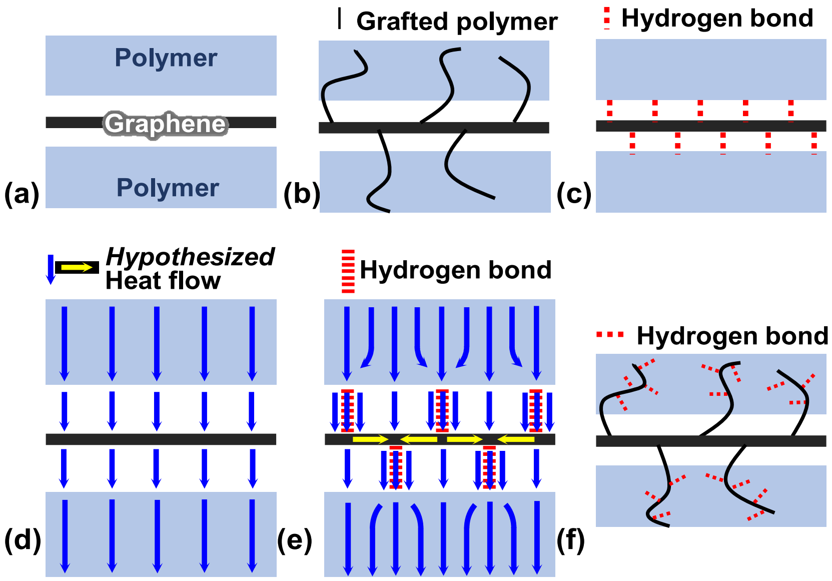
Polymer
Graphene
Polymer
(a)
Grafted polymer
(b)
Hydrogen bond
(c)
Hypothesized
Heat flow
(d)
Hydrogen bond
(e)
Hydrogen bond
(f)

Fig. 1.8 Schematics of (a) a polymer/pristine graphene interface, (b) a polymer/polymer-grafted graphene interface, and (c) a polymer/functionalized graphene interface (with hydrogen bonds). (d) Heat flux without hydrogen bonds. (e) Hypothesized heat flux with hydrogen bonds providing additional thermal pathways. (f) A hierarchical heat spreader combining (b) and (c).

At pristine graphene/PMMA interface (Fig. 1.8(a)), heat is conducted via the interfacial van der Waals interaction (Fig. 1.8(d)). The weak strength of the van der Waals interaction makes the conduction inefficient. To increase the coupling between the graphene and the polymer matrix, polymer chains (Fig. 1.8(b)) [79] and functionalize groups [80] have been introduced to the graphene surfaces. These polymer chains and functional groups are covalently bonded to the graphene, serving as “bridges” between the polymer matrix and the graphene nanofillers to improve thermal conduction. The morphology of the polymer chains can be straight or randomly coiled, depending on the length, density, and stiffness of the chains.

Recent advances in chemical functionalization provide an additional stimulus to extend the applications of low-dimensional materials including carbon nanotubes [87] and graphene [88]. This study aimed to verify whether hydrogen bonds can facilitate the thermal transport perpendicular to material interfaces (Fig. 1.8(c)) by creating new pathways (Fig. 1.8(e)). Furthermore, a hierarchical design illustrated in Fig. 1.8 (f) was proposed to combine the concepts of polymer-grafted graphene (Fig. 1.8 (b)) and hydrogen-bonded interface (Fig. 1.8(c)). There are several parameters including the chain morphology and density of hydrogen bonds explored for the desired thermal properties.

1.3 Outline of Dissertation

This dissertation is organized by a multi-paper format. Each of the following chapters has been published in a journal or submitted as a research paper. References are placed at the end of each chapter, and supporting materials for all chapters can be found at the end of the dissertation.

The remaining portion of this dissertation is organized as follows. Chapter 2 [89] investigates how hydrogen bonding affects thermal transport in beta sheet nanocrystals of spider silk. The effect of amino acid sequence on the thermal conductivity of beta sheet nanocrystals in silkworm silk, spider silk, and synthetic silk is described in Chapter 3 [90]. In Chapter 4 [91], we explore the role of hydrogen bonds in thermal transport in nylon nanofibers along the chain direction and the effect of hydrogen bond density. Chapter 5 [92] focuses on how hydrogen bonds influence interfacial thermal transport between graphene and the PMMA matrix. Chapter 6 demonstrates the effect of the morphology of polymer chains grafted onto graphene on interfacial thermal transport in polymer nanocomposites. A hierarchical design to enhance interfacial thermal transport is proposed and verified in Chapter 7. Finally, conclusions and future studies are described in Chapter 8.

REFERENCES

[1] Jain, A., and Goodson, K. E., 2011, "Thermal microdevices for biological and biomedical applications," J Therm Biol, 36(4), pp. 209-218.

[2] Pop, E., 2010, "Energy Dissipation and Transport in Nanoscale Devices," Nano Res, 3(3), pp. 147-169.

[3] Han, Z., and Fina, A., 2011, "Thermal conductivity of carbon nanotubes and their polymer nanocomposites: A review," Progress in Polymer Science, 36(7), pp. 914-944.

[4] Xue, X. J., Wang, F., and Liu, X. G., 2011, "Emerging functional nanomaterials for therapeutics," J Mater Chem, 21(35), pp. 13107-13127.

[5] Cahill, D. G., Braun, P. V., Chen, G., Clarke, D. R., Fan, S. H., Goodson, K. E., Keblinski, P., King, W. P., Mahan, G. D., Majumdar, A., Maris, H. J., Phillpot, S. R., Pop, E., and Shi, L., 2014, "Nanoscale thermal transport. II. 2003-2012," Appl. Phys. Rev., 1(1), p. 011305.

[6] Cahill, D. G., Ford, W. K., Goodson, K. E., Mahan, G. D., Majumdar, A., Maris, H. J., Merlin, R., and Sr, P., 2003, "Nanoscale thermal transport," J. Appl. Phys., 93(2), pp. 793-818.

[7] Leitner, D. M., 2008, "Energy flow in proteins," Annu. Rev. Phys. Chem., 59, pp. 233-259.

[8] Burendahl, S., and Nilsson, L., 2012, "Computational studies of LXR molecular interactions reveal an allosteric communication pathway," Proteins, 80(1), pp. 294-306.

[9] Miño-Galaz, G. A., 2015, "Allosteric Communication Pathways and Thermal Rectification in PDZ-2 Protein: A Computational Study," J. Phys. Chem. B, 119(20), pp. 6179-6189.

[10] Ota, N., and Agard, D. A., 2005, "Intramolecular signaling pathways revealed by modeling anisotropic thermal diffusion," J Mol Biol, 351(2), pp. 345-354.

[11] Chen, G., 2005, Nanoscale Energy Transport and Conversion, Oxford University Press, USA.

[12] Maldovan, M., 2012, "Transition between ballistic and diffusive heat transport regimes in silicon materials," Applied Physics Letters, 101(11), p. 113110.

[13] Ai, B. Q., and Hu, B. B., 2011, "Heat conduction in deformable Frenkel-Kontorova lattices: Thermal conductivity and negative differential thermal resistance," Phys Rev E, 83(1), pp. 011131.

[14] Sun, T., Wang, J. X., and Kang, W., 2013, "Van der Waals interaction-tuned heat transfer in nanostructures," Nanoscale, 5(1), pp. 128-133.

[15] Zhong, W. R., 2010, "Different thermal conductance of the inter- and intrachain interactions in a double-stranded molecular structure," Phys Rev E, 81(6), pp. 061131.

[16] Diaz, E., Gutierrez, R., and Cuniberti, G., 2011, "Heat transport and thermal rectification in molecular junctions: A minimal model approach," Phys Rev B, 84(14), p. 144302..

[17] Hone, J., Batlogg, B., Benes, Z., Johnson, A. T., and Fischer, J. E., 2000, "Quantized phonon spectrum of single-wall carbon nanotubes," Science, 289(5485), pp. 1730-1733.

[18] Pettes, M. T., and Shi, L., 2009, "Thermal and Structural Characterizations of Individual Single-, Double-, and Multi-Walled Carbon Nanotubes," Adv. Funct. Mater., 19(24), pp. 3918-3925.

[19] Singh, D., Murthy, J. Y., and Fisher, T. S., 2011, "Mechanism of thermal conductivity reduction in few-layer graphene," J Appl Phys, 110(4), p. 044317.

[20] Ghosh, S., Bao, W. Z., Nika, D. L., Subrina, S., Pokatilov, E. P., Lau, C. N., and Balandin, A. A., 2010, "Dimensional crossover of thermal transport in few-layer graphene," Nat. Mater., 9(7), pp. 555-558.

[21] Yang, J. K., Yang, Y., Waltermire, S. W., Wu, X. X., Zhang, H. T., Gutu, T., Jiang, Y. F., Chen, Y. F., Zinn, A. A., Prasher, R., Xu, T. T., and Li, D. Y., 2012, "Enhanced and switchable nanoscale thermal conduction due to van der Waals interfaces," Nat Nanotechnol, 7(2), pp. 91-95.

[22] Hwang, G. S., and Kaviany, M., 2009, "Molecular dynamics simulation of effective thermal conductivity of vapor-filled nanogap and nanocavity," J Appl Phys, 106(2), p. 024317.

[23] Shenogina, N., Godawat, R., Keblinski, P., and Garde, S., 2009, "How Wetting and Adhesion Affect Thermal Conductance of a Range of Hydrophobic to Hydrophilic Aqueous Interfaces," Phys Rev Lett, 102(15), p. 156101.

[24] Shen, M., Evans, W. J., Cahill, D., and Keblinski, P., 2011, "Bonding and pressure-tunable interfacial thermal conductance," Phys Rev B, 84(19), p. 195432.

[25] Hu, M., Keblinski, P., and Schelling, P. K., 2009, "Kapitza conductance of silicon\char21{}amorphous polyethylene interfaces by molecular dynamics simulations," Phys Rev B, 79(10), p. 104305.

[26] Hu, L., Zhang, L., Hu, M., Wang, J.-S., Li, B., and Keblinski, P., 2010, "Phonon interference at self-assembled monolayer interfaces: Molecular dynamics simulations," Phys Rev B, 81(23), p. 235427.

[27] Luo, T., and Lloyd, J. R., 2010, "Non-equilibrium molecular dynamics study of thermal energy transport in Au–SAM–Au junctions," International Journal of Heat and Mass Transfer, 53(1–3), pp. 1-11.

[28] Ge, Z. B., Cahill, D. G., and Braun, P. V., 2006, "Thermal conductance of hydrophilic and hydrophobic interfaces," Phys Rev Lett, 96(18), p. 186101.

[29] Prasher, R., 2009, "Acoustic mismatch model for thermal contact resistance of van der Waals contacts," Applied Physics Letters, 94(4), p. 041905.

[30] Aakeroy, C. B., and Seddon, K. R., 1993, "The Hydrogen-Bond and Crystal Engineering," Chem Soc Rev, 22(6), pp. 397-407.

[31] Steiner, T., 2002, "The hydrogen bond in the solid state," Angew Chem Int Edit, 41(1), pp. 48-76.

[32] Arunan, E., Desiraju, G. R., Klein, R. A., Sadlej, J., Scheiner, S., Alkorta, I., Clary, D. C., Crabtree, R. H., Dannenberg, J. J., Hobza, P., Kjaergaard, H. G., Legon, A. C., Mennucci, B., and Nesbitt, D. J., 2011, "Definition of the hydrogen bond (IUPAC Recommendations 2011)," Pure Appl Chem, 83(8), pp. 1637-1641.

[33] Steiner, T., 2002, "The Hydrogen Bond in the Solid State," Angewandte Chemie International Edition, 41(1), pp. 48-76.

[34] Perrin, C. L., and Nielson, J. B., 1997, "“STRONG” HYDROGEN BONDS IN CHEMISTRY AND BIOLOGY," Annual Review of Physical Chemistry, 48(1), pp. 511-544.

[35] Jones, S., and Thornton, J. M., 1996, "Principles of protein-protein interactions," Proceedings of the National Academy of Sciences, 93(1), pp. 13-20.

[36] Guo, M., Pitet, L. M., Wyss, H. M., Vos, M., Dankers, P. Y. W., and Meijer, E. W., 2014, "Tough Stimuli-Responsive Supramolecular Hydrogels with Hydrogen-Bonding Network Junctions," Journal of the American Chemical Society, 136(19), pp. 6969-6977.

[37] Keten, S., Xu, Z., Ihle, B., and Buehler, M. J., 2010, "Nanoconfinement controls stiffness, strength and mechanical toughness of [beta]-sheet crystals in silk," Nat Mater, 9(4), pp. 359-367.

[38] Kim, G.-H., Lee, D., Shanker, A., Shao, L., Kwon, M. S., Gidley, D., Kim, J., and Pipe, K. P., 2015, "High thermal conductivity in amorphous polymer blends by engineered interchain interactions," Nat Mater, 14(3), pp. 295-300.

[39] Mino-Galaz, G. A., and Gutierrez, G., 2015, "Hydrogen bonds and asymmetrical heat diffusion in alpha-helices. A computational analysis," Chemical Physics Letters, 635, pp. 16-22.

[40] Mino, G., Barriga, R., and Gutierrez, G., 2014, "Hydrogen Bonds and Heat Diffusion in alpha-Helices: A Computational Study," J. Phys. Chem. B, 118(34), pp. 10025-10034.

[41] Omenetto, F. G., and Kaplan, D. L., 2010, "New Opportunities for an Ancient Material," Science, 329(5991), pp. 528-531.

[42] Giesa, T., Arslan, M., Pugno, N. M., and Buehler, M. J., 2011, "Nanoconfinement of Spider Silk Fibrils Begets Superior Strength, Extensibility, and Toughness," Nano Lett, 11(11), pp. 5038-5046.

[43] Lewis, R. V., 2006, "Spider silk: Ancient ideas for new biomaterials," Chem Rev, 106(9), pp. 3762-3774.

[44] Yang, Y., Chen, X., Shao, Z. Z., Zhou, P., Porter, D., Knight, D. P., and Vollrath, F., 2005, "Toughness of spider silk at high and low temperatures," Adv Mater, 17(1), pp. 84-88.

[45] Altman, G. H., Diaz, F., Jakuba, C., Calabro, T., Horan, R. L., Chen, J. S., Lu, H., Richmond, J., and Kaplan, D. L., 2003, "Silk-based biomaterials," Biomaterials, 24(3), pp. 401-416.

[46] Huang, X. P., Liu, G. Q., and Wang, X. W., 2012, "New Secrets of Spider Silk: Exceptionally High Thermal Conductivity and Its Abnormal Change under Stretching," Adv Mater, 24(11), pp. 1482-1486.

[47] Xing, C., Munro, T., White, B., Ban, H., Copeland, C. G., and Lewis, R. V., 2014, "Thermophysical properties of the dragline silk of Nephila clavipes spider," Polymer, 55(16), pp. 4226-4231.

[48] Yu, X., and Leitner, D. M., 2005, "Heat flow in proteins: Computation of thermal transport coefficients," The Journal of Chemical Physics, 122(5), p. 054902.

[49] Liu, G. Q., Huang, X. P., Wang, Y. J., Zhang, Y. Q., and Wang, X. W., 2012, "Thermal transport in single silkworm silks and the behavior under stretching," Soft Matter, 8(38), pp. 9792-9799.

[50] Zhang, J., Rajkhowa, R., Li, J. L., Liu, X. Y., and Wang, X. G., 2013, "Silkworm cocoon as natural material and structure for thermal insulation," Mater Design, 49, pp. 842-849.

[51] Haggenmueller, R., Guthy, C., Lukes, J. R., Fischer, J. E., and Winey, K. I., 2007, "Single wall carbon nanotube/polyethylene nanocomposites: Thermal and electrical conductivity," Macromolecules, 40(7), pp. 2417-2421.

[52] Lefèvre, T., Rousseau, M.-E., and Pézolet, M., 2007, "Protein Secondary Structure and Orientation in Silk as Revealed by Raman Spectromicroscopy," Biophys J, 92(8), pp. 2885-2895.

[53] Van Beek, J. D., Hess, S., Vollrath, F., and Meier, B. H., 2002, "The molecular structure of spider dragline silk: Folding and orientation of the protein backbone," Proceedings of the National Academy of Sciences, 99(16), pp. 10266-10271.

[54] Nova, A., Keten, S., Pugno, N. M., Redaelli, A., and Buehler, M. J., 2010, "Molecular and Nanostructural Mechanisms of Deformation, Strength and Toughness of Spider Silk Fibrils," Nano Lett, 10(7), pp. 2626-2634.

[55] Liu, J., and Yang, R. G., 2010, "Tuning the thermal conductivity of polymers with mechanical strains," Phys Rev B, 81(17), p. 174122.

[56] Xiao, S. B., Stacklies, W., Cetinkaya, M., Markert, B., and Grater, F., 2009, "Mechanical Response of Silk Crystalline Units from Force-Distribution Analysis," Biophys J, 96(10), pp. 3997-4005.

[57] Huang, X., Liu, G., and Wang, X., 2012, "New Secrets of Spider Silk: Exceptionally High Thermal Conductivity and Its Abnormal Change under Stretching," Adv Mater, 24(11), pp. 1482-1486.

[58] Hayashi, C. Y., and Lewis, R. V., 2000, "Molecular Architecture and Evolution of a Modular Spider Silk Protein Gene," Science, 287(5457), pp. 1477-1479.

[59] Scheller, J., Guhrs, K. H., Grosse, F., and Conrad, U., 2001, "Production of spider silk proteins in tobacco and potato," Nat Biotechnol, 19(6), pp. 573-577.

[60] Lazaris, A., Arcidiacono, S., Huang, Y., Zhou, J. F., Duguay, F., Chretien, N., Welsh, E. A., Soares, J. W., and Karatzas, C. N., 2002, "Spider silk fibers spun from soluble recombinant silk produced in mammalian cells," Science, 295(5554), pp. 472-476.

[61] An, B., Jenkins, J. E., Sampath, S., Holland, G. P., Hinman, M., Yarger, J. L., and Lewis, R., 2012, "Reproducing Natural Spider Silks' Copolymer Behavior in Synthetic Silk Mimics," Biomacromolecules, 13(12), pp. 3938-3948.

[62] Chanda, M., and Roy, S. K., 2006, Plastics Technology Handbook, CRC Press.

[63] Choy, C. L., 1977, "Thermal conductivity of polymers," Polymer, 18(10), pp. 984-1004.

[64] Assael, M. J., Botsios, S., Gialou, K., and Metaxa, I. N., 2005, "Thermal conductivity of polymethyl methacrylate (PMMA) and borosilicate crown glass BK7," Int J Thermophys, 26(5), pp. 1595-1605.

[65] Choy, C. L., Luk, W. H., and Chen, F. C., 1978, "Thermal conductivity of highly oriented polyethylene," Polymer, 19(2), pp. 155-162.

[66] Henry, A., and Chen, G., 2008, "High Thermal Conductivity of Single Polyethylene Chains Using Molecular Dynamics Simulations," Physical Review Letters, 101(23), p. 235502.

[67] Zhong, Z., Wingert, M. C., Strzalka, J., Wang, H.-H., Sun, T., Wang, J., Chen, R., and Jiang, Z., 2014, "Structure-induced enhancement of thermal conductivities in electrospun polymer nanofibers," Nanoscale, 6(14), pp. 8283-8291.

[68] Shen, S., Henry, A., Tong, J., Zheng, R., and Chen, G., 2010, "Polyethylene nanofibres with very high thermal conductivities," Nat. Nanotechnol., 5(4), pp. 251-255.

[69] Zhang, T., and Luo, T. F., 2012, "Morphology-influenced thermal conductivity of polyethylene single chains and crystalline fibers," J. Appl. Phys., 112(9), p. 094304.

[70] Shen, S., Henry, A., Tong, J., Zheng, R. T., and Chen, G., 2010, "Polyethylene nanofibres with very high thermal conductivities," Nat Nanotechnol, 5(4), pp. 251-255.

[71] Dou, L., Zheng, Y., Shen, X., Wu, G., Fields, K., Hsu, W.-C., Zhou, H., Yang, Y., and Wudl, F., 2014, "Single-Crystal Linear Polymers Through Visible Light–Triggered Topochemical Quantitative Polymerization," Science, 343(6168), pp. 272-277.

[72] Henry, A., Chen, G., Plimpton, S. J., and Thompson, A., 2010, "1D-to-3D transition of phonon heat conduction in polyethylene using molecular dynamics simulations," Phys. Rev. B, 82(14), p. 144308.

[73] Potts, J. R., Dreyer, D. R., Bielawski, C. W., and Ruoff, R. S., 2011, "Graphene-based polymer nanocomposites," Polymer, 52(1), pp. 5-25.

[74] Huxtable, S. T., Cahill, D. G., Shenogin, S., Xue, L. P., Ozisik, R., Barone, P., Usrey, M., Strano, M. S., Siddons, G., Shim, M., and Keblinski, P., 2003, "Interfacial heat flow in carbon nanotube suspensions," Nature Materials, 2(11), pp. 731-734.

[75] Kim, H., Abdala, A. A., and Macosko, C. W., 2010, "Graphene/Polymer Nanocomposites," Macromolecules, 43(16), pp. 6515-6530.

[76] Balandin, A. A., Ghosh, S., Bao, W. Z., Calizo, I., Teweldebrhan, D., Miao, F., and Lau, C. N., 2008, "Superior thermal conductivity of single-layer graphene," Nano Letters, 8(3), pp. 902-907.

[77] Berber, S., Kwon, Y. K., and Tomanek, D., 2000, "Unusually high thermal conductivity of carbon nanotubes," Physical Review Letters, 84(20), pp. 4613-4616.

[78] Luo, T. F., and Lloyd, J. R., 2012, "Enhancement of Thermal Energy Transport Across Graphene/Graphite and Polymer Interfaces: A Molecular Dynamics Study," Adv Funct Mater, 22(12), pp. 2495-2502.

[79] Wang, M., Hu, N., Zhou, L., and Yan, C., 2015, "Enhanced interfacial thermal transport across graphene–polymer interfaces by grafting polymer chains," Carbon, 85, pp. 414-421.

[80] Wang, Y., Zhan, H. F., Xiang, Y., Yang, C., Wang, C. M., and Zhang, Y. Y., 2015, "Effect of Covalent Functionalization on Thermal Transport across Graphene–Polymer Interfaces," The Journal of Physical Chemistry C, 119(22), pp. 12731-12738.

[81] Cahill, D. G., and Pohl, R. O., 1987, "Thermal-Conductivity of Amorphous Solids above the Plateau," Phys. Rev. B, 35(8), pp. 4067-4073.

[82] Choi, J. Y., Kim, S. W., and Cho, K. Y., 2014, "Improved thermal conductivity of graphene encapsulated poly(methyl methacrylate) nanocomposite adhesives with low loading amount of graphene," Compos Sci Technol, 94, pp. 147-154.

[83] Han, Z. D., and Fina, A., 2011, "Thermal conductivity of carbon nanotubes and their polymer nanocomposites: A review," Prog Polym Sci, 36(7), pp. 914-944.

[84] Hong, W. T., and Tai, N. H., 2008, "Investigations on the thermal conductivity of composites reinforced with carbon nanotubes," Diam Relat Mater, 17(7-10), pp. 1577-1581.

[85] Jiang, X., and Drzal, L. T., 2012, "Multifunctional high-density polyethylene nanocomposites produced by incorporation of exfoliated graphene nanoplatelets 2: Crystallization, thermal and electrical properties," Polymer Composites, 33(4), pp. 636-642.

[86] Marconnet, A. M., Panzer, M. A., and Goodson, K. E., 2013, "Thermal conduction phenomena in carbon nanotubes and related nanostructured materials," Reviews of Modern Physics, 85(3), pp. 1295-1326.

[87] Balasubramanian, K., and Burghard, M., 2005, "Chemically Functionalized Carbon Nanotubes," Small, 1(2), pp. 180-192.

[88] Chua, C. K., and Pumera, M., 2013, "Covalent chemistry on graphene," Chemical Society Reviews, 42(8), pp. 3222-3233.

[89] Zhang, L., Chen, T., Ban, H., and Liu, L., 2014, "Hydrogen bonding-assisted thermal conduction in β-sheet crystals of spider silk protein," Nanoscale, 6(14), pp. 7786-7791.

[90] Zhang, L., Bai, Z., Ban, H., and Liu, L., 2015, "Effects of the amino acid sequence on thermal conduction through β-sheet crystals of natural silk protein," Phys. Chem. Chem. Phys., 17(43), pp. 29007-29013.

[91] Zhang, L., Ruesch, M., Zhang, X., Bai, Z., and Liu, L., 2015, "Tuning thermal conductivity of crystalline polymer nanofibers by interchain hydrogen bonding," RSC Adv., 5(107), pp. 87981-87986.

[92] Zhang, L., Bai, Z., and Liu, L., 2016, "Exceptional Thermal Conductance across Hydrogen ‐ Bonded Graphene/Polymer Interfaces," Adv. Mater. Interfaces, 3(13).

CHAPTER 2

HYDROGEN BONDING-ASSISTED THERMAL CONDUCTION IN β-SHEET CRYSTALS OF SPIDER SILK PROTEIN

2.1 Abstract

Using atomistic simulations, we demonstrate that β-sheet, an essential component of spider silk protein, has a thermal conductivity 1-2 orders of magnitude higher than that of some other protein structures reported in the literature. In contrast to several other nanostructured materials of similar bundled/layered structures (e.g. few-layer graphene and bundled carbon nanotubes), the β-sheet is found to uniquely feature enhanced thermal conductivity with increased number of constituting units, i.e. β-strands. Phonon analysis identifies inter-β-strand hydrogen bonding as the main contributor to the intriguing phenomena, which prominently influences the state of phonons in both low- and high-frequency regimes. A thermal resistance model further verifies the critical role of hydrogen bonding in the thermal conduction through the β-sheet structures.

2.2 Introduction

Spider silk has been a focus of intense research in the past decade due to its extraordinary mechanical properties including large extensibility and high stiffness, strength, and toughness.[1-4] These properties, along with the inherent biocompatibility, have made spider silk a versatile material with enormous potential for many space, biological,

---

Zhang, L., Chen, T., Ban, H. and Liu, L., 2014. Hydrogen bonding-assisted thermal conduction in β-sheet crystals of spider silk protein. Nanoscale, 6(14), pp.7786-7791.

and medical applications.[5] Recently, another striking property of spider silk was discovered. The thermal conductivity of *Nephila clavipes* dragline silk was measured up to 416 $Wm^{-1}K^{-1}$, comparable to that of copper.[6] Despite the experimental progress, fundamental understanding of the thermal transport process in spider silk is still lacking. Although thermal analysis has been performed on several other proteins including myoglobin and green fluorescent protein,[7] spider silk needs to be investigated separately due to its unique microstructure and protein sequence. Improved understanding of these fundamental issues will not only provide insights into the thermal behavior of natural spider silk but may also guide a rational design of synthetic spider silk,[8, 9] which has become increasingly important to enable the scalable production of materials with spider silk-like properties.

In terms of the protein sequence, spider dragline silk such as *Nephila clavipes* dragline features abundant β-sheet motifs (e.g. poly-A[10]) that are believed to underpin the silk's exceptional mechanical properties.[2, 11, 12] As illustrated in Figure 2.1(a-c), these β-sheet motifs form numerous β-sheet crystal units embedded in an amorphous matrix consisting of 3_1 helices and β-turns (formed by other motifs including GGX and GPGXX).[13, 14] Each of these β-sheet units comprises multiple β-strands interlocked by hydrogen bonding, leading to high elastic modulus ~20 GPa.[11] Due to the intimate relationship between thermal conductivity and elasticity (i.e. $\kappa \sim \sqrt{E}$ where E is Young's modulus and κ is thermal conductivity),[6] it is straightforward to hypothesize that β-sheet crystals are good thermal conductors. Hence, as the first step to understand thermal transport phenomena in spider silk, this work will be focused on the β-sheet portion of spider silk protein.

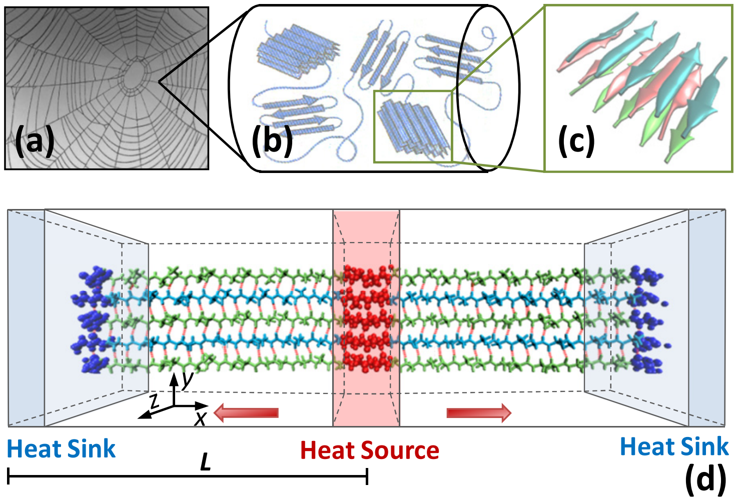

Figure 2.1. Dragline from the (a) *Nephila clavipes* orb web comprises numerous (b) β-sheet crystal units embedded in an amorphous matrix. (c) Each β-sheet unit consists of β-strands interlocked by hydrogen bonding. (d) For calculating thermal conductivity in β-sheets, a non-equilibrium MD system was employed in which heat flow was generated from the heat source (red region) to the heat sink (blue regions). *L* denotes the characteristic length of the model.

Theoretically, as phonons propagate through a β-sheet crystal unit, neighboring β-strands are bound to mechanically interact, scattering or synchronizing the phonon transport process depending on the strength of the inter-strand interactions.[15] Similar processes have been explored for several other nanostructured materials with similar bundled/layered structures, including bundled carbon nanotubes (CNTs),[16] multi-walled CNTs,[17] and few-layer graphene.[18, 19] Due to the weak van der Waals interactions between constituting units, thermal conductivities of these materials were found to decrease as the number of constituting units increases. In other words, the bundled or multi-layered architecture contributes negatively to these materials' thermal properties. Conversely, strong covalent bonding is found to enhance the thermal conductivity of SiC nanowires; as the cross-sectional area of the nanowire increases, thermal conductivity increases.[20] Since the strength of hydrogen bonding is between those of van der Waals and covalent bonding, it is unknown whether the bundling of β-strands contributes positively or negatively to the thermal conduction through β-sheet protein.

2.3 Models

In order to quantify the thermal conductivity and to reveal the bundling effects, we performed thermal analysis on several atomistic models of the β-sheet protein. Figure 2.1(d) illustrates the model of an anti-parallel β-sheet comprising five β-strands, each having 16 alanine residues. We focused this study on poly-alanine β-sheets because it predominantly exists in the *Nephila clavipes* dragline silk as the β-sheet crystal units.[13, 21] For a systematic study, models with different sizes were considered. They are named as A*n*-*m*-1 where *n* is the number of alanine residues in one β-strand, and *m* is the number of β-strands; "1" means the β-sheet structures considered in this study are β-sheet monolayers. Figure 2.2(a) illustrates the atomistic structure of all-alanine β-sheet protein in two configurations (i.e. parallel and anti-parallel) and both configurations were considered in this study. Each of the alanine residues is shown to comprise three backbone atoms (-N-C_α-C-) and several side chains/atoms including a methyl group (denoted by R), an oxygen atom, a hydrogen atom (denoted by H) bonded to a nitrogen atom, and another hydrogen atom (denoted by HA) bonded to the α-carbon atom (C_α). The parallel and anti-parallel configurations feature different pairings of side chains/atoms in neighboring β-strands to form hydrogen bonding. To eliminate phonon-boundary scattering, periodic boundary conditions were applied along all three directions. The unit cell was set to be large enough (40 nm) along the y- and z-directions to prevent periodic images of the β-sheet from interacting with each other in these directions.

2.4 Results and Discussion

Figure 2.2(b) plots the thermal conductivities (denoted by κ) calculated for ten β-sheets that are composed of the same β-strands having 16 alanine residues. Despite having the same constituting units, these β-sheets differ in the number of β-strands and the configuration of atomistic arrangement (i.e. A16-*m*-1, where *m* = 1, 3, 5, 7, and 9, in the parallel and anti-parallel configurations, respectively). In both configurations, the thermal properties show prominent width/bundling effects. As *m* is increased from 1 to 9, thermal conductivity is increased from 1.85 to 4.09 $Wm^{-1}K^{-1}$ for parallel β-sheets; and is increased from 1.85 to 4.30 $Wm^{-1}K^{-1}$ for anti-parallel β-sheets. In either case, a plateau is expected when *m* becomes sufficiently large.

These results are striking for two reasons. First, the calculated thermal conductivities of spider silk β-sheets are 1-2 orders of magnitude higher than those previously reported for other protein structures (e.g. < 0.3 $Wm^{-1}K^{-1}$ for both green fluorescent protein and myoglobin[7]). It is important to note that, the referenced calculations for both green fluorescent protein and myoglobin[7] considered free boundary conditions, while the present work considered periodical boundary conditions and an energy exchange algorithm[22] under the Muller-Plathe framework.[23, 24] It is known that boundary conditions can influence thermal conductivities. However, since both the free boundary conditions and the energy exchange could scatter phonon transport, they are not expected to affect the conclusion significantly.

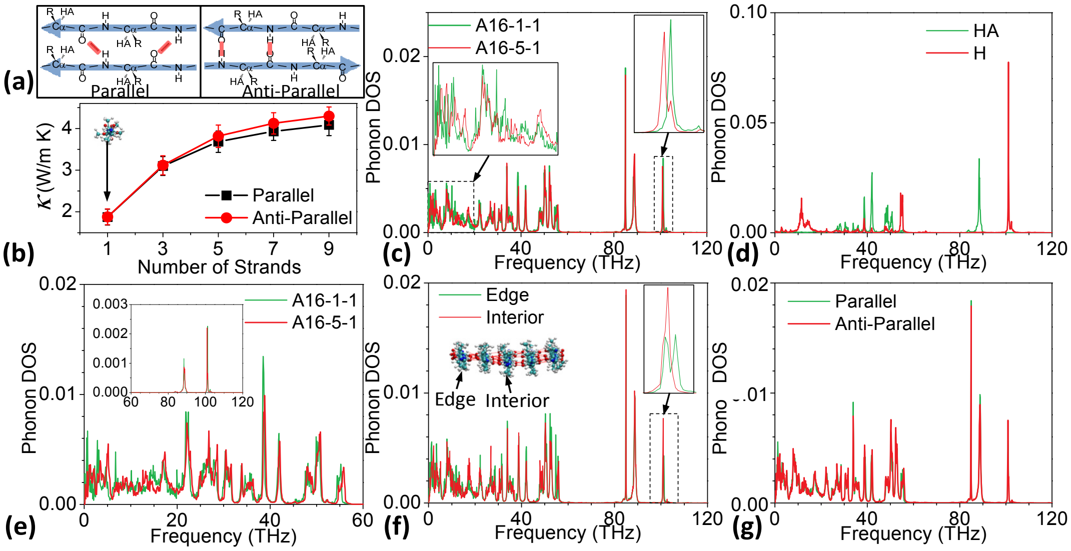

Figure 2.2. (a) Two configurations of hydrogen bonding (red lines) in β-sheet protein where each R represents a side chain. (b) Thermal conductivity versus the number of β-strands. Error bars denote standard deviations of conductivity. (c) Phonon DOS profiles of two anti-parallel β-sheet structures. (d) Partial phonon DOS projected on H atoms (hydrogen atoms bonded to nitrogen atoms) and HA atoms (hydrogen atoms bonded to α-carbon atoms) for A16-1-1. (e) Partial phonon DOS projected on backbone atoms for two anti-parallel β-sheets. Inset plots the phonon spectra from 60 to 120 THz. (f) Phonon DOS profiles for edge and interior β-strands. (g) Phonon DOS profiles for parallel and anti-parallel A16-5-1 β-sheets.

Second, while the bundling of β-strands is shown to increase thermal conductivity, many nanomaterials with similar structures (e.g. bundled CNTs and few-layer graphene) have exhibited the opposite trend. For example, the thermal conductivity of four-layer graphene is 53.6% lower than that of the two-layer graphene[19] and about 75% lower than that of the monolayer graphene.[25]

These distinctions in thermal transport characteristics must be related to microstructural differences. Comparing the molecular structures of β-sheets and other comparable nanomaterials, we note that the β-sheet is uniquely composed of hydrogen-bonded repetitive constituting units (β-strands). Further investigation suggests that, the hydrogen bonding between neighboring β-strands influences the phonon states in β-sheets in both low- and high-frequency regimes. Figure 2.2(c) plots the phonon DOS for the anti-parallel A16-1-1 and A16-5-1 β-sheets. In the high-frequency end, the phonon mode at 101.2 THz in A16-1-1 is partially shifted to 100.8 THz in A16-5-1 [right inset of Figure 2.2(c)]. According to a partial DOS analysis [Figure 2.2(d)], the phonon mode at 101.2 THz in A16-1-1 corresponds to the vibration of H atoms which are important constituent elements of β-sheet hydrogen bonds. Such side chains/atoms, as demonstrated by previous studies on the thermal transport in chemically functionalized graphene[26] and CNTs[27, 28], should reduce thermal conductivity by localizing high-frequency phonons[29] that may further scatter the low-frequency phonon transport in the backbone structures. Can the formation of hydrogen bonding in β-sheets delocalize the trapped high-frequency phonons and contribute directly to the enhancement of thermal conductivity in bundled β-strands? Based on the frequency shift from 101.2 to 100.8 THz as demonstrated in the phonon DOS analysis, it is only evident that the inter-β-strand hydrogen bonding slightly lowers the frequency of phonons localized in the -N-H side chains. The hydrogen bonding is, however, not strong enough to significantly delocalize the trapped high-frequency phonons.

A more significant effect of hydrogen bonding on the thermal transport through the spider silk β-sheet protein is in the low-frequency regime. As shown in the left inset of Figure 2.2(c), the phonon spectrum for A16-5-1 shows an apparent “blue shift” in the low-frequency regime compared with that of A16-1-1. The frequencies of the first few phonon modes are found to increase from 0.4, 3.0 and 4.7 THz (A16-1-1) to 1.2, 3.6 and 5.2 THz

(A16-5-1), respectively. Moreover, the density of phonon at 5.2 THz is significantly increased, leading to a broadened band extending from 0 to 6.0 THz. According to the partial phonon DOS projected on only backbone atoms [Figure 2.2(e)], these low-frequency phonon modes correspond to backbone vibrations. This "blue shift" in bundled β-strands is driven by the formation of hydrogen bonding. Similar to cytoskeletal actin bundles,[30] the β-sheet is mechanically strengthened by hydrogen bonding; the numerous inter-strand hydrogen bonds play a positive role in resisting relative motion between neighboring β-strands, thus improving the overall stiffness of the bundled structure and enhancing the phonon frequency in the low-frequency regime. With the blue-shifted, broadened low-frequency phonon modes, phonons are given more ability to carry heat and overcome on-site potentials[15, 31, 32] thus facilitating thermal conduction.

To further illustrate the effects of hydrogen bonding on phonon transport, we divide all β-strands in a β-sheet into two groups, i.e. edge and interior strands [the inset of Figure 2.2(f)]. Compared with the edge β-strands, interior β-strands are more hydrogen-bonded and therefore should exhibit different thermal transport characteristics. Phonon DOS [Figure 2.2(f)] shows that interior β-strands have a blue shift in the low-frequency regime and a slightly lowered frequency in the high-frequency regime at around 101.2 THz. These trends are consistent with those identified when comparing a β-sheet (hydrogen- bonded) with an individual β-strand (not hydrogen-bonded).

All thermal transport mechanisms discussed above are analyzed for anti-parallel β-sheets because they are more abundant in spider dragline silk.[21] Parallel β-sheets should have similar thermal transport mechanisms because their phonon DOS profiles are very similar to those of their anti-parallel counterparts [Figure 2.2(g)]. Despite the similarity, some differences can still be identified. Compared with the anti-parallel A16-5-1 β-sheet, the parallel A16-5-1 shows an increased phonon density at 88.6 THz and a decreased phonon density at 100.8 THz. According to partial phonon DOS analysis [Figure 2.2(d)], the former frequency corresponds to the vibration of HA atoms and the latter corresponds to that of H atoms. Different from their counterparts in the anti-parallel β-sheet, HA atoms in the parallel configuration can partially serve as hydrogen bonding donors. This bifurcated hydrogen bonding[33] in parallel β-sheets weakens the inter-strand interaction thus reducing the thermal conductivity [Figure 2.2(b)].

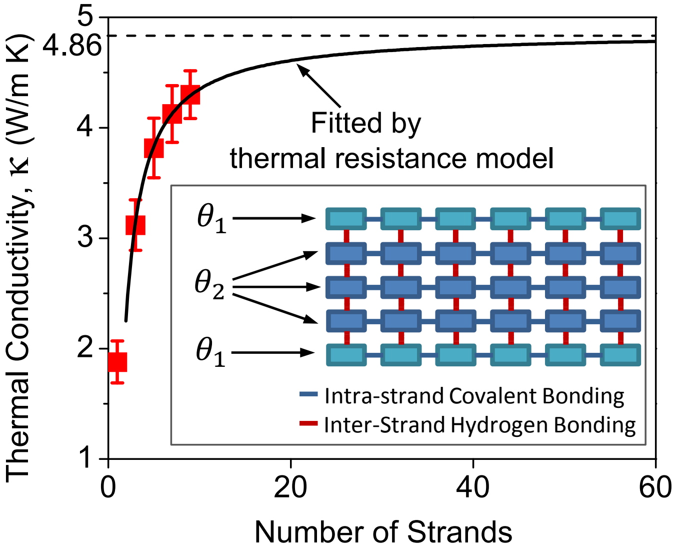

Figure 2.3. Thermal conductivities of anti-parallel 16-alanine β-sheets predicted by a thermal resistance model (black curve) and extracted from MD simulation (red squares). The curve converges to an upper limit of 4.86 $Wm^{-1}K^{-1}$ (dash line). A schematic of the thermal resistance model is shown in the inset. Effective thermal resistances of each edge and interior strands are denoted by θ_1 and θ_2, respectively.

The width/bundling effects on the thermal conduction in β-sheets are further rationalized by using a simple theoretical model. Structurally, the β-sheet under investigation is equivalent to a network of alanine residues connected by intra-strand covalent bonds and inter-strand hydrogen bonds (inset of Figure 2.3). It is apparent that the two edge β-strands (cyan) are less hydrogen-bonded than the interior β-strands (blue). We, therefore, hypothesize that the edge and interior β-strands have different equivalent thermal resistances (i.e. θ_{edge} and θ_{interior}, respectively) due to the critical role of hydrogen bonding in facilitating thermal conduction. The effective thermal resistance of the β-sheet (θ_{eff}) can be evaluated by $1/\theta_{\text{eff}} = 2/\theta_{\text{edge}} + (m-2)/\theta_{\text{interior}}$, where m is the total number of β-strands. With the relationship $\theta = L/(\kappa \cdot A)$ where L and A denote the length and cross-sectional area of a thermal conducting material, the effective thermal conductivity of the β-sheet, κ_{eff}, can be derived as $m\kappa_{\text{eff}} = 2\kappa_{\text{edge}} + (\text{m}-2)\kappa_{\text{interior}}$, where κ_{edge} and κ_{interior} denote the thermal conductivities of each single edge and interior β-strand, respectively. With this equation, κ_{edge} and κ_{interior} can be fitted by any two known thermal conductivity values for β-sheets of different widths. Using the thermal conductivities of anti-parallel A16-3-1 and A16-5-1 β-sheets, κ_{edge} and κ_{interior} are solved to be 2.25 and 4.86 $\text{Wm}^{-1}\text{K}^{-1}$, respectively. The thermal conductivities of A16-7-1 and A16-9-1 β-sheets are then predicted to be 4.11 and 4.28 $\text{Wm}^{-1}\text{K}^{-1}$ (Figure 2.3), respectively, with negligible errors (< 1%) compared with the results extracted directly from simulations.

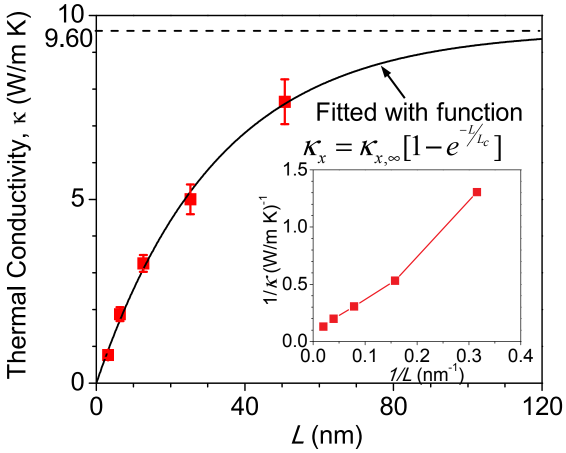

Figure 2.4. Thermal conductivity versus length for individual poly-A β-strands. Simulation results are fitted by a function with two parameters, $\kappa_{x,\infty}$ and L_c. The fitted curve converges to 9.60 Wm^{-1}K^{-1} (dash line). The inset plots the nonlinear relation between the inverse of thermal conductivity and the inverse of length.

As the number of β-strands further increases, the thermal conductivity of β-sheets converges to that of the interior strand, κ_{interior}, which represents a 163% increase with respect to that of the individual β-strand. It is important to note that, although the present example is for anti-parallel A16-*m*-1 β-sheets, the theoretical model applies for other cases with different lengths, sequences, and hydrogen bonding arrangements.

In addition to width, the thermal conductivity of β-sheets also depends on length (or the number of amino acids in one β-strand). To illustrate the length effect, we consider five β-strands with 8, 16, 32, 64, and 128 alanine residues, respectively. According to Figure 2.4, thermal conductivity increases nonlinearly with the length. Since low-frequency phonons travel several orders of magnitude longer than high-frequency phonons in β-sheets, the Matthiessen rule [34] which assumes a single mean free path for all phonons does not apply (see the inset of Figure 2.4, where $1/\kappa$ is shown to be nonlinear with $1/L$).

Alternatively, we apply $\kappa_x = \kappa_{x,\infty}(1-e^{-L/L_c})$ [35] to quantify length effect and to understand the transition from ballistic to diffusive phonon transport. In the equation, L is the length of the β-sheet, $\kappa_{x,\infty}$ is the thermal conductivity when L is infinitely large, and L_c is the characteristic length of ballistic-to-diffusive transition. By further defining $L_{0.99}$ as the effective mean free path for diffusive transport, i.e. $\kappa_x |_{L=L_{0.99}} = 0.99\kappa_{x,\infty}$, we calculate $\kappa_{x,\infty}$ and $L_{0.99}$ to be 9.60 $\mathrm{Wm^{-1}K^{-1}}$ and 14.91 nm, respectively, for the all-alanine β-strand. Combined with the width effects, long and wide β-sheets are predicted to have large thermal conductivities (> 20 $\mathrm{Wm^{-1}K^{-1}}$ by estimation).

Finally, there are several points that deserve mentioning about the present study. First, this work was focused on single-layer β-sheets to probe the intriguing role of hydrogen bonds. In natural and synthetic spider silk, however, β-sheets usually self-assemble into multi-layered structures [Figure 2.1(b-c)]. Without hydrogen bonds between the neighboring layers in multi-layered β-sheet structures, the inter-sheet interaction will decrease the thermal conductivity (similar to the change from graphene to graphite). For demonstration, a series of computation has been performed for A16-7-*p* β-sheets ($p = 1, 3, 5, 7, 9$) where p denotes the number of β-sheet layers. As p increases from 1 to 9, thermal conductivity drops from 4.2 $\mathrm{Wm^{-1}K^{-1}}$ to about 4.0 $\mathrm{Wm^{-1}K^{-1}}$, due to the phonon scattering caused by neighboring layers. Second, it is important to note that the thermal conductivity computed for β-sheets is an order of magnitude lower than that experimentally measured for spider silk. Since spider silk is a complex material that consists of many different proteins and skin materials, more research efforts are required to achieve a full understanding of the material system.

2.5 Conclusions

To summarize, the β-sheet protein of spider dragline silk is found to have thermal conductivities 1-2 orders of magnitude higher than those of other proteins. The associated thermal conduction characteristics are highly size-dependent. When the length and width of the β-sheet protein is increased, thermal conductivity increases no matter how β-strands are arranged (parallel or anti-parallel). Although the layered/bundled architecture has been previously shown to adversely affect thermal conduction in bundled CNTs and few-layer graphene,[15-19] we find that the formation of β-sheets from β-strands has the effect of increasing thermal conduction. Phonon DOS analysis identifies inter-strand hydrogen bonding as the main contributor to these intriguing phenomena, which enhances thermal conduction by blue-shifting phonon frequency in the low-frequency regime. The critical role of inter-strand hydrogen bonding is further verified by a thermal resistance model. Indeed, these results echo several previous investigations which underscore the importance of inter-strand or inter-layer interactions in determining the thermal properties of materials of similar structures.[15, 36] The present study is expected to provide theoretical insights into the thermal transport mechanisms in spider silk protein, and to stimulate future designing efforts to engineer innovative spider silk-inspired materials.

2.6 Methods

2.6.1 Calculation of Thermal Conductivity

The reverse non-equilibrium molecular dynamics method developed by Muller-Plathe[23, 24] was employed to calculate thermal conductivity. This algorithm requires that the system contains two copies of the model to be analyzed. The model and its image were positioned in the system so that they were physically connected and symmetric about their center along the direction of the intended heat flow (x-direction in this study). The entire system was divided into N slabs along the x direction ($N = 32$ for this work). A heat flux was then numerically generated from a "hot" region [i.e. "heat source" in Figure 2.1(d)] to a "cold region" (i.e. "heat sink"). Specifically, at a prescribed frequency, we exchanged energy between the "hottest" atom (with the highest kinetic energy) in the first slab and the "coldest" atom (with the lowest kinetic energy) in the (N/2+1)th slab, based on a virtual elastic collision algorithm.[22] By this method, energy and momentum were both conserved during the energy exchange, even when two particles of different masses were considered. Continued energy exchange caused a higher temperature in the (N/2+1)th slab than that in the first slab, thus leading to a temperature gradient and heat flux in the system [e.g. red arrows in Figure 2.1(d)]. The induced heat flux was evaluated by $J = \Delta E / 2tA$, where t is the time interval between two energy exchanges, ΔE is the averaged kinetic energy transferred per energy exchange, A is the cross-sectional area of the material, and the coefficient "2" reflects the two symmetric heat transport paths from the hot slab to the cold slab. The approach adopted by us to determine A can be found in Section A3 in SI. Finally, by Fourier's law, thermal conductivity was calculated by $\kappa = -J / \frac{dT}{dx}$, where $\frac{dT}{dx}$ was the temperature gradient along the *x*-direction. A representative *T*-*x* curve for the A16-7-1 β-sheet can be found in Section A4 in SI, along with a description of the approach to find $\frac{dT}{dx}$. Due to the symmetric nature of the system, the characteristic length, *L*, of the model equals to half the system length.

2.6.2 Phonon Density of States Analysis

Phonon density of states (DOS) was calculated to further unveil thermal transport mechanisms. Fourier transformation of velocity autocorrelation function (VAF) was calculated for all/selected atoms following the equation:

$$\rho(\omega) = \frac{1}{\sqrt{2\pi}} \int_0^{+\infty} e^{-i\omega t} \frac{\langle v(t) \cdot v(0) \rangle}{\langle v(0) \cdot v(0) \rangle} dt \tag{2.1}$$

Where $\rho(\omega)$ is the DOS with the angular frequency ω, $v(t)$ is atomic velocity, and <•> denotes an average over the selected atoms.

2.6.3 Simulation Details

All simulations in this study were performed using LAMMPS.[37] CHARMM22 force field[38] was employed to describe interatomic interactions. Particle-particle particle-mesh method (PPPM) was adopted to address long range Coulomb's interactions with a root mean square accuracy of 10^{-4}. Nosé-Hoover thermostat was employed to maintain system temperature at desired values. Time step was set to be 1 fs. Prior to each simulation for obtaining thermal conductivity, the initial molecular structure was relaxed by minimization with the conjugate gradient method, followed by molecular dynamics equilibrium at the temperature of 300 K for 5 ns. Then, a heat flux was induced by enabling the Muller-Plathe algorithm. The simulation was performed for 450 ns and only the last 400 ns was used to sample the temperature profile and heat flow. For all cases, no noticeable difference was identified between the thermal conductivities calculated using the 50 ns - 250 ns simulation results and the 250 ns - 450 ns simulation results, indicating that the calculated thermal conductivities were stable with time. Moreover, to eliminate possible spurious global rotation of the molecule, global angular momentum was subtracted from the momentum of each atom at all steps. To avoid protein denaturation at high temperatures,[39] simulation parameters were optimized to ensure that the temperature difference between the hottest and coldest slabs in the system was 30±2 K.

2.7 Acknowledgment

We thank Prof. Randolph V. Lewis for helpful discussions. The work is supported by Utah State University.

NOTES AND REFERENCES

Supplementary Information (SI) is available in Appendix A: structure of the β-sheets, computational model, determination of area and temperature gradient, and additional phonon DOS results.

1. F. G. Omenetto and D. L. Kaplan, *Science*, 2010, **329**, 528-531.
2. T. Giesa, M. Arslan, N. M. Pugno and M. J. Buehler, *Nano Lett*, 2011, **11**, 5038-5046.
3. R. V. Lewis, *Chem Rev*, 2006, **106**, 3762-3774.
4. Y. Yang, X. Chen, Z. Z. Shao, P. Zhou, D. Porter, D. P. Knight and F. Vollrath, *Adv Mater*, 2005, **17**, 84-88.
5. G. H. Altman, F. Diaz, C. Jakuba, T. Calabro, R. L. Horan, J. S. Chen, H. Lu, J. Richmond and D. L. Kaplan, *Biomaterials*, 2003, **24**, 401-416.
6. X. P. Huang, G. Q. Liu and X. W. Wang, *Adv Mater*, 2012, **24**, 1482-1486.
7. X. Yu and D. M. Leitner, *The Journal of Chemical Physics*, 2005, **122**, 054902-054911.
8. J. Scheller, K. H. Guhrs, F. Grosse and U. Conrad, *Nat Biotechnol*, 2001, **19**, 573-577.
9. A. Lazaris, S. Arcidiacono, Y. Huang, J. F. Zhou, F. Duguay, N. Chretien, E. A. Welsh, J. W. Soares and C. N. Karatzas, *Science*, 2002, **295**, 472-476.
10. M. Xu and R. V. Lewis, *P Natl Acad Sci USA*, 1990, **87**, 7120-7124.
11. S. Keten, Z. Xu, B. Ihle and M. J. Buehler, *Nat Mater*, 2010, **9**, 359-367.
12. A. Nova, S. Keten, N. M. Pugno, A. Redaelli and M. J. Buehler, *Nano Lett*, 2010, **10**, 2626-2634.
13. J. D. van Beek, S. Hess, F. Vollrath and B. H. Meier, *Proceedings of the National Academy of Sciences*, 2002, **99**, 10266-10271.
14. T. Lefèvre, M.-E. Rousseau and M. Pézolet, *Biophysical journal*, 2007, **92**, 2885-2895.

15. T. Sun, J. X. Wang and W. Kang, *Nanoscale*, 2013, **5**, 128-133.

16. J. Hone, B. Batlogg, Z. Benes, A. T. Johnson and J. E. Fischer, *Science*, 2000, **289**, 1730-1733.

17. M. T. Pettes and L. Shi, *Adv. Funct. Mater.*, 2009, **19**, 3918-3925.

18. D. Singh, J. Y. Murthy and T. S. Fisher, *J Appl Phys*, 2011, **110**, 044317.

19. S. Ghosh, W. Z. Bao, D. L. Nika, S. Subrina, E. P. Pokatilov, C. N. Lau and A. A. Balandin, *Nat. Mater.*, 2010, **9**, 555-558.

20. K. Termentzidis, T. Barreteau, Y. X. Ni, S. Merabia, X. Zianni, Y. Chalopin, P. Chantrenne and S. Volz, *Phys Rev B*, 2013, **87**, 125410.

21. S. Keten and M. J. Buehler, *Appl Phys Lett*, 2010, **96**, 153701.

22. C. Nieto-Draghi and J. B. Avalos, *Mol Phys*, 2003, **101**, 2303-2307.

23. F. Muller-Plathe, *J Chem Phys*, 1997, **106**, 6082-6085.

24. M. M. Zhang, E. Lussetti, L. E. S. de Souza and F. Muller-Plathe, *J Phys Chem B*, 2005, **109**, 15060-15067.

25. A. A. Balandin, S. Ghosh, W. Z. Bao, I. Calizo, D. Teweldebrhan, F. Miao and C. N. Lau, *Nano Lett*, 2008, **8**, 902-907.

26. J. Y. Kim, J. H. Lee and J. C. Grossman, *Acs Nano*, 2012, **6**, 9050-9057.

27. C. W. Padgett and D. W. Brenner, *Nano Lett*, 2004, **4**, 1051-1053.

28. S. K. Chien, Y. T. Yang and C. K. Chen, *Appl Phys Lett*, 2011, **98**, 033107.

29. N. Go, T. Noguti and T. Nishikawa, *P Natl Acad Sci-Biol*, 1983, **80**, 3696-3700.

30. M. Bathe, C. Heussinger, M. M. A. E. Claessens, A. R. Bausch and E. Frey, *Biophysical Journal*, 2008, **94**, 2955-2964.

31. W. R. Zhong, *Phys Rev E*, 2010, **81**, 061131.

32. O. M. Braun and Y. S. Kivshar, *Physics Reports*, 1998, **306**, 1-108.

33. I. Rozas, I. Alkorta and J. Elguero, *J Phys Chem A*, 1998, **102**, 9925-9932.

34. L. Liu and X. Chen, *J Appl Phys*, 2010, **107**, 033501

35. J. A. Thomas, R. M. Iutzi and A. J. H. McGaughey, *Phys Rev B*, 2010, **81**, 045413.

36. J. K. Yang, Y. Yang, S. W. Waltermire, X. X. Wu, H. T. Zhang, T. Gutu, Y. F. Jiang, Y. F. Chen, A. A. Zinn, R. Prasher, T. T. Xu and D. Y. Li, *Nat. Nanotechnol.*, 2012, **7**, 91-95.

37. S. Plimpton, *J. Comput. Phys.*, 1995, **117**, 1-19.

38. A. D. MacKerell, D. Bashford, M. Bellott, R. L. Dunbrack, J. D. Evanseck, M. J. Field, S. Fischer, J. Gao, H. Guo, S. Ha, D. Joseph-McCarthy, L. Kuchnir, K. Kuczera, F. T. K. Lau, C. Mattos, S. Michnick, T. Ngo, D. T. Nguyen, B. Prodhom, W. E. Reiher, B. Roux, M. Schlenkrich, J. C. Smith, R. Stote, J. Straub, M. Watanabe, J. Wiorkiewicz-Kuczera, D. Yin and M. Karplus, *J Phys Chem B*, 1998, **102**, 3586-3616.

39. D. Paschek and A. E. Garcia, *Phys Rev Lett*, 2004, **93**, 238105.

CHAPTER 3

EFFECTS OF AMINO ACID SEQUENCE ON THERMAL CONDUCTION THROUGH β-SHEET CRYSTALS OF NATURAL SILK PROTEIN

3.1 Abstract

Recent experiments have discovered very different thermal conductivities between the spider silk and the silkworm silk. Decoding the molecular mechanisms underpinning the distinct thermal properties may guide the rational design of synthetic silk materials and other biomaterials for multifunctionality and tunable properties. However, such an understanding is lacking, mainly due to the complex structure and phonon physics associated with the silk materials. Here, using non-equilibrium molecular dynamics, we demonstrate that amino acid sequence plays a key role in the thermal conduction process through β-sheets, an essential building block of natural silks and a variety of other biomaterials. Three representative β-sheet types, i.e. poly-A, poly-(GA), and ploy-G, are shown to have distinct structural features and phonon dynamics leading to different thermal conductivities. Fundamental understanding of the sequence effects may stimulate the design and engineering of polymers and biopolymers for desired thermal properties.

3.2 Introduction

Natural silk materials produced by spiders and silkworms[1] have drawn considerable attention in the past couple of decades due to their extraordinary mechanical properties,[2, 3]

Zhang, L., Bai, Z., Ban, H. and Liu, L., 2015. Effects of the amino acid sequence on thermal conduction through β-sheet crystals of natural silk protein. Physical Chemistry Chemical Physics, 17(43), pp.29007-29013.

biodegradability, and biocompatibility.[4, 5] These unique properties have enabled diverse applications of natural silk materials in making biomedical sutures[6] and implantable devices,[7] and in drug delivery as the drug carriers targeting cancer cells.[8, 9] Recently, these materials were made even more attractive for their thermal properties. The dragline silk made by *Nephila clavipes*, a golden orb-web spider, was measured to have a thermal conductivity of 1.2-151 $Wm^{-1}K^{-1}$, surpassing many materials.[10, 11] By contrast, the thermal conduction in silkworm silk is much less efficient. With thermal conductivities as low as 0.54 $Wm^{-1}K^{-1}$,[12] silkworm silk-based textiles have been used as a thermal insulator for thousands of years.[13] From a fundamental point of view, it is striking that the spider and silkworm silks (Figure 3.1*ab*), both spun by arthropods, have such distinct thermal conducting capabilities.

Structurally, both spider and silkworm silks are made of proteins rich in β-sheet, a protein secondary structure consisting of aligned polypeptide strands interlocked by hydrogen bonds. In these silk proteins, the abundant β-sheet crystals are embedded in a semi-amorphous matrix of 3_1 helices and β-turns (Figure 3.1*c*),[14] contributing significantly to the physical properties of the silk materials. For instance, our previous study has shown that the thermal conductivity of the poly-alanine (poly-A) β-sheet,[15] an essential building block of the *Nephila clavipes* spider silk, can be 1-2 orders of magnitude higher than that reported for other protein structures.[16] The main contributor to this phenomenon is the hydrogen bonding between the β-strands that form the β-sheets. As heat is carried by phonons in the β-sheet, the interstrand hydrogen bonds blue-shift the frequencies of the low-frequency phonon modes, which further enhance thermal conduction.

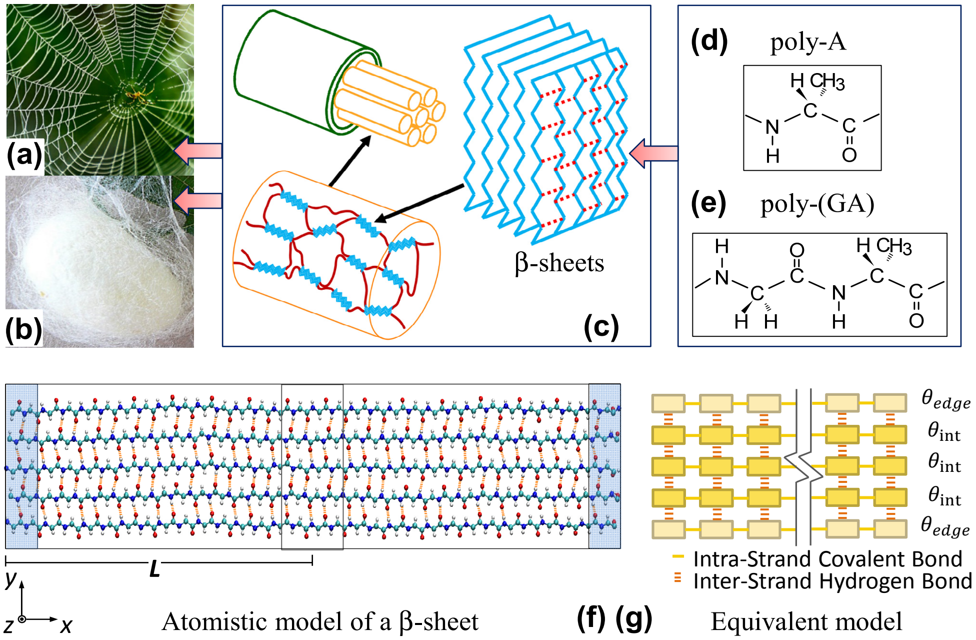
(a)
(b)
(c)
β-sheets
(d) poly-A
H CH3
N
C
C
H
O
(e) poly-(GA)
H
N
C
H H
O
C
N
H
H CH3
C
C
O
y
z
x
L
Atomistic model of a β-sheet
(f) (g)
Equivalent model
θ_{edge}
θ_{int}
θ_{int}
θ_{int}
θ_{edge}
Intra-Strand Covalent Bond
Inter-Strand Hydrogen Bond

Figure 3.1. Natural silk from (a) the *Nephila clavipes* spider and (b) the *Bombyx mori* silkworm has a similar hierarchical structure, where (c) β-sheet protein structure serves as an essential building block. In natural silk proteins, the β-sheets form numerous crystalline domains (blue) that are embedded in an amorphous matrix (red curves). Each of the β-sheets consists of multiple β-strands interlocked by hydrogen bonds (red dash lines). The β-sheets in different types of natural silk may have different amino acid sequences. For example, the β-sheets in the *Nephila clavipes* spider silk feature repeated (d) poly-A motifs, while those in the *Bombyx mori* silkworm silk are formed by repeated (e) poly-(GA) motifs. (f) To compute the thermal conductivity of a β-sheet, heat flow is generated from the "heat source" (red region) to the "heat sink" (blue region) by a velocity swapping algorism. *L* denotes the characteristic length of the model. (g) The β-sheet is analogous to a network of thermal resistors. Each strand is represented by a line of thermal resistors whose total resistance is denoted by θ_{edge} or θ_{int}, depending on the location of the strand.

Despite the progress, it remains unclear how heat is conducted differently in the β-sheets constituting the spider and silkworm silks. Structural biology has revealed that the β-sheets in different types of natural silk feature different amino acid sequences. For instance, the dragline silk from the *Nephila clavipes* spider has abundant repeats of poly-Alanine (poly-A) (Figure 3.1*d*) while the cocoon silk from the *Bombyx mori* silkworm features poly-(Glycine-Alanine) [poly-(GA)] repeats (Figure 3.1*e*).[14, 17] Such a difference in the protein sequence has been found responsible for the distinct mechanical properties of different types of β-sheets.[18] Nevertheless, how thermal conduction is affected by the protein sequence is relatively unknown. Deciphering the correlation between the thermal properties and the protein sequence may improve our fundamental understanding of the nanoscale thermal transport phenomena in biomaterials. The results may further guide the design of synthetic silk materials[19, 20] to achieve tunable thermal properties with inherent biocompatibility, which is desired by many biomedical applications that demand high-performance thermal regulation. A word of caution though is that β-sheet nanocrystals only account for ~30% of the residues in the *N. clavipes* dragline,[14, 21] and ~50% in the *B. mori* silk.[14, 22] The amorphous phase is also critical in determining the overall thermal properties of the silks. However, compared with β-sheets, the amorphous phase is typically associated with more phonon scattering and shorter mean free path of phonons leading to slower thermal conduction.[23] Therefore, this work focuses on the β-sheets which are the main thermal conductors in silks, aiming to reveal the effects of amino acid sequence on their intrinsic thermal conductivities.

To assist the understanding of the thermal transport process in β-sheets, it is helpful to draw an analogy between the protein β-sheets and other low-dimensional nanomaterials including nanotubes and nanowires and search for similarities and distinctions in the thermal transport mechanisms. First, we note that all β-strands in the β-sheets (Figure 3.1*de*) feature numerous side chains/atoms (e.g. $-CH_3$ and -H) that are anchored to the backbone of the polypeptide chains (i.e. -N-C-C-). This is analogous to the carbon nanotubes functionalized by chemical attachments of alien molecules or atoms. Second, the poly-(GA) β-strand in Figure 3.1*e* is analogous to the superlattice nanowires that have alternating elements along the length direction. Previous studies have shown that: 1) carbon nanotubes functionalized by phenyl rings[24] and hydrogen atoms[25] have lower thermal conductivities than their pristine counterparts due to the reduced phonon mean free path; and 2) most superlattice nanowires have lower thermal conductivities than the nanowires of pure composition,[26] mainly due to the prominent phonon scattering at the material interfaces. It is hypothesized that the similar structural features dictate the thermal conduction process in β-sheets as well, while the detailed mechanisms are to be revealed.

Here we report a non-equilibrium molecular dynamics study of the thermal transport phenomena in three representative β-sheet types, i.e. poly-(GA), poly-A, and poly-G. The poly-(GA) β-sheet is abundant in the *Bombyx mori* silkworm silk, while the ploy-A β-sheet dominates in the *Nephila clavipes* spider silk. The poly-G β-sheet is a conceptual sequence for comparison. The analysis allows us to probe the fundamental physics underpinning the different thermal conductivities of natural silk materials. By systematically investigating the effects of sequence and structure, we will show in detail the phonon dynamics and molecular mechanisms associated with the thermal transport processes. The results will be further discussed in comparison with those reported earlier on the thermal conduction in synthetic low-dimensional materials. The conclusions may expand our understanding of the role of hydrogen bonds in facilitating thermal conduction in β-sheets and guide the design of biomaterials for desired thermal properties.

3.3 Models and Methods

Full-atom atomistic models were constructed for the β-sheets with specific sequences and various sizes. We note that each β-sheet may exist in two different forms, i.e. the parallel and antiparallel configurations. This study is focused on the antiparallel β-sheets only, because they are more dominant in the *Nephila clavipes* dragline and *Bombyx mori* cocoon silks [17]. Each β-sheet model is composed of a specific number of β-strands that have the same characteristic length of 6.15 nm. The model is named as X*m*-*n*-1, where X indicates the repeated residues in the peptide, *m* is the total number of the repeats in a single β-strand, *n* is the number of β-strands in each layer, and "1" means that this study focuses on monolayer β-sheets. To eliminate phonon scattering with geometric boundaries, periodic boundary conditions were applied along all three directions. The unit cell was set to be large (40 nm) along the *y*- and *z*-directions to prevent periodic images of the β-sheet from interacting with each other in these directions. In all these models, about 70% hydrogen bonds form between the β-strands, which confirms that the structures are stable and appropriate for subsequent simulations (see details in ESI). It deserves mentioning that in this study, all β-sheets were placed in a vacuum to focus on their intrinsic thermal conductivities. In real silk materials, however, there are several extrinsic factors that may affect the thermal conduction process, e.g. interaction with the amorphous phase and the surrounding water molecules. Between the two factors, water may have fewer influences due to its low presence in natural silks.[27, 28] The amorphous phase may scatter phonon transport in β-sheets and change their thermal conductivities to some extent. However, we believe the interaction with the amorphous phase will not overturn the sequence effects to be revealed by this study.

The reverse non-equilibrium molecular dynamics method developed by Muller-Plathe[29] was employed to calculate the thermal conductivity. The method has been applied to many different material systems including polymers, nanotubes, nanowires, and liquids,[30] and has been shown to give consistent results as the equilibrium Green-Kubo method.[31] To apply the method, it is required that the system contains two copies of the β-sheet to be analyzed, i.e. the original model and an image, both physically connected and symmetric about their center along the direction of intended heat flow (*x*-direction in this study). The entire system was then divided into *N* slabs along the *x*-direction. A heat flux was numerically generated by continuously swapping the velocities of the "coldest" atoms (with the lowest kinetic energy) in the "heat source" slab and the "hottest" atoms (with the highest kinetic energy) in the "heat sink" slab (Figure 3.1*f*). Fourier's law was then employed to evaluate the thermal conductivity based on the heat flux generated in the system and the heat flux-induced thermal gradient. During this velocity-swap process, a virtual elastic collision model[32] was employed to ensure the conservation of both system energy and momentum equilibrium. The induced heat flux was evaluated by $J = \Delta E/2tA$, where t denotes the time interval between two swaps, ΔE is the averaged kinetic energy transferred per swap, A is the cross-sectional area of the material, and the coefficient "2" reflects the two symmetric heat transport paths from the hot slab to the cold slab. Finally, by Fourier's law, thermal conductivity was calculated by $\kappa = -J/\frac{dT}{dx}$, where $\mathrm{d}T/\mathrm{d}x$ is the temperature gradient along the *x*-direction. Due to the symmetric nature of the system, the characteristic length, *L*, of the model equals to half the system length.

All simulations were performed using LAMMPS[33] with the CHARMM22 force field[34] to describe the interatomic interactions. Particle-particle particle-mesh method (PPPM) was adopted to address long range Coulomb's interactions with a root mean square accuracy of 10^{-4}. Nosé-Hoover thermostat was employed to maintain system temperature at desired values. Time step was set to be 1 fs. Prior to each simulation for obtaining thermal conductivity, the initial molecular structure was relaxed by minimization with the conjugate gradient method, followed by molecular dynamics equilibration at the temperature of 300 K for 5 ns. Then, a heat flux was induced by enabling the Muller-Plathe algorithm. The simulation was performed for 450 ns, and only the last 400 ns was used to sample the temperature profile and heat flow. For all cases, no noticeable difference was identified between the thermal conductivities calculated using the 50 ns - 250 ns simulation results and those calculated using the 250 ns - 450 ns simulation results, indicating that the calculated thermal conductivities were stable with time. Moreover, to eliminate possible spurious global rotation of the molecule, global angular momentum was subtracted from the momentum of every atom at all steps. To avoid protein denaturation at high temperatures,[35] simulation parameters were optimized to ensure that the temperature difference between the hottest and coldest slabs in the system was 30±2 K.

In addition to the computation of thermal conductivity, phonon density of states (DOS) was also evaluated to further reveal the thermal transport mechanisms. Fourier transformation of the velocity autocorrelation function (VAF) was calculated for all/selected atoms following the equation $\rho(\omega)=\frac{1}{\sqrt{2\pi}}\int_0^{+\infty} e^{-i\omega t}\frac{\langle v(t)\cdot v(0)\rangle}{\langle v(0)\cdot v(0)\rangle}dt$, where $\rho(\omega)$ is the DOS with the angular frequency ω, $v(t)$ is atomic velocity, and <•> denotes an average over the selected atoms.

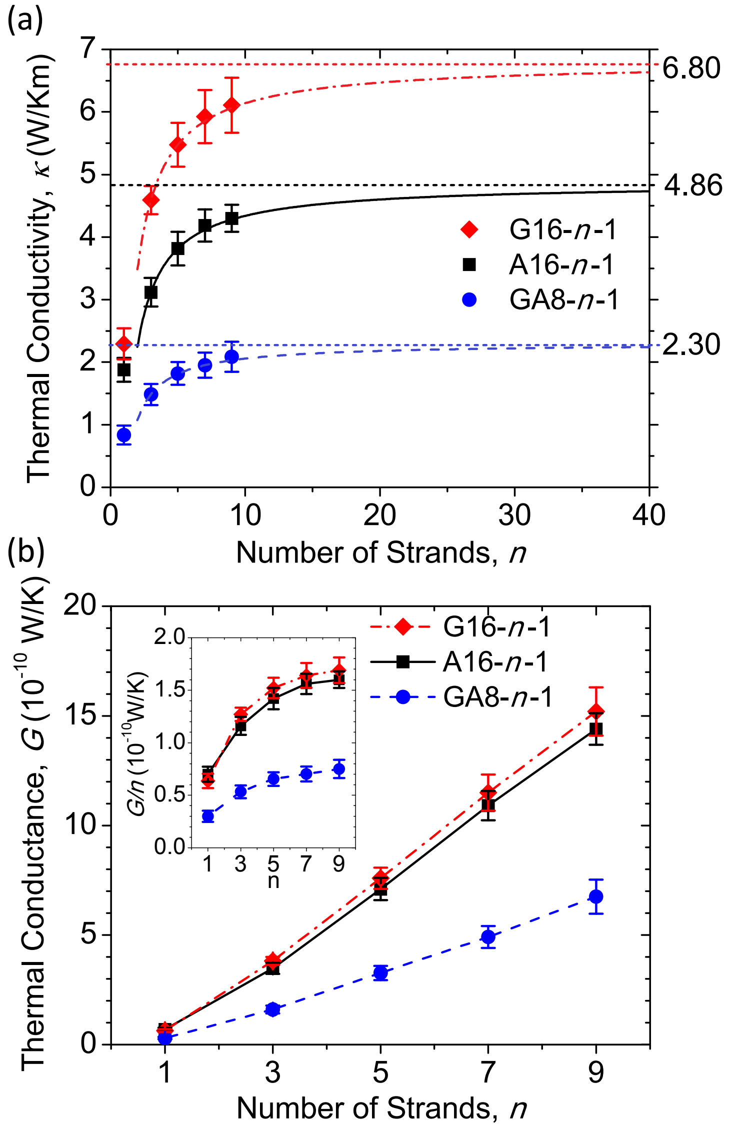

Figure 3.2. (a) Thermal conductivity and (b) thermal conductance versus the number of β-strands (n) for the poly-A, poly-G, and poly-(GA) β-sheets. The results in (a) are fitted by a thermal resistance model to predict the thermal conductivities of larger β-sheets. The inset in (b) plots the thermal conductance divided by the number of β-strands.

3.4 Results and Discussions

Figure 3.2*a* plots the computed thermal conductivities of all the β-sheets under investigation. To reveal the sequence and size effects, all β-sheets were built to have the same length of 16 residues, while the width was varied by changing the number of the β-strands. The results show prominent width effects. As the number of β-strands increases from 1 to 9, the thermal conductivity of the poly-(GA) β-sheet increases from 0.84 to 2.09 $Wm^{-1}K^{-1}$ (blue circles in Figure 3.2*a*). Additionally, it can be speculated that the thermal conductivity should converge to a certain value as the β-sheet becomes infinitely large. Similarly, the poly-G and poly-A β-sheets also give the same ascending trend. The thermal conductivity of the poly-A β-sheet increases from 1.85 to 4.30 $Wm^{-1}K^{-1}$ (black squares), while that of the poly-G β-sheet increases from 2.29 to 6.11 $Wm^{-1}K^{-1}$ (red diamonds). The size effects are attributed to the hydrogen bonds interlocking β-strands to form the β-sheets, which blue-shift the frequencies of the low-frequency phonon modes and facilitate thermal conduction. Similar hydrogen bond effects have been discovered in a-helices to enhance thermal diffusion.[36]

All of these results agree with a thermal resistance model developed in our previous work[15] which reveals that: 1) the thermal conductivity of a β-sheet increases with the number of β-strands in the β-sheet (*n*); 2) the thermal conductivity of any β-strand in the β-sheet depends on the degree of hydrogen bonding; and 3) as *n* becomes infinitely large, the thermal conductivity of a monolayer β-sheet converges to that of an interior β-strand in the β-sheet. Figure 3.1*f* shows a poly-A β-sheet (A-16-5-1) that has five β-strands interlocked by hydrogen bonds. The thermal resistance model simplifies the β-sheet as a network of residues as shown in Figure 3.1*g*. The β-strands are further divided into two groups – edge strands and interior strands, with their thermal conductivities denoted by κ_{edge} and κ_{int}, respectively. The overall thermal conductivity of the β-sheet is derived as $\kappa = 2\kappa_{\text{edge}} / n + (n-2)\kappa_{\text{int}} / n$. Using the results in Figure 3.2*a*, κ_{edge} and κ_{int} of the poly-A, poly-G, and poly-(GA) β-sheets are evaluated and tabulated in Table 3.1. It is readily seen for all the three types of β-sheets, edge β-strands and interior β-strands have different thermal conductivities; κ_{int} is higher than κ_{edge}, and both of them are higher than κ_{single}, the thermal conductivity of a stand-alone β-strand of the same type. This is consistent with the fact that the interior β-strands are connected with more hydrogen bonds than the edge β-strands in a β-sheet, and a stand-alone β-strand has no hydrogen bond. Furthermore, the model also predicts increasing thermal conductivity with *n*, which agrees with the computational results in Figure 3.2*a*. As *n* keeps increasing, $\kappa_{\infty} = \kappa|_{n\to\infty} = \kappa_{\text{int}}$ gives the upper limit of the thermal conductivity.

Table 3.1. Computed thermal conductivities of three standalone β-strands (κ_{single}), and the interior and edge β-strands in the corresponding β-sheets (κ_{int} and κ_{edge}).

β-sheet	Thermal Conductivity (W/K·m)		
	$n = 1$	$n > 2$	
	κ_{single}	κ_{edge}	κ_{int}
A16-*n*-1	1.85	2.25	4.86
GA8-*n*-1	0.84	1.07	2.30
G16-*n*-1	2.29	3.49	6.80

The results in Figure 3.2*a* and Table 3.1 also show prominent effects of the amino acid sequence. At any particular width, the poly-G β-sheet gives the highest thermal conductivity among the three types of β-sheet under investigation, poly-A β-sheet the second, and poly-(GA) β-sheet the lowest. In terms of the upper limit of thermal conductivity (κ_∞), the poly-G β-sheet (G16-*n*-1) is approximately 40% higher than the poly-A β-sheet (A16-*n*-1) and 196% higher than the poly-(GA) β-sheet (GA8-*n*-1). In addition to affecting the thermal conduction in β-sheets where hydrogen bonds play a key role, the sequence of amino acids also influences the conduction of heat in standalone β-strands. As shown in Table 1, the thermal conductivity of the standalone GA8-1-1 β-strand is calculated to be the lowest, 55% lower than that of A16-1-1, and 63% lower than that of G16-1-1. The similar ranking between the standalone β-strands and the β-sheets implies that the sequence effects are inherent to proteins and not strongly influenced by hydrogen bonds.

These results are consistent with previous experimental measurements and provide clues for us to understand the varied thermal properties among different natural silks. As an essential building block of the *Nephila clavipes* spider silk protein, the poly-A β-sheet is shown by our computation to be a good thermal conductor, which contributes to the experimentally measured high thermal conductivity of the spider silk. Similarly, the low thermal conductivity of the *Bombyx mori* silkworm silk is partly attributable to the inefficient thermal conduction in poly-(GA) β-sheet. Furthermore, the computational results also provide a hint on the peptide design for engineering superior thermal-conducting biomaterials. Given the high thermal conductivities of the poly-A β-sheets, incorporating more poly-A motifs in the peptides may form β-sheets of better thermal conducting capabilities, thereby improving the thermal properties of the biomaterials. This is particularly pertinent to the design of synthetic silk materials in which amino acid sequence can be engineered following an optimized blueprint.

To reveal the mechanisms underlying the different thermal conductivities between the poly-A and poly-G β-sheets, we first convert the thermal conductivities into the thermal conductances. Thermal conductivity (κ) is the property of material to conduct heat, while thermal conductance (G) is the property of a plate of particular length and cross section to conduct heat. They are correlated by $\kappa = L \cdot G / A$, where A is the cross-sectional area, and L is the length of the plate. To calculate G for any β-sheet under investigation, we note that κ and L are readily available while A is lacking. The cross-sectional area of low-dimensional materials such as graphene and nanotubes have been studied for decades, and there are many approaches available. In this study, the cross-sectional area of a β-sheet was evaluated based on a time- and spatial-averaging approach. As illustrated in Figure 3.3, a β-sheet under equilibrium was simulated for 1 ps, during which 1000 snapshots were stored. The position of a β-strand was quantified by averaging the coordinates of all backbone atoms constituting the strand over the 1000 snapshots. The cross-sectional area per stand (A_{strand}) was then calculated based on the area occupied by the β-strand on an averaging basis. In this way, A_{strand} was evaluated to be 25.46 Å^2 for the poly-A β-sheets, 21.46 Å^2 for the poly-(GA) β-sheets, and 17.08 Å^2 for the poly-G β-sheets.

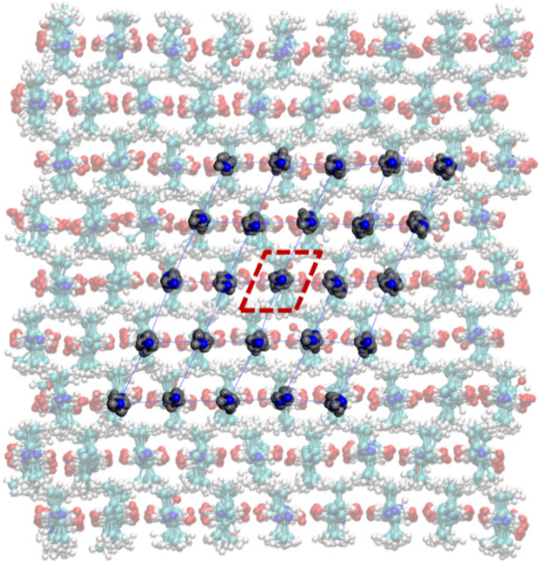

Figure 3.3. Evaluation of the cross-sectional area of a poly-A β-strand based on the equilibrium positions of the interior β-strands in a β-sheet.

Using the areas and thermal conductivities computed above, the thermal conductances of all β-sheets under investigation are calculated and plotted in Figure 3.2*b*. Similar with the thermal conductivity, the thermal conductance is also found to increase with the number of β-strands, which again, demonstrates that hydrogen bonding facilitates thermal transport in β-sheets. More importantly, it is striking to discover that the poly-G and poly-A β-sheets have very close thermal conductances despite their distinct thermal conductivities. In other words, the difference in sequence (i.e. poly-A versus poly-G) only affects the thermal conductivity significantly, while not changing the thermal conductance notably. Given $\kappa = L \cdot G / A$, the poly-G and poly-A β-sheets (with same L) have almost the same G, so $\kappa \sim 1/A$. That is, to tune the thermal conductivity of a β-sheet made with homogeneous amino acids, we may engineer the side chains to change the effective area of the β-sheet. For example, the short side chains in the poly-G β-sheet can reduce the cross sectional area effectively, thereby increasing the thermal conductivity to the largest extent among the three types of β-sheet under investigation.

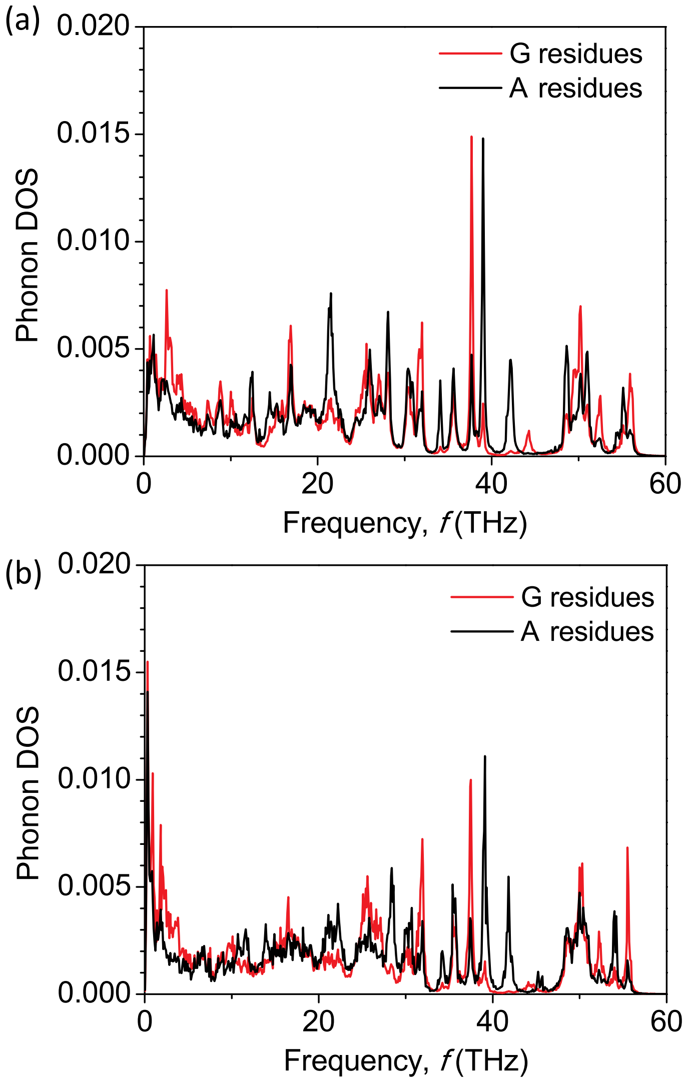

Figure 3.4. Partial phonon DOS projected on the glycine and alanine residues of (a) a GA8-5-1 β-sheet and (b) a standalone GA8-1-1 β-strand.

On the other hand, the poly-(GA) β-sheets are shown to have lower thermal conductivities than their counterparts with homogenous compositions (poly-A and poly-G). To understand how the heterogeneous composition affects thermal conduction, we have conducted phonon DOS (density of states) analysis on the poly-(GA) β-sheets. Figure 3.4*a* plots the partial phonon DOS of the GA8-5-1 β-sheet projected on the glycine and alanine residues, respectively. Very different phonon modes spanning from 0 to 60 THz are identified between the two types of residues. For example, the glycine residues are associated with unique peaks at 0.71, 2.71, 44.33, and 52.65THz, and have higher densities at 7.13, 8.96, 16.76, 31.85, 37.74, 50.23, and 55.86 THz; by comparison, the alanine residues show unique peaks at 1.18, 34.11, and 42.34THz, and have higher densities at 12.51, 21.44, 28.04, 38.78, and 49.02 THz. Based on these results, phonon dynamics is distinct in the glycine and alanine residues. When such phonons are carrying heat through the β-sheets, some of them may reflect back or experience mode conversion at the interfaces between the two different types of residues, dramatically decreasing the efficiency of thermal conduction. This is analogous to that in superlattice nanowires which are composed of alternating materials in a periodic pattern. Several investigations[26] have shown reduced thermal conductivities of superlattice nanowires compared with that of the constituting materials,[37] based on similar mechanisms.

We note that, despite the similarities, the β-sheets have several unique characteristics that differ them from the superlattice nanowires. First, superlattice nanowires feature alternating chemical elements along the length direction which form many interfaces between the materials. In β-sheets, however, the chemical composition of the main phonon transport pathway, i.e. the backbone, is the same for all residues; distinct types of residues are different in their side chains, which impose strong influences on the transport of phonon through the backbone chains. Second, the thermal transport in β-sheets is further complicated by the unique hydrogen bonding interactions between the neighboring β-strands. Figure 3.4*b* plots the partial phonon DOS of the standalone GA8-1-1 β-strand projected on the glycine and alanine residues, respectively. The two types of residues show very different phonon modes. And more importantly, by comparing Figure 3.4*b* with Figure 3.4*a*, it is readily seen that the low-frequency phonon modes in β-sheets are widened and have blue-shifted frequencies, due to the inter-strand hydrogen bonds. Indeed, in the β-sheets with heterogeneous amino acid compositions, the effects of alternating residues and hydrogen bonds are coupled, which complicates the thermal transport phenomena.

All sequence effects shown above were discussed using monolayer β-sheets as the model material. It is unknown, whether or not the revealed sequence effects would hold when multiple β-sheets stack to form nanocrystals. To answer this question, we simulated several multilayer β-sheets with the poly-A and poly-(GA) sequences. The results demonstrate that the sequence of amino acids influences the monolayer and multilayer β-sheets in a similar way. Figure 3.5 plots the thermal conductivities of two monolayer β-sheets (i.e. A16-7-1 and GA8-7-1), and four multilayer nanocrystals (i.e. A16-7-3, GA8-7-5, A16-7-3, and GA8-7-5). The thermal conductivities of all poly-A β-sheets are about twice as high as that of their poly-(GA) counterparts. In other words, the sequence effects discussed earlier for monolayer β-sheets hold in multilayer β-sheets. Another important finding is that the thermal conductivities of the poly-A (or poly-(GA)) β-sheets keep almost a constant as the number of layers varies. That means the stacking of β-sheets does not change thermal conductivities significantly; phonon transport in the hydrogen-bonded β-sheets is not much influenced by the vdW interactions between the β-sheets.

The results shown in Figure 3.5 demonstrate that the thermal conductivities of the poly-A β-sheets (~4 $Wm^{-1}K^{-1}$) are higher than that of the poly-(GA) β-sheets (~2 $Wm^{-1}K^{-1}$). The sequence effects partly explain the different thermal conductivities between the *N. clavipes* dragline (~1.2 $Wm^{-1}K^{-1}$) and the *B. mori* silkworm silk (~0.54 $Wm^{-1}K^{-1}$), as the former silk has abundant poly-A β-sheets while the latter has rich poly-(GA) β-sheets. The differences between our simulation results and the experimentally measured values are mainly attributed to the complex compositions and structures of natural silks. As mentioned earlier, β-sheet nanocrystals only account for ~30% of the residues in the *N. clavipes* dragline, and ~50% in the *B. mori* silk. Moreover, each silk fiber is composed of multiple silk fibroins along with a skin layer and a periphery layer.[14] Therefore, in addition to the intrinsic thermal conductivities of the β-sheets, several other factors contribute to the overall thermal conductivities of the silks. These factors include the amorphous phase (most important), the interfaces between the amorphous and the β-sheet phases, water molecules, and the skin and core periphery materials. The influences of these factors, particularly the amorphous phase and its interfaces with β-sheet nanocrystals, may be a topic of future study.

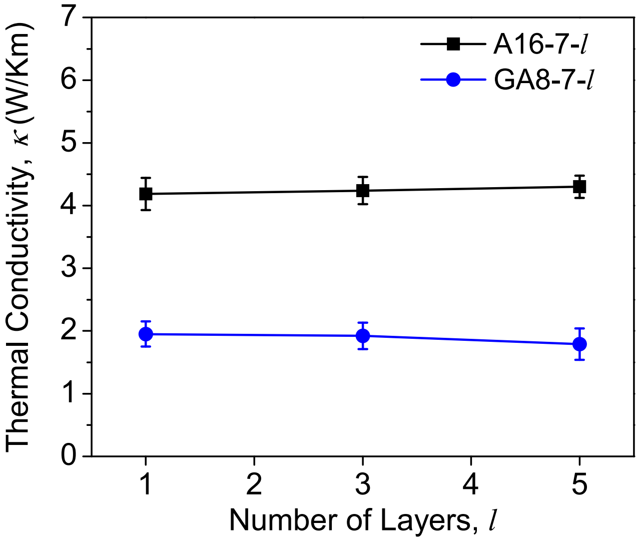

Figure 3.5. Thermal conductivity versus the number of layers in β-sheet structures with the poly-A and poly-(GA) sequences. Each layer has seven β-strands and each strand has 16 residues.

3.5 Conclusions

To summarize, key molecular mechanisms underpinning the thermal conduction in three representative β-sheet types [i.e. poly-A, poly-(GA), and ploy-G] are studied to reveal the intrinsic effects of the amino acid sequence. With any of these sequences, β-sheets are shown to have thermal conductivities increasing with the number of β-strands, demonstrating the positive contributions of hydrogen bonds to heat transfer. At the same size, the poly-A β-sheet shows a thermal conductivity twofold higher than that of the corresponding poly-(GA) β-sheet, which partly explains why the *Nephila clavipes* dragline spider silk has higher thermal conductivity than the *Bombyx mori* silkworm cocoon silk. Moreover, the poly-G β-sheet shows the highest thermal conductivity among the three β-sheet types under investigation. All these sequence effects are caused by the distinct structures and unique phonon dynamics associated with the β-sheets. First, the alternating residues in the poly-(GA) β-sheets cause severe phonon mode mismatch across the G-A interfaces which obstruct thermal transport. Second, the β-sheets of homogeneous residues (i.e. poly-G and ploy-A) surprisingly demonstrate comparable thermal conductances despite the distinct thermal conductivities; the difference between their thermal conductivities is caused by the different cross-sectional areas which are tunable by side chain design. All these conclusions suggest that, by properly designing the amino acid sequence, protein β-sheets can be engineered to produce multifunctional synthetic silk and other biomaterials with tunable thermal properties.

3.6 Acknowledgments

We are grateful to the insightful discussions with Prof. Randolph V. Lewis, and the financial support by Utah State University.

REFERENCES

1. C. L. Craig, *Annu Rev Entomol*, 1997, **42**, 231-267.
2. F. G. Omenetto and D. L. Kaplan, *Science*, 2010, **329**, 528-531.
3. Z. Z. Shao and F. Vollrath, *Nature*, 2002, **418**, 741-741.
4. Y. Shen, S. L. Redmond, J. M. Papadimitriou, B. M. Teh, S. Yan, Y. Wang, M. D. Atlas, R. J. Marano, M. H. Zheng and R. J. Dilley, *Biomed Mater*, 2014, **9**, 015015.
5. Y. Z. Wang, H. J. Kim, G. Vunjak-Novakovic and D. L. Kaplan, *Biomaterials*, 2006, **27**, 6064-6082.
6. G. H. Altman, F. Diaz, C. Jakuba, T. Calabro, R. L. Horan, J. S. Chen, H. Lu, J. Richmond and D. L. Kaplan, *Biomaterials*, 2003, **24**, 401-416.
7. L. Meinel, R. Fajardo, S. Hofmann, R. Langer, J. Chen, B. Snyder, G. Vunjak-Novakovic and D. Kaplan, *Bone*, 2005, **37**, 688-698.
8. A. Florczak, A. Mackiewicz and H. Dams-Kozlowska, *Biomacromolecules*, 2014, **15**, 2971-2981.
9. B. Subia, S. Chandra, S. Talukdar and S. C. Kundu, *Integrative Biology*, 2014, **6**, 203-214.
10. X. P. Huang, G. Q. Liu and X. W. Wang, *Adv Mater*, 2012, **24**, 1482-1486.
11. C. Xing, T. Munro, B. White, H. Ban, C. G. Copeland and R. V. Lewis, *Polymer*, 2014, **55**, 4226-4231.
12. G. Q. Liu, X. P. Huang, Y. J. Wang, Y. Q. Zhang and X. W. Wang, *Soft Matter*, 2012, **8**, 9792-9799.
13. J. Zhang, R. Rajkhowa, J. L. Li, X. Y. Liu and X. G. Wang, *Mater Design*, 2013, **49**, 842-849.
14. T. Lefèvre, M.-E. Rousseau and M. Pézolet, *Biophys J*, 2007, **92**, 2885-2895.
15. L. Zhang, T. Chen, H. Ban and L. Liu, *Nanoscale*, 2014, **6**, 7786-7791.
16. B. M. Foley, C. S. Gorham, J. C. Duda, R. Cheaito, C. J. Szwejkowski, C. Constantin, B. Kaehr and P. E. Hopkins, *The Journal of Physical Chemistry Letters*, 2014, **5**, 1077-1082.

17. J. D. van Beek, S. Hess, F. Vollrath and B. H. Meier, *Proceedings of the National Academy of Sciences*, 2002, **99**, 10266-10271.

18. S. B. Xiao, W. Stacklies, M. Cetinkaya, B. Markert and F. Grater, *Biophys J*, 2009, **96**, 3997-4005.

19. B. An, J. E. Jenkins, S. Sampath, G. P. Holland, M. Hinman, J. L. Yarger and R. Lewis, *Biomacromolecules*, 2012, **13**, 3938-3948.

20. A. Lazaris, S. Arcidiacono, Y. Huang, J. F. Zhou, F. Duguay, N. Chretien, E. A. Welsh, J. W. Soares and C. N. Karatzas, *Science*, 2002, **295**, 472-476.

21. C. Riekel, C. Bränden, C. Craig, C. Ferrero, F. Heidelbach and M. Müller, *Int J Biol Macromol*, 1999, **24**, 179-186.

22. F. Lucas, J. T. B. Shaw and S. G. Smith, *Nature*, 1956, **178**, 861-861.

23. J. Liu and R. G. Yang, *Phys Rev B*, 2010, **81**, 174122.

24. C. W. Padgett and D. W. Brenner, *Nano Lett*, 2004, **4**, 1051-1053.

25. R. Q. Pan, Z. J. Xu, Z. Y. Zhu and Z. X. Wang, *Nanotechnology*, 2007, **18**, 285704.

26. M. Hu and D. Poulikakos, *Nano Lett*, 2012, **12**, 5487-5494.

27. T. A. Blackledge, C. Boutry, S.-C. Wong, A. Baji, A. Dhinojwala, V. Sahni and I. Agnarsson, *Journal of Experimental Biology*, 2009, **212**, 1981-1989.

28. P. M. Cunniff, S. A. Fossey, M. A. Auerbach, J. W. Song, D. L. Kaplan, W. W. Adams, R. K. Eby, D. Mahoney and D. L. Vezie, *Polym Advan Technol*, 1994, **5**, 401-410.

29. F. Muller-Plathe, *J Chem Phys*, 1997, **106**, 6082-6085.

30. E. A. Algaer and F. Müller-Plathe, *Soft Materials*, 2011, **10**, 42-80.

31. P. K. Schelling, S. R. Phillpot and P. Keblinski, *Physical Review B*, 2002, **65**, 144306.

32. C. Nieto-Draghi and J. B. Avalos, *Mol Phys*, 2003, **101**, 2303-2307.

33. S. Plimpton, *J. Comput. Phys.*, 1995, **117**, 1-19.

34. A. D. MacKerell, D. Bashford, M. Bellott, R. L. Dunbrack, J. D. Evanseck, M. J. Field, S. Fischer, J. Gao, H. Guo, S. Ha, D. Joseph-McCarthy, L. Kuchnir, K. Kuczera, F. T. K. Lau, C. Mattos, S. Michnick, T. Ngo, D. T. Nguyen, B. Prodhom, W. E. Reiher, B. Roux, M. Schlenkrich, J. C. Smith, R. Stote, J. Straub, M. Watanabe, J. Wiorkiewicz-Kuczera, D. Yin and M. Karplus, *J Phys Chem B*, 1998, **102**, 3586-3616.

35. D. Paschek and A. E. Garcia, *Phys Rev Lett*, 2004, **93**, 238105.

36. G. Miño, R. Barriga and G. Gutierrez, *The Journal of Physical Chemistry B*, 2014, **118**, 10025-10034.

37. X. B. Li and R. G. Yang, *Phys Rev B*, 2012, **86**, 054305.

CHAPTER 4

TUNING THERMAL CONDUCTIVITY OF CRYSTALLINE POLYMER NANOFIBERS BY INTERCHAIN HYDROGEN BONDING

4.1 Abstract

Polymers are widely used but they suffer from an apparent bottleneck of inefficient thermal conduction. Here, using non-equilibrium molecular dynamics, we demonstrate that hydrogen-bonded crystalline polymer nanofibers may have thermal conductivities 1-2 orders of magnitude higher than that of engineering polymers. Interchain hydrogen bonds serve as “soft grips” to restrict the torsional motion of polymer chains, leading to enhanced thermal conductivities. The degree of enhancement can be tuned by changing the density of hydrogen bonds, and the number of chains comprising the polymer nanofiber/nanosheet. Further analysis of the dihedral distribution and the phonon dispersion curves attribute such phenomena to the unique effects of hydrogen bonds in confining structural disorder and facilitating phonon transport. The study suggests an important way to tune the thermal conductivity of crystalline polymers.

4.2 Introduction

Polymers are key materials in many engineering technologies for their low mass density, high corrosion resistance, excellent manufacturability, and low costs.[1] Despite the many advantages, the material suffers from an apparent bottleneck. The thermal

---

Zhang, L., Ruesch, M., Zhang, X., Bai, Z. and Liu, L., 2015. Tuning thermal conductivity of crystalline polymer nanofibers by interchain hydrogen bonding. RSC Advances, 5(107), pp.87981-87986.

conductivities of most bulk polymers are only 0.1-1 W/Km,[2] making them inferior to metals and ceramics for applications demanding efficient thermal management. In the meanwhile, however, single polyethylene chains have been reported to be highly conducting with a thermal conductivity of 350 W/m K.[3] The drastic difference underscores the significant influences of molecular structure on the thermal conductivities of polymers, in which hydrogen bond may play a key role.

Fundamentally, the thermal conductivity of polymers is governed by factors including chain morphology, alignment, and the interchain atomistic interactions. For standalone polyethylene chains, nonstraight morphologies including waviness and torsion negatively impact the along-chain thermal conduction.[4] When multiple chains form a nanofiber or a bulk material, chain alignment becomes critical. An ultra-drawn polyethylene nanofiber has demonstrated a high thermal conductivity of 104 W/Km, mainly due to the enhanced phonon transport in mechanically aligned polymer chains.[5] In addition to chain alignment, the strength of the interchain atomistic interaction also influences thermal transport profoundly.[6] In general, thermal conductivity is reduced by weak van der Waals (vdW) interactions, as evidenced in the studies of carbon nanotube bundles,[7] few-layer graphene,[8, 9] and polyethylene nanofibers.[10]

Ten to one hundred times stronger than the vdW interaction,[11] the hydrogen bonding in polymers can enhance existing thermal pathways and create new ones to more efficiently conduct heat. In a recent experimental work, two polymers, i.e. poly(N-acryloyl piperidine) and poly(acrylic acid), were mixed to form a blend in which the interchain hydrogen bonds exerted forces to hold the polymer chains, improving both the interchain and intra-chain heat transfer. Due to this effect, the thermal conductivity of the blend was measured to be 1.5 W/Km, an order of magnitude higher than that of the constituting polymers, i.e. 0.19 and 0.22 W/Km.[12] The experimental study is consistent with our computational work on protein β-sheets. Different from bundled carbon nanotubes and few-layer graphene, β-sheets showed increased thermal conductivities when formed by more constituting units (i.e. β-strands).[13, 14] The unusual trend was attributed to the interchain hydrogen bonds, which blueshift and broaden the low-frequency phonon bands leading to enhanced thermal conduction. Similar effects have also been demonstrated in α-helices, where hydrogen bonds create new thermal pathways to enhance thermal diffusion.[15]

Inspired by these findings, hydrogen bond engineering has opened a new avenue to tune the thermal properties of polymers. Nevertheless, a fundamental understanding of the effects of hydrogen bond location, density, and orientation is still lacking. In this work, we use crystalline nylon as a model material to investigate the effects of hydrogen bond density on the nanoscale thermal transport process. We choose nylon because its amide groups (-NH-CO-) can facilitate the formation of hydrogen bonds between the neighboring chains [Figure 4.1(a)], leading to stable crystalline structures.[16] The non-equilibrium molecular dynamics study will allow us to reveal how thermal conductivity is correlated with the density of hydrogen bonds, and how phonon transport is facilitated by the interchain hydrogen bonds. The results are expected to guide a rational design of hydrogen-bonded crystalline polymers for improved thermal conductivities.

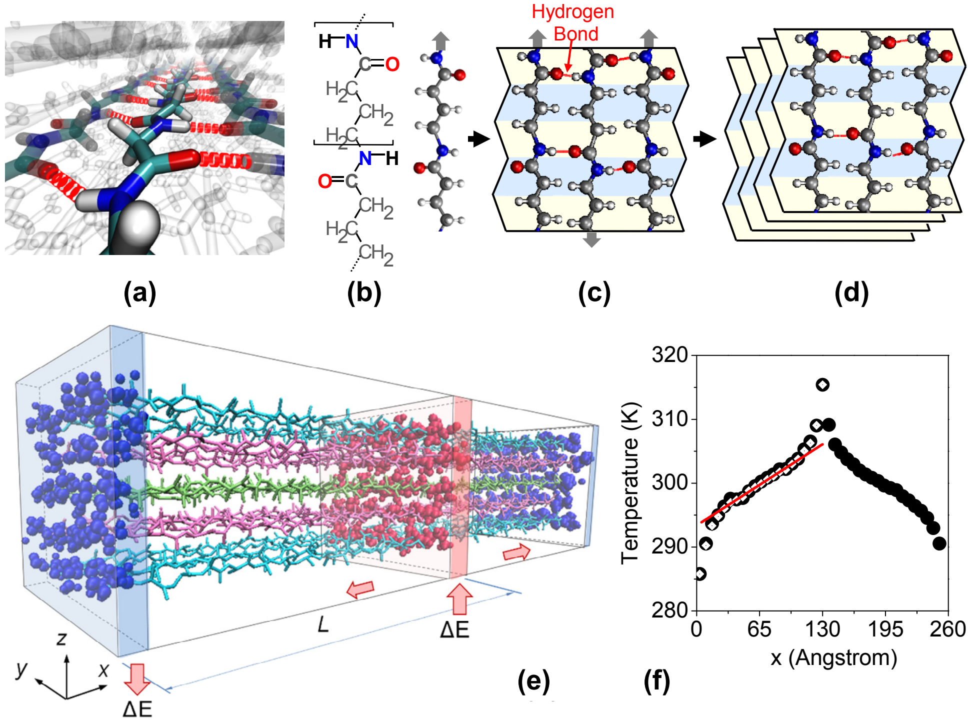

Figure 4.1. (a) Illustration of hydrogen bonds in crystalline polymers. (b) Molecular structure of an extended polymer chain of nylon 4. Silver, blue, white, and red spheres represent the carbon, nitrogen, hydrogen, and oxygen atoms, respectively. (c) Multiple such chains are interlocked by hydrogen bonds to form a crystalline nanosheet. (d) Multiple such nanosheets stack to form a nylon crystal. Arrows in (b) and (c) indicate the directions of the polymer chains defined from NH to CO. Chains with alternating directions indicate the anti-parallel arrangement leading to the α-form crystal. (e) A computational model of a crystalline nylon nanofiber. Non-equilibrium molecular dynamics simulation is performed to induce a heat flux from the heat source (red slab) to the heat sink (blue slab). (f) An example temperature profile (solid spheres) along the direction of heat flux (*x*-direction). The temperature gradient is evaluated by linear regression of the linear portion (red line), which further leads to the thermal conductivity.

4.3 Models and Methods

4.3.1 Models

Previous studies have shown that interchain interactions are critical to determining the thermal properties of polymers. In crystalline nylon, hydrogen bonding dominates the interaction within the polymer sheets, while vdW forces govern the interaction between the sheets. To reveal the effects of both factors on the thermal conduction process, we performed a systematic study using nylon nanofibers of different sizes, i.e. nylon-n-p-m-q, where n is the number of carbon atoms in each repeat unit, p is the number of repeat units per chain, m is the number of chains per sheet, and q is the number of sheets in the nanofiber [Figure 4.1(e)]. Figure 4.1(b-d) illustrates the molecular structure of crystalline nylon. As a polyamide, nylon consists of numerous copies of [-NH-CO-$(CH_2)_{n-1}$-], where n denotes the number of carbon atoms in each repeat unit. Different numbers of n lead to different nylon materials. For example, $n = 4$ gives nylon 4 which has the molecular structure [-NH-CO-$(CH_2)_3$-] [Figure 4.1(b)]. When many of such polymer chains are bundled, the chains are interlocked by hydrogen bonds to form crystalline sheets [Figure 4.1(c)], which may further stack to form crystals [Figure 4.1(d)]. Here, we note that nylon chains are directional (from NH to CO). Arranging the chains in the anti-parallel and parallel patterns would lead to different forms of the material (i.e. the α and γ forms). This work is focused on the α-form nylon because it is more stable and more conducting.[13, 14, 17]

4.3.2 Structural Relaxation

The molecular structures of the nanofibers were relaxed by minimization with the conjugate gradient method, followed by molecular dynamics equilibration of 5 ns at 300 K using the NVT ensemble and the time step of 1 fs. All simulations were performed using LAMMPS[18] with the OPLSAA force field.[19] OPLSAA has been shown by a previous comparative study to be the most effective force field in describing the hydrogen bonding energy and in maintaining the stability of several hydrogen-bonded molecular complexes.[20]

All force field parameters used in our simulations can be found in Appendix C, Section 1. Particle-particle particle mesh method (PPPM) was adopted to account for the long-range Coulomb's interactions. Periodic boundary condition was applied along all the three directions. Large unit cell sizes were assumed along the transverses directions to minimize the artificial interactions between the images of the molecular structure. Nose-Hoover thermostat was employed to maintain the temperature at specified values.

4.3.3 Non-Equilibrium Molecular Dynamics

To apply the method,[21] it is required that the system contains two copies of the nanofiber to be analyzed, i.e. the original structure and an image, both physically connected and symmetric about their center along the direction of intended heat flow (x-direction in this study). The entire system was then divided into N slabs along the x-direction. A heat flux was generated by continuously swapping the velocities of the "coldest" atoms (with the lowest kinetic energy) in the "heat source" slab and the "hottest" atoms (with the highest kinetic energy) in the "heat sink" slab. During this velocity-swap process, a virtual elastic collision model[22] was employed to ensure the conservation of both system energy and momentum equilibrium. By adjusting the swapping frequency, the temperatures of the hot and cold regions were controlled to be approximately 300±15 K in all cases. Due to the symmetric nature of the system, the characteristic length, L, of the model equals to half the system length. The simulations were performed using the NVE ensemble. The time step was set to be 0.5 fs, small enough to capture the dynamics of the hydrogen bonds. We note that, to reach the equilibrium state where a stable temperature profile is formed, models of different sizes would need different lengths of simulations (10~30 ns). Only after equilibrium can we calculate the temperature in the slabs (based on the production run of 10~30 ns) and calculate the thermal conductivity.

4.3.4 Calculation of Thermal Conductivity

Each non-equilibrium molecular dynamics simulation led to a temperature profile similar to that shown in Figure 4.1(f). The temperature profile is nonlinear due to the perturbation caused by the artificial velocity swapping. An average was taken between the temperature profiles to the left and right of the heat source. Line regression was then calculated to obtain the temperature gradient. On the other hand, the induced heat flux was evaluated by $J=\Delta E/2tA$, where t denotes the time interval between two swaps, ΔE is the averaged kinetic energy transferred per swap, A is the cross-sectional area of the material, and the coefficient "2" reflects the two symmetric heat transport paths from the hot slab to the cold slab. The value of A was calculated based on the chain-averaged cross-sectional area in the multilayer nanocrystals. Finally, by Fourier's law, thermal conductivity was calculated by $\kappa=-J/\frac{dT}{dx}$, where $\frac{dT}{dx}$ is the temperature gradient along the x-direction.

4.3.5 Phonon Dispersion Curves

Phonon dispersion curves were calculated based on the finite displacement method by using the PHONOPY[23] and LAMMPS[18] packages. In the calculation, each unit cell comprised of two repeat units along the chain direction to ensure geometric periodicity. All atoms in the unit cell form a basis. There are 14 atoms in the basis of the single-chain nylon 2, and 28 atoms in the basis of the double-chain nylon 2. In a supercell of 4 unit cells, LAMMPS was used to calculate the pairwise force when one atom was positively or negatively displaced by a small distance along one of the three Cartesian coordinate directions. The derived force values were used to calculate the force constants which form the dynamic matrix. Finally, the phonon dispersion relations were derived from the eigenvalues of the dynamical matrix.

4.4 Results and Discussion

4.4.1 Hydrogen Bonding-Enhanced Thermal Conductivity

Figure 4.2(a) demonstrates that indeed, the interchain hydrogen bonds facilitate thermal conduction in crystalline nylon nanosheets. We start from monolayer nanosheets because hydrogen bonding dominates the interchain interaction which allows us to pinpoint its effects on thermal transport. Four types of nylon nanosheets were considered, i.e. nylon 2 (glycine), nylon 4, nylon 8, and nylon 10. For each of them, the number of nylon chains was varied from 2 to 3, 5, 7, and 9. All nanosheets were made to have 20 repeat units along the chain direction. Due to the different numbers of carbon atoms in the repeat units, the nylon nanosheets have different lengths (see Table 4.1 for the lengths of the polymer chains of different types). The thermal conductivity of each nanosheet was then calculated and normalized by that of a single polymer chain of the same type and same length (see Table 4.1 for the thermal conductivities of the single polymer chains). The normalized thermal conductivity provides a means to quantify the change in thermal conductivity caused by hydrogen bonds. As shown in Figure 4.2(a), the thermal conductivities of all nylon nanosheets increase with the number of chains. This echoes our previous study on protein β-sheets, both showing positive contributions of hydrogen bonds to the nanoscale thermal transport process.

Table 4.1. Length and thermal conductivity of four fully extended nylon chains. Each of them has 20 repeat units along the chain direction.

	nylon 2	nylon 4	nylon 8	nylon 10
Length (nm)	7.7	12.7	22.9	28
Thermal Conductivity (W/Km)	5.31	5.77	6.48	7.83

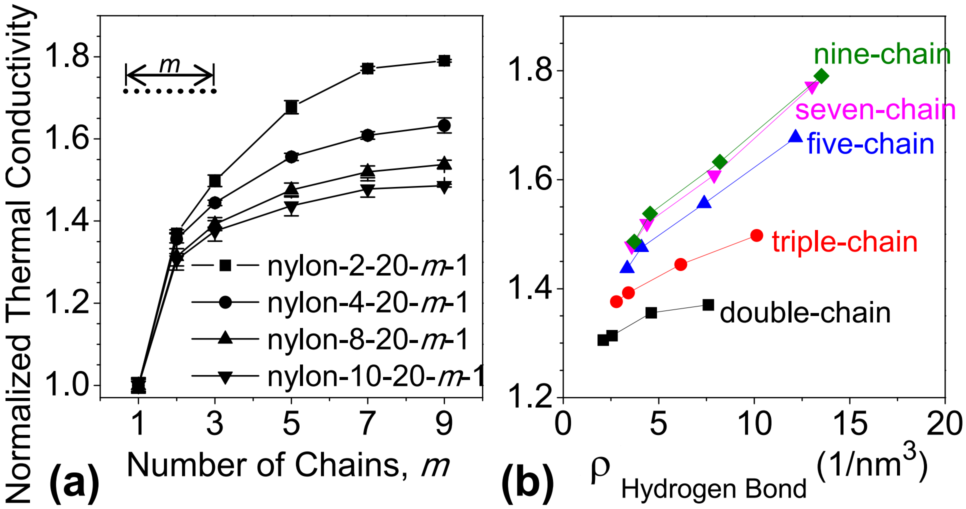

Figure 4.2. (a) Normalized thermal conductivity of 20 nylon nanosheets with different types and different widths (characterized by *m*). The thermal conductivity of each nanosheet is normalized by that of a nylon single chain (*m* = 1) that has the same type. The normalized thermal conductivity provides a means to quantify the change in thermal conductivity caused by hydrogen bonds. (b) Normalized thermal conductivity versus the number density of hydrogen bonds in the nanosheet.

Furthermore, it is discovered that the degree of enhancement in thermal conductivity is controlled by the density of hydrogen bonds. Figure 4.2(b) plots the normalized thermal conductivity as a function of the number density of hydrogen bonds in the nanosheet. Five lines are shown, and they correspond to the nanosheets of different widths (or different numbers of chains, *m*). In each line, there are four data points which correspond to the four types of nylon. The type of nylon and the number of chains both determine the density of hydrogen bonds in a nanosheet. Overall, we find that the normalized thermal conductivity (i.e. the degree of enhancement) increases with the density of hydrogen bonds which, again, demonstrate the positive contributions of hydrogen bonds to heat transfer.

It is worth pointing out that the thermal conductivities revealed by our simulations for crystalline nylon nanofibers are much higher than that reported for bulk nylon materials (typically 0.25 W/m K[24]). The different thermal conductivities result from the different structures of these materials. In bulk nylon, polymer chains are randomly oriented with weakly coupled chains, and there are numerous impurities and imperfections. All these factors lead to high phonon scattering, short phonon mean free path, and hence low thermal conductivities. In the crystalline nylon nanofibers, however, the polymer chains are highly oriented, and defects are reduced, all of which contribute to the improved thermal conduction. Such high thermal conductivities of polymer nanofibers have been experimentally demonstrated using nylon 11 nanofibers with the thermal conductivities measured to be about 1.6 W/m K.[25] Our work presented in this paper provides a systematic fundamental understanding of why thermal conduction is improved in the nylon polymer nanofibers, and how hydrogen bonds contribute to this improvement.

4.4.2 Hydrogen Bonding Increases Phonon Group Velocity

To reveal the phonon physics, dispersion curves were generated for selected crystalline nylon 2 nanosheets using the finite displacement method. Figure 4.3(a) plots the phonon dispersion curves of a single-chain and a double-chain nylon 2 nanosheets. It is readily seen that phonons at low frequencies are predominantly excited by the Boltzmann distribution; and most optical phonon branches, especially those with higher frequencies, have a group velocity of zero. Therefore, it is confirmed that heat is mainly transferred by acoustic phonons. To further understand the effects of hydrogen bonds, Figure 4.3(b) plots the three acoustic phonon branches for the single-, double-, and triple-chain nanosheets, respectively. The slope of each phonon branch indicates the group velocity at a specific ξ. The slope of a line connecting Γ and X in Figure 4.3(b) defines the average group velocity.

From the single chain to the hydrogen-bonded triple-chain nanosheet, acoustic phonons of all polarization branches demonstrate a blueshift owing to the increasing hydrogen bonds. The blueshift in frequency is directly linked with the increase of group velocities. Specifically, hydrogen bonds increase the group velocity of longitudinal acoustic (LA) phonons when ξ falls in the range of 0.23-0.38; for out-of-plane acoustic (ZA) and transverse acoustic(TA) phonons, however, hydrogen bonds increase the group velocity almost throughout the entire first Brillouin zone. Therefore, the confinement of chains in a hydrogen bonded environment can, either partially or entirely, increase the group velocities of acoustic phonons in all polarization branches. This partially explains the enhanced thermal conductivities of the hydrogen-bonded crystalline polymers. By phonon Boltzmann transport equation,[26] the thermal conductivity of a one-dimensional system $k_x = C_v \cdot v_x \cdot \Lambda$, where C_v is the heat capacity, v_x is the representative group velocity of phonons, and Λ is the phonon mean free path. Higher average group velocity in hydrogen-bonded polymers contributes to enhancing the thermal conductivities.

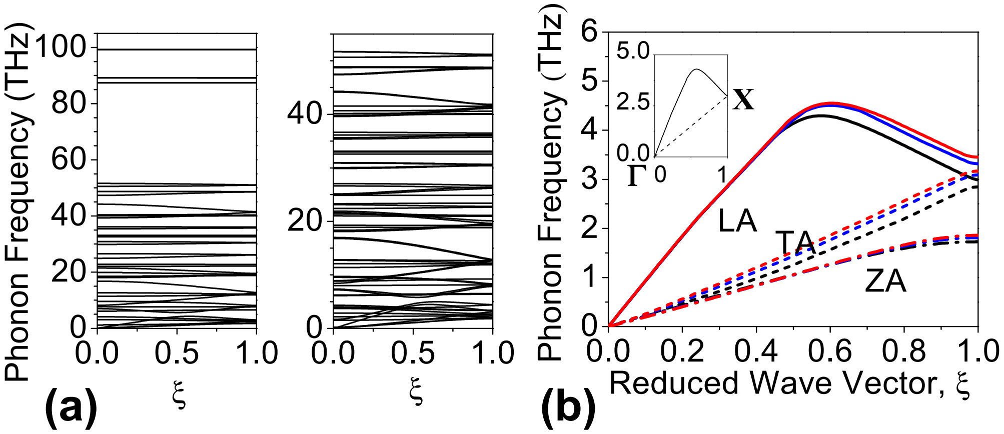

Figure 4.3. (a) Phonon dispersion curves of nylon2-2-1-1 (left) and nylon2-2-2-1(right). ξ is the reduced wave vector defined to be $q_x/(\pi/a_x)$, where q_x and a_x are the wave vector component and the lattice constant in the x direction, respectively. For nylon2-2-2-1, frequencies higher than 55 THz are truncated for visual clarity. (b) Acoustic phonon branches are compared between nylon2-2-1-1 (black), nylon2-2-2-1 (blue), and nylon2-2-4.43-1 (red). LA, TA, and ZA refer to the longitudinal, transverse, and out-of plane acoustic phonon branches, respectively. The slope of these phonon dispersion curves indicates the group velocity. Inset of (b) shows the definition of the average group velocity, i.e. the slope of a line connecting the origin (Γ) and the point X (the intersection between the phonon branch and the line with $\xi = 1$).

4.4.3 Hydrogen Bonding Improves Inter-Chain Lattice Ordering

In addition to increasing phonon transport velocity, hydrogen bonds also improve structural ordering which reduces phonon scattering. The importance of structural ordering to efficient thermal conduction has been demonstrated in many previous studies.[4, 27] For polymers (even for those with well-aligned chains), there is an important factor that can cause structural disorder and thereby obstruct thermal conduction – torsion of the chains. In a recent computational study of polyethylene nanofibers [4], Zhang et al. tuned the torsion of chains by adjusting the dihedral parameters in the force field; the polymers with restricted torsional motion were found to have higher thermal conductivities. Using the same approach, similar conclusions have been reached for crystalline nylon polymers (see ESI, Figure C.1). It is hypothesized that, in hydrogen-bonded polymer nanofibers, the interchain hydrogen bonds can confine torsional motion, thereby improving thermal conductivity.

To demonstrate the critical role of hydrogen bonds in improving structural ordering, we statistically analyzed the dihedral distribution in the single-chain, double-chain, and triple-chain nylon 2 nanosheets. Dihedral A-B-C-D is defined by four successively chemical bonded atoms A, B, C, and D; and it describes the torsional angle between the A-B-C plane and B-C-D plane about the axis connecting B and C. There are 12 types of dihedrals in nylon 2. Figure 4.4(a) plots the angle distribution of all dihedrals for each of the three nanosheets, respectively. There are seven peaks identified, centered about ±180°, ±122.7°, ±57.8°, and 0°. The dihedrals centered about ±180° are C-N-CT-C, CT-N-C-CT, N-C-CT-N, and H-N-C-O, which mainly represent the torsion of the main chain; the dihedrals centered about ±122.7° are H-N-CT-HC and O-C-CT-HC, which describe the torsion involving hydrogen bond donors (H) and acceptors (O) with respect to HC; the dihedrals centered about ±57.8° are C-N-CT-HC and N-C-CT-HC; the dihedrals centered about 0° are H-N-CT-C, H-N-C-CT, O-C-CT-N, and CT-N-C-O, which also characterize the torsion involving hydrogen bond donors and acceptors about the main chain. The angle distribution of each of these dihedrals can be found in Appendix C, Figure C.2.

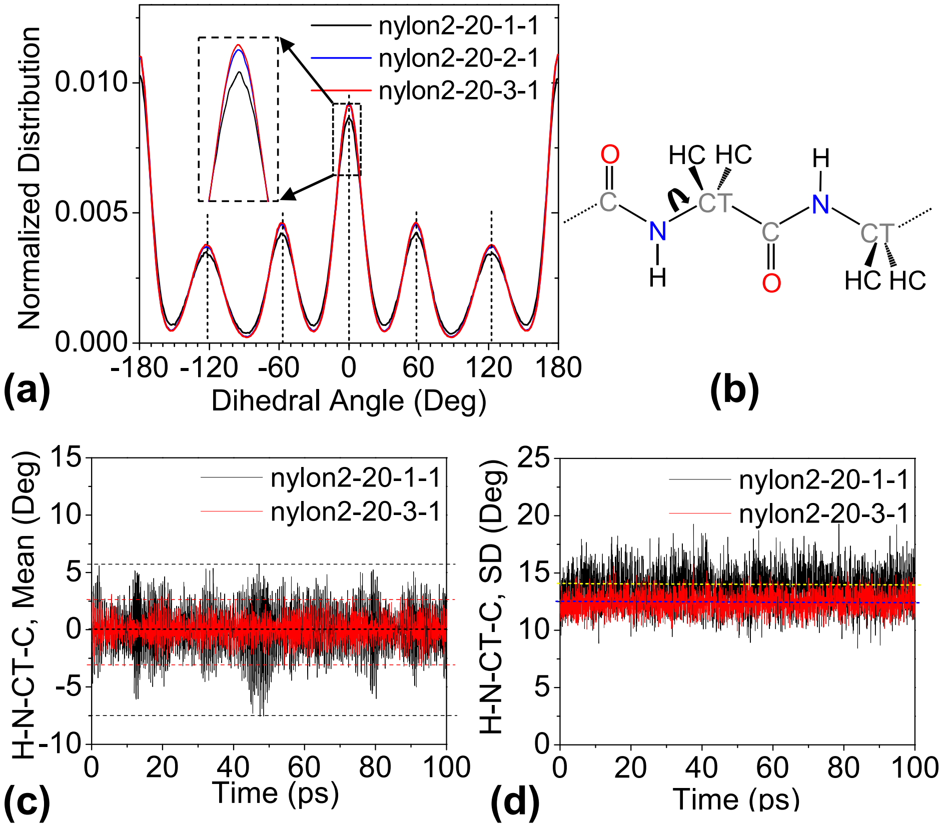

Figure 4.4. (a) Normalized distribution of all dihedrals in the nylon2-20-*m*-1 nanosheets where *m* is 1, 2, and 3, respectively. (b) The H-N-CT-C dihedral. (c) The mean of all H-N-CT-C dihedrals versus time. Dashed lines show the average, upper bound, and lower bound of the dihedrals. Inset defines the H-N-CT-C dihedral as the torsional angle between the H-N-CT plane and the N-CT-C plane. (d) The standard deviation of all H-N-CT-C dihedrals versus time. Dashed lines show the average.

Comparing the dihedral distributions, we find that the hydrogen-bonded triple-chain nanosheet has the highest and sharpest peaks among the three nylon 2 nanosheets under investigation. In other words, the dihedrals in the triple-chain nanosheet are less deviated from their equilibrium values, leading to less twisted and more ordered chains. In such crystalline polymers, the hydrogen bond donors and acceptors have higher probabilities to reside on the same plane of the main chain atoms; and the rotation of all side atoms about the main chain is strongly restricted. All these factors contribute to an improved interchain lattice order of the polymers, leading to enhanced thermal conductivities.

More statistical analysis was performed to further demonstrate the variation of the various dihedrals over time. At each time step, all dihedral angles of the same type were averaged to give a mean value; and the standard deviation (SD) was evaluated as well to quantify the fluctuation. Both the mean and the standard deviation are shown in Figure 4.4(c-d) as functions of time for the H-N-CT-C dihedral [Figure 4.4(b)]. The data of other 11 dihedrals can be found in Appendix C, Figure C.3-Figure C.4. Apparently, all history curves in Figure 4.4(c) fluctuate about 0^o which is the equilibrium angle of the H-N-CT-C dihedral. Due to the hydrogen bonds that restrict torsion, the triple-chain nylon 2 nanosheet demonstrates the most stable H-N-CT-C dihedral (with the least deviation from 0^o). All these results, again, demonstrate the positive effects of hydrogen bonds in maintaining highly ordered crystalline polymers for efficient thermal conduction.

4.4.4 Coupled Effects of Inter-Sheet VdW Interaction and Intra-Sheet Hydrogen Bonding

The above analysis is focused on polymer nanosheets to reveal the critical contributions of hydrogen bonds to the nanoscale thermal transport. As many of such nanosheets stack to form nanofibers, the vdW interaction takes effect and dominates the interchain interactions between the nanosheets. While hydrogen bonding has been shown to facilitate thermal conduction in crystalline polymer nanosheets, the vdW interaction is known to be a factor obstructing thermal conduction in many other materials[8, 28, 29]. As both of them compete in the crystalline nanofibers, which one will win? To answer this question, we computed the thermal conductivities of four nylon 2 nanofibers, i.e. nylon2-20-*m*-*m* with *m* varied from 2 to 3, 5, and 7, and the results are shown in Figure 4.5(a). As the nanofiber grows in both transverse directions, the thermal conductivity keeps increasing with a tendency to converge. The main contributor to the increased thermal conductivity is, again, the intra-sheet hydrogen bonds. Comparing the dihedral distributions of the single chain and the 2×2 nanofiber in Figure 4.5(b), we find that the 2×2 nanofiber has sharper peaks implying more ordered structure.

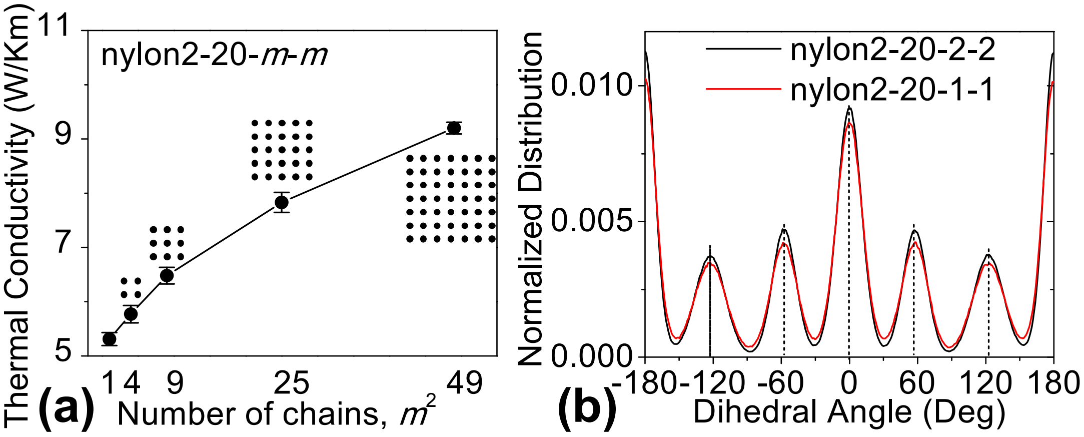

Figure 4.5. (a) Thermal conductivity of multilayer nylon 2 nanofibers, nylon2-20-m-m, where m is 1, 2, 3, 5, and 7. Here, thermal conductivity is plotted against the number of chains to show the dependence of thermal conductivity on the cross-sectional area of the polymer nanofibers. (b) Normalized dihedral distribution of the nylon2-20-2-2 nanofiber and the nylon2-20-1-1 single chain.

It is worthwhile to further compare Figure 4.5(a) with Figure 4.2(a). The former shows the variation of thermal conductivity from 1D to 3D, while the latter shows the variation of thermal conductivity from 1D to 2D. Structurally, in the 2D sheets, the polymer chains are bundled by hydrogen bonds; in the 3D fibers, the sheets stack as facilitated by the inter-sheet vdW interaction. In general, it is found that the inter-sheet vdW interaction in the 3D nanofibers adversely affects the improvement caused by the intra-sheet hydrogen bonds. However, due to the prominent effects of hydrogen bonds, the thermal conductivity still increases as the nylon nanofibers grow in transverse directions. This trend is opposite to that previously shown for the polyethylene nanofibers; due to the nonexistence of hydrogen bonds in polyethylene, the thermal conductivity of the polyethylene nanofibers was shown to decrease from 1D to 2D and from 2D to 3D.[10]

4.5 Conclusions

In summary, we have demonstrated that the interchain hydrogen bonds in crystalline polymers serve as “soft grips” to restrict the torsional motion of polymer chains, leading to enhanced thermal conductivities. Higher thermal conductivities can be achieved by increasing the density of hydrogen bonds, or by increasing the number of chains comprising the polymer nanofibers/nanosheets. This is opposite to the effects of the vdW interaction. Many previous studies have shown that the vdW interaction obstructs heat transfer in carbon nanostructures; as a bundled/layered structure comprises of more and more carbon nanotubes or graphene layers, thermal conductivity decreases.[8, 28] The unique contribution of hydrogen bonding to heat transfer is linked with its profound effects on the structural ordering and phonon transport. Suggested by the analysis of the dihedral distribution and phonon dispersion, the hydrogen bonds in crystalline polymers restrict torsion, blueshift acoustic phonon branches, and increase the averages group velocities of phonons. Such effects of hydrogen bonds can be applied to rationally design crystalline polymers for improved thermal conductivities.

4.6 Acknowledgments

This work was financially supported by Utah State University. The authors appreciate fruitful discussions with Prof. Lingti Kong (Shanghai Jiao Tong University).

NOTES AND REFERENCES

1. M. Chanda and S. K. Roy, *Plastics Technology Handbook*, CRC Press2006.
2. C. L. Choy, *Polymer*, 1977, **18**, 984-1004.
3. A. Henry and G. Chen, *Phys Rev Lett*, 2008, **101**, 235502.
4. T. Zhang and T. F. Luo, *J Appl Phys*, 2012, **112**, 094304.
5. S. Shen, A. Henry, J. Tong, R. T. Zheng and G. Chen, *Nat Nanotechnol*, 2010, **5**, 251-255.
6. T. Sun, J. X. Wang and W. Kang, *Nanoscale*, 2013, **5**, 128-133.
7. J. Hone, B. Batlogg, Z. Benes, A. T. Johnson and J. E. Fischer, *Science*, 2000, **289**, 1730-1733.
8. S. Ghosh, W. Z. Bao, D. L. Nika, S. Subrina, E. P. Pokatilov, C. N. Lau and A. A. Balandin, *Nat Mater*, 2010, **9**, 555-558.
9. D. Singh, J. Y. Murthy and T. S. Fisher, *J Appl Phys*, 2011, **110**, 044317.
10. A. Henry, G. Chen, S. J. Plimpton and A. Thompson, *Phys Rev B*, 2010, **82**, 144308.
11. T. Steiner, Angewandte Chemie International Edition, 2002, **41**, 48-76.
12. G.-H. Kim, D. Lee, A. Shanker, L. Shao, M. S. Kwon, D. Gidley, J. Kim and K. P. Pipe, *Nat Mater*, 2015, **14**, 295-300.
13. L. Zhang, T. Chen, H. Ban and L. Liu, *Nanoscale*, 2014, **6**, 7786-7791.
14. L. Zhang, Z. Bai, H. Ban and L. Liu, *Phys Chem Chem Phys*, 2015.
15. G. Miño, R. Barriga and G. Gutierrez, *The Journal of Physical Chemistry B*, 2014, **118**, 10025-10034.
16. S. Dasgupta, W. B. Hammond and W. A. Goddard, *J Am Chem Soc*, 1996, **118**, 12291-12301.
17. Y. Y. Li and W. A. Goddard, *Macromolecules*, 2002, **35**, 8440-8455.
18. S. Plimpton, *J Comput Phys*, 1995, **117**, 1-19.

19. W. Damm, A. Frontera, J. TiradoRives and W. L. Jorgensen, *J Comput Chem*, 1997, **18**, 1955-1970.

20. R. S. Paton and J. M. Goodman, *J Chem Inf Model*, 2009, **49**, 944-955.

21. F. Muller-Plathe, *J Chem Phys*, 1997, **106**, 6082-6085.

22. C. Nieto-Draghi and J. B. Avalos, *Mol Phys*, 2003, **101**, 2303-2307.

23. A. Togo and I. Tanaka, *Scripta Mater*, 2015, **108**, 1-5.

24. A. L. Moore, A. T. Cummings, J. M. Jensen, L. Shi and J. H. Koo, *Journal of Heat Transfer*, 2009, **131**, 091602-091602.

25. Z. X. Zhong, M. C. Wingert, J. Strzalka, H. H. Wang, T. Sun, J. Wang, R. K. Chen and Z. Jiang, *Nanoscale*, 2014, **6**, 8283-8291.

26. G. Chen, *Nanoscale energy transfer and conversion*, Oxford University Press2005.

27. J. Liu and R. G. Yang, *Phys Rev B*, 2012, **86**, 104307.

28. M. T. Pettes and L. Shi, *Adv Funct Mater*, 2009, **19**, 3918-3925.

29. Z. D. Han and A. Fina, *Prog Polym Sci*, 2011, **36**, 914-944.

CHAPTER 5

EXCEPTIONAL THERMAL CONDUCTANCE ACROSS HYDROGEN-BONDED GRAPHENE/POLYMER INTERFACES

5.1 Abstract

Ineffective heat transfer between dissimilar materials of drastically different properties is a challenge for many areas including nanoelectronics and nanocomposites. Here, using atomistic simulations, we demonstrate that the thermal conductance across the interfaces between graphene and poly(methyl methacrylate) (PMMA) can be improved by 273% by introducing hydrogen-bond-capable hydroxyl groups to the interfaces. Stronger than van der Waals interactions, the hydrogen bonds are found to improve the interfacial association, thereby enhancing the coupling of low-frequency vibrational modes. Using the integrated autocorrelation of interfacial heat power, we show directly that the hydrogen bond donors, i.e. oxygen atoms in the hydroxyl groups, build the most effective thermal transport pathways at the graphene/PMMA interfaces. The enhanced interfacial thermal conductance is tunable in a wide range by varying the degree of functionalization, with an upper limit imposed by the saturation of hydrogen bonding. All these results suggest the design of "hydrogen-bonded material interfaces" for drastically improving interfacial thermal transport towards a wide range of applications.

Zhang, L., Bai, Z. and Liu, L., 2016. Exceptional Thermal Conductance across Hydrogen‐Bonded Graphene/Polymer Interfaces. Advanced Materials Interfaces, 3(13).

5.2 Introduction

Material interfaces are crucial to determining the thermal properties of many heterogeneous materials and structures including nanoelectronics, superlattice nanowires, and nanocomposites.[1-8] Among them, polymeric nanocomposites incorporating graphene[9] or carbon nanotubes[10] have demonstrated thermal conductivities in the order of 10 W m^{-1} K^{-1}, much lower than that of their constituents, e.g. graphene (~5000 W m^{-1} K^{-1}) and carbon nanotubes (2000~6600 W m^{-1} K^{-1}).[11,12] The drastic discrepancy is not within the scope of the effective medium theory,[13,14] but is attributable to the interfaces between the low-dimensional carbon materials and the polymeric matrix. In general, at material interfaces, phonon transport is scattered which inhibits heat flow and lowers the interfacial thermal conductance (or Kapitza conductance).[15] Previous studies have shown that the interfacial thermal conductance at the graphene/polymer and nanotube/polymer interfaces are as low as 12-60 MW m^{-2} K^{-1},[8,13] which drastically compromises the exceptional thermal properties of graphene and nanotubes, thereby reducing the overall conductivities of the nanocomposites.

To improve the interfacial thermal conduction, interfaces between dissimilar materials need to be engineered for reduced phonon scattering. Current approaches include, but are not limited to, controlling interfacial adhesion,[16-18] improving interfacial stiffness,[19,20] strengthening interfacial interactions,[21,22] and manipulating phonon modes.[23-25] For graphene/polymer nanocomposites, in particular, the interfacial thermal transport can be improved by changing the orientation of few-layer graphene,[8] grafting graphene with polymer chains,[26] and functionalizing graphene for tailored phonon modes.[27] In the first approach, the improvement results from the high thermal conductivity of graphene/graphite in the basal plane along with the enhanced interfacial coupling.[28,29] In the other two, the polymer chains and functional groups serve as thermal bridges to couple the vibrational modes of graphene with those of the polymeric matrix, thereby minimizing phonon scattering and improving thermal transport.

Despite the progress, little attention has been drawn to the manipulation of bonding strength at the graphene/polymer interfaces for improved heat transfer. In most nanocomposites,[26,27] molecular interactions at material interfaces are dominated by van der Waals forces. It is hypothesized that, interfacial heat transfer can be significantly improved by enabling hydrogen bonds at the interfaces. The hypothesis is made based on three reasons. First, the strength of hydrogen bonds ranges from 10 to 190 kJ mol^{-1}, 1~2 orders of magnitude higher than that of the van der Waals interactions.[30,31] Second, recent advances in surface treatment[32] have made it relatively simple to anchor hydrogen-bond-capable chemical groups to the graphene surfaces to enable hydrogen bonds with many polymers. Third, hydrogen-bond-facilitated thermal conduction has been recently demonstrated in several other material systems including crystalline polymer nanofibers,[33] amorphous polymer blends,[34] along with silk β-sheets[35,36] and α-helices.[37,38] However, the use of hydrogen bonds to improve the interfacial thermal transport at graphene/polymer interfaces has not yet been reported.

Here, using reverse non-equilibrium molecular dynamics along with various vibrational mode and structural analysis tools, we demonstrate that the presence of hydrogen bonds (in hydroxyl-functionalized graphene/PMMA composites) significantly improves the thermal conductance across the graphene/polymer interfaces; and the improvement is controllable by varying the density of hydrogen bonds. To provide more physical insights, we analyzed the vibrational density of states at the material interfaces, cumulative correlation between the vibrational modes, and the integrated autocorrelation of interfacial heat power exchange. The analyses show that the incorporation of hydrogen bonds improves the coupling of low-frequency vibrational modes at the interfaces between the graphene and PMMA, which contributes directly to the enhancement of interfacial thermal conductance. We further demonstrate that among all components of the hydroxyl-functionalized graphene embedded in PMMA, the oxygen atoms in hydroxyl groups (which are also hydrogen bond donors) contribute the most to the enhanced interfacial thermal conductance. All these results suggest that hydrogen bonds improve the interfacial thermal conductance, and hydrogen-bonded interfaces should be targeted for improving heat transfer.

5.3 Results and Discussion

This study investigates three types of filler materials, i.e. pristine monolayer graphene (**Figure 5.1**b), hydroxyl (-OH) functionalized graphene (Figure 5.1c), and methyl (-CH_3) functionalized graphene. They form different nanocomposites when embedded in the amorphous PMMA matrix (e.g. Figure 5.1a). The three nanocomposites are denoted by MLG, MLG-OH, and MLG-CH_3, respectively. Among these three systems, MLG-OH is the only one that can form hydrogen bonds at the graphene/PMMA interfaces (Figure 5.1c); in the other two, filler materials interact with PMMA via van der Waals interactions only.

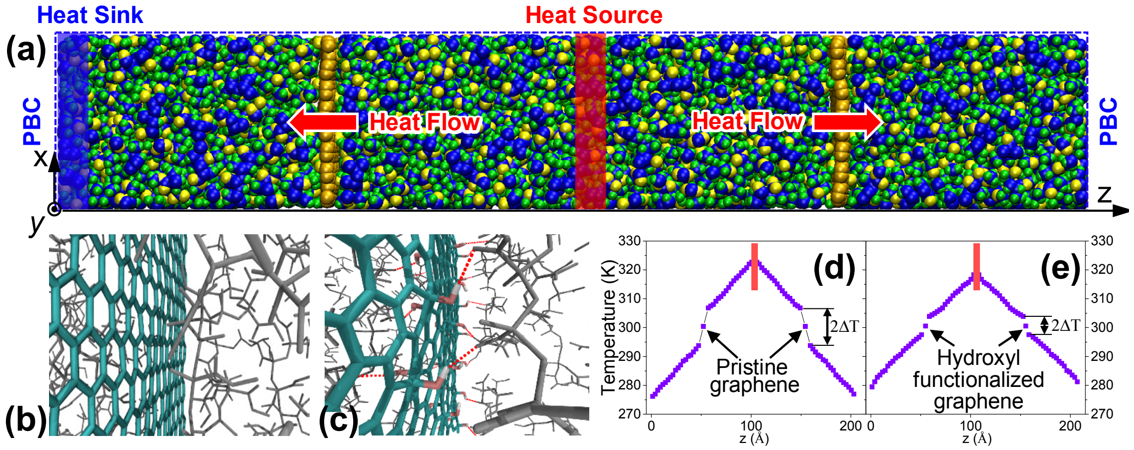

Figure 5.1. (a) A molecular dynamics simulation system to calculate interfacial thermal conductance: vertical layers of gold spheres: monolayer graphene or functionalized graphene; blue, yellow, and green spheres: carbon, oxygen, and hydrogen atoms of the PMMA matrix. Heat flow is generated from the "heat source" (red slab) to the "heat sink" (blue slab) by using a velocity swapping scheme. (b) The interface between graphene (cyan) and PMMA (grey) is dominated by van der Waals interactions. (c) The interface between hydroxyl-functionalized graphene (cyan) and PMMA (grey) involves numerous hydrogen bonds (red dashed lines). Temperature profiles generated in the systems incorporating (d) graphene/PMMA interfaces and (e) hydroxyl-functionalized graphene/PMMA interfaces.

The hydroxyl group is appropriate to represent hydrogen-bond-capable functional groups because it is widely present in graphene surfaces.[39-42] The methyl group is a reasonable comparison to the hydroxyl group because of the similar molecular weights and chain lengths. In both MLG-OH and MLG-CH_3, functional groups are covalently bonded to both sides of the graphene in "para" positions, which are the most energetically favorable sites for functionalization.[43] All systems have the same cross-sectional size of 34.45 Å × 34.10 Å, which is adequately large to account for the size effect on interfacial thermal conductance for two reasons.[8,27,44] First, a previous study of graphene/paraffin nanocomposites has demonstrated that 85% and 93% of phonon contribution to the interfacial thermal conductance can be captured when the simulation cell is larger than

19.68 Å and 39.39 Å in the cross-section, respectively.[8] Second, 35 Å is sufficient to account for the contribution of all vibrational modes to the thermal transport in amorphous polymers.[8] In all systems, the PMMA matrix is composed of 36 chains, each having 40 monomers. PMMA does not have hydrogen bonds by itself; but both oxygen atoms in an ester group may serve as hydrogen bond acceptors, forming hydrogen bonds with the hydroxyl groups anchored to the graphene.[45-47] The thermal conductance at a graphene/PMMA interface can be calculated by a ratio between the heat flux[48] and the temperature drop across the interface (Figure 5.1d-e).[44]

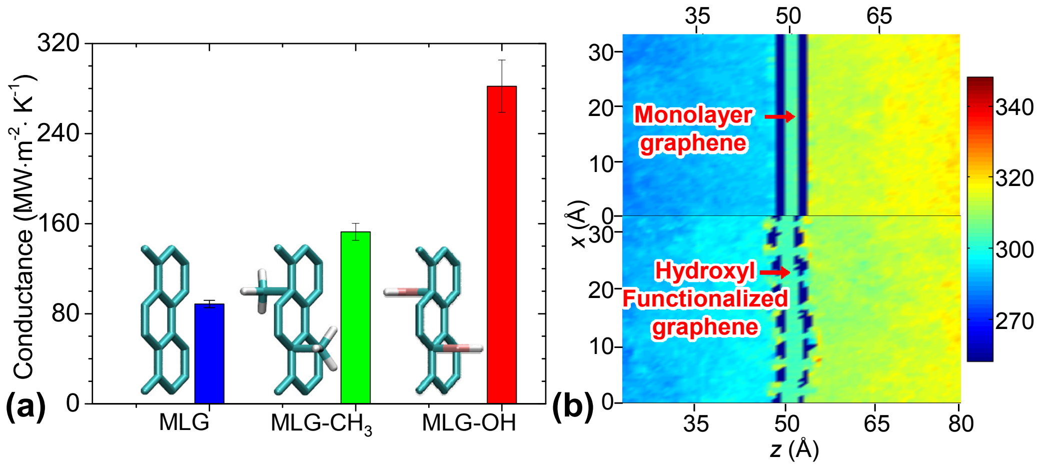

Figure 5.2. (a) Interfacial thermal conductance at graphene/PMMA (MLG), methyl-functionalized graphene/PMMA (MLG-CH_3), and hydroxyl-functionalized graphene/PMMA (MLG-OH) interfaces. Insets show unit cells of the filler materials (cyan: carbon; white: hydrogen; pink: oxygen). (b) Temperature distributions near the MLG (top panel) and MLG-OH (bottom panel) interfaces. Dark blue regions are gaps between the filler material and the matrix.

Figure 5.2a shows the graphene/PMMA interfacial thermal conductance in MLG, MLG-CH_3, and MLG-OH, respectively. The latter two have the same degree of functionalization of 12.5% (see the insets of Figure 5.2a; 12.5% is the default degree of functionalization in this work unless otherwise stated). By functionalizing the pristine graphene with hydroxyl groups, the interfacial thermal conductance is increased by 218%, from 88.68 $MW\cdot m^{-2}\cdot K^{-1}$ to 282.06 $MW\cdot m^{-2}\cdot K^{-1}$; in comparison, functionalization with methyl groups leads to a much less improvement of 91%. Given that hydrogen bonds are stronger than van der Waals interactions, our result agrees with a previous prediction that interfacial thermal conductance increases monotonously with the strength of interfacial bonding.[16] Nevertheless, this result contradicts another study analyzing the interfaces between graphene and paraffin ($C_{30}H_{62}$);[27] the work by Want *et al.* shows that, at the degree of functionalization of 5.36%, methyl groups enhance the interfacial thermal conductance by 67%, more than the improvement caused by hydroxyl groups (7%). This result (i.e. methyl groups improve interfacial thermal conductance more than hydroxyl groups) is opposite to our conclusion. The inconsistency results from a fundamental difference between the material systems: PMMA in our work is hydrogen-bond-capable, while paraffin is not. Simply put, the hydroxyl group outperforms the methyl group when hydrogen bonds exist at the interfaces; and without hydrogen bonds, the hydroxyl group becomes inferior, demonstrating the critical role of hydrogen bonds.

To directly visualize the effect of hydroxyl groups on interfacial thermal conduction, Figure 5.2b plots the temperature distributions in both MLG and MLG-OH systems. As shown in the top panel, thick gaps (dark blue) exist between the graphene and the PMMA due to the steric repulsion, which inhibits heat transfer leading to a sharp drop in the temperature profile (Figure 5.1d). When the graphene is functionalized by hydroxyl groups (bottom panel of Figure 5.2b), the gaps are partly diminished with stronger association between the two materials, which helps spread the heat more effectively and evenly leading to a lower temperature drop across the interfaces (Figure 5.1e).

To further demonstrate the high interfacial association enabled by hydrogen bonds, **Figure 5.3** plots the atomic number density of PMMA in the vicinity of graphene in all three systems. Interfacial distance (which is defined as the distance from graphene to the first peak of PMMA) is found to be 3.65 Å, 4.63 Å, and 6.51 Å for MLG, MLG-OH, and MLG-CH3, respectively. Due to the steric repulsion of functional groups, MLG-OH and MLG-CH3 have further distributions of PMMA and larger interfacial distances than MLG (also see **Figure D.1**). Between the two functionalized systems, MLG-OH shows a smaller interfacial gap. The reasons are twofold. First, the strong hydrogen bonds attenuate the steric repulsion at the material interfaces (right inset of Figure 5.3). Second, methyl groups are tetrahedral and they interact with PMMA via weak van der Waals forces only, which make the steric repulsion more significant (left inset of Figure 5.3). Due to the known correlation between interfacial adhesion and thermal conductance,[8,16,17] the smaller interfacial distance in MLG-OH should improve thermal conductance. To further quantify the interfacial adhesion in these three systems, we studied the mechanical strength at the interfaces by pulling the graphene or functionalized graphene apart from the PMMA (**Figure D.2**). Among the three systems, MLG-OH is shown to have the highest interfacial strength (618.7 MPa) due to hydrogen bonds. MLG-CH3 has the lowest strength (427.4

MPa) due to the steric repulsion. Both the interfacial distance and strength studies suggest that, the interfacial hydrogen bonds in MLG-OH attenuate steric repulsion and strengthen the interface, both contributing positively to improve the interfacial thermal conductance over that achieved in MLG-CH_3. A word of caution, though, is that the correlation between interfacial strength and conductance seems to break down when comparing a "smooth" graphene/PMMA interface and a "rough" methyl-functionalized graphene/PMMA interface, as MLG-CH_3 shows a larger interfacial conductance but a lower interfacial strength than MLG.

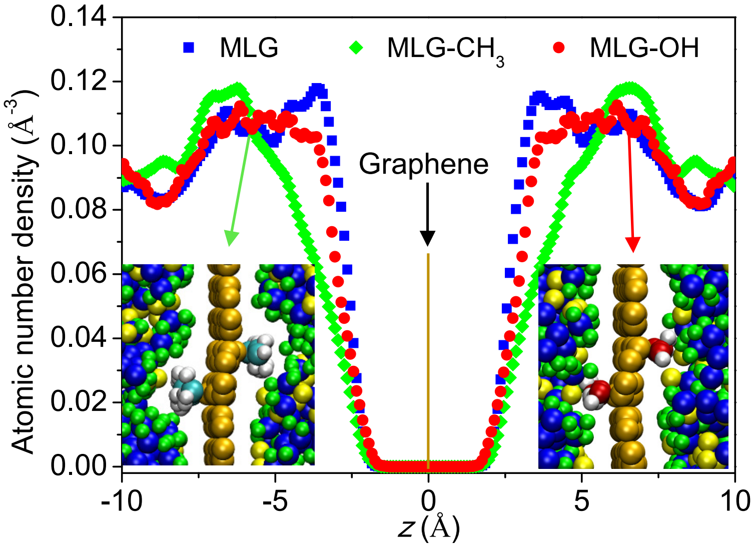

Figure 5.3. Atomic number density of PMMA in the vicinity of graphene in the MLG, MLG-CH_3, and MLG-OH systems. The graphene is positioned at $z = 0$. Left and right insets: snapshots of the MLG-CH_3 and MLG-OH interfaces (gold: graphene; cyan, white, and red: carbon, hydrogen, and oxygen in functional groups; green, blue, and yellow: PMMA).

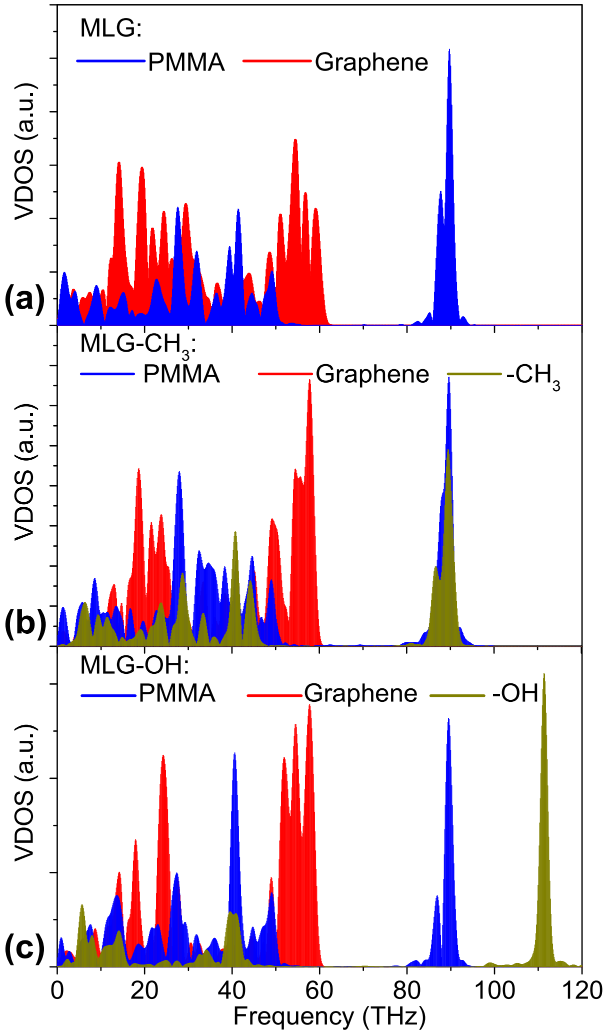

Figure 5.4. Vibrational density of states (VDOS) of different components of (a) MLG, (b) MLG-CH$_3$, and (c) MLG-OH.

Based on the acoustic mismatch and diffusive mismatch models,[49] interfacial thermal conductance is higher when the vibrational modes of two materials are better matched.[15] We calculated the vibrational density of states (VDOS) for the graphene, functional groups (if exist), and PMMA, respectively, in all three material systems, shown in **Figure 5.4**. It deserves noting that the diffusive mismatch model usually calculates the phonon transmission coefficients by using the properties of bulk materials without involving real interfaces.[15] To address this issue, our calculations were performed in the vicinity of the graphene only (maximum 15 Å from the graphene).

Figure 5.4a shows that in MLG, the VDOS peaks of PMMA and graphene have significant mismatch, especially at low frequencies. By comparison, the other two systems show well matched VDOS between the functional groups and the PMMA matrix (Figure 5.4b-c): in MLG-CH_3, VDOS peaks overlap at 6.60, 9.28, 23.93, 40.89, 44.43, and 89.36 THz; and in MLG-OH, VDOS peaks overlap at 5.98, 7.56, 14.52, and 40.53 THz. In particular, MLG-OH shows more significant coupling between the low-frequency vibrational modes, which are important to improving interfacial thermal transport.[44] We further separate the in-plane vibrational modes from the out-of-plane ones. It is found that, in MLG, the matched vibrational modes (between graphene and PMMA) are mainly of the out-of-plane type (**Figure D.3**a-b). This result is consistent with a previous finding that the coupling between the out-of-plane vibrational modes of graphene and a polymer (phenol formaldehyde) at low frequencies offers the most important channel for thermal transport across the interfaces.[44] We further discover that, in MGL-OH and MLG-CH_3, the matched low-frequency vibrational modes (between functional groups and PMMA; < 20 THz) are mainly of the in-plane type (Figure D**.3**c-f).

To clearly show the coupling of low-frequency vibrational modes which denominate interfacial thermal transport, the cumulative correlation factor (see Methods) is employed to quantitatively study the coupling of vibrational modes up to a cutoff frequency, at the interface between two materials. A high cumulative correlation factor at a low cutoff frequency would indicate good coupling of low-frequency vibrational modes and hence, imply high thermal conductance across the interface.[44] Since the coupling between graphene and PMMA is comparable in all three material systems (**Figure D.4**c-d), this discussion is focused on the coupling between functional groups and PMMA.

Figure 5.5 plots the cumulative correlation factors between hydroxyl and PMMA in MLG-OH, between methyl and PMMA in MLG-CH_3, and between graphene and PMMA in MLG. Four regions are defined. In region I (< 28.08 THz), the cumulative correlation factor between hydroxyl and PMMA in MLG-OH is ranked the highest. In the other two primary regions (II and IV), the cumulative correlation factor between methyl and PMMA in MLG-CH_3 is ranked the highest, particularly when the frequency exceeds 89 THz; the sharp increase at ~89 THz agrees with the overlapping of peaks at 89.36THz as shown in Figure 5.4b. All these results support the finding that MLG-OH has the highest interfacial thermal conductance. Indeed, the primary contributor to interfacial thermal conduction is the coupling of low-frequency vibrational modes, which is the most significant in MLG-OH due to the hydrogen-bond-capable hydroxyl groups, as shown in Figure 5.5. Furthermore, the high coupling between hydroxyl and PMMA is found to be mainly associated with the in-plane vibrational modes (Figure D.**4**a-b). In addition, we note that the cumulative correlation factor defined is exactly the same as the correlation factor used in the literature,[27,50] when the cutoff frequency exceeds the maximum frequency of all vibrational modes. Therefore, the correlation factors for graphene/PMMA in MLG, hydroxyl/PMMA in MLG-OH, and methyl/PMMA in MLG-CH_3 can be extracted from Figure 5.5, respectively, as 0.009, 0.011, and 0.029. These results are in reasonable agreement with the reported values of 0.006, 0.007, and 0.437 for similar systems with paraffin as the matrix.[27]

We further study the integrated autocorrelation of interfacial heat power, to enable a quantitative evaluation of the contributions made by different thermal conducting channels to the interfacial thermal transport. Fundamentally, interfacial thermal conductance is proportional to the integrated autocorrelation of interfacial heat power at a material interface.

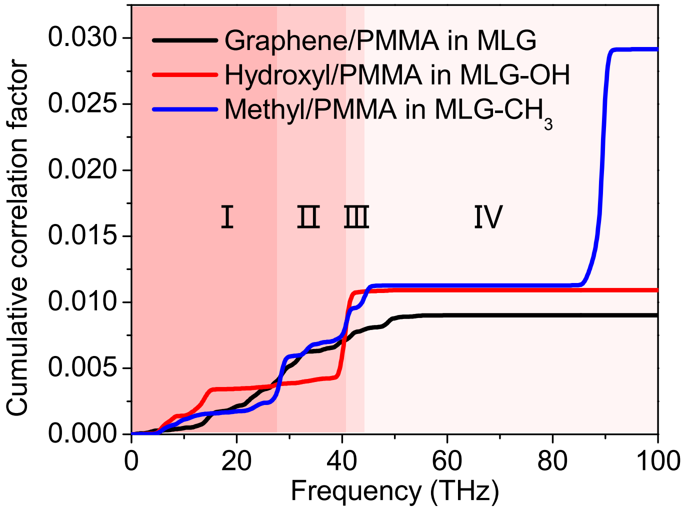

Figure 5.5. Cumulative correlation factor calculated between the graphene and PMMA in MLG, between the hydroxyl groups and PMMA in MLG-OH, and between the methyl groups and PMMA in MLG-CH3. Four regions are defined (I: < 28.08 THz; II: < 40.4 THz; III: < 44.7 THz; IV: > 44.7 THz).

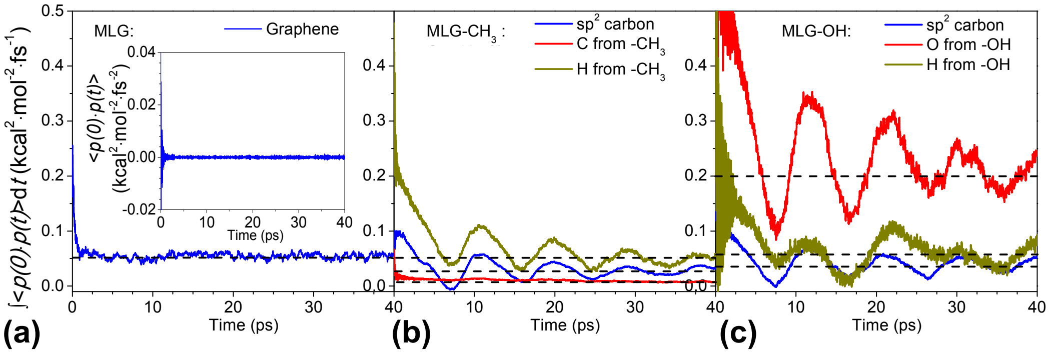

Figure 5.6. The integrated autocorrelation of interfacial heat power (a) between the graphene and PMMA in MLG, (b) between three components of the functionalized graphene (i.e. *sp*^{2} carbon atoms, and the carbon and hydrogen atoms from the methyl groups) and PMMA in MLG-CH3, and (c) between three components of the functionalized graphene (i.e. *sp*^{2} carbon atoms, and the oxygen and hydrogen atoms from the hydroxyl groups) and PMMA in MLG-OH.

Figure 5.6 plots the integrated autocorrelation of interfacial heat power for: (a) one channel (i.e. *sp*^{2} carbon atoms of graphene) in MLG, (b) three channels (i.e. *sp*^{2} carbon atoms of graphene, carbon atoms of methyl groups, and hydrogen atoms of methyl groups) in MLG-CH3, and (c) three channels (i.e. *sp*^{2} carbon atoms of graphene, oxygen atoms of hydroxyl groups, and hydrogen atoms of hydroxyl groups) in MLG-OH. Each channel is associated with an essential component of the filler material, and this study aims to understand how these channels contribute differently to the interfacial thermal transport. Note that, the *sp*^{3} carbon atoms of the functionalized graphene are excluded from this discussion due to the screening by functional groups (**Figure D.5**).

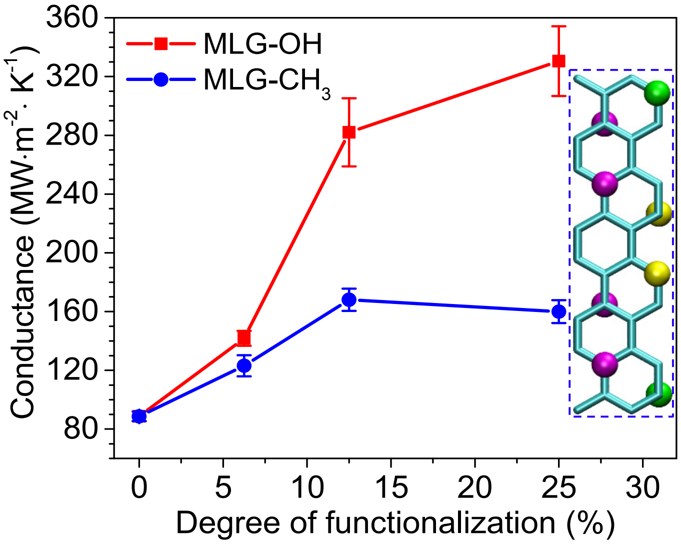

Figure 5.7. Interfacial thermal conductance versus the degrees of functionalization in MLG-OH and MLG-CH_3. Inset shows the sites of functionalization (6.25% functionalization: yellow; 12.5% functionalization: magenta; 25% functionalization: yellow, green, and magenta).

Among all the channels in the three material systems, the channel associated with the oxygen atoms in hydroxyl groups is found to contribute the most to the interfacial thermal conductance (Figure 5.6). By contrast, the contribution made by the carbon atoms in methyl groups is negligible, mainly due to the screening by the hydrogen atoms in the tetrahedral structures. In both MLG-OH and MLG-CH_3, the contributions made by the sp^2 carbon atoms in graphene are lower than that in MLG, due to the screening by functional groups; and the contributions made by the hydrogen atoms in functional groups are comparable. The dominance of hydrogen bond donors (i.e. oxygen atoms in hydroxyl groups), again, supports the importance of hydrogen bonds in improving interfacial thermal conductance.

The enhanced interfacial thermal conductance is tunable in a wide range by varying the degree of functionalization. To study this effect, we calculated the interfacial thermal conductance for MLG-OH and MLG-CH_3 at the degree of functionalization of 6.25 %, 12.5 %, and 25 %, respectively (see the inset of **Figure 5.7**). As shown in Figure 5.7, the interfacial thermal conductance in MLG-OH increases with the degree of functionalization, and shows a tendency to converge at high degrees of functionalization. In MLG-CH_3, the interfacial thermal conductance first increases and then decreases achieving a maximum at the 12.5% functionalization. Furthermore, the enhancement due to functionalization is more significant in MLG-OH. At the 6.25% functionalization, hydroxyl and methyl groups enhance the interfacial thermal conductance by 60% and 39%, respectively, which is quite different from 7% and 67% previously reported for the interfaces between paraffin and graphene at the degree of functionalization of 5.36%;[27] the discrepancy is caused by the hydrogen-bond-forming capability of PMMA. When the degree of functionalization is increased to 25%, hydroxyl groups enhance the interfacial thermal conductance by 273%, while methyl groups only lead to an improvement of 80%. All these results demonstrate the advantages of using hydrogen-bond-capable functionalization to improve interfacial thermal conduction.

The convergence shown in Figure 5.7 for MLG-OH can be understood by analyzing the formation of hydrogen bonds and the integrated autocorrelation of interfacial heat power. **Figure 5.8**a plots the number of hydrogen bonds formed between the hydroxyl-functionalized graphene and PMMA on one side of the graphene. As the degree of functionalization increases from 6.25% to 12.5% and 25%, the number of hydrogen bonds increases from 4.59 to 8.45 and 11.46. Despite the increase, the rate of hydrogen bond formation (defined by the total number of hydrogen bonds divided by the total number of hydrogen-bond-capable functional groups) is reduced from 32.8% to 30.2% and 20.5%. This reduction results from the saturation of hydrogen bonding in the hydrogen bond acceptors, i.e. oxygen atoms in the ester groups of PMMA. Figure 5.8b plots the converged integrated autocorrelation of interfacial heat power function for the three thermal conducting channels in MLG-OH, at different degrees of functionalization (see **Figure D.6** for full curves). The main contributor, i.e. oxygen atoms in hydroxyl groups, also shows a tendency to converge (Figure 5.8b), which is consistent with the trend shown in the interfacial thermal conductance (Figure 5.7) and the rate of hydrogen bond formation (Figure 5.8a). Meanwhile, the channel associated with the *sp*^{2} carbon atoms shows a descending trend, due to the increased screening by functional groups.

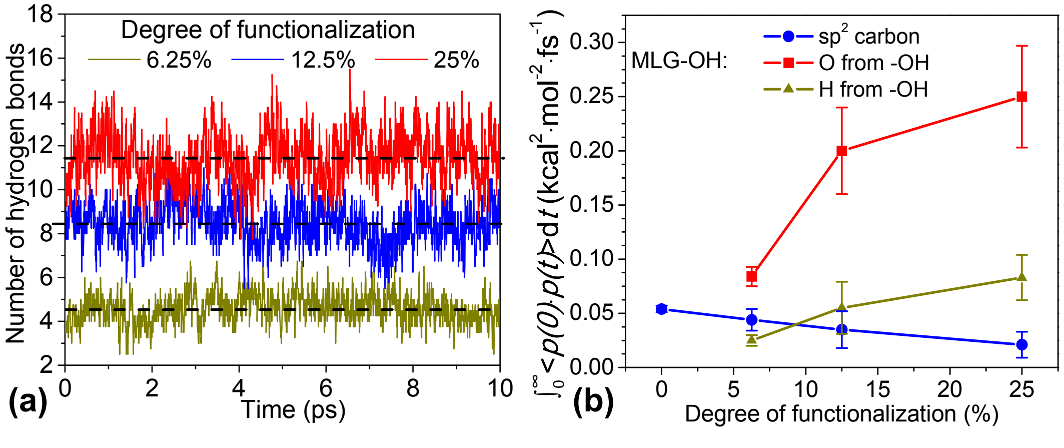

Figure 5.8. (a) Number of hydrogen bonds versus time at a hydroxyl-functionalized graphene/PMMA interface (the graphene is functionalized at the degree of functionalization of 6.25%, 12.5% and 25%). Dashed lines show the averages. (b) Converged integrated autocorrelation of interfacial heat power between PMMA and three components of the hydroxyl-functionalized graphene (i.e. *sp*^{2} carbon atoms, and the oxygen and hydrogen atoms from the hydroxyl groups) at three degrees of functionalization.

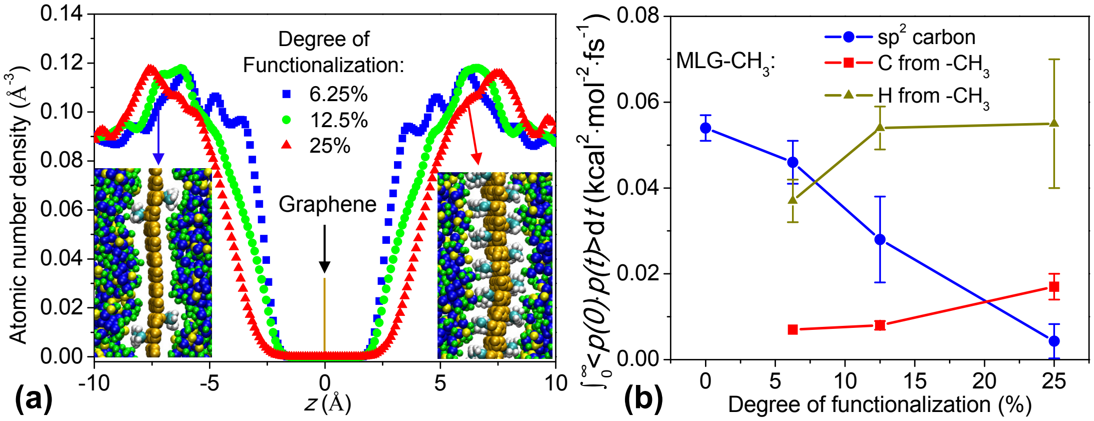

Figure 5.9. (a) Atomic number density of PMMA in MLG-CH3 with different degrees of functionalization. The graphene is positioned at $z = 0$. Left and right insets: snapshots of the interfaces at 6.25% and 25% degrees of functionalization. (b) Converged integrated autocorrelation of interfacial heat power between PMMA and three components of the methyl-functionalized graphene (i.e. sp^2 carbon atoms, and the carbon and hydrogen atoms from the methyl groups) at three degrees of functionalization.

To understand the “bell-shaped” interfacial thermal conductance in MLG-CH3, we analyzed the effects of the degree of functionalization on the distribution of PMMA and the integrated autocorrelation of interfacial heat power. Based on the plots of atomic number density in **Figure 5.9**a, the PMMA is “pushed” away from the graphene by the increased functional groups. This is also demonstrated in the insets of Figure 5.9, where dense functional groups prevent PMMA from staying in between. The increased separation between graphene and PMMA will inevitably reduce thermal transport via the channel associated with the sp^2 carbon atoms. This is supported by Figure 5.9b, where the contribution made by the sp^2 carbon atoms is shown to decrease significantly with the increasing functionalization (see **Figure D.7** for full curves). Meanwhile, the contributions made by the carbon and hydrogen atoms in methyl groups both increase. These two factors (i.e. weakened channel of sp^2 carbon atoms and strengthened channels associated with the methyl groups) compete, leading to the "bell-shaped" interfacial thermal conductance in MLG-CH_3. Similar phenomena are not present in MLG-OH. In fact, in MLG-OH, the steric repulsion at high degrees of functionalization is significantly compromised by the strong attraction of hydrogen bonding. This is supported by **Figure D.8**, where PMMA is shown to be closer to the hydroxyl-functionalized graphene than the methyl-functionalized graphene. The result, again, demonstrates the unique advantages enabled by hydrogen bonds in improving interfacial thermal transport.

5.4 Conclusion

Interfaces between dissimilar materials play a key role in various thermal transport processes, which strongly depend on not only the coupling of vibrational modes between materials, but also the strength of interfacial bonding.[15,20,22,23,49,51] This work demonstrates that, facilitated by hydrogen bonds, the hydroxyl-functionalized graphene/PMMA interfaces have much improved thermal conductance, 218% higher than that of the pristine graphene/PMMA interfaces and 68% higher than that of the methyl-functionalized graphene/PMMA interfaces. The improvement is attributed to three main factors. First, the strong hydrogen bonds enhance interfacial association and counteract the steric repulsion of functional groups, leading to thermally less abrupt interfaces and more effective thermal transport. Second, hydrogen bonds improve the coupling of low-frequency vibrational modes between materials, which further reduces phonon scattering. Third, the hydrogen bond donors (i.e. oxygen atoms in hydroxyl groups) form the most effective thermal conducting channel among all components of the functionalized graphene, serving as "thermal bridges" to drastically enhance thermal conduction. All these effects vary with the degree of functionalization. At the hydroxyl-functionalized graphene/PMMA interfaces, higher degree of functionalization leads to the saturation of hydrogen bonds and the convergence of interfacial thermal conductance. At the methyl-functionalized graphene/PMMA interfaces, higher degree of functionalization weakens the thermal conducting channel of sp^2 carbon atoms while enhancing the channels associated with the functional groups, leading to a "bell-shaped" curve of interfacial thermal conductance. All these results suggest that hydrogen-bonded interfaces should be targeted to improve the interfacial heat transfer in nanocomposites and many other heterogeneous materials and structures for a wide range of applications. It is worthy to note that covalent functionalization has been shown to lower the in-plane thermal conductivity of graphene while improving the interfacial thermal conductance.[52,53] While the present study has shed light on improving directional thermal conduction perpendicular to material interfaces, the effects on a nanocomposite with randomly oriented fillers will involve both interfacial thermal conductance and the in-plane conductance which is yet to be studied. This will be a topic for our future study.

5.5 Experimental Section

5.5.1 Interfacial Thermal Conductivity Calculations

Interfacial thermal conductivity was calculated using the reverse non-equilibrium molecular dynamics (RNEMD) method.[48] The entire system was divided into 200 slabs along the direction of intended heat flow (i.e. z-direction in Figure 5.1a). Heat flux was induced from the "heat source" slab (i.e. the red slab) to the "heat sink" slab (i.e. the blue slab) by using a velocity swapping approach. Specifically, the velocity of the "hottest" atom (with the highest kinetic energy) in the "heat sink" was swapped with that of the "coldest" atom (with the lowest kinetic energy) in the "heat source", following a virtual elastic collision model[54] where energy and momentum are both conserved. Continual velocity swapping led to higher temperature in the "heat source" slab than that in the "heat sink" slab, forming a temperature difference and heat flux in the system. The temperature difference in our simulations was controlled to be 45 K ±5 K, by carefully adjusting the frequency of velocity swapping. The induced heat flux was evaluated by $J = \Delta E / (2tA)$, where t is the time interval between two swaps, ΔE is the averaged kinetic energy transferred per swap, A is the cross-sectional area of the material, and the coefficient "2" accounts for the two symmetric heat transport paths in the system from the "heat source" to the "heat sink". Interfacial thermal conductance (G) was derived by $G = J / \Delta T$, where ΔT is the temperature drop across graphene/polymer interface, as illustrated in Figure 5.1d-e.

5.5.2 Molecular Dynamics

All molecular dynamics simulations were performed using LAMMPS.[55] OPLSAA force field[56,57] was employed to describe the interatomic interactions for two reasons. First, it has been widely used to simulate graphene,[58,59] polymers,[60,61] and their interfacial properties. Second, OPLSAA has been reported to be the most effective force field in reproducing the energy of hydrogen bonds and maintaining the stability of several hydrogen-bonded molecular complexes.[62] The geometric mixing rule was used to evaluate the non-bonded parameters between different types of atoms. Particle-particle particle mesh method (PPPM) was adopted to account for the long-range Coulomb's interactions with a root mean square accuracy of 10^{-4}. The models of PMMA, graphene, and functionalized graphene were separately prepared and fully equilibrated. The structure of PMMA was created using the self-avoiding random walks method.[63] The initial structure was relaxed in NPT at 300 K and 1 atm for 1 ns, and then relaxed in NVT at 300 K for 1 ns. Similar procedures were applied to relax the models of graphene and the functionalized graphene. Then, the graphene/PMMA nanocomposites were built by sandwiching the filler material between well relaxed PMMA (Figure 5.1a). Periodic boundary conditions were applied along all three directions. Each nanocomposites system was first minimized using the conjugate gradient algorithm, and then annealed using NVT to remove the residual stress. During the annealing treatment, the system was first heated up from 300 K to 500 K for 200 ps, then relaxed at 500 K for 500 ps and finally, cooled down to 300 K for 200 ps. After annealing, the system was relaxed again in NPT at 300 K and 1 atm for 500 ps, followed by the relaxation in NVT at 300 K for 500 ps. In all the simulations described above, time step was set to be 1 fs. In all the following simulations, time step was set to be 0.25 fs to fully capture the hydrogen bonding interactions. Each system was equilibrated again using the smaller time step (relaxed in NVT at 300 K for 1 ns and then relaxed in NVE for 1ns). With this procedure, all systems were fully relaxed for the subsequent RNEMD analysis to calculate the interfacial thermal conductance, and the equilibrium molecular dynamics analyses for extracting VDOS, integrated autocorrelation of interfacial heat power, and the number of hydrogen bonds, as described below.

5.5.3 Vibrational Density of States (VDOS)

VDOS provides valuable insights into the vibrational modes for all atoms in a system, or a group of selected atoms. It is calculated by the Fourier transformation of the velocity autocorrelation function (VACF):

$$\mathrm{VDOS}(f)=\int_0^{+\infty} e^{-i2\pi f\tau}C_v(\tau)\,\mathrm{d}\tau \tag{5.1}$$

Here, VDOS(*f*) is the VDOS at the frequency of *f*, and $C_v(\tau)$ is a normalized VACF defined by:

$$C_v(\tau)=\frac{\left\langle \vec{v}(\tau)\cdot\vec{v}(0)\right\rangle}{\left\langle \vec{v}(0)\cdot\vec{v}(0)\right\rangle} \tag{5.2}$$

where $\vec{v}(\tau)$ is the velocity vector of an atom as a function of time *τ*, <•> denotes the average for a group of selected atoms, and $\left\langle \vec{v}(\tau)\cdot\vec{v}(0)\right\rangle$ is given by:

$$\left\langle \vec{v}(\tau)\cdot\vec{v}(0)\right\rangle=\left\langle \vec{v}(m\Delta t)\cdot\vec{v}(0)\right\rangle=\frac{1}{3NN'}\sum_{j=0}^{N'}\sum_{i=1}^{N}\vec{v}_i(\mathrm{j}\Delta t)\cdot\vec{v}_i(\mathrm{j}\Delta t+m\Delta t) \tag{5.3}$$

Here, Δt is the sampling interval of velocity and the interval of autocorrelation time, *m* is given a value such that the product of *m* and Δt equals to the autocorrelation time, *N* is the total number of atoms, *i* is the *i*th atom, *j* varies from 0 to *N'* such that the summation ranges over all snapshots in the sampling series, and "3" refers to the length of the velocity vector.

To calculate the out-of-plane partial VDOS, only the *z*-components of velocities are included in the calculation of $\vec{v}_i(\mathrm{j}\Delta t)\cdot\vec{v}_i(\mathrm{j}\Delta t+m\Delta t)$, and "3" is replaced by "1". To calculate the in-plane partial VDOS, only the *x* and *y* components of velocities are included in the calculation of $\vec{v}_i(\mathrm{j}\Delta t)\cdot\vec{v}_i(\mathrm{j}\Delta t+m\Delta t)$, and "3" is replaced by "2" . In this study, Δt is set to be 2 fs (i.e. 8 time steps in the simulation), and m ranges from 0 to 8192. The velocity autocorrelation function for each case is an average of five separate runs of the molecular dynamics simulations, to achieve acceptable coverage of frequency and resolution of VDOS.

5.5.4 Cumulative Correlation Factor

To quantify the match/mismatch between the VDOS of different materials at their interfaces, a cumulative correlation factor (M) is defined based on the correlation factor defined in the literature.[23,44] An important feature of the cumulative correlation factor is that it quantifies the match or agreement between two sets of VDOS up to a specific cutoff frequency ($\bar{f}$). The equation of M reads:

$$M_{\mathrm{X}}(\bar{f})=\frac{\int_0^{\bar{f}}\mathrm{VDOS}_{\mathrm{PMMA}}(f)\cdot\mathrm{VDOS}_{\mathrm{X}}(f)\,\mathrm{d}f}{\int_0^{\infty}\mathrm{VDOS}_{\mathrm{X}}(f)\,\mathrm{d}f\cdot\int_0^{\infty}\mathrm{VDOS}_{\mathrm{PMMA}}(f)\,\mathrm{d}f} \tag{5.4}$$

where $\mathrm{VDOS}_{\mathrm{PMMA}}$ denotes the VDOS of PMMA while $\mathrm{VDOS}_{\mathrm{X}}$ denotes the VDOS of X (which can be graphene, or hydroxyl groups, or methyl groups). A lower cumulative correlation factor would indicate a more significant mismatch in the VDOS below the cutoff frequency. When $\bar{f}$ approaches infinity or larger than the maximum frequency of all key vibrational modes, the cumulative correlation factor is identical to the correlation factor.

5.5.5 Integrated Autocorrelation of Interfacial Heat Power

Based on the Green-Kubo relationship, interfacial thermal conductance is correlated with the fluctuation of the heat power exchanged across an interface.[64] Specifically, interfacial thermal conductance (G) is proportional to the integrated autocorrelation of interfacial heat power:

$$G \propto \int_0^\infty \langle p(t) \cdot p(0) \rangle \, \mathrm{d}t \tag{5.5}$$

Here, $\langle p(t) \cdot p(0) \rangle$ denotes the autocorrelation of the interfacial heat power, and $p(t)$ is the instantaneous interfacial heat power exchanged between the matrix and a group of selected atoms of the filler material:[65]

$$p(t) = \sum_{\substack{i \in \text{PMMA} \\ j \in \text{X}}} \vec{F}_{ij} \cdot \vec{v}_i - \sum_{\substack{i \in \text{PMMA} \\ j \in \text{X}}} \vec{F}_{ji} \cdot \vec{v}_j \tag{5.6}$$

where PMMA means the matrix, X means a group of atoms from the filler material, $\vec{F}_{ij}$ is the force vector on atom i exerted by atom j, and $\vec{v}_i$ is the velocity vector of atom i. The integrated autocorrelation of interfacial heat power decays to a finite value when the autocorrelation time is infinitely long. Molecular dynamics simulations were performed to calculate the integrated autocorrelation of interfacial heat power. Since the integrated autocorrelation of interfacial heat power oscillates with time, only the last half period of oscillation (see **Figure D.9**) in the tail of the 40 ps autocorrelation time was averaged to approximate the converged integrated autocorrelation of interfacial heat power. The error was estimated by the difference between the averaged value and the maximum value of the last half period of oscillation. Five separate molecular dynamics runs were performed to achieve more reliable results.

5.5.6 Identification of Hydrogen Bonds

Hydrogen bonds were identified for the purposes of visualization and discussion (e.g. Figure 5.8a). Although there are several different criteria available for identifying hydrogen bonds,[31] we employed the default criterion used by VMD (**Figure D.10**).[66] The criterion includes two parts: 1) the distance between the hydrogen bond donor (D) and the acceptor (A) is less than 3.0Å, and 2) the angle of D-H-A is less than 20 degrees. Using different criteria would result in slightly different numbers of hydrogen bonds. However, this would not affect molecular dynamics simulations since no identification of hydrogen bonds is involved. Moreover, using different criteria would not affect the major conclusions drawn from this study.

REFERENCES

[1] M. E. Siemens, Q. Li, R. Yang, K. A. Nelson, E. H. Anderson, M. M. Murnane, H. C. Kapteyn, Nat. Mater. 2010, 9, 26.

[2] M. Hu, D. Poulikakos, Nano Lett. 2012, 12, 5487.

[3] H. K. Lyeo, D. G. Cahill, Physical Review B 2006, 73, 144301.

[4] S. H. Song, K. H. Park, B. H. Kim, Y. W. Choi, G. H. Jun, D. J. Lee, B. S. Kong, K. W. Paik, S. Jeon, Adv Mater 2013, 25, 732.

[5] K. M. F. Shahil, A. A. Balandin, Nano Lett. 2012, 12, 861.

[6] A. P. Yu, P. Ramesh, M. E. Itkis, E. Bekyarova, R. C. Haddon, J. Phys. Chem. C 2007, 111, 7565.

[7] C. C. Teng, C. C. M. Ma, C. H. Lu, S. Y. Yang, S. H. Lee, M. C. Hsiao, M. Y. Yen, K. C. Chiou, T. M. Lee, Carbon 2011, 49, 5107.

[8] T. F. Luo, J. R. Lloyd, Adv Funct Mater 2012, 22, 2495.

[9] J. R. Potts, D. R. Dreyer, C. W. Bielawski, R. S. Ruoff, Polymer 2011, 52, 5.

[10] Z. Han, A. Fina, Prog. Polym. Sci. 2011, 36, 914.

[11] A. A. Balandin, S. Ghosh, W. Z. Bao, I. Calizo, D. Teweldebrhan, F. Miao, C. N. Lau, Nano Lett 2008, 8, 902.

[12] S. Berber, Y. K. Kwon, D. Tomanek, Phys. Rev. Lett. 2000, 84, 4613.

[13] S. T. Huxtable, D. G. Cahill, S. Shenogin, L. P. Xue, R. Ozisik, P. Barone, M. Usrey, M. S. Strano, G. Siddons, M. Shim, P. Keblinski, Nat. Mater. 2003, 2, 731.

[14] H. Kim, A. A. Abdala, C. W. Macosko, Macromolecules 2010, 43, 6515.

[15] D. G. Cahill, P. V. Braun, G. Chen, D. R. Clarke, S. Fan, K. E. Goodson, P. Keblinski, W. P. King, G. D. Mahan, A. Majumdar, H. J. Maris, S. R. Phillpot, E. Pop, L. Shi, Applied Physics Reviews 2014, 1, 011305.

[16] N. Shenogina, R. Godawat, P. Keblinski, S. Garde, Phys. Rev. Lett. 2009, 102, 156101.

[17] K. Zheng, F. Y. Sun, X. Tian, J. Zhu, Y. M. Ma, D. W. Tang, F. S. Wang, Acs Applied Materials & Interfaces 2015, 7, 23644.

[18] F. Y. Sun, T. Zhang, M. M. Jobbins, Z. Guo, X. Q. Zhang, Z. L. Zheng, D. W. Tang, S. Ptasinska, T. F. Luo, Adv Mater 2014, 26, 6093.

[19] M. Hu, P. Keblinski, P. K. Schelling, Physical Review B 2009, 79, 104305.

[20] M. Shen, W. J. Evans, D. Cahill, P. Keblinski, Physical Review B 2011, 84, 195432.

[21] L. Zhang, Z. Bai, H. Ban, L. Liu, Phys. Chem. Chem. Phys. 2015, 17, 29007.

[22] P. J. O'Brien, S. Shenogin, J. X. Liu, P. K. Chow, D. Laurencin, P. H. Mutin, M. Yamaguchi, P. Keblinski, G. Ramanath, Nat. Mater. 2013, 12, 118.

[23] M. D. Losego, M. E. Grady, N. R. Sottos, D. G. Cahill, P. V. Braun, Nat. Mater. 2012, 11, 502.

[24] S. Majumdar, J. A. Sierra-Suarez, S. N. Schiffres, W. L. Ong, C. F. Higgs, A. J. H. McGaughey, J. A. Malen, Nano Lett. 2015, 15, 2985.

[25] M. Hu, J. V. Goicochea, B. Michel, D. Poulikakos, Nano Lett. 2010, 10, 279.

[26] M. Wang, N. Hu, L. Zhou, C. Yan, Carbon 2015, 85, 414.

[27] Y. Wang, H. F. Zhan, Y. Xiang, C. Yang, C. M. Wang, Y. Y. Zhang, The Journal of Physical Chemistry C 2015, 119, 12731.

[28] G. Yuan, X. Li, Z. Dong, A. Westwood, Z. Cui, Y. Cong, H. Du, F. Kang, Carbon 2012, 50, 175.

[29] A. Yu, P. Ramesh, M. E. Itkis, E. Bekyarova, R. C. Haddon, The Journal of Physical Chemistry C 2007, 111, 7565.

[30] C. B. Aakeroy, K. R. Seddon, Chem. Soc. Rev. 1993, 22, 397.

[31] T. Steiner, Angew Chem Int Edit 2002, 41, 48.

[32] V. Georgakilas, M. Otyepka, A. B. Bourlinos, V. Chandra, N. Kim, K. C. Kemp, P. Hobza, R. Zboril, K. S. Kim, Chem Rev 2012, 112, 6156.

[33] L. Zhang, M. Ruesch, X. L. Zhang, Z. T. Bai, L. Liu, Rsc Advances 2015, 5, 87981.

[34] G. H. Kim, D. Lee, A. Shanker, L. Shao, M. S. Kwon, D. Gidley, J. Kim, K. P. Pipe, Nat Mater 2015, 14, 295.

[35] L. Zhang, Z. T. Bai, H. Ban, L. Liu, Phys. Chem. Chem. Phys. 2015, 17, 29007.

[36] L. Zhang, T. L. Chen, H. Ban, L. Liu, Nanoscale 2014, 6, 7786.

[37] G. A. Mino-Galaz, G. Gutierrez, Chem. Phys. Lett. 2015, 635, 16.

[38] G. Mino, R. Barriga, G. Gutierrez, J. Phys. Chem. B 2014, 118, 10025.

[39] D. R. Dreyer, S. Park, C. W. Bielawski, R. S. Ruoff, Chem. Soc. Rev. 2010, 39, 228.

[40] A. M. Dimiev, T. A. Polson, Carbon 2015, 93, 544.

[41] D. R. Dreyer, A. D. Todd, C. W. Bielawski, Chem. Soc. Rev. 2014, 43, 5288.

[42] W. Gao, L. B. Alemany, L. J. Ci, P. M. Ajayan, Nature Chemistry 2009, 1, 403.

[43] N. Ghaderi, M. Peressi, J. Phys. Chem. C 2010, 114, 21625.

[44] L. Hu, T. Desai, P. Keblinski, Physical Review B 2011, 83, 195423.

[45] G. Goncalves, S. M. A. Cruz, A. Ramalho, J. Gracio, P. A. A. P. Marques, Nanoscale 2012, 4, 2937.

[46] T. Ramanathan, A. A. Abdala, S. Stankovich, D. A. Dikin, M. Herrera-Alonso, R. D. Piner, D. H. Adamson, H. C. Schniepp, X. Chen, R. S. Ruoff, S. T. Nguyen, I. A. Aksay, R. K. Prud'homme, L. C. Brinson, Nature Nanotechnology 2008, 3, 327.

[47] V. H. Pham, T. T. Dang, S. H. Hur, E. J. Kim, J. S. Chung, Acs Applied Materials & Interfaces 2012, 4, 2630.

[48] F. MullerPlathe, J. Chem. Phys. 1997, 106, 6082.

[49] E. T. Swartz, R. O. Pohl, Reviews of Modern Physics 1989, 61, 605.

[50] B. W. Li, J. H. Lan, L. Wang, Phys. Rev. Lett. 2005, 95, 104302.

[51] M. Hu, D. Poulikakos, Int. J. Heat Mass Transfer 2013, 62, 205.

[52] X. Mu, X. Wu, T. Zhang, D. B. Go, T. Luo, Sci. Rep. 2014, 4, 3909

[53] S. K. Chien, Y. T. Yang, C. K. Chen, Appl Phys Lett 2011, 98, 033107.

[54] C. Nieto-Draghi, J. B. Avalos, Mol. Phys. 2003, 101, 2303.

[55] S. Plimpton, Journal of Computational Physics 1995, 117, 1.

[56] W. L. Jorgensen, D. S. Maxwell, J. Tirado-Rives, J. Am. Chem. Soc. 1996, 118, 11225.

[57] M. L. P. Price, D. Ostrovsky, W. L. Jorgensen, J Comput Chem 2001, 22, 1340.

[58] P. Lazar, F. Karlicky, P. Jurecka, M. Kocman, E. Otyepkova, K. Safarova, M. Otyepka, J. Am. Chem. Soc. 2013, 135, 6372.

[59] S. C. Lin, M. J. Buehler, Nanotechnology 2013, 24, 165702.

[60] S. Y. Kuang, J. D. Gezelter, J. Phys. Chem. C 2011, 115, 22475.

[61] R. Godawat, S. N. Jamadagni, S. Garde, Proc. Natl. Acad. Sci. U.S.A. 2009, 106, 15119.

[62] R. S. Paton, J. M. Goodman, Journal of Chemical Information and Modeling 2009, 49, 944.

[63] K. Binder, *Monte Carlo and Molecular Dynamics Simulations in Polymer Science*, Oxford University Press, New York and Oxford 1995.

[64] J. L. Barrat, F. Chiaruttini, Mol. Phys. 2003, 101, 1605.

[65] G. Domingues, S. Volz, K. Joulain, J.-J. Greffet, Phys. Rev. Lett. 2005, 94, 085901.

[66] W. Humphrey, A. Dalke, K. Schulten, J. Mol. Graph. Model. 1996, 14, 33.

CHAPTER 6

POLYMERIC SELF-ASSEMBLED MONOLAYERS ANOMALOUSLY IMPROVE THERMAL TRANSPORT ACROSS GRAPHENE/POLYMER INTERFACES

6.1 Abstract

Ultralow thermal conductivities of bulk polymers greatly limit their applications in areas demanding fast heat dissipation, such as flexible electronics and microelectronics. Therefore, polymeric composites incorporating highly thermally conductive filler materials (e.g. graphene and carbon nanotubes) have been produced to address the issue. However, despite some enhancement, thermal conductivities of these materials are still far below theoretical predictions, mainly due to the inefficient thermal transport across material interfaces. Here, using molecular dynamics simulations, we demonstrate that polyethylene (PE) self-assembled monolayer (SAM) functionalized graphene surfaces at a high grafting density can drastically improve interfacial thermal conduction between graphene and the matrix of poly (methyl methacrylate) (PMMA). In contrast to abrupt temperature drop across pristine graphene/PMMA interfaces, temperature field in the vicinity of a PE-grafted graphene/PMMA interface is continuous with a smoother transition and higher thermal conductance. This anomalous improvement is attributed to three factors that closely relate to the grafting density of the SAM of PE. First, the SAM with high grafting densities features highly extended chains that enhance along-chain thermal conduction. Second, the strong covalent bonding between the SAM and the graphene

---

This chapter is accepted by ACS Applied Materials & Interfaces. Coauthor: Professor Ling Liu.

facilitates heat transfer at their joints. Third, the SAM and the PMMA matrix are both organic materials, leading to enhanced interfacial vibrational coupling. Molecular mechanisms underpinning these phenomena are systematically elucidated by analyzing the temperature field, density distribution, Herman's orientation factor, the vibrational density of states, cumulative correlation factor, the integrated autocorrelation of interfacial heat power, and interfacial adhesion. All results suggest the incorporation of SAMs at a high grafting density or extremely extended polymer brushes for drastically improved interfacial thermal transport between hard and soft materials towards a wide range of applications.

6.2 Keywords

Interfacial thermal conductance, self-assembled monolayers, functionalized graphene, polymeric composite, molecular dynamics

6.3 Introduction

Compared with other solid materials including metals and ceramics, polymers feature a unique combination of low density, excellent ductility and flexibility, a wide spectrum of electrical insulation, and good chemical stability. These advantages make polymers a promising material for optoelectronic devices,[1] wearable devices,[2] flexible electronics,[3] and other applications.[4] Nevertheless, polymers have a crucial bottleneck that greatly limits their applications in organic electronics and microelectronics, i.e. their low thermal conductivities in the order of 0.1 W m^{-1} K^{-1}. Enormous efforts have been devoted to improving the thermal transport properties of polymers, which typically fall into three categories. First, control the morphology of polymer chains to take advantage of the highly efficient thermal transport process in extended polymers.[5-6] Second, engineer interchain molecular interactions in both amorphous and nanocrystalline polymers to create new and enhance existing thermal transport pathways.[7-9] Third, introduce materials of high thermal conductivities, e.g. graphene with the conductivity of ~5000 W m^{-1} K^{-1},[10] to form composites with enhanced properties.[11] The first two methods have shown tremendous success in improving the thermal conductivity of polymers, but both of them lack a facile method for mass-production of the materials.[5] The third method implies multifunctionality and easier mass production. For instance, various graphene/polymer composites have demonstrated unique electrical,[12] dielectric,[13] and mechanical properties,[14] which greatly extend their applications in various fields such as electrochemical devices and actuators.[15-16] However, the thermal properties of the produced composite materials are often below expectations.

Thermal transport in polymer nanocomposites and nanodevices is usually compromised by material interfaces that widely exist between material constituents. Improved dispersion of filler materials including graphene can significantly boost the overall thermal[17] and mechanical properties[18] of various composite materials. The methods that can achieve this goal include hydrogen passivation and ultrasonication,[18] chemical or physical functionalization,[19] and mechanical methods.[17] With well-dispersed filler materials, thermal transport efficiency at individual interfaces becomes critical, which underscores the significance of the present research. At these interfaces, heat carriers such as phonons are scattered, lowering interfacial thermal conductance (Kapitza conductance). In principle, interfacial thermal resistance is dominated by the mismatch between the vibrational density of states of two materials forming the interface.[20] Typically, materials with drastically dissimilar properties, e.g. organic and inorganic materials, have low overlap in the vibrational density of states, resulting in strong interfacial phonon scattering and low interfacial thermal conductance. Among the wide spectrum of frequencies, coupling of phonons in low frequencies is more important in determining interfacial thermal transport;[21] and such coupling is recently found to be directly correlated with interfacial bonding.[22-23] Since most nanocomposites have weak interfaces governed by van der Waals interactions, they have low thermal conductivities of only 60~80 MW m^{-2} K^{-1},[21,24] significantly below the predictions made by the effective medium theory assuming perfect interfaces.

Interfacial thermal conduction may be drastically improved by structurally and chemically tuning material interfaces,[22,25] e.g. noncovalent or covalent functionalization.[26-30] For example, by noncovalently functionalizing the octane/graphene interface with phonon-spectrum linker molecules alkyl (C_8)-pyrene, the out-of-plane interfacial thermal conductance can be improved by 22% due to the drastically reduced vibrational mismatch.[26] A similar extent of improvement of about 25% has been achieved between graphene and epoxy, by using a 2.38% coverage of 1-pyrenebutyl, 1-pyrenebutyric acid, or 1-pyrenebutylamine on graphene surfaces.[27] Compared with noncovalent functionalization, covalent functionalization of graphene has shown more improvements to interfacial thermal conductance, mainly due to the stronger interfacial bonding. Among many candidates for functionalizing graphene, butyl was reported to be one of the best performings at graphene/epoxy[27] and graphene/polyethylene[28] interfaces. The improvement was found as high as 400%[27] at a 9.52% coverage and 129%[28] at a 5.36%

coverage, respectively. To further elucidate the importance of interfacial bonding, we compared two functional groups, i.e. methyl and hydroxyl, which have different molecular interactions with the poly(methyl methacrylate) (PMMA) matrix. While the methyl group only forms weak van der Waals interactions with PMMA, the hydroxyl group enables the much stronger hydrogen bonding. Molecular dynamics simulations have demonstrated that, due to the stronger interfacial hydrogen bonding, hydroxyl-functionalized graphene has 273% higher interfacial thermal conductance than the pristine graphene in PMMA.[31] In addition to this solid/solid interface, hydrogen bonding has also been reported to serve as an efficient thermal transport pathway[31-32] and significantly improve interfacial thermal transport at solid/liquid interfaces, e.g. the gold/organic liquid interface.[33]

Despite the significant progress, improving interfacial thermophysical performance by manipulating the conformation of functional molecules has not been fully understood. In this study, we probe the use of self-assembled monolayers (SAMs) for controlling interfacial thermal transport between graphene and polymers. SAMs are thin molecular assemblies spontaneously formed on surfaces by physical or chemical adsorption.[34-35] Modification of surfaces or interfaces with SAMs has been a routine approach to control surface/interface properties such as adhesion,[36] friction,[37] wetting,[38] thermal properties,[33,39-41] and electronic properties[42] for a wide range of applications in biotechnology and nanotechnology.[43] Surface functionalization of graphene with polymer molecules can be achieved by atomic transfer radical polymerization,[44] irradiation-induced polymerization,[45] ring-open metathesis polymerization,[19] thiol-ene click reactions,[46] esterification/amidation reactions,[47] etc. In situ measurements demonstrated that SAMs have several growth regimes including the striped phase, transition phase, and dense phase.[48-49] Each phase has a distinct molecular structure with a certain coverage density on the surfaces. At the early stage, the coverage density is low, and molecules are flat on the surface. With the increased coverage densities, more molecules “stand up” from the surface, forming a crystalline structure upon surface saturation. Morphology of the polymer molecules and their coverage density both affect interfacial thermal transport significantly.

Here, we demonstrate that polymeric SAMs can significantly increase interfacial thermal transport between monolayer graphene and the polymer matrix. Molecular dynamics simulations were applied to study interfacial thermal transport between PMMA and graphene with the SAMs of polyethylene at varying densities. Most of the previous studies on SAMs-facilitated interfacial thermal conductance are related to metals,[22,41] or focus on the effect of bonding strength between SAMs and surrounding materials,[22,33] and little attention is paid to the effect of molecular morphology on thermal transport efficiency. To provide more physical insights, temperature field, density distribution, Herman’s orientation factor, the vibrational density of states, cumulative correlation factor, the integrated autocorrelation of interfacial heat power, and interfacial adhesion were analyzed. These analyses enable a systematic investigation of correlations between the coverage density, chain conformation and orientation, and thermal energy transport. These results would provide a fundamental understanding in applying SAMs to tune interfacial thermal conductance between hard and soft materials towards a wide range of applications.

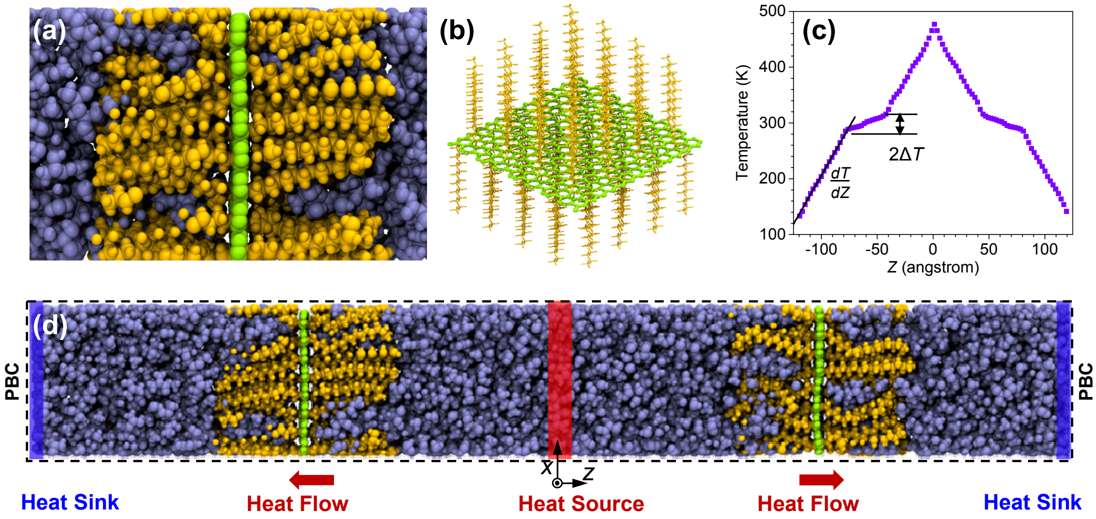

Figure 6.1. (a) Atomistic model of the graphene/polymer interface: a graphene monolayer (green) is functionalized with polyethylene (PE) chains (orange), and sandwiched in between two blocks of the poly (methyl methacrylate) (PMMA) matrix (blue). (b) A 3D view of the PE-functionalized graphene. (c) A representative temperature profile generated by reverse non-equilibrium molecular dynamics (RNEMD) simulation. Here, $2\Delta T$ is the total temperature drop across the interfaces; and $\mathrm{d}T/\mathrm{d}Z$ is the temperature gradient in PMMA. (d) An example computational system for RNEMD simulation with periodic boundary conditions (PBC) applied along all directions.

6.4 Computational Methods

6.4.1 Models

Atomistic models of multiple PMMA/graphene interfaces (**Figure 6.1**a) were prepared for molecular dynamics (MD) simulations. Graphene was functionalized by different numbers of polyethylene (PE) chains within a cross-sectional area of 34.45 Å × 34.10 Å. On the one hand, PE chains are chosen to functionalize graphene for the following reasons. First, butyl group as a short PE molecule was found to be one of the best to functionalize graphene for high interfacial thermal conductance across graphene/epoxy[27] and graphene/polyethylene[28] interfaces. Second, extended PE nanofibers were reported to have extremely high thermal conductivity from 50 W m^{-1} K^{-1} to 104 W m^{-1} K^{-1},[5,50] and single extended PE chain even has thermal conductivity larger than 350 W m^{-1} K^{-1}.[51] One of the motivations of this study is to take advantage of the high thermal conductivity of PE crystalline chains. Third, a linear PE chain is composed of repeat units of small side groups, and hence it represents an ideal candidate to study the structure effect on interfacial thermal transport theoretically. On the other hand, PMMA is chosen as the matrix since it is widely used in polymer composites and the bonding strength between PMMA and functionalized graphene can be manipulated by bond design, e.g. using hydrogen bonds, in the future study.

All PE chains were uniformly and covalently bonded to both sides of the graphene. The systems are abbreviated as "G*X*PE8", where "*X*" denotes the number of PE chains attached to each side of the graphene (See (**Figure 6.1**b) and "8" represents the number of repeat units, i.e. C_2H_4, in each PE chain. When "*X*" is large, polymer chains are attached at a high density, leading to the crystalline polymer monolayer as illustrated in (**Figure 6.1**b. Initial models of PMMA were built by the self-avoiding random walk method with 40 repeat units per chain. Graphene and PE-functionalized graphene were built by using our in-house code. All material constituents were fully equilibrated, respectively, before being merged in VMD[52] to form the nanocomposite ((**Figure 6.1**d). The cross-section of each system was made large enough to overcome intrinsic size effects on interfacial thermal transport.[11,23,40] According to a previous study on the graphene/paraffin interface, 35 Å is sufficient to account for dominant contributions by all vibrational modes to interfacial thermal conduction.[11] Periodic boundary conditions were applied along all directions. It is worth noting that the PE chains in our model are free from agglomeration despite the immiscible nature of PE and PMMA blends.[53-54] In the present model, PE chains are covalently bonded to graphene and they are relatively short. The relatively high bending rigidity of short PE chains, together with the high stiffness of graphene, makes the PE chains difficult (and in some cases impossible) to agglomerate or fully contact with graphene.

6.4.2 Equilibration

MD simulations were performed using LAMMPS.[55] The OPLSAA force field[56-57] was employed to describe interatomic interactions, which has been widely used to simulate graphene,[26] polymers,[58-59] and their interfaces. Initial structures of polymers were minimized using the conjugate gradient algorithm, followed by the relaxation in NPT at 300 K and 1 atm for 1 ns, and then in NVT at 300 K for 1 ns. Minimization and annealing were then applied to remove residual stresses. For annealing, the system was first heated up to 800 K from 300 K within 300 ps, relaxed at 800 K for 500 ps, and finally cooled down to 300 K in 300 ps. After that, the system was relaxed for 500 ps in NPT at 300 K and 1 atm, followed by the relaxation of 500 ps in NVT at 300 K. Time step size was fixed to be 1 fs in equilibration, and 0.5 fs in subsequent production runs. To prepare for production runs, structures were further equilibrated for 1 ns in NVT at 300 K, with the reduced time step of 0.5 fs.

6.4.3 Interfacial Thermal Conductance.

Reverse non-equilibrium molecular dynamics (RNEMD) was applied to calculate interfacial thermal conductance using computational systems illustrated in (**Figure 6.1**d.

Numerically imposing a heat flux by velocity swapping, RNEMD calculates temperature drop (ΔT) across the interface (e.g. (**Figure 6.1**c) and heat flux (J) in the system to find interfacial thermal conductance using $G = J/\Delta T$. In this study, each system was divided into 100 slabs along the direction of intended heat flow, i.e. the z-direction in (**Figure 6.1**d. Heat flux was generated from the "heat source" slab (red) to the "heat sink" slab (blue) by swapping the kinematic energies of the hottest atom in the heat sink and the coolest atom in the heat source. A virtual elastic collision model[60] was applied to maintain energy and momentum conservation during velocity swapping. After the system reached the steady state, ΔT was evaluated from the temperature profile; and J was calculated by $J = \Delta E/(2tA)$, where t is the time interval of velocity swapping, ΔE is the averaged kinetic energy transferred per swap, A is the cross-sectional area of the system, and the coefficient "2" is due to the two symmetric heat transport paths in the system. To achieve results of higher fidelity, $2\Delta T$ was controlled to be 45 K ±5 K in this study for all systems by carefully adjusting the frequency of velocity swapping. Interfacial thermal conductance was calculated by using the RNEMD data sampled over 50 ns after the system reached the steady state. A by-product was the thermal conductivity of PMMA, which was calculated based on the RNEMD data by using $K = J/(\mathrm{d}T/\mathrm{d}z)$, where $\mathrm{d}T/\mathrm{d}z$ is the temperature gradient in PMMA ((**Figure 6.1**c). To verify G calculated by RNEMD, nonequilibrium molecular dynamics method (NEMD) was adopted as an alternative approach. There are two differences between RNEMD and NEMD. First, NEMD only analyzes half of the system used in RNEMD (e.g. the non-gray part in **Figure E.1**). Second, NEMD fixes the temperature of both heat sink and source; in this work, they were fixed at 250 K and 400 K, respectively, by Langevin thermostats.

6.4.4 Temperature Contour and Atomic Number Density

NEMD was also used to calculate temperature contours of the system. At the steady state, data of atomic temperature and position over a 5 ns simulation period was analyzed. The system was equally divided into 80×560 cells in the *y*-*z* plane, respectively. Atoms were binned into these cells based on their *y* and *z* coordinates at every step. Temperature and atomic number density contours were plotted by averaging the atomic temperature and number in each cell. When the atomic number density of a cell was less than 0.5% of the density averaged by all cells over the whole system, the temperature of that cell was set to zero as an indication of insufficient atoms.

6.4.5 Herman's Orientation Factor

Herman's orientation factor[61] is widely adopted to describe the degree of orientation of a polymer with respect to any direction of interest. It is defined by $S = 1.5\langle\cos^2\theta\rangle - 0.5$, where θ refers to the angle of a polymer chain with respect to the direction of interest (i.e. z-axis in this study), and $\langle\cdot\rangle$ represents an average over all chains of the polymer. Three values of *S* are important, including 1, 0, and -0.5. They indicate a polymer chain perfectly aligned with the *z*-axis, completely amorphous, and perfectly perpendicular to the *z*-axis, respectively. Only main chains of polymers were considered for this calculation. Chain vector of the *i*th non-chain-end atom of the main chain was defined as the vector pointing from the (i-1)th main chain atom to the (i+1)th main chain atom. Localized degree of orientation was evaluated by binning atoms into 80×560 cells in the y-z plane, in which the average Herman's orientation factor was calculated. Equilibrium MD was performed for 11 ns in NVE to collect data for Herman's orientation analysis. The same simulation data was also used to evaluate the vibrational density of states and the integrated autocorrelation of interfacial heat power, as described below.

6.4.6 Vibrational Density of States (VDOS)

VDOS describes atomic vibrational modes of a system. VDOS analysis of two materials can elucidate the mismatch of vibrational modes between these materials at their interfaces. VDOS can be calculated by the Fourier transformation of the velocity autocorrelation function:

$$\mathrm{VDOS}(f) = \int_0^{+\infty} e^{-i2\pi f\tau} C_v(\tau)\, \mathrm{d}\tau \tag{6.1}$$

Here, VDOS is a function of frequency f and $C_v(\tau)$ is the normalized velocity autocorrelation function defined by:

$$C_v(\tau) = \frac{\langle \vec{v}(\tau)\cdot\vec{v}(0)\rangle}{\langle \vec{v}(0)\cdot\vec{v}(0)\rangle} \tag{6.2}$$

where $\vec{v}(\tau)$ is the velocity vector with respect to an autocorrelation time τ, and <·> denotes an average over a group of atoms. Equilibrium MD was performed to collect atomic velocities for evaluating VDOS. Fifty samples of the same system with different initial velocities seeding were used to calculate VDOS of the system. In each sample, atomic velocities were recorded every 2 fs.

6.4.7 Cumulative Correlation Factor

A cumulative correlation factor (*M*) was defined to quantify the consistency between the vibrational modes of two materials comprising an interface, considering all frequencies below a threshold $\bar{f}$:

$$M(\bar{f}) = \frac{\int_0^{\bar{f}} \mathrm{VDOS_A}(f) \cdot \mathrm{VDOS_B}(f)\ \mathrm{d}f}{\int_0^{\infty} \mathrm{VDOS_A}(f)\ \mathrm{d}f \cdot \int_0^{\infty} \mathrm{VDOS_B}(f)\ \mathrm{d}f} \tag{6.3}$$

Here, the subscripts, "A" and "B", denote two material components forming the interface. A lower *M* value means a larger vibrational mismatch between the two materials, considering vibrational modes below a cutoff frequency $\bar{f}$. When $\bar{f}$ is larger than the maximum frequency of all vibrational modes, the cumulative correlation factor is identical to the correlation factor defined in previous studies.[62]

6.4.8 Integrated Autocorrelation of Interfacial Heat Power

Interfacial thermal conductance is proportional to the integrated autocorrelation of interfacial heat power according to Green-Kubo fluctuation theorem, i.e. $\int_0^{\infty} \langle p(t) \cdot p(0) \rangle\ \mathrm{d}t$, where $p(t)$ is the instantaneous interfacial heat power exchanged between two materials, e.g. PMMA and a group of atoms in the filler material (denoted by *P*):

$$p(t) = \sum_{\substack{i \in \mathrm{PMMA} \\ j \in P}} \vec{F}_{ij} \cdot \vec{v}_i - \sum_{\substack{i \in \mathrm{PMMA} \\ j \in P}} \vec{F}_{ji} \cdot \vec{v}_j \tag{6.4}$$

Here, $\vec{F}_{ij}$ is the force vector applied by the *j*th atom on the *i*th atom, and $\vec{v}_i$ is the velocity vector of the *i*th atom. The upper limit of autocorrelation time was set to be 40 ps. The total simulation was 10 ns at equilibrium.

6.4.9 Interfacial Adhesion

The pullout process of functionalized graphene from PMMA was simulated by NEMD to evaluate interfacial adhesion. Only a part of the well-equilibrated system as illustrated in **Figure 6.2** was used in the simulation. The PMMA matrix to the left of plane "1" was fixed. The graphene along with all atoms on the right side of plane "2" was set to be rigid. The center of mass (COM) of the rigid part was driven to move along the *z* direction at a constant velocity of 20 m/s. All atoms between planes "1" and "2" including a small amount of PMMA and PE chains to the left of the graphene, were flexible with a temperature of 300 K controlled by NVT. Time step was 0.1 fs. The applied force was sampled as a function of interfacial separation. The integral of the force-displacement curve was used to quantify the interfacial adhesion.

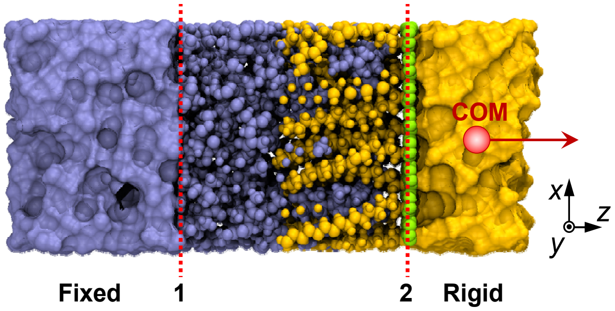

Figure 6.2. Atomistic model for pullout simulation (blue: PMMA; orange: PE; green: graphene). Atoms to the left of plane "1" and those to the right of plane "2" are constrained to be rigid, respectively. Atoms between planes "1" and "2" are flexible. During pullout, the center of mass (COM) of the rigid part in orange is moved at a constant velocity along the +*z* direction.

6.5 Results and Discussion

6.5.1 Validation of Computation

Computational models and methods were validated against previous computational and experimental results from the literature, using the example of a pristine graphene/PMMA interface with the cross-section of 34.45 Å × 34.10 Å. First, the density of PMMA was calculated to be 1.12 g cm^{-3} after the system reached equilibrium, which agrees well with experimentally measured density of 1.1−1.19 g cm^{-3}.[63] Second, the interfacial thermal conductance was calculated to be 88.66 MW m^{-2} K^{-1}, which falls into the range of previously reported values of 60~150 MW m^{-2} for comparable systems including graphene/polyethylene and graphene/liquid octane.[21,24,64] Third, interfacial thermal conductance results calculated by RNEMD and NEMD were consistent, with a difference less than 3.34%. Fourth, the thermal conductivity of PMMA was calculated to be 0.208±0.008 W m^{-1}K^{-1}, which is in good agreement with experimental results ranging from 0.19 to 0.25 W m^{-1}K^{-1}.[65]

6.5.2 Effect of Grafting Density on Interfacial Thermal Conductance

In situ measurements have shown that end-tethered polymer chains are flat on the solid surfaces at low coverage densities, while high-density polymer molecules feature extended ("stand-up") crystalline status.[48-49] To understand how grafting density affects interfacial thermal conductance, multiple systems of G*X*PE8 were analyzed with *X* ranging from 0 to 1, 2, 4, 8, 16, and 32. The grafting density of both sides of graphene is 0, 0.17, 0.34, 0.68, 1.36, 2.72, and 5.45 chains/nm^2, respectively. Another measure of the grafting density is the degree of functionalization, which is defined as the ratio of the number of sp^3 carbon atoms (i.e. anchoring points for polymer chains) to the total number of carbon atoms in graphene. The corresponding degree of functionalization is 0%, 0.45%, 0.89%, 1.79%, 3.57%, 7.14%, and 14.29%, respectively. As shown in **Figure 6.3**, interfacial thermal conductance increases with the number of grafted chains, *X*. The ascending rate is almost a constant before *X* takes 8; and after that, the ascending rate gradually decreases and a plateau is expected. Compared with the pristine graphene/PMMA interface (*X* = 0), G32PE8 with a PE coverage of 7.14 % on graphene has interfacial thermal conductance drastically increased by 431.3%. The drastic improvement of interfacial thermal conductance is due to the collective contributions of several factors including continuity of the temperature field, chain conformation, chain orientation, vibrational coupling, interfacial power exchange and adhesion, all of which will be analyzed quantitatively in following sections.

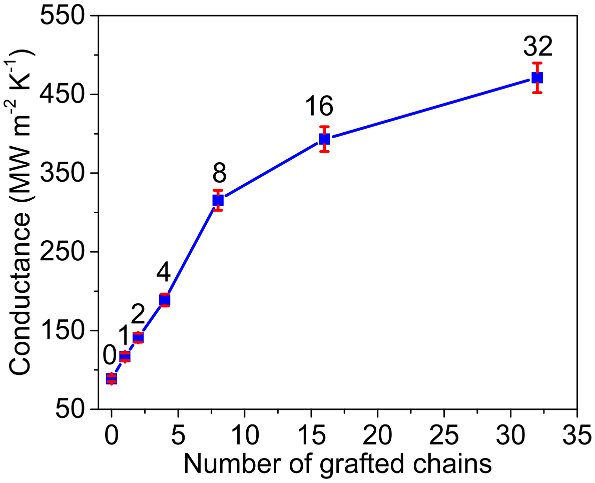

Figure 6.3. Interfacial thermal conductance in G*X*PE8 versus *X*, the number of PE chains grafted to each side of graphene. Numbers of *X* are also labeled above the data points.

6.5.3 Temperature Field

Figure 6.4 plots temperature distributions in G32PE8 and G1PE8, respectively, when heat flow is applied perpendicular to interfaces. There are two major findings. On one hand, the incorporation of dense PE chains in G32PE8 leads to a much smoother temperature transition at the interface. As shown in **Figure 6.4**a,c, the region between the two vertical red dashed lines is filled with major PE chains blended with PMMA chains. The temperature gradient in this region is much lower than that outside, indicating faster heat conduction. The calculated thermal conductivity of blended materials in this region is 1.158 ± 0.22 W m^{-1} K^{-1}, which is 5.56 times the conductivity of the PMMA matrix. As will be discussed in the following section, the faster thermal transport in this blending region is closely related to the morphology of polymer chains. On the other hand, continuity of temperature field is drastically improved by densely grafted polymer chains. When only one PE chain is attached to each side of the graphene (G1PE8), steric repulsion causes a spatial gap between the graphene and the PMMA matrix in a large part of the interface, leading to a zone with almost no atom or temperature, as evidenced in **Figure 6.4**d by the thick black lines. By incorporating dense PE monolayer, such discontinuity diminishes, leading to improved heat conduction as demonstrated in **Figure 6.4**c. The spots where the temperature field becomes continuous are grafting points of PE chains. In these positions, PE chains are covalently bonded to the graphene, making the temperature field continuous.

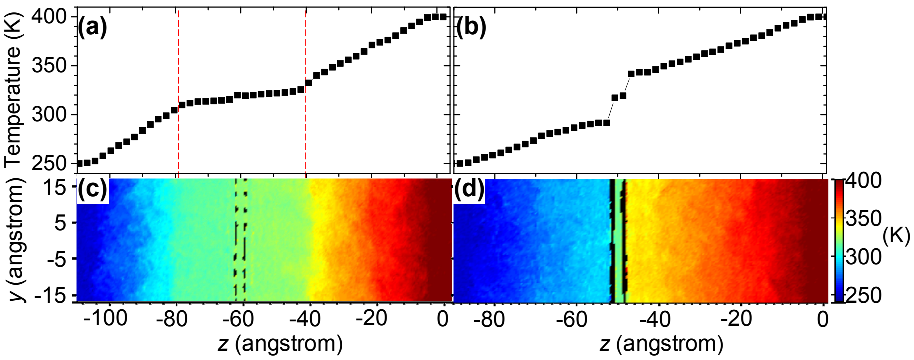

Figure 6.4. Temperature profiles for (a) G32PE8 and (b) G1PE8. The two vertical red dashed lines show a region filled with dense PE chains along with some PMMA chains. The matching temperature contours are also plotted for (c) G32PE8 and (d) G1PE8. Black regions are voids with almost no atoms.

6.5.4 Chain Conformation

Chain conformation at the interface is prominently controlled by the density of grafted polymers. **Figure 6.5**a,b show atomic number density distributions associated with a single polymer chain at each side of graphene, in both G32PE8 and G1PE8 systems. In G32PE8, the chains shown in the figure are randomly chosen from the total 64 chains. Density distributions associated with some other chains can be found in **Figure E.2**. In both systems, PE chains are shown to be perpendicular to the plane of graphene near the grafting points due to the stiffness of the covalent bonding. Also due to this constraint, the atomic number density plot of each PE chain in G32PE8 takes the shape of a reversed taper from the grafting point, showing the standing up status of PE chains. Moreover and most importantly, the PE chains in G32PE8 are found to be more extended and straighter than the sparsely grafted and more isolated chains in G1PE8, which can also be verified by the end-to-end distance and the height normalized by the fully extended PE chains, shown in **Figure E.3**. Theoretically, in G32PE8, PE chains are close enough to have strong steric repulsion that keeps the chains relatively straight. By contrast, in G1PE8, PE chains are free from the confinement effect and flat on the graphene surface, leading to their hook-like shape. The morphology of grated PE chains plays a key role in thermal transport processes. As demonstrated in several previous studies, extended polymer chains have higher along-chain thermal conductivities than their amorphous counterparts.[39,51,66] Indeed, as shown in **Figure 6.5**c, temperature drops little (10 K) in G32PE8 from the head of a PE chain to the head of the other on the opposite side of graphene (see **Figure E.4** for results of other chains); however, in G1PE8 with the same overall temperature variation, the head-to-head temperature drop is 54 K. Both results demonstrate more efficient thermal transport in G32PE8 with the extended PE chains perpendicular to the graphene surface, which echo with the finding from **Figure 6.4**a,c that temperature transition is smoother across the interface in G32PE8. It is worth noting that the extent to which thermal conductivity is enhanced by extending polymers varies in the literature. For instance, according to an experimental study, PMMA brushes have marginal (about 10%) increase in thermal conductivity compared with spun-cast PMMA.[67] The improvement of conductivity is lower than what is shown by our and other's studies. Here, the most critical governing factor is whether chains are "actually" extended or not. In our model, covalent bonding to ultra-stiff graphene and the use of dense, relatively short PE chains keep the PE chains "stand up" in extended configurations. The normalized height of chains (actual height divided by the length of fully extended chains) approaches 0.90, much higher than that in the PMMA study (0.25[67]).

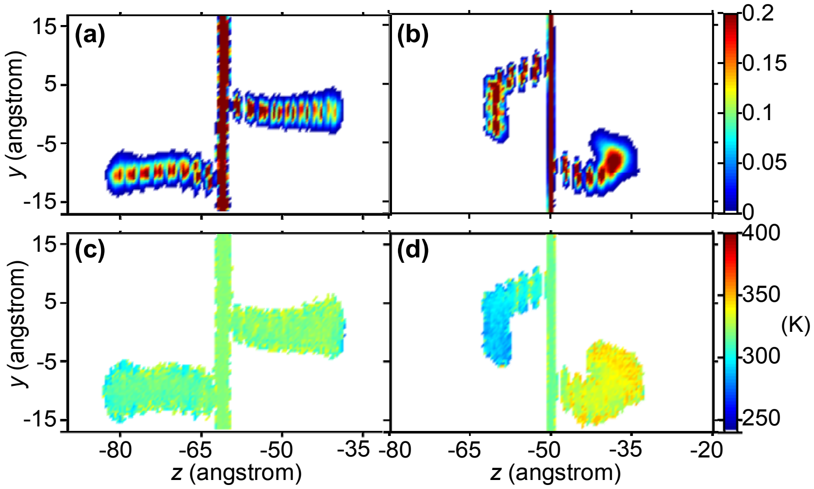

Figure 6.5. Atomic number density distributions of graphene and selected PE chains for (a) G32PE8 and (b) G1PE8. Temperature contours are also plotted for (c) G32PE8 and (d) G1PE8.

6.5.5 Herman's Orientation Factor

In this section, chain morphology is more quantitatively characterized by Herman's orientation factor, a quantitative measure of the degree of orientation of polymer chains with respect to a direction of interest. In this work, the direction of interest is along heat flow and perpendicular to graphene, i.e. the *z*-direction. **Figure 6.6** shows variations of Herman's orientation factor in the PE and PMMA components of four systems, respectively. The red (1), cyan (0), and blue (-0.5) represent that polymer chains are perfectly aligned with the *z*-axis, amorphous, and perpendicular to the *z*-axis, respectively. The white regions in the middle of all subplots are occupied by graphene. **Figure 6.6**a,c,e,g depict variations of Herman's orientation factor in the PE chains of G*X*PE8 where *X* takes 32, 16, 8, and 1, respectively. All fixed ends of the PE chains are in red (i.e. perpendicular to graphene) due to the stiffness of the covalent bonding with graphene.

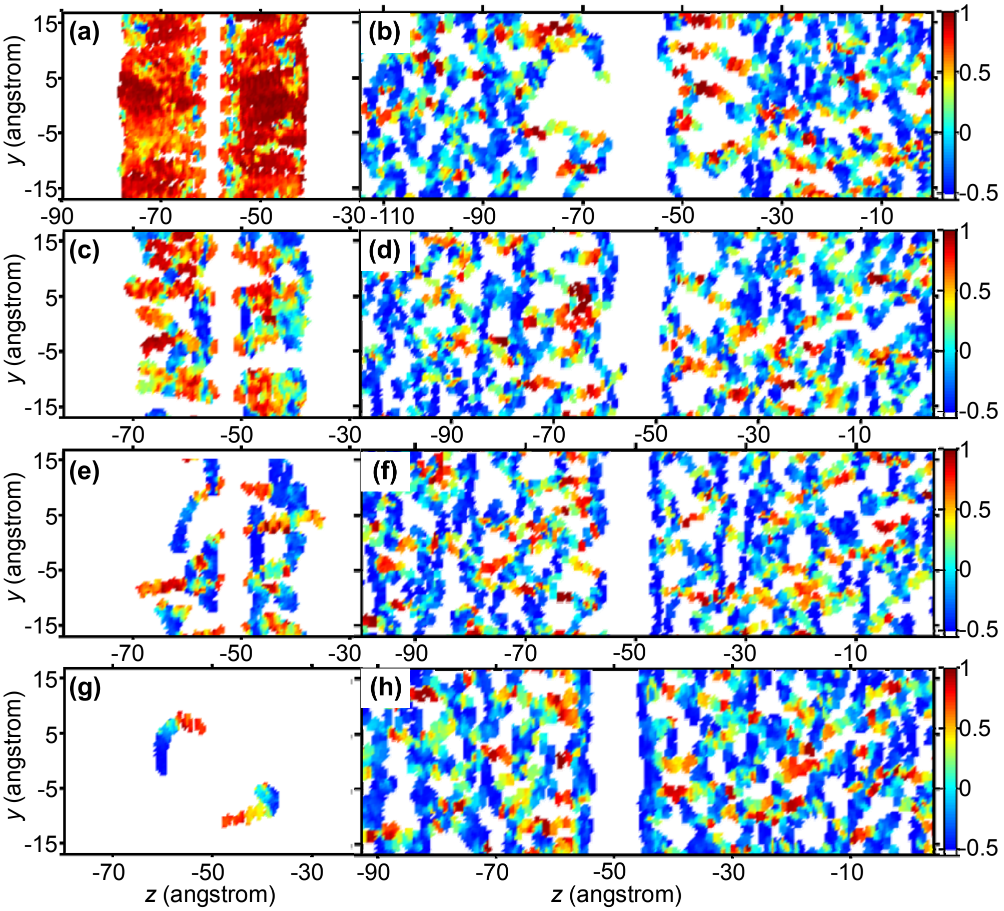

Figure 6.6. Distributions of the local Herman's orientation factor for PE chains (a,c,e,g) and PMMA chains (b,d,f,h) in G32PE8, G16PE8, G8PE8, and G1PE8, respectively

Most importantly, at higher PE coverage (e.g. G32PE8), not only the fixed ends are red, but most PE chains also turn red indicating good alignment with the direction of heat flow. These results echo with the finding from **Figure 6.5**, both showing drastically improved chain alignment in the dense polymer monolayer. The alignment of matrix chains is also improved at high grafting densities. As shown in **Figure 6.6**b,d,f,h, at higher *X*, several consecutive cells in the vicinity of graphene are shown to be red. Note that these PMMA chains are not covalently bonded to graphene or the PE chains. They are aligned with the

PE chains mainly due to nonbonded interactions. The excellent alignment demonstrated for both PE and PMMA near graphene (**Figure E.5**) collectively contributes to the highly efficient thermal conduction in the blending region defined in **Figure 6.4**.

6.5.6 Vibrational Coupling

Molecular design of interfaces may significantly influence interfacial thermal conductance,[26-28] in which the vibrational coupling between materials plays a key role. The dense PE monolayer grafted to graphene, like a linker or vibrational mediator, drastically improves the overall vibrational coupling between graphene and PMMA, leading to improved interfacial thermal conduction. **Figure 6.7**a,b show the partial vibrational density of states (VDOS) for PE, PMMA and sp^2 carbon of graphene in G32PE8 and G1PE8, respectively. At high grafting density, the VDOS of sp^2 carbon of graphene has a peak at 50.65 THz due to the interaction with sp^3 carbon atoms (i.e. grafting points) (**Figure 6.7**a), which highly overlaps with a vibrational mode of PMMA. However, this overlap does not significantly contribute to the interfacial thermal transport due to the PE sandwiched in between. More quantitative analysis can be found in the following analysis of the integrated autocorrelation of interfacial heat power exchange. At low grafting densities (e.g. G1PE8), graphene has most of its surface in direct contact with PMMA; and PE “bridges” are sparse. At the graphene/PMMA subinterface, due to their drastically different physical properties, graphene and PMMA inevitably have poor vibrational coupling. As shown in **Figure 6.7**b, the VDOS peaks of sp^2 carbon mainly locate at about 14.1, 19.2, 53.8, and 58.7 THz. Very few overlaps are found between the VDOS curves of graphene and PMMA. The poor vibrational coupling is also evidenced in the plot of the cumulative correlation factor

(**Figure 6.7**c). At all frequencies, the cumulative correlation is weak between graphene and PMMA in G1PE8 (black solid line). By comparison, at the PE/PMMA subinterface, both materials are polymers and have similar properties. Indeed, as shown in **Figure 6.7**b, a significant overlap is found at 89.6 THz between PE and PMMA, demonstrating excellent vibrational coupling between these two materials. A similar conclusion can be drawn from **Figure 6.7**c too. The strong coupling between PE and PMMA plays an increasingly important role as the PE-grafting density grows. With more PE chains grafted to graphene (e.g. G32PE8) (**Figure 6.7**a,c), the vibrational coupling between materials is similar to that shown for G1PE32, but there are more PE/PMMA interfaces present. Hence, the overall vibrational mismatch across the interface is much alleviated, leading to boosted heat power exchange across the interface, as demonstrated in the following section.

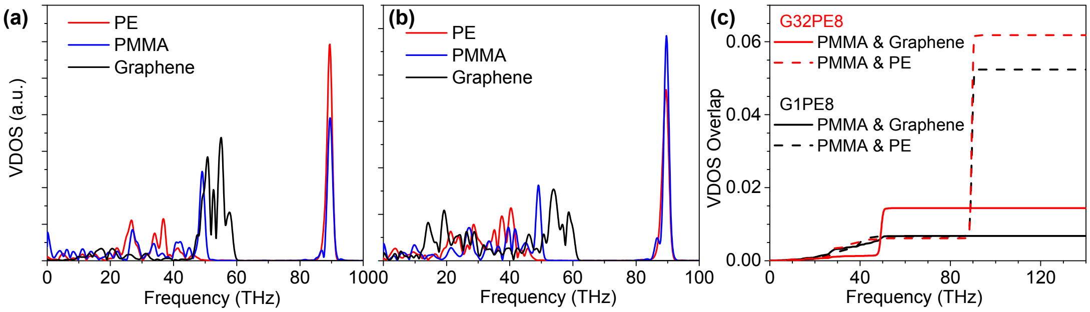

Figure 6.7. The vibrational density of states (VDOS) of PE, PMMA, and graphene in (a) G32PE8 and (b) G1PE8. (c) The cumulative correlation factor between PMMA and graphene (solid lines) and between PMMA and PE (dashed lines) in both G32PE8 (red) and G1PE8 (black) systems.

6.5.7 Integrated Autocorrelation of Interfacial Heat Power

Integrated autocorrelation of heat power is a quantitative measure of the thermal energy exchanged across an interface via a particular path or a particular pair of atom groups. Summing up the contributions by all paths will give interfacial thermal conductance. **Figure 6.8**a plots the integrated autocorrelation between PMMA and graphene in four systems with increasing PE-grafting density, while **Figure 6.8**b plots that between PMMA and PE in the same systems. All curves fluctuate with time initially but all of them converge at the end. Dashed lines are drawn to designate the converged values. As shown in **Figure 6.8**a, the energy exchanged via the graphene→PMMA path decreases with the increasing number of PE chains from 1 to 8, 16, and 32; and in particular, the value is almost zero when 32 PE chains are grafted. The physical understanding is straightforward. As more chains are grafted, the contact area between graphene and the PMMA matrix decreases, which reduces energy transport via this path due to the screening by PE chains. On the contrary, **Figure 6.8**b shows that the energy exchanged via the PE→PMMA path increases with the PE-grafting density. Except for G1PE8, the energy exchanged via the path is much larger than that exchanged via the graphene→PMMA path. The results echo the finding from **Figure 6.7** that heat transfer between PE and PMMA is much more efficient than that between graphene and PMMA. Both analyses demonstrate that highly extended PE monolayers are an efficient linker material to bridge two dissimilar materials, graphene and PMMA, for faster thermal transport across the interface.

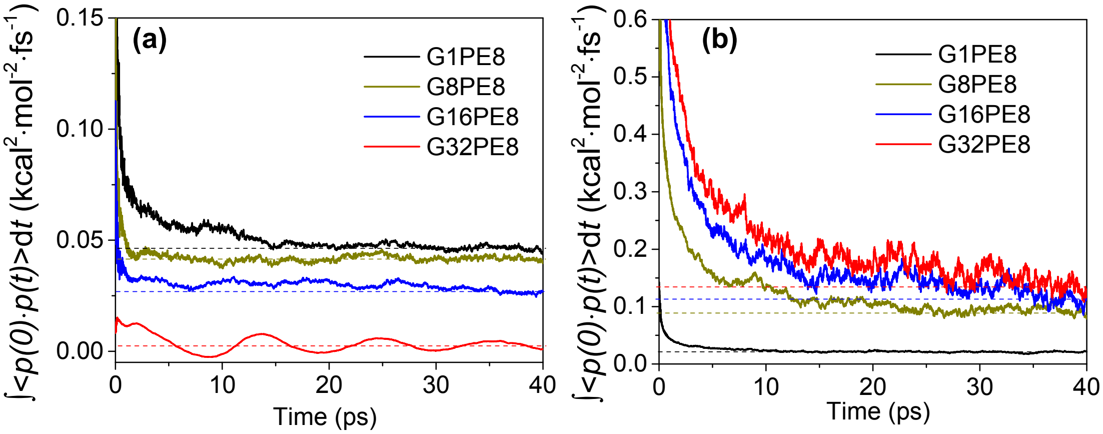

Figure 6.8. The integrated autocorrelation of interfacial heat power exchange (a) between graphene (sp^2 carbons) and PMMA and (b) between PE and PMMA for four systems with increasing X. Dashed lines show converged values of the integral.

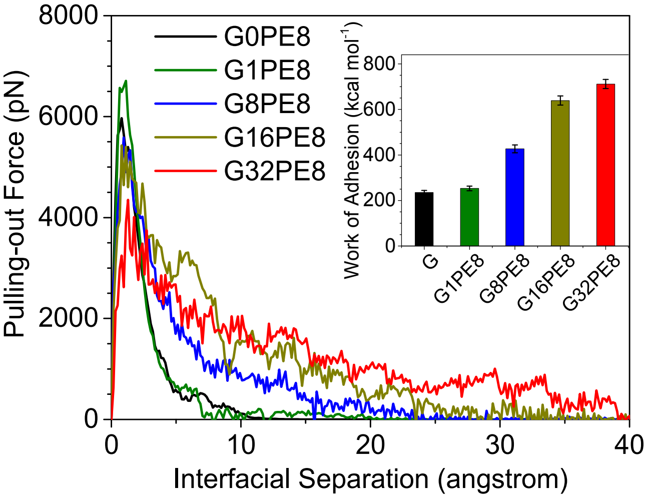

Figure 6.9. Pullout force versus interfacial separation for five systems with increasing X. The inset plots the work of adhesion for the five systems by integrating the force-separation curves.

6.5.8 Interfacial Adhesion

Direct correlation between interfacial adhesion and interfacial thermal conductance has been found previously for solid/solid and solid/liquid interfaces by experimental measurements and MD simulations.[68-69] Different from VDOS which focuses on one particular material, work of adhesion includes the contributions of two materials forming the interface. **Figure 6.9** plots the pullout force as a function of spatial separation when breaking several PE-functionalized graphene/PMMA interfaces. The peak point in the curves represents the maximum force required to break an interface, which further gives the failure strength. The results show that, with more PE chains grafted to the graphene, interfacial strength is lowered and the pullout requires a longer time to complete due to the interaction between crystalline PE monolayer and the PMMA chains embedded in the PE monolayer. In other words, mechanically, G1PE8 has a more brittle interface while G32PE8 has a more ductile one. Both strength and failure separation contribute to the overall interfacial work of adhesion, which is plotted in the inset of **Figure 6.9** for the five systems under investigation. More work is required to break the interface with more PE chains grafted to graphene. This is consistent with our finding in **Figure 3** that interfacial thermal conductance increases with the PE-grafting density, which, again, demonstrates the relationship between interfacial adhesion and interfacial thermal conductance.

6.6 Conclusions

In this work, we demonstrate that decorating interfaces with polymeric self-assembled monolayers (SAMs) of high coverage density can significantly increase interfacial thermal conductance between drastically dissimilar materials. By grafting the

SAM of PE to graphene surfaces with a coverage of 7.14 % on each side, the interfacial thermal conductance between graphene and a PMMA matrix is improved by 431.3%. The anomalous enhancement is attributed to three governing factors: 1) extended and well-aligned polymer chains in a PE/PMMA blending region, 2) excellent vibrational coupling between PE and PMMA, and 3) covalent bonding between graphene and PE chains. To be more specific, first, both atomic number density and Herman's orientation analyses depict that grafted PE chains of high coverage density feature extended chains standing up from graphene surface, while PE chains grafted at low densities are flat on graphene surfaces. The extended conformation of dense PE monolayer is due to the steric repulsion between PE chains and the stiff covalent bonding between PE and graphene. Such interchain interactions also enforce strong restrictions on the conformation of PMMA molecules, forming a relatively crystallized PE-PMMA blending region. The close-to-crystalline polymer conformation significantly facilitates along-chain thermal transport, leading to a thermal conductivity 456% higher than that of the pure PMMA. Second, PE is much better than graphene in vibrational coupling with PMMA. As the grafting density grows, more PE chains replace graphene to interact directly with PMMA; and more thermal energy is exchanged via the PE → PMMA path than the relatively inefficient graphene→PMMA path. Meanwhile, the length of the PE chains embedded in PMMA also extends the mechanical interaction between the two molecules, which boosts interfacial adhesion. Both factors contribute to alleviating the overall interfacial vibrational mismatch, making heat conduction more efficient. Third, covalent bonding enables efficient thermal transport between graphene and PE chains, which establishes a final link in the highly effective thermal transport pathway: graphene → dense PE monolayer (blended with PMMA) → PMMA. The proposed polymer grafting approach demonstrates the feasibility to engineer the interface towards drastically improved thermal transport between dissimilar materials.

6.7 Associated Content

6.7.1 Supporting Information

A schematic for nonequilibrium molecular dynamics simulation system **(Figure E.1**); Atomic number density of graphene and two random chosen polyethylene chains in G32PE8 (**Figure E.2**); Normalized end-to-end distance and height of PE for G*X*PE8 (**Figure E.3**); Temperature contour (**Figure E.4**) of graphene and two random chosen polyethylene chains in G32PE8; Local Herman's orientation factors of both functional polyethylene and PMMA matrix (**Figure E.5**).

6.8 Acknowledgments

This work was financially supported by Utah State University. Lin Zhang acknowledges financial support by the Dissertation Fellowship and the Graduate Research and Creative Opportunity Grant from Utah State University.

REFERENCES

(1) Vezie, M. S.; Few, S.; Meager, I.; Pieridou, G.; Dorling, B.; Ashraf, R. S.; Goni, A. R.; Bronstein, H.; McCulloch, I.; Hayes, S. C.; Campoy-Quiles, M.; Nelson, J., Exploring the Origin of High Optical Absorption in Conjugated Polymers. *Nat. Mater.* **2016,** *15* (7), 746-753.

(2) Wen, Z.; Yeh, M.-H.; Guo, H.; Wang, J.; Zi, Y.; Xu, W.; Deng, J.; Zhu, L.; Wang, X.; Hu, C.; Zhu, L.; Sun, X.; Wang, Z. L., Self-Powered Textile for Wearable Electronics by Hybridizing Fiber-Shaped Nanogenerators, Solar Cells, and Supercapacitors. *Sci. Adv.* **2016,** *2* (10), e1600097.

(3) Wang, Y.; Zhu, C.; Pfattner, R.; Yan, H.; Jin, L.; Chen, S.; Molina-Lopez, F.; Lissel, F.; Liu, J.; Rabiah, N. I.; Chen, Z.; Chung, J. W.; Linder, C.; Toney, M. F.; Murmann, B.; Bao, Z., A Highly Stretchable, Transparent, and Conductive Polymer. *Sci. Adv.* **2017,** *3* (3), e1602076.

(4) Dudem, B.; Ko, Y. H.; Leem, J. W.; Lim, J. H.; Yu, J. S., Hybrid Energy Cell with Hierarchical Nano/Micro-Architectured Polymer Film to Harvest Mechanical, Solar, and Wind Energies Individually/Simultaneously. *ACS Appl. Mater. Interfaces* **2016,** *8* (44), 30165-30175.

(5) Shen, S.; Henry, A.; Tong, J.; Zheng, R.; Chen, G., Polyethylene Nanofibres with Very High Thermal Conductivities. *Nat. Nanotechnol.* **2010,** *5* (4), 251-255.

(6) Zhong, Z.; Wingert, M. C.; Strzalka, J.; Wang, H.-H.; Sun, T.; Wang, J.; Chen, R.; Jiang, Z., Structure-Induced Enhancement of Thermal Conductivities in Electrospun Polymer Nanofibers. *Nanoscale* **2014,** *6* (14), 8283-8291.

(7) Zhang, L.; Chen, T.; Ban, H.; Liu, L., Hydrogen Bonding-Assisted Thermal Conduction in [Small Beta]-Sheet Crystals of Spider Silk Protein. *Nanoscale* **2014,** *6* (14), 7786-7791.

(8) Zhang, L.; Ruesch, M.; Zhang, X.; Bai, Z.; Liu, L., Tuning Thermal Conductivity of Crystalline Polymer Nanofibers by Interchain Hydrogen Bonding. *RSC Adv.* **2015,** *5* (107), 87981-87986.

(9) Zhang, L.; Bai, Z.; Ban, H.; Liu, L., Effects of the Amino Acid Sequence on Thermal Conduction through [Small Beta]-Sheet Crystals of Natural Silk Protein. *Phys. Chem. Chem. Phys.* **2015,** *17* (43), 29007-29013.

(10) Balandin, A. A.; Ghosh, S.; Bao, W.; Calizo, I.; Teweldebrhan, D.; Miao, F.; Lau, C. N., Superior Thermal Conductivity of Single-Layer Graphene. *Nano Lett.* **2008,** *8* (3), 902-907.

(11) Kim, H.; Abdala, A. A.; Macosko, C. W., Graphene/Polymer Nanocomposites. *Macromolecules* **2010,** *43* (16), 6515-6530.

(12) Xie, S. H.; Liu, Y. Y.; Li, J. Y., Comparison of the Effective Conductivity between Composites Reinforced by Graphene Nanosheets and Carbon Nanotubes. *Appl. Phys. Lett.* **2008,** *92* (24), 243121.

(13) Wang, D. R.; Bao, Y. R.; Zha, J. W.; Zhao, J.; Dang, Z. M.; Hu, G. H., Improved Dielectric Properties of Nanocomposites Based on Poly(Vinylidene Fluoride) and Poly(Vinyl Alcohol)-Functionalized Graphene. *ACS Appl. Mater. Interfaces* **2012,** *4* (11), 6273-6279.

(14) Vadukumpully, S.; Paul, J.; Mahanta, N.; Valiyaveettil, S., Flexible Conductive Graphene/Poly(Vinyl Chloride) Composite Thin Films with High Mechanical Strength and Thermal Stability. *Carbon* **2011,** *49* (1), 198-205.

(15) Gao, Z.; Song, N. N.; Zhang, Y. Y.; Li, X. D., Cotton-Textile-Enabled, Flexible Lithium-Ion Batteries with Enhanced Capacity and Extended Lifespan. *Nano Lett.* **2015,** *15* (12), 8194-8203.

(16) Gao, Z.; Bumgardner, C.; Song, N. N.; Zhang, Y. Y.; Li, J. J.; Li, X. D., Cotton-Textile-Enabled Flexible Self-Sustaining Power Packs Via Roll-to-Roll Fabrication. *Nat. Commun.* **2016,** *7*, 11586.

(17) Atif, R.; Inam, F., Reasons and Remedies for the Agglomeration of Multilayered Graphene and Carbon Nanotubes in Polymers. *Beilstein J. Nanotechnol.* **2016,** *7*, 1174-1196.

(18) Yang, Y. C.; Rigdon, W.; Huang, X. Y.; Li, X. D., Enhancing Graphene Reinforcing Potential in Composites by Hydrogen Passivation Induced Dispersion. *Sci. Rep.* **2013,** *3*, 2086.

(19) Kim, H.; Kobayashi, S.; AbdurRahim, M. A.; Zhang, M. L. J.; Khusainova, A.; Hillmyer, M. A.; Abdala, A. A.; Macosko, C. W., Graphene/Polyethylene Nanocomposites: Effect of Polyethylene Functionalization and Blending Methods. *Polymer* **2011,** *52* (8), 1837-1846.

(20) Cahill, D. G.; Braun, P. V.; Chen, G.; Clarke, D. R.; Fan, S.; Goodson, K. E.; Keblinski, P.; King, W. P.; Mahan, G. D.; Majumdar, A., Nanoscale Thermal Transport. II. 2003–2012. *Appl. Phys. Rev.* **2014,** *1* (1), 011305.

(21) Hu, L.; Desai, T.; Keblinski, P., Determination of Interfacial Thermal Resistance at the Nanoscale. *Phys. Rev. B* **2011,** *83* (19), 195423.

(22) Losego, M. D.; Grady, M. E.; Sottos, N. R.; Cahill, D. G.; Braun, P. V., Effects of Chemical Bonding on Heat Transport across Interfaces. *Nat. Mater.* **2012,** *11* (6), 502-506.

(23) Shen, M.; Evans, W. J.; Cahill, D.; Keblinski, P., Bonding and Pressure-Tunable Interfacial Thermal Conductance. *Phys. Rev. B* **2011,** *84* (19), 195432.

(24) Luo, T.; Lloyd, J. R., Enhancement of Thermal Energy Transport across Graphene/Graphite and Polymer Interfaces: A Molecular Dynamics Study. *Adv. Funct. Mater.* **2012,** *22* (12), 2495-2502.

(25) Sun, F.; Zhang, T.; Jobbins, M. M.; Guo, Z.; Zhang, X.; Zheng, Z.; Tang, D.; Ptasinska, S.; Luo, T., Molecular Bridge Enables Anomalous Enhancement in Thermal Transport across Hard - Soft Material Interfaces. *Adv. Mater. (Weinheim, Ger.)* **2014,** *26* (35), 6093-6099.

(26) Lin, S. C.; Buehler, M. J., The Effect of Non-Covalent Functionalization on the Thermal Conductance of Graphene/Organic Interfaces. *Nanotechnology* **2013,** *24* (16), 165702.

(27) Wang, Y.; Yang, C.; Pei, Q.-X.; Zhang, Y., Some Aspects of Thermal Transport across the Interface between Graphene and Epoxy in Nanocomposites. *ACS Appl. Mater. Interfaces* **2016,** *8* (12), 8272-8279.

(28) Wang, Y.; Zhan, H. F.; Xiang, Y.; Yang, C.; Wang, C. M.; Zhang, Y. Y., Effect of Covalent Functionalization on Thermal Transport across Graphene-Polymer Interfaces. *J. Phys. Chem. C* **2015,** *119* (22), 12731-12738.

(29) Wang, Y.; Yang, C. H.; Mai, Y. W.; Zhang, Y. Y., Effect of Non-Covalent Functionalisation on Thermal and Mechanical Properties of Graphene-Polymer Nanocomposites. *Carbon* **2016,** *102*, 311-318.

(30) Gao, Y. Y.; Muller-Plathe, F., Increasing the Thermal Conductivity of Graphene-Polyamide-6,6 Nanocomposites by Surface-Grafted Polymer Chains: Calculation with Molecular Dynamics and Effective-Medium Approximation. *J. Phys. Chem. B* **2016,** *120* (7), 1336-1346.

(31) Zhang, L.; Bai, Z.; Liu, L., Exceptional Thermal Conductance across Hydrogen - Bonded Graphene/Polymer Interfaces. *Adv. Mater. Interfaces* **2016,** *3* (13), 1600211.

(32) Mino-Galaz, G. A., Allosteric Communication Pathways and Thermal Rectification in PDZ-2 Protein: A Computational Study. *J. Phys. Chem. B* **2015,** *119* (20), 6179-6189.

(33) Zhang, T.; Gans-Forrest, A. R.; Lee, E.; Zhang, X. Q.; Qu, C.; Pang, Y. S.; Sun, F.; Luo, T. F., Role of Hydrogen Bonds in Thermal Transport across Hard/Soft Material Interfaces. *ACS Appl. Mater. Interfaces* **2016,** *8* (48), 33326-33334.

(34) Song, P.; Sangeeth, C. S. S.; Thompson, D.; Du, W.; Loh, K. P.; Nijhuis, C. A., Noncovalent Self-Assembled Monolayers on Graphene as a Highly Stable Platform for Molecular Tunnel Junctions. *Adv. Mater. (Weinheim, Ger.)* **2016,** *28* (4), 631-639.

(35) Ulman, A., Formation and Structure of Self-Assembled Monolayers. *Chem. Rev.* **1996,** *96* (4), 1533-1554.

(36) Faucheux, N.; Schweiss, R.; Lutzow, K.; Werner, C.; Groth, T., Self-Assembled Monolayers with Different Terminating Groups as Model Substrates for Cell Adhesion Studies. *Biomaterials* **2004,** *25* (14), 2721-2730.

(37) Elinski, M. B.; Menard, B. D.; Liu, Z. T.; Batteas, J. D., Adhesion and Friction at Graphene/Self-Assembled Monolayer Interfaces Investigated by Atomic Force Microscopy. *J. Phys. Chem. C* **2017,** *121* (10), 5635-5641.

(38) Xu, Z.; Song, K.; Yuan, S. L.; Liu, C. B., Microscopic Wetting of Self-Assembled Mono Layers with Different Surfaces: A Combined Molecular Dynamics and Quantum Mechanics Study. *Langmuir* **2011,** *27* (14), 8611-8620.

(39) Wang, Z. H.; Carter, J. A.; Lagutchev, A.; Koh, Y. K.; Seong, N. H.; Cahill, D. G.; Dlott, D. D., Ultrafast Flash Thermal Conductance of Molecular Chains. *Science* **2007,** *317* (5839), 787-790.

(40) Majumdar, S.; Malen, J. A.; McGaughey, A. J. H., Cooperative Molecular Behavior Enhances the Thermal Conductance of Binary Self-Assembled Monolayer Junctions. *Nano Lett.* **2017,** *17* (1), 220-227.

(41) Majumdar, S.; Sierra-Suarez, J. A.; Schiffres, S. N.; Ong, W. L.; Higgs, C. F.; McGaughey, A. J. H.; Malen, J. A., Vibrational Mismatch of Metal Leads Controls Thermal Conductance of Self-Assembled Monolayer Junctions. *Nano Lett.* **2015,** *15* (5), 2985-2991.

(42) Markov, A.; Greben, K.; Mayer, D.; Offenhausser, A.; Wordenweber, R., In Situ Analysis of the Growth and Dielectric Properties of Organic Self-Assembled Monolayers: A Way to Tailor Organic Layers for Electronic Applications. *ACS Appl. Mater. Interfaces* **2016,** *8* (25), 16451-16456.

(43) Senaratne, W.; Andruzzi, L.; Ober, C. K., Self-Assembled Monolayers and Polymer Brushes in Biotechnology: Current Applications and Future Perspectives. *Biomacromolecules* **2005,** *6* (5), 2427-2448.

(44) Fang, M.; Wang, K. G.; Lu, H. B.; Yang, Y. L.; Nutt, S., Single-Layer Graphene Nanosheets with Controlled Grafting of Polymer Chains. *J. Mater. Chem.* **2010,** *20* (10), 1982-1992.

(45) Steenackers, M.; Gigler, A. M.; Zhang, N.; Deubel, F.; Seifert, M.; Hess, L. H.; Lim, C. H. Y. X.; Loh, K. P.; Garrido, J. A.; Jordan, R.; Stutzmann, M.; Sharp, I. D., Polymer Brushes on Graphene. *J. Am. Chem. Soc.* **2011,** *133* (27), 10490-10498.

(46) Salavagione, H. J., Promising Alternative Routes for Graphene Production and Functionalization. *J. Mater. Chem. A* **2014,** *2* (20), 7138-7146.

(47) Liu, Z.; Robinson, J. T.; Sun, X. M.; Dai, H. J., PEGylated Nanographene Oxide for Delivery of Water-Insoluble Cancer Drugs. *J. Am. Chem. Soc.* **2008,** *130* (33), 10876-10877.

(48) Yamada, R.; Uosaki, K., In Situ Scanning Tunneling Microscopy Observation of the Self-Assembly Process of Alkanethiols on Gold(111) in Solution. *Langmuir* **1998,** *14* (4), 855-861.

(49) Poirier, G. E.; Pylant, E. D., The Self-Assembly Mechanism of Alkanethiols on Au(111). *Science* **1996,** *272* (5265), 1145-1148.

(50) Henry, A.; Chen, G.; Plimpton, S. J.; Thompson, A., 1d-to-3d Transition of Phonon Heat Conduction in Polyethylene Using Molecular Dynamics Simulations. *Phys. Rev. B* **2010,** *82* (14), 144308.

(51) Henry, A.; Chen, G., High Thermal Conductivity of Single Polyethylene Chains Using Molecular Dynamics Simulations. *Phys. Rev. Lett.* **2008,** *101* (23), 235502.

(52) Humphrey, W.; Dalke, A.; Schulten, K., Vmd: Visual Molecular Dynamics. *J. Mol. Graphics* **1996,** *14* (1), 33-38.

(53) Mekhilef, N.; Verhoogt, H., Phase Inversion and Dual-Phase Continuity in Polymer Blends: Theoretical Predictions and Experimental Results. *Polymer* **1996,** *37* (18), 4069-4077.

(54) Xu, Y.; Thurber, C. M.; Macosko, C. W.; Lodge, T. P.; Hillmyer, M. A., Poly(Methyl Methacrylate)-Block-Polyethylene-Block-Poly(Methyl Methacrylate) Triblock Copolymers as Compatibilizers for Polyethylene/Poly(Methyl Methacrylate) Blends. *Ind. Eng. Chem. Res.* **2014,** *53* (12), 4718-4725.

(55) Plimpton, S., Fast Parallel Algorithms for Short-Range Molecular-Dynamics. *J. Comput. Phys.* **1995,** *117* (1), 1-19.

(56) Jorgensen, W. L.; Maxwell, D. S.; Tirado-Rives, J., Development and Testing of the OPLS All-Atom Force Field on Conformational Energetics and Properties of Organic Liquids. *J. Am. Chem. Soc.* **1996,** *118* (45), 11225-11236.

(57) Price, M. L. P.; Ostrovsky, D.; Jorgensen, W. L., Gas-Phase and Liquid-State Properties of Esters, Nitriles, and Nitro Compounds with the OPLS-Aa Force Field. *J Comput Chem* **2001,** *22* (13), 1340-1352.

(58) Godawat, R.; Jamadagni, S. N.; Garde, S., Characterizing Hydrophobicity of Interfaces by Using Cavity Formation, Solute Binding, and Water Correlations. *Proc. Natl. Acad. Sci. U.S.A.* **2009,** *106* (36), 15119-15124.

(59) Kuang, S. Y.; Gezelter, J. D., Simulating Interfacial Thermal Conductance at Metal-Solvent Interfaces: The Role of Chemical Capping Agents. *J. Phys. Chem. C* **2011,** *115* (45), 22475-22483.

(60) Nieto-Draghi, C.; Avalos, J. B., Non-Equilibrium Momentum Exchange Algorithm for Molecular Dynamics Simulation of Heat Flow in Multicomponent Systems. *Mol. Phys.* **2003,** *101* (14), 2303-2307.

(61) Hermans, P. H.; Hermans, J. J.; Vermaas, D.; Weidinger, A., Deformation Mechanism of Cellulose Gels. IV. General Relationship between Orientation of the Crystalline and That of the Amorphous Portion. *J. Polym. Sci.* **1948,** *3* (1), 1-9.

(62) Li, B. W.; Lan, J. H.; Wang, L., Interface Thermal Resistance between Dissimilar Anharmonic Lattices. *Phys. Rev. Lett.* **2005,** *95* (10), 104302.

(63) Fetters, L. J.; Lohse, D. J.; Richter, D.; Witten, T. A.; Zirkel, A., Connection between Polymer Molecular-Weight, Density, Chain Dimensions, and Melt Viscoelastic Properties. *Macromolecules* **1994,** *27* (17), 4639-4647.

(64) Liu, Y.; Huang, J.; Yang, B.; Sumpter, B. G.; Qiao, R., Duality of the Interfacial Thermal Conductance in Graphene-Based Nanocomposites. *Carbon* **2014,** *75*, 169-177.

(65) Assael, M.; Antoniadis, K.; Wu, J., New Measurements of the Thermal Conductivity of PMMA, BK7, and Pyrex 7740 up to 450k. *Int. J. Thermophys.* **2008,** *29* (4), 1257-1266.

(66) Liu, J.; Yang, R., Tuning the Thermal Conductivity of Polymers with Mechanical Strains. *Phys. Rev. B* **2010,** *81* (17), 174122.

(67) Losego, M. D.; Moh, L.; Arpin, K. A.; Cahill, D. G.; Braun, P. V., Interfacial Thermal Conductance in Spun-Cast Polymer Films and Polymer Brushes. *Appl. Phys. Lett.* **2010,** *97* (1).

(68) Shenogina, N.; Godawat, R.; Keblinski, P.; Garde, S., How Wetting and Adhesion Affect Thermal Conductance of a Range of Hydrophobic to Hydrophilic Aqueous Interfaces. *Phys. Rev. Lett.* **2009,** *102* (15), 156101.

(69) Ramos-Alvarado, B.; Kumar, S.; Peterson, G. P., Solid–Liquid Thermal Transport and Its Relationship with Wettability and the Interfacial Liquid Structure. *J. Phys. Chem. Lett.* **2016,** *7* (17), 3497-3501.

CHAPTER 7

ENHANCED INTERFACIAL THERMAL TRANSPORT OF GRAPHENE/POLYMER NANOCOMPOSITES VIA A HIERARCHICALLY HYDROGEN-BONDED MOLECULAR HEAT SPREADER

7.1 Abstract

Interfacial thermal transport properties play a vital role in many technologies. Engineering interfaces by materials such as self-assembled monolayers and polymer brushes have attracted a lot of attention. Here, we demonstrate that polymer monolayer with a hierarchical network of hydrogen bonds significantly improves interfacial thermal transport of polymer nanocomposites. In this study, Polyvinyl alcohol (PVA) chains were grafted onto the surfaces of graphene, which form hydrogen bonds with the poly (methyl methacrylate) (PMMA) matrix. At the PVA coverage of 7.14%, interfacial thermal conductance is drastically improved by 520%, mainly due to three physical phenomena occuring at the PMMA/graphene interface: (1) hydrogen bonds improve the vibrational overlap between PVA and PMMA; (2) PVA chains are extended even at low coverage, which facilitates along-chain thermal conduction; and (3) covalent bonding between graphene and PVA chains enable efficient heat transfer. In addition, our study demonstrates that there is no universal relationship between interfacial thermal conductance and interfacial adhesion. These results provide new important insights to design interfaces of polymer nanocomposite and biomaterials for desired properties and a wide range of applications.

This chapter is submitted to *Nanoscale*. Coauthor: Professor Ling Liu.

7.2 Introduction

Interfacial thermal transport properties play a crucial role in the performances of many innovative technologies such as nanocomposites,[1, 2] thermoelectrics,[3, 4] nanoelectronics,[5] and biomedical devices[6-8]. Typically, an interface inhibits transmission of heat energy between mechanically dissimilar materials, making it a bottleneck of thermal transport especially when the characteristic length of a structure is comparable to the mean free path of energy carriers[9]. For instance, graphene/polymer nanocomposites usually have low interfacial thermal conductance in the order of 60~80 MW m^{-2} K^{-1},[10-12] which is one of the primary reasons for the low thermal conductivity of nanocomposites. Due to the critical role of material interfaces in determining thermal properties and applications of a variety of materials, there is a critical need to develop new approaches for drastically improved interfacial heat transfer in these materials.

Interfacial thermal conductance is dictated by the group velocity and the transmission coefficient of phonons, which are affected by interfacial bonding strength and the vibrational density of states of materials comprising the interface.[9] To understand the effect of interfacial bonding strength, parametric studies were performed at a graded interface by increasing the energy parameter (ε) of an LJ interfacial interatomic potential to several folds of the original value (ε_0). Simulation results show that the interfacial thermal conductance between silicon and amorphous polyethylene[13] was increased by six times with $\varepsilon/\varepsilon_0 = 5$, and the value between graphene and paraffin[12] was enhanced by more than three times with $\varepsilon/\varepsilon_0 = 6$. Phonon wave packet simulations elucidated that the transmission coefficients of longitudinal and transverse acoustic wave packets were enlarged by increasing the bonding strength and that the frequency spectrum of efficiently transmitted phonons was broadened when $\varepsilon/\varepsilon_0$ was increased to 5 from 1.[13] Concerning the vibrational density of states, large mismatch of vibrational density usually leads to low interfacial thermal conductance.[14] These understandings provide basic guidelines to tailor interfacial thermal conductance by material interface engineering.

Hence, enormous efforts have been made to introduce an intermediate material as a vibrational linker to alleviate the vibrational mismatch and take advantage of interfacial bonding strength. These interface materials fall into three categories determined by the interatomic interaction between them and the surrounding materials: noncovalent-noncovalent bonding, noncovalent-covalent bonding, and covalent-covalent bonding. In the first category, enhancement of interfacial thermal transport is limited due to the weak secondary bonding at the interface. For instance, alkyl (C_8)-pyrene molecules were inserted into octane and graphene, making the out-of-plane interfacial thermal conductance improved by 22%.[15] Additionally, interfacial thermal conductance between graphene and paraffin was enhanced by more than 15% by 1-pyrenebutyl, 1-pyrenebutyric acid or 1-pyrenebutylamine.[16] Even submonolayer water can fairly increase interfacial thermal conductance across hydrophilic quartz[17] in between graphene oxide (graphene) and lipid membranes[6] owing to highly enhanced vibrational overlap. The second strategy takes advantage of the strong covalent bonding between functional molecules and materials at the interface, and maintains large flexibility for desiging the secondary bonding with atoms on the other side of the interface. For example, hydrogenation of monolayer graphene can significantly improve interfacial thermal transport between silicene/graphene bilayer and graphene/phosphorene bilayer.[18, 19] When butyl molecules were covalently bonded to graphene surfaces, the interfacial thermal conductance across graphene/epoxy[20] and graphene/polyethylene[21] was improved by 400% at a 9.52% coverage and 129% at a 5.36 coverage, respectively. With a higher vibrational overlap, butyl outperforms several other functional molecules. In both cases, the interaction between functional molecules and polymer matrix are van der Waals interactions, which are very weak in bonding strength. As a result, researchers are using hydrogen bonds to engineer the interface between functional groups and polymer matrix[22] and the interface between self-assembled monolayer and organic liquid[23] for enhanced interfacial thermal transport. In the last case, the design flexibility is severely restricted since it is difficult to design covalent bonds between the interface material and the surrounding materials on both sides. Most of these studies are related to self-assembled monolayers (SAMs). SAMs were covalently bonded to metal/dielectric,[24] carbon nanotube arrays/metal,[25] graphene/metal,[26] and metal/metal[27] interfaces, demonstrating bonding-improved interfacial thermal transport. Despite the progress, there are few studies on manipulating interfacial bonding strength in polymer nanocomposites and little attention is paid to the thermal transport efficiency of intermediate materials.

Here, we demonstrate that a hierarchical heat spreader of polymer monolayer can significantly enhance interfacial thermal conductance in polymer nanocomposites by molecular dynamics simulations. A polymer monolayer was designed to bridge the graphene/polymer interface via strength-gradient bonds. In detail, one end of polymer chains is covalently bonded to graphene, and the other end can form hydrogen bonds with the polymer matrix. Moreover, hydrogen bonds can form between chains of polymer monolayers and facilitate thermal transport along polymer chains. The covalently bonded polymer layers on graphene such as polymer brushes and self-assembled monolayer have attracted a lot of attention and can be achieved by atomic transfer radical polymerization,[28, 29] irradiation-induced polymerization,[30] ring-open metathesis polymerization,[31] thiol-ene click reactions,[32] and esterification/amidation reactions,[33, 34] etc. Furthermore, functionalization of graphene with polymer can improve the dispersion of graphene in polymer nanocomposites, which further improves the thermal and mechanical properties of the entire composites.[35, 36] In this study, we elucidate the dependences of interfacial thermal transport on grafting density, chain length, chain conformation, and hydrogen bonding density. The results provide new insights to tune interfacial thermal transport in nanocomposites, proteins and synthetic materials for nanodevices and other biomedical applications.

7.3 Modeling and Simulations

7.3.1 Modeling

In this work, full atomic models of nanocomposites were built by combining polyvinyl alcohol (PVA) functionalized graphene and a poly-(methyl methacrylate) (PMMA) matrix, as shown in **Fig. 7.1**(a). PVA molecules were chosen since they can be grafted onto graphene by ester linkage[37] and can form hydrogen bonds with the PMMA matrix. Each PVA chain has eight repeat units of CH_2-CH(OH), and was covalently bonded to graphene uniformly. The PVA-grafted graphene has a cross-sectional area of 34.45 Å × 34.10 Å after relaxation, which is large enough to capture dominant contributions by all vibrational modes to interfacial thermal conduction.[12] The PMMA matrix was built by the self-avoiding random walk method,[38] with 40 repeat units per chain. Both material components were generated by our in-house codes, well equilibrated separately, and then merged in VMD[39] to form the nanocomposite. Periodic boundary conditions were applied in all three directions. Interatomic interactions were described by the OPLSAA force field[40, 41], which has been widely used to simulate polymers, graphene, and their interfaces.[15, 21, 42, 43] The formed nanocomposite model is denoted as "G*X*PVA" for brevity, where *X* is the number of PVA chains. The effect of chain density can be studied by varying the value of *X*. Hydrogen bonds can form between PVA and PMMA as well as between densely packed PVA chains (see **Fig. 7.1**(b)).

7.3.2 Simulations

All molecular dynamics simulations (MD) were carried out by LAMMPS.[44] We took four steps to prepare the nanocomposites for production runs. First, the initial atomic model of PMMA was minimized by the conjugate gradient algorithm, equilibrated in the NPT ensemble at 300 K and 1.0 atm for 1.0 ns, and finally equilibrated in the NVT ensemble at 300 K for 1.0 ns. Second, each atomic model of the nanocomposite was generated by sandwiching PVA functionalized graphene between several copies of the PMMA matrix generated from the first step. Third, the nanocomposite was annealed in the NPT ensemble at 1.0 atm to remove residual stresses. During annealing, the temperature of the system was heated up from 300 K to 800 K, kept at 800 K for 500 ps, and then cooled down to 300 K at a rate of 1.667 K/ps. After that, the system was relaxed in NPT and NVT for 500 ps, respectively. In all these three steps, the time step was 1.0 fs. Lastly, a further relaxation was performed in NVT at 300 K for 1.0 ns with the time step of 0.5 fs. In all production runs, the time step was fixed to be 0.5 fs which is small enough to capture vibration of hydrogen atoms.

Reverse non-equilibrium molecular dynamics (RNEMD) method proposed by Muller-Plathe[45] was applied to calculate interfacial thermal conductance, as illustrated in **Fig. 7.1**(a). Interfacial thermal conductance (G) was calculated by $G = J / \Delta T$, where J is the heat flux imposed by numerical manipulation and ΔT is the temperature drop evaluated across the interface. As shown in **Fig. 7.1**(a), the entire system was evenly divided into 100 slabs in the z direction. An amount of heat energy was added to the heat source (the red slab), and the same amount energy was subtracted from the heat sink (the blue slab). This manipulation was achieved by velocity swapping with a virtual elastic collision model[46] to maintain momentum conservation. As a result, a heat flow was generated from the heat source to the heat sink along both of the positive and negative z directions. Numerically, heat flux was calculated by $J = \Delta E / (2tA)$, where ΔE is the energy added to the heat source in the duration of t, A is the cross-sectional area of the system, and “2” is due to two symmetric heat transport paths from the heat source to the heat sink. As illustrated in **Fig. 7.1**(b), temperature drop across the interface was denoted by $2\Delta T$, which was controlled to be 45 ± 5 K by controlling the frequency of velocity swapping. In addition, thermal conductance of the PMMA matrix was calculated by $k = J/(dT/dz)$, where dT/dz is the temperature gradient of PMMA, as shown in **Fig. 7.1**(c).

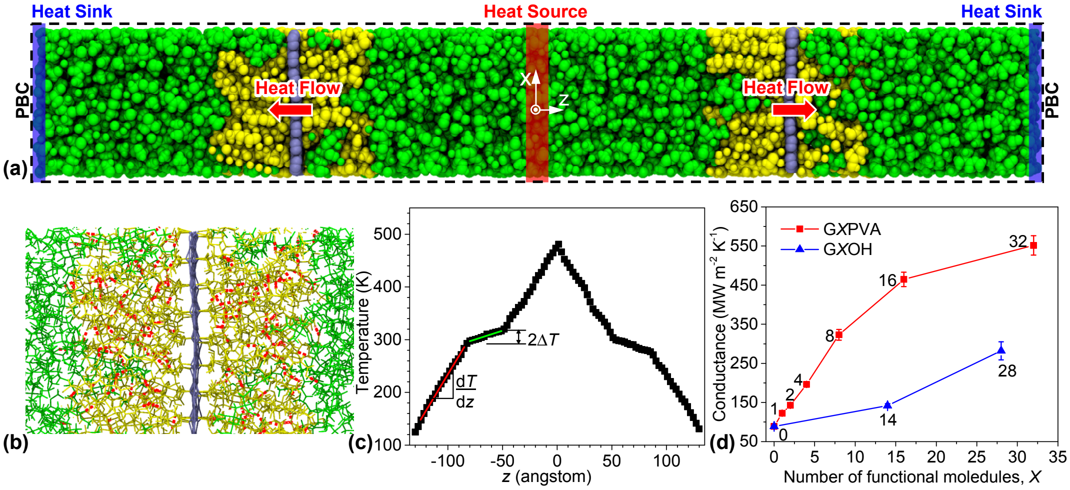

Fig. 7.1. (a) A representative system for nonequilibrium molecular dynamics simulation. The full atomistic model was built with: polyvinyl alcohol (PVA, yellow spheres) functionalized graphene (ice blue spheres) and the poly-(methyl methacrylate) (PMMA) matrix (green spheres). Periodic boundary conditions (PBC) were applied in all three directions. (b) A snapshot of the interfacial structure between PVA functionalized graphene and PMMA. Red lines stand for hydrogen bonds. (c) Temperature profile of G32PVA generated by RNEMD simulation. The total temperature drop across the interface is denoted by $2\Delta T$. Temperature gradient of PMMA (denoted by $\mathrm{d}T/\mathrm{d}z$) is found by curve fitting. (d) Interfacial thermal conductance versus the number of functional molecules grafted on graphene (*X*) for G*X*PVA and G*X*OH, respectively. Data of G*X*OH is from a previous work[22] investigating the hydroxyl-functionalized graphene/PMMA interface.

To visualize temperature contours of the nanocomposite, we also performed nonequilibrium molecular dynamics simulation (NEMD) with the temperature of atoms in the heat source and heat sink fixed to be 400 K and 250 K, respectively. Temperature was controlled by the Langevin thermostat[47] in the NVE ensemble. As shown in **Fig. F.1**, atoms of a part of the system were fixed during the simulation. Atomic temperatures and positions were stored in the simulation over a period of 5.0 ns, after a steady state was reached.

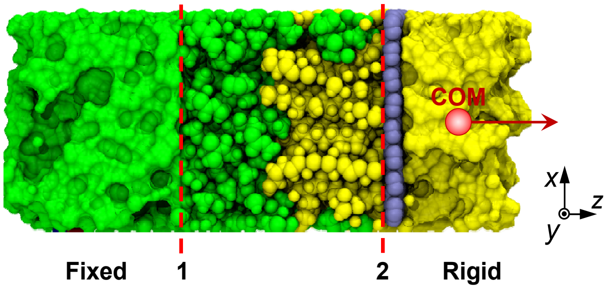

Fig. 7.2. An atomistic model for the molecular dynamics simulation of the pull-out process. Atoms of PMMA (green) to the left of plane "1" are fixed. Atoms of PVA (yellow) to the right of plane "2" are fixed. Atoms of graphene (ice blue) and those between "1" and "2" are movable. The center of mass (COM) of graphene and the rigid part of PVA is moved at a constant velocity in the +*z* direction.

The interfacial mechanical properties of G*X*PVA were evaluated by pulling out PVA functionalized graphene from PMMA matrix. Only a part of the well-equilibrated system was extracted and relaxed for the pull-out simulation, as shown in **Fig. 7.2**. The simulation was performed in the NVT ensemble with the time step of 0.1 fs. Atoms of the PMMA matrix to the left of plane "1" and those of PVA to the right of plane "2" were fixed as rigid, while the rest of the system was movable. Center of mass (COM) of the rigid PVA and graphene was moved at a constant velocity of 20 m/s along the +*z* direction. The pulling force was evaluated at different separations. The force-displacement curve was integrated to evaluate the interfacial adhesion, which is proportional to the interface toughness.

7.4 Results and Discussion

7.4.1 Validation

To test computational models and methods, we compared the results of this study with experimental and computational values in the literature in four aspects. First, mass density of the PMMA matrix relatively far away from the interface in well relaxed G*X*PVA is 1.14 ± 0.03 g cm^{-3}, which is in the range of experimental values, 1.1~1.19 g cm^{-3}.[43] Second, interfacial thermal conductances of G32PVA calculated by RNEMD and NEMD are 551.53 ± 24.81 MW m^{-2} K^{-1} and 570.83 MW m^{-2} K^{-1}, respectively, which agree well with each other. Third, interfacial thermal conductance of G0PVA (pristine graphene/PMMA nanocomposite) was evaluated as 88.66 MW m^{-2} K^{-1}, which fits into the range of 60~150 MW m^{-2} K^{-1} of similar pristine graphene/polymer interfaces.[10-12] Lastly, thermal conductivity of the PMMA matrix is 0.20 ±0.01 W m^{-1}K^{-1}, which is also in good agreement with the experimentally measured values from 0.19 to 0.25 W m^{-1}K^{-1}.[48]

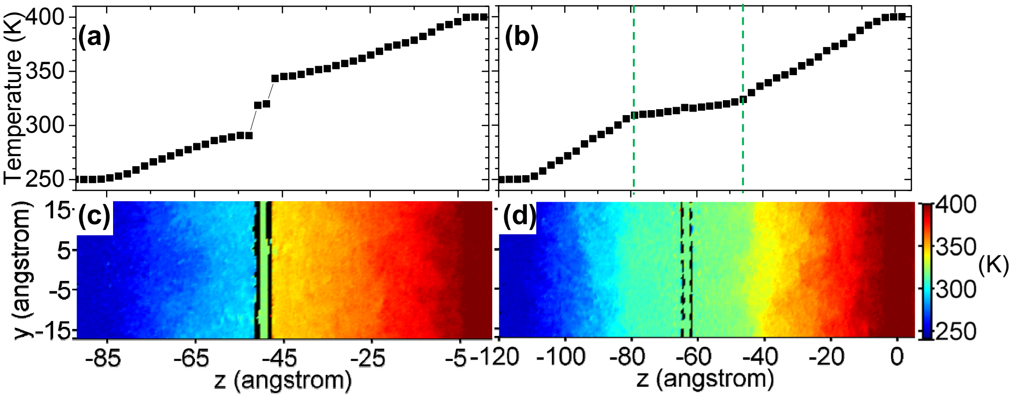

Fig. 7.3. Temperature profiles of (a) G1PVA and (b) G32PVA from nonequilibrium molecular dynamics simulation. Temperature contours of (c) G1PVA and (d) G32PVA. Two vertical green lines in (b) show the PVA/PMMA blending region. Vertical black lines in (c) and (d) show regions with no atoms.

7.4.2 Effect of Grafting Density on Interfacial Thermal Conductance

Fig. 7.1(d) shows interfacial thermal conductance of G*X*PVA, where *X* ranges from 0 to 1, 2, 4, 8, 16, and 32. The corresponding degree of functionalization is 0%, 0.45%, 0.89%, 1.79%, 3.57%, 7.14%, and 14.29%, respectively. As more PVA chains are grafted on graphene, interfacial thermal conductance increases and then saturates at a high value. Specifically, G32PVA has interfacial thermal conductance 6.2 times that across the pristine graphene/PMMA interface. Compared with the hydroxyl-functionalized graphene/PMMA interface investigated in our previous work,[22] the present system with a hierarchical hydrogen bond network is found to have considerably larger ascending rate in the conductance-X plot, especially when $X < 16$. Two PVA chains perform better than fourteen hydroxyl groups in the enhancement of interfacial thermal conductance.

Fig. 7.3 plots the temperature profile and temperature contour for G1PVA and G32PVA, respectively. Nonequilibrium molecular dynamics simulation of both systems was performed with the temperature fixed at 400 K and 250 K in the heat source and heat sink, respectively. Total duration was 5.0 ns in the steady state. Atoms were binned into 80 × 560 cells in y and z directions, respectively, based on their coordinates. Temperature was obtained by averaging atomic temperatures in each cell. It is worth mentioning that the heat flux of G32PVA was 20% more than that of G1PVA, as shown in **Fig. F.2**. There are two primary findings. First, thermal transport across the interface of G32PVA is much more efficient than that of G1PVA. An abrupt temperature drop across the interface on the temperature profile of G1PVA in **Fig. 7.3**(a) indicates a large thermal resistance and poor interfacial thermal transport. Consistent with the abrupt temperature drop, the color of cells changes sharply from dark red to deep blue along the -*z* direction in **Fig. 7.3**(c). The two black rectangular regions between graphene and PMMA indicate that there is almost no atom occupancy due to steric repulsion. By contrast, no abrupt temperature drop exists on the temperature profile of G32PVA in **Fig. 7.3**(b). The region delimited by two green segments in **Fig. 7.3**(b) is occupied by a blend of PVA and PMMA. This region features low temperature variations and much smaller temperature drop compared with that of G1PVA, indicating efficient heat conduction. Second, covalently bonded PVA chains facilitate thermal transport across the interface. Two black regions in **Fig. 7.3**(c) become much thinner in **Fig. 7.3**(c) and break into pieces. The cells where graphene is grafted with PVA chains exhibit the same color with graphene, indicating a continuous and uniform temperature field.

7.4.3 Effect of Grafting Density on Interfacial Morphology

Interfacial molecular morphology significantly affects thermal transport behavior of polymers. For example, extended polymer chains and nanofibers have been reported to have thermal conductance several orders of magnitude higher than their amorphous counterparts.[49-51] To visualize the morphology of PVA chains on graphene, we studied the atomic number density of PVA chains and graphene in G1PVA and G32PVA, respectively, as shown in **Fig. 7.4**(a)-(b). Atomic coordinates were recorded during a simulation of over 5 ns. Atoms of the system were binned into 80 × 560 cells. Here, only graphene and a pair of PVA chains were plotted for clarity. It is worthy to note that the shown PVA chains were randomly chosen from G32PVA, and the distance between their grafting points is comparable to that of G1PVA. **Fig. F.3** illustrates another four pairs of PVA chains randomly chosen from G32PVA. It is well known that self-assembled monolayers are usually flat on the substrate at low coverage densities. As the coverage density increases, chains may stand up from the surface, forming a "crystalline" structure until surface saturation is reached.[52, 53] Contrary to conventional wisdom, the PVA chains in this study feature extended configurations even at very low grafting densities (e.g. G1PVA), although they are not as extended as the PVA chains in G32PVA.

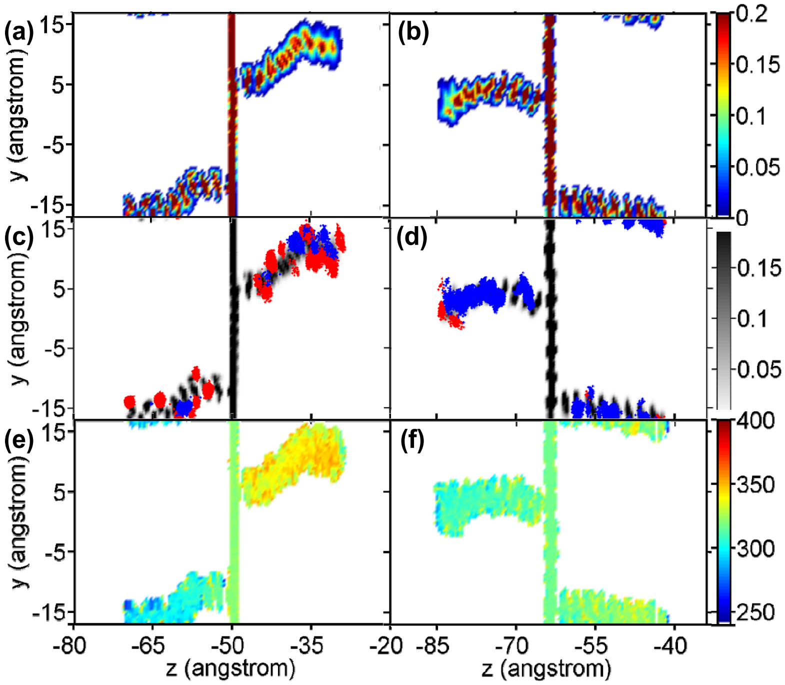

Fig. 7.4. Contour plots of atomic number density (a) and (b), plots of hydrogen bonds (c) and (d), and contour plots of temperature (e) and (f) for graphene and a pair of PVA chains in G1PVA and G32PVA, respectively. PVA chains in (b), (d), and (f) are the same pair and they are randomly chosen from the 32 chains of G32PVA. Each dot in (c) and (d) denotes the position of a hydrogen atom forming a hydrogen bond. Red dots stand for the hydrogen bonds between PVA and PMMA while blue dots represent those between PVA chains.

To unveil the mechanism extending PVA chains, we evaluated the distribution of hydrogen bonds based on over 10000 output frames, as illustrated in **Fig. 7.4**(c)-(d). A red point stands for a hydrogen bond between PVA and PMMA, while a blue one represents a hydrogen bond between PVA chains. The criteria used to identify a hydrogen bond are (see **Fig. F.4**): (1) the distance between the hydrogen bond donor (D) and the acceptor (A) is smaller than 3.0 Å; and (2) the angle of D-H (hydrogen)-A is smaller than 25º. **Fig. 7.4**(c) shows that hydrogen bonds formed between PVA and PMMA in G1PVA are more than those between PVA chains. Moreover, hydrogen bonds between PVA and PMMA were evenly distributed along the PVA chains. The results indicate that extended PVA chains are more energetically favorable as more and stronger hydrogen bonds are formed. On the other hand, intra-chain hydrogen bonds are found to contribute to the bending of PVA chains. All interchain and intrachain hydrogen bonds as well as the short length of chains contribute to the incomplete extension of PVA chains. Different from G1PVA, G32PVA have fewer hydrogen bonds formed between PVA and PMMA than those formed between PVA chains (see **Fig. F.5** for more examples). Furthermore, most of the hydrogen bonds between PVA and PMMA reside at the free ends of chains. Both steric repulsion and interchain hydrogen bonds result in much straighter PVA chains. Based on these analyses, PVA chains are extended in G1PVA and G32PVA due to different mechanisms.

Extended PVA polymer chains in both G1PVA and G32PVA facilitate interfacial thermal transport. For verification, temperature contours of graphene and a pair of PVA chains are plotted in **Fig. 7.4**(e)-(f). G1PVA is shown to have much larger temperature difference between the free ends of PVA chains than G32PVA does. Indeed, local temperature distribution represents the combined effects of thermal transport properties of local materials and the surrounding environment temperature. As shown in **Fig. 7.4**(e), the temperature of PVA chains varies sharply across the graphene, while varying much slowly along chains on each side of the graphene. Moreover, PVA chains show insignificant temperature changes along chains than the rest of the system (**Fig. F.6**), indicating that PVA conduct heat more efficiently than other parts of G1PVA. Moreover, at the heat source, temperature of PVA side chains is lower than that of the whole system but higher than that of the main chains of PVA. At the heat sink, PVA side chains have a temperature higher than the whole system but lower than PVA main chains. As a result, the larger temperature difference between the free ends of PVA in G1PVA originates from the more prominent temperature variation of surrounding materials. By comparison, temperature varies very slightly along the PVA chains of G32PVA as shown in **Fig. 7.4**(f). **Fig. F.7** shows that the PVA chains in G32PVA have comparable temperature distributions, and temperature varies insignificantly along the chains except for the free ends. All these findings manifest that extended PVA chains facilitate thermal transport in the region where PVA and PMMA are blended.

Fig. 7.5 presents the atomic number density distributions of PVA and PMMA with respect to the distance to the surface of grapheme. To calculate the atomic number density, atoms were binned into cells of 0.2 Å in the *z*-direction starting from the surface of graphene. Over 8000 frames were analyzed and averaged. As shown in **Fig. 7.5**(a), PVA in G*X*PVA (with $X = 1, 8, 16$ and 32) show sharp peaks in the region within 5 Å away from the grapheme surface, indicating that PVA chains are mostly in stand-up configurations and of semi-crystalline properties. These characteristics are consistent with the chain conformation shown in **Fig. 7.4**(a)-(b). More importantly, PVA in G32PVA shows very long-range ordering with a plateau formed up to 16 Å away from the graphene surface. The long-range ordering results from the combined effects of steric repulsion and interchain hydrogen bonding of PVA. **Fig. 7.5**(b) shows the atomic distribution of PMMA near the interface. With increased number of PVA chains on graphene, fewer PMMA atoms can enter the region in the vicinity of the graphene surface. Particularly, PMMA atoms are rarely seen within 5 Å of the graphene surface in G32PVA. All these structural effects lead to a unique feature of G32PVA that crystalline PVA exclusively exists within 15 Å from graphene, where thermal transport is drastically facilitated.

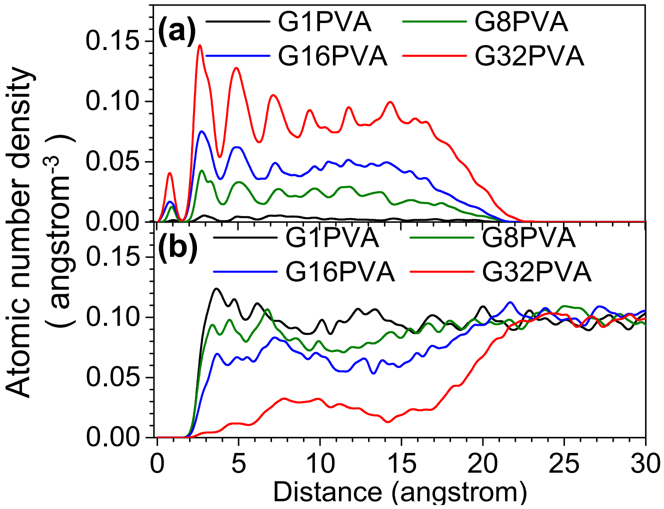

Fig. 7.5. Atomic number density distributions of (a) PVA and (b) PMMA versus the distance to the surface of graphene.

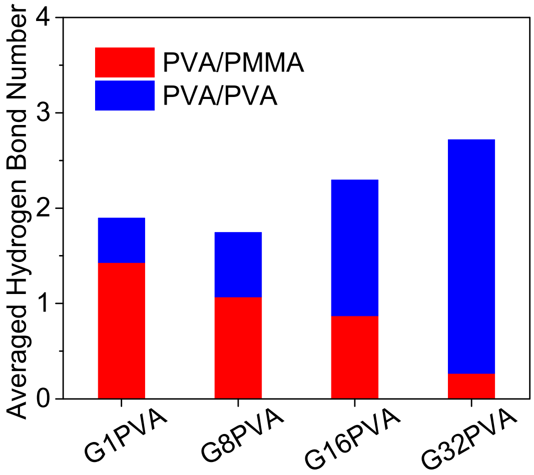

Fig. 7.6. Averaged number of hydrogen bonds per PVA chain.

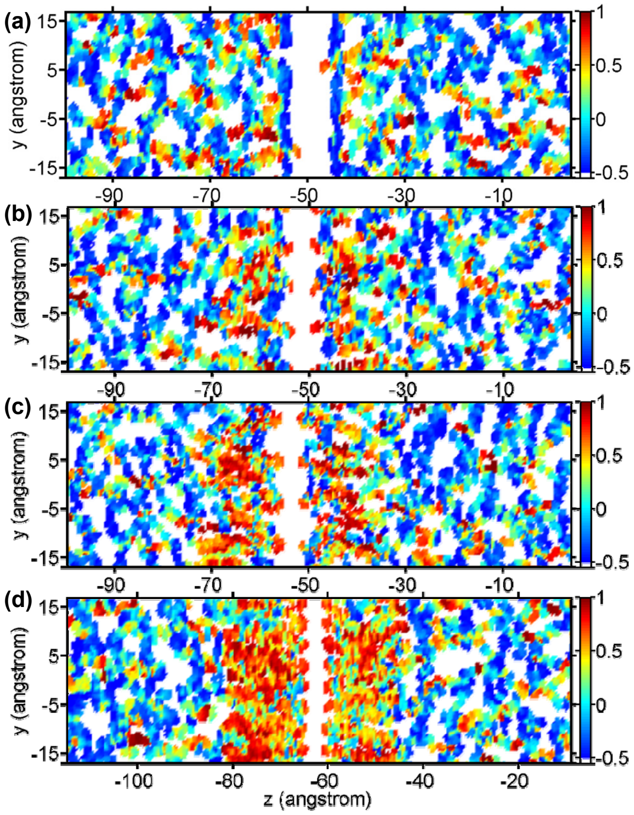

Fig. 7.7. Local Herman's orientation factor of main chains of PMMA and PVA in G*X*PVA with $X = 1$ (a), 8 (b), 16 (c), and 32 (d).

To understand the distribution of interfacial hydrogen bonds, hydrogen bonds in PVA chains and those between PVA and PMMA are studied independently. Fig. 7.6 shows the average number of hydrogen bonds in each PVA chain obtained from equilibrium MD simulations of over 60 ps. By increasing the number of PVA chains attached to the graphene surface (i.e. *X* of G*X*PVA), the number of hydrogen bonds between PVA and PMMA (red) decreases, while the number within and between PVA chains (blue) increases. Specifically, the blue hydrogen bonds of G1PVA were formed between hydroxyl groups within the same PVA chain. However, those of G32PVA were mainly between PVA chains since the PVA chains are more extended than that of G1PVA, and the space between adjacent hydroxyl groups in the same chains is increased. Previous studies have shown that intra-chain hydrogen bonds slightly facilitate thermal transport along the chain[54, 55] and that interchain hydrogen bonds contribute significantly to the high thermal conductivities of bundled polymer chains.[56-58] The drastically increased hydrogen bonds between PVA chains should facilitate thermal transport along each PVA chain. Moreover, the total number of hydrogen bonds of PVA and between PVA and PMMA increases with the number of PVA chains (**Fig. F.8**). The increased hydrogen bonds enhance thermal transport both through PVA and from PVA to PMMA.

To depict the chain orientation of PVA and PMMA in their blending region, we calculated the Herman's orientation factor for each G*X*PVA system. Herman's orientation factor[59] is extensively used to evaluate the orientation of polymer chains. It is defined as $S = 1.5 \langle \cos^2\theta \rangle - 0.5$, where θ is the angle between the polymer chain and a predefined direction, and $\langle \cdot \rangle$ represents an average over the system spatially. In particular, *S* values of 1.0 and -0.5 indicate that the polymer chain is perfectly aligned with and perpendicular to the predefined direction, respectively; while the value of 0.0 means that the polymer is completely amorphous. In this study, the local Herman's orientation factors was calculated by binning main chain atoms into 80 × 560 cells in the *y*-*z* plane; and *S* was evaluated in each cell using *z*-axis as the reference direction. Atomic coordinates were collected by equilibrium MD simulations of over 10.0 ns in the NVE ensemble. The chain direction at the *j*th atom of the main chain is defined from the (*j*-1)th atom to the (*j*+1)th atom. The calculated *S* values are plotted in **Fig. 7.7(a)-(d)**. The white rectangular region in the middle of each figure is where the graphene sheet is located. Orange blobs near the graphene sheet mostly correspond to PVA chains grafted onto the graphene. All these PVA chains are in indistinguishable colors, verifying that all PVA chains are uniformly oriented in stand-up configurations (see **Fig. F.9**). With more PVA chains present in the vicinity of graphene, PMMA chains can hardly enter the region and those entering the region tend to show extended configurations (see **Fig. F.9**). Accordingly, the entire blending region show orange colors, indicating oriented chains and improved thermal transport.

7.4.4 Role of Polymer Monolayer

The vibrational density of states (VDOS) analysis is widely used to differentiate the vibrational modes of materials forming an interface. VDOS can be calculated by the Fourier transformation of the velocity autocorrelation function as:

$$\mathrm{VDOS}(f) = \int_0^{+\infty} e^{-i2\pi f\tau} C_v(\tau)\, \mathrm{d}\tau \qquad (7.1)$$

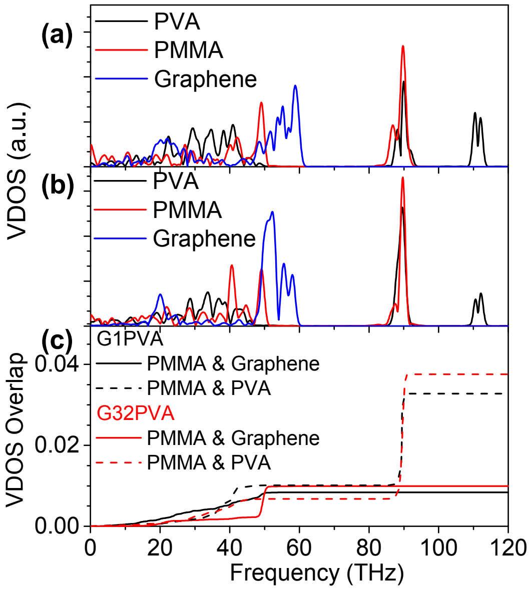

Fig. 7.8 Partial vibrational density of states (VDOS) of (a) G1PVA and (b) G32PVA. (c) Cumulative correlation factor. VDOS is decomposed into three groups, namely, PVA, PMMA, and *sp*^{2} carbon atoms of graphene.

Here, VDOS is a function of frequency *f*, and $C_v(\tau)$ is the normalized velocity autocorrelation function. Atomic velocities were obtained from equilibrium MD simulations with the sampling period of 2.0 fs. Based on VDOS, a cumulative correlation factor (*M*) has been defined to quantify the cumulative overlap of vibrational modes between two materials up to a cutoff frequency of $\bar{f}$:

$$M(\bar{f}) = \frac{\int_0^{\bar{f}} \mathrm{VDOS}_A(f) \cdot \mathrm{VDOS}_B(f)\, \mathrm{d}f}{\int_0^{\infty} \mathrm{VDOS}_A(f)\, \mathrm{d}f \cdot \int_0^{\infty} \mathrm{VDOS}_B(f)\, \mathrm{d}f} \tag{7.2}$$

where subscripts *A* and *B* denote two materials comprising the interface. A large value of cumulative correlation factor indicates a high overlap of vibrational modes between two materials (below the cutoff frequency) and hence a good interfacial thermal conduction. The cumulative correlation factor is equivalent to the correlation factor defined in previous studies when the cutoff frequency is larger than the maximum frequency of all vibrational modes.[60, 61]

PVA is found to serve as an excellent linker material mediating the vibrational mismatch between graphene and PMMA in G32PVA. **Fig. 7.8**(a) and (b) plots the VDOS of G1PVA and G32PVA decomposed into three groups, namely, PVA, PMMA and *sp*^{2} carbon atoms of graphene, respectively. Obviously, all vibrational modes of graphene are below 61THz. With increasing PVA chains on graphene, more *sp*^{2} carbon atoms are transform into *sp*^{3} carbon, leading to a broad peak at 51.5 THz in the VDOS of G32PVA. This vibrational mode has a good overlap with PMMA as shown in **Fig. 7.8**(b). However, this coupling does not contribute much to the interfacial thermal transport in G32PVA since graphene and PMMA in this system are not in direct contact. On the other hand, PMMA has vibrational modes below 50 THz and around 89.9 THz. The later vibrational mode corresponds to C-H stretch and has no overlap with the VDOS of graphene but high coincidence with that of PVA. In addition to that, PVA also has prominent vibrational modes at 110.5 THz and 112.4 THz relating to the vibration of hydroxyl groups. These high-frequency vibrational modes of PVA have no overlap with that of PMMA and graphene. However, hydroxyl groups have been found to facilitate thermal transport across the Au/organic liquid interface[23] and the graphene/PMMA matrix.[22] Therefore, overlap of vibrational modes is just one mechanism of improving interfacial thermal conduction, which may cooperate with other mechanisms. From the VDOS analyses, PVA is shown to have much higher overlap with PMMA than graphene does, with all vibrational modes included as shown in **Fig. 7.8**(c). Due to the confinement effect of PVA chains on PMMA, the overlap between PVA and PMMA in G32PVA is slightly higher than that in G1PVA.

The contributions of different heat transfer paths can be quantified by the integrated autocorrelation of interfacial heat power in the form of $\int_0^\infty \langle p(t) \cdot p(0) \rangle \, \mathrm{d}t$, where $p(t)$ is the instantaneous interfacial heat power exchanged between two materials at the interface. According to Green-Kubo fluctuation theorem, the integrated autocorrelation of interfacial heat power is proportional to interfacial thermal conductance.

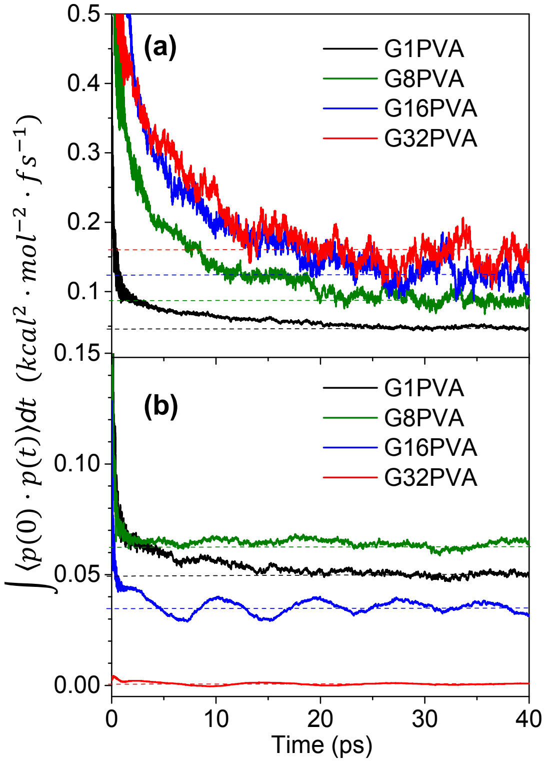

Fig. 7.9 Integrated autocorrelation of interfacial heat power (a) between PVA and PMMA and (b) between graphene (*sp*^{2} carbons) and PMMA. The dashed lines show converged values of the integrals.

In this study, the contributions of two non-bonded interfacial heat transfer paths are analyzed as shown in **Fig. 7.9**, where converged values are showed by the dashed lines. **Fig. 7.9**a shows that the converged value between PVA and PMMA increases with the number of *X* from 1 to 8, 16, and 32, meaning that heat conduction is more efficient from PVA to PMMA when more PVA chains exist. On the other hand, the converged value between graphene and PMMA first increases and then decreases with the number of PVA chains. There are two competing factors affecting interfacial thermal transport between PMMA and graphene. Due to hydrogen bonds, PMMA is attracted to be closer to PVA, which increases the interaction between PMMA and graphene.[23] Meanwhile, steric repulsion between PVA chains leads to fewer PMMA chains blended with PVA. As shown in **Fig. 7.5**, the number density of PMMA in the blending region of G8PVA is slightly lower than that of G1PVA. As a result, the benefit from having more PVA chains is more significant than the loss. On the other hand, the number density drops sharply with more than eight PVA chains. The effect of PVA chains dominates and less heat is transferred directly from graphene to PMMA. It is worth noting that heat energy transferred between PVA and PMMA is much larger than that between graphene and PMMA, except for G1PVA. All these results show that PVA chains serve as an efficient heat transfer channel.

7.4.5 Dependence on Interfacial Adhesion

How interfacial thermal conductance depends on the interfacial adhesion has attracted considerable interests. Different from vibrational modes of materials which represent bonding stiffness at equilibrium, interfacial adhesion describes the interfacial bonding strength and affinity between materials forming the interface. **Fig. 7.10** plots the pullout force with the separation between PVA-functionalized graphene and the PMMA matrix. The peak pullout force represents the force required to break the interface. Both the peak force and the endurance are shown to increase with the number of PVA chains. In these systems, the PMMA matrix is well mixed with PVA chains with hydrogen bonds in between, which enhances the interfacial bonding strength. Compared with G8PVA and G16PVA, G32PVA shows lower pullout force and endurance, since less PMMA chains penetrate into the forest of PVA chains leading to a "flat" interface between the two materials. In this study, the work of adhesion is evaluated by the integration of the force-separation curve. As shown in the inset of **Fig. 7.10**, the work of adhesion of G*X*PVA increases with *X* from 0 to 16 and then sharply drops from G16PVA to G32PVA. This finding is different from most previous results that interfacial thermal conductance increase with the work of adhesion at solid/liquid interface[62-64] and interfacial toughness at metal/ monolayer interface.[24] The discrepancy verifies that [65] that the correlation between interfacial thermal conductance and interfacial adhesion is not universal.

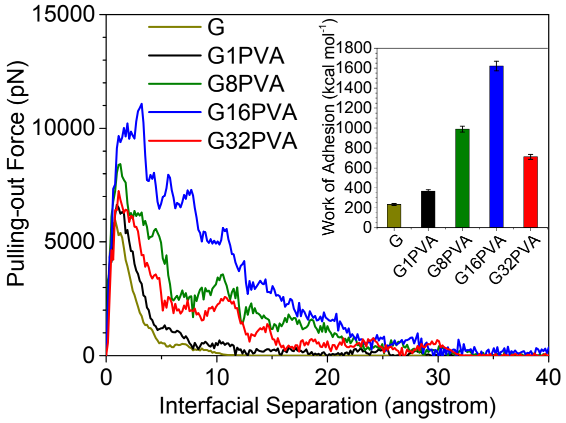

Fig. 7.10. Pullout force versus interfacial separation. *G* denotes the pristine graphene/PMMA interface. The inset plots the work of adhesion for different interfaces.

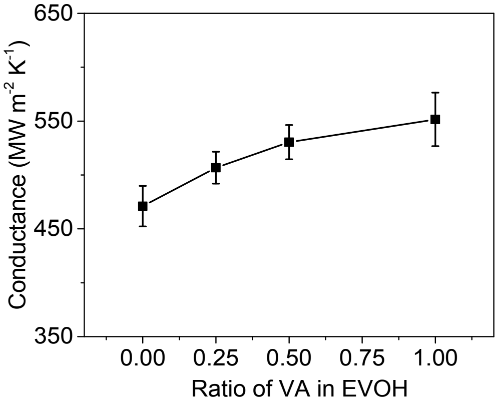

Fig. 7.11. Interfacial thermal conductance versus the proportion of vinyl alcohol (VA) units in the copolymer of ethylene and vinyl alcohol (EVOH).

7.4.6 Effect of Hydrogen Bonding Density

To further elucidate the role of hydrogen bonding, we studied interfacial thermal conductance of systems with 32 ethylene vinyl alcohol (EVOH) chains. EVOH is a copolymer of ethylene and vinyl alcohol with the chemical formula of $-[(C_2H_4)_x - (C_2H_3OH)_y]_m$. Hydrogen bonds form between vinyl alcohol and PMMA, and between vinyl alcohol and vinyl alcohol. Hydrogen bond formation capability is controllable by varying the proportion of vinyl alcohol in the system with total number of carbon atoms fixed in the main chains of EVOH. Here, fours systems are compared with (x, y, m) equal to (0, 1, 8), (1, 1, 4), (3, 1, 2), and (8, 0, 1), respectively. Their maximum hydrogen bond formation capabilities are evaluated to be 1.0, 0.5, 0.25, and 0, respectively. Particularly, graphene is functionalized by only polyvinyl alcohol chains in the system with (0, 1, 8), and only polyethylene chains for that with (8, 0, 1). As shown in **Fig. 7.11**, interfacial thermal conductance increases with the hydrogen bonding density and the proportion of vinyl alcohol groups. Compared with graphene functionalized with polyethylene chains, graphene with polyvinyl alcohol chains has interfacial thermal conductance increases by 17.1% by two factors. First, the hydrogen bonding between vinyl alcohol molecules facilitates thermal transport along EVOH chains. Second, the hydrogen bonding between vinyl alcohol and PMMA assists thermal transport across the interface.

7.5 Conclusion

A hierarchical heat spreader of polymer monolayer is introduced to tune interfacial thermal conductance between graphene and the PMMA polymer matrix. Thermal properties and morphology of molecules at the interface are studied by molecular dynamics simulations. Compared with pristine monolayer graphene, functionalized graphene shows drastically enhanced (5.2 times) interfacial thermal conductance by grafting 32 polyvinyl alcohol (PVA). The addition of only a few PVA chains can result in the same improvements caused by much denser hydroxyl groups. The hydrogen-bonded interface features insignificant temperature drop and a smooth temperature field across the interface. There are three factors contributing to the significantly enhanced interfacial thermal conduction. First, both the extended conformation and interchain hydrogen bonding improve the along-chain conductivity of PVA. The denser PVA monolayer is semi-crystalline due to interchain steric repulsion and hydrogen bonding. Even the sparse PVA monolayer shows the stand-up configuration due to the hydrogen bonds formed with PMMA. Second, PVA has better vibrational overlap with PMMA than graphene. Both the high overlap and the hydrogen bonding between PMMA and PVA improve heat transfer across the interface. Third, the covalent bonding between graphene and PVA chains enables efficient thermal transport. All these three factors constitute an efficient thermal transport path: graphene → PVA → PMMA.

Additionally, interfacial thermal conductance is found to not fully correlated with interfacial adhesion, which diverges away from some of the previous reports. When the number of grafted PVA chains is below 16, interfacial thermal conductance increases with the work of adhesion needed to pull functionalized graphene out from the matrix. However, as the number of PVA chains further increases from 16 to 32, interfacial adhesion drastically decreases while interfacial thermal conductance keeps increasing. In other words, it is not universal that interfacial thermal conductance increases with interfacial adhesion. Finally, the role of hydrogen bonding is further demonstrated by varying the proportion of vinyl alcohol repeat units in the EVOH-functionalized graphene/PMMA interface. Interfacial thermal conductance increases with the amount of vinyl alcohol units as well as the density of hydrogen bonds. Interfacial thermal conductance of graphene grafted with PVA chains is 17.1% higher than that of graphene grafted with polyethylene chains of the same number and the same length. In addition to improving interfacial thermal conductance, the hierarchically hydrogen-bonded molecular interface may also improve dispersion of graphene which is critical to the overall properties of composites. The concept opens a new avenue to tune interfacial thermal transport in polymer composites and biomaterials towards a variety of applications.

7.6 Acknowledgments

This work is financially supported by Utah State University. Lin Zhang acknowledges the Dissertation Fellowship and the Graduate Research and Creative Opportunity Grant from Utah State University.

REFERENCES

1. S. Stankovich, D. A. Dikin, G. H. B. Dommett, K. M. Kohlhaas, E. J. Zimney, E. A. Stach, R. D. Piner, S. T. Nguyen and R. S. Ruoff, *Nature*, 2006, **442**, 282-286.

2. N. Zhao, M. Yang, Q. Zhao, W. Gao, T. Xie and H. Bai, *Acs Nano*, 2017, **11**, 4777-4784.

3. D. Ding, D. Wang, M. Zhao, J. Lv, H. Jiang, C. Lu and Z. Tang, *Adv. Mater.*, 2017, **29**, 1603444-n/a.

4. M. Hu and D. Poulikakos, *Nano Lett.*, 2012, **12**, 5487-5494.

5. J. O. Tenorio-Pearl, E. D. Herbschleb, S. Fleming, C. Creatore, S. Oda, W. I. Milne and A. W. Chin, *Nat. Mater.*, 2017, **16**, 208-213.

6. Y. Wang, Z. Qin, M. J. Buehler and Z. Xu, *Nat. Commun.*, 2016, **7**, 12854.

7. R. Kempaiah, A. Chung and V. Maheshwari, *Acs Nano*, 2011, **5**, 6025-6031.

8. A. E. Nel, L. Madler, D. Velegol, T. Xia, E. M. V. Hoek, P. Somasundaran, F. Klaessig, V. Castranova and M. Thompson, *Nat. Mater.*, 2009, **8**, 543-557.

9. D. G. Cahill, P. V. Braun, G. Chen, D. R. Clarke, S. H. Fan, K. E. Goodson, P. Keblinski, W. P. King, G. D. Mahan, A. Majumdar, H. J. Maris, S. R. Phillpot, E. Pop and L. Shi, *Appl. Phys. Rev.*, 2014, **1**, 011305.

10. L. Hu, T. Desai and P. Keblinski, *Phys. Rev. B*, 2011, **83** ,195423.

11. Y. Liu, J. Huang, B. Yang, B. G. Sumpter and R. Qiao, *Carbon*, 2014, **75**, 169-177.

12. T. Luo and J. R. Lloyd, *Adv. Funct. Mater.*, 2012, **22**, 2495-2502.

13. M. Hu, P. Keblinski and P. K. Schelling, *Phys. Rev. B*, 2009, **79**, 104305.

14. R. J. Stevens, L. V. Zhigilei and P. M. Norris, *Int. J. Heat Mass Transfer*, 2007, **50**, 3977-3989.

15. S. C. Lin and M. J. Buehler, *Nanotechnology*, 2013, **24**, 165702.

16. Y. Wang, C. H. Yang, Y. W. Mai and Y. Y. Zhang, *Carbon*, 2016, **102**, 311-318.

17. M. Hu, J. V. Goicochea, B. Michel and D. Poulikakos, *Nano Lett.*, 2010, **10**, 279-285.

18. B. Liu, J. A. Baimova, C. D. Reddy, A. W. K. Law, S. V. Dmitriev, H. Wu and K. Zhou, *ACS Appl. Mater. Interfaces*, 2014, **6**, 18180-18188.

19. Y. Hong, J. C. Zhang and X. C. Zeng, *Nanoscale*, 2016, **8**, 19211-19218.

20. Y. Wang, C. Yang, Q.-X. Pei and Y. Zhang, *ACS Appl. Mater. Interfaces*, 2016, **8**, 8272-8279.

21. Y. Wang, H. F. Zhan, Y. Xiang, C. Yang, C. M. Wang and Y. Y. Zhang, *J. Phys. Chem. C*, 2015, **119**, 12731-12738.

22. L. Zhang, Z. Bai and L. Liu, *Adv. Mater. Interfaces*, 2016, **3**, 1600211.

23. T. Zhang, A. R. Gans-Forrest, E. Lee, X. Q. Zhang, C. Qu, Y. S. Pang, F. Sun and T. F. Luo, *ACS Appl. Mater. Interfaces*, 2016, **8**, 33326-33334.

24. P. J. O'Brien, S. Shenogin, J. X. Liu, P. K. Chow, D. Laurencin, P. H. Mutin, M. Yamaguchi, P. Keblinski and G. Ramanath, *Nat. Mater.*, 2013, **12**, 118-122.

25. S. Kaur, N. Raravikar, B. A. Helms, R. Prasher and D. F. Ogletree, *Nat. Commun.*, 2014, **5**, 3082.

26. T. Jiang, X. Zhang, S. Vishwanath, X. Mu, V. Kanzyuba, D. A. Sokolov, S. Ptasinska, D. B. Go, H. G. Xing and T. Luo, *Nanoscale*, 2016, **8**, 10993-11001.

27. S. Majumdar, J. A. Sierra-Suarez, S. N. Schiffres, W. L. Ong, C. F. Higgs, A. J. H. McGaughey and J. A. Malen, *Nano Lett.*, 2015, **15**, 2985-2991.

28. M. Fang, K. Wang, H. Lu, Y. Yang and S. Nutt, *J. Mater. Chem.*, 2009, **19**, 7098-7105.

29. M. Fang, K. Wang, H. Lu, Y. Yang and S. Nutt, *J. Mater. Chem.*, 2010, **20**, 1982-1992.

30. M. Steenackers, A. M. Gigler, N. Zhang, F. Deubel, M. Seifert, L. H. Hess, C. H. Y. X. Lim, K. P. Loh, J. A. Garrido and R. Jordan, *J. Am. Chem. Soc.*, 2011, **133**, 10490-10498.

31. H. Kim, S. Kobayashi, M. A. AbdurRahim, M. J. Zhang, A. Khusainova, M. A. Hillmyer, A. A. Abdala and C. W. Macosko, *Polymer*, 2011, **52**, 1837-1846.

32. H. J. Salavagione, *J. Mater. Chem. A*, 2014, **2**, 7138-7146.

33. Z. Liu, J. T. Robinson, X. Sun and H. Dai, *J. Am. Chem. Soc.*, 2008, **130**, 10876-10877.

34. H. J. Salavagione, M. A. Gomez and G. Martínez, *Macromolecules*, 2009, **42**, 6331-6334.

35. Y. Yang, W. Rigdon, X. Huang and X. Li, 2013, **3**, 2086.

36. X. Zhou, T. Wu, K. Ding, B. Hu, M. Hou and B. Han, *Chem. Commun.*, 2010, **46**, 386-388.

37. D. Wang, Y. Bao, J.-W. Zha, J. Zhao, Z.-M. Dang and G.-H. Hu, *ACS Appl. Mater. Interfaces*, 2012, **4**, 6273-6279.

38. K. Binder, *Monte Carlo and Molecular Dynamics Simulations in Polymer Science*, Oxford University Press, New York and Oxford, 1995.

39. W. Humphrey, A. Dalke and K. Schulten, *J. Mol. Graphics*, 1996, **14**, 33-38.

40. W. L. Jorgensen, D. S. Maxwell and J. Tirado-Rives, *J. Am. Chem. Soc.*, 1996, **118**, 11225-11236.

41. M. L. P. Price, D. Ostrovsky and W. L. Jorgensen, *J Comput Chem*, 2001, **22**, 1340-1352.

42. P. Lazar, F. Karlicky, P. Jurecka, M. Kocman, E. Otyepkova, K. Safarova and M. Otyepka, *J. Am. Chem. Soc.*, 2013, **135**, 6372-6377.

43. L. J. Fetters, D. J. Lohse, D. Richter, T. A. Witten and A. Zirkel, *Macromolecules*, 1994, **27**, 4639-4647.

44. S. Plimpton, *J. Comput. Phys.*, 1995, **117**, 1-19.

45. F. MullerPlathe, *J. Chem. Phys.*, 1997, **106**, 6082-6085.

46. C. Nieto-Draghi and J. B. Avalos, *Mol. Phys.*, 2003, **101**, 2303-2307.

47. T. Schneider and E. Stoll, *Phys. Rev. B*, 1978, **17**, 1302-1322.

48. M. Assael, K. Antoniadis and J. Wu, *Int. J. Thermophys.*, 2008, **29**, 1257-1266.

49. T. Zhang and T. Luo, *J. Phys. Chem. B*, 2016, **120**, 803-812.

50. S. Shen, A. Henry, J. Tong, R. Zheng and G. Chen, *Nat Nano*, 2010, **5**, 251-255.

51. A. Henry and G. Chen, *Phys. Rev. Lett.*, 2008, **101**, 235502.

52. F. Schreiber, A. Eberhardt, T. Y. B. Leung, P. Schwartz, S. M. Wetterer, D. J. Lavrich, L. Berman, P. Fenter, P. Eisenberger and G. Scoles, *Phys. Rev. B*, 1998, **57**, 12476-12481.

53. G. Poirier and E. Pylant, *SCIENCE-NEW YORK THEN WASHINGTON-*, 1996, 1145-1147.

54. G. A. Miño-Galaz and G. Gutierrez, *Chem. Phys. Lett.*, 2015, **635**, 16-22.

55. G. Mino, R. Barriga and G. Gutierrez, *J. Phys. Chem. B*, 2014, **118**, 10025-10034.

56. L. Zhang, M. Ruesch, X. Zhang, Z. Bai and L. Liu, *RSC Adv.*, 2015, **5**, 87981-87986.

57. L. Zhang, T. Chen, H. Ban and L. Liu, *Nanoscale*, 2014, **6**, 7786-7791.

58. L. Zhang, Z. Bai, H. Ban and L. Liu, *Phys. Chem. Chem. Phys.*, 2015, **17**, 29007-29013.

59. P. H. Hermans, J. J. Hermans, D. Vermaas and A. Weidinger, *J. Polym. Sci.*, 1948, **3**, 1-9.

60. B. W. Li, J. H. Lan and L. Wang, *Phys. Rev. Lett.*, 2005, **95**, 104302.

61. Y. Wang, H. F. Zhan, Y. Xiang, C. Yang, C. M. Wang and Y. Y. Zhang, *The Journal of Physical Chemistry C*, 2015, **119**, 12731-12738.

62. Y. Wang and P. Keblinski, *Appl. Phys. Lett.*, 2011, **99**, 073112.

63. N. Shenogina, R. Godawat, P. Keblinski and S. Garde, *Phys. Rev. Lett.*, 2009, **102**, 156101.

64. Z. Ge, D. G. Cahill and P. V. Braun, *Phys. Rev. Lett.*, 2006, **96**, 186101.

65. B. Ramos-Alvarado, S. Kumar and G. P. Peterson, *J. Phys. Chem. Lett.*, 2016, **7**, 3497-3501.

CHAPTER 8

CONCLUSIONS AND FUTURE WORK

The objective of this work is to explore how hydrogen bonding affects nanoscale thermal transport at interfaces of bundled nanostructures and interfaces between dissimilar materials. To this end, three representative materials systems were investigated, including nanocrystals of silk proteins, nanocrystalline polymer fibers, and functionalized graphene/polymer nanocomposites. In the first two cases, heat conducts along polymer chains, which is parallel to the interface between neighboring chains. In nanocomposites, heat flow is perpendicular to material interfaces. In all cases, hydrogen bonds are found to significantly facilitate nanoscale thermal transport.

In bundled nanostructures of the beta strands and polymer chains, hydrogen bonds form between the constituting units of the materials. Along-chain thermal conductivities increase with the number of individual beta strands and polymer chains before plateaus are reached, which are several times higher than those of single components. By a thermal resistance model, we find that interior beta strands have higher thermal conductivities than the edge strands due to the larger number of hydrogen bonds formed between interior strands. When beta strands are composed of the same type of amino acids, the thermal conductance of each strand is comparable. The poly-G beta sheet shows the highest thermal conductivity due to the smaller cross-sectional area and small side groups. By comparison, thermal conductivity of the poly-GA beta sheet is much lower due to the alternating amino acids along the chains and resulting phonon scattering. The density effect of hydrogen bonds is investigated by varying the number of CH_2 in the repeating units of nylon. Thermal conductivity increases with the density of hydrogen bonds. In addition, MD results indicate that hydrogen bonds restrict the torsion of polymer chains and increase the stiffness of the polymer nanofiber. As a result, group velocities of longitudinal and transverse acoustic phonons are enhanced significantly, which enables fast transport of heat carriers. All these results demonstrate the possibility of improving thermal transport by designing hydrogen bonds.

We investigated the effect of hydrogen bonds on thermal transport at the interface between mechanically dissimilar materials in nanocomposites. Hydroxyl groups are introduced to the surfaces of graphene to form hydrogen bonds with the PMMA matrix. Interfacial thermal conductance is enhanced by 218% compared with that between pristine graphene and PMMA, and 68% larger than that between CH_3 functionalize graphene and PMMA. The enhancement originates from three factors. First, strong hydrogen bonds pull PMMA molecules closer to the graphene surfaces, which enhances interfacial association. Second, hydroxyl groups have better vibrational coupling with PMMA at low frequencies. Last but not least, hydrogen bonding provides a heat transfer channel which is much more efficient than that between graphene and the polymer matrix. All the results suggest that hydrogen bonded interface can have much improved interfacial thermal conduction than their non-hydrogen-bonded counterparts.

Interfacial thermal conduction can also be improved by introducing linker materials which feature long molecular chains. For instance, grafting graphene with 7.14% polyethylene chains improves the interfacial thermal conductance by 431.3% between graphene and PMMA, mainly due to four reasons. First, PE chains are covalently grafted on graphene, which assists heat transport from graphene to PE. Second, when grafting density is high, polyethylene chains feature extended conformation and have thermal conductivity 456% higher than that of the bulk PMMA. Third, vibration coupling between PE and PMMA is much larger than that between graphene and PMMA. Furthermore, alignment of PE chains results in a larger contact area with the embedded PMMA matrix and higher work of adhesion.

Based on these understanding, a hierarchical heat spreader is proposed to further enhance interfacial thermal transport between organic and inorganic materials. Instead of PE, polyvinyl alcohol (PVA) chains are grafted onto graphene to improve interfacial thermal conduction. Different from PE chains, PVA chains are extended on graphene even at a low coverage density. When the coverage density is high, hydrogen bonds form not only between PVA and PMMA but also between PVA chains. With the same length of 32 polymer chains, PVA-grafted graphene with PMMA show an interfacial thermal conductivity 17.1% larger than that between PE-grafted graphene with PMMA. In addition to enhancing interfacial thermal transport, hydrogen bonds may also improve the dispersion of graphene fillers. A word of caution is that interfacial thermal conductance does not always have a linear correlation with the interfacial adhesion.

Despite the significant progress, there are still plenty of topics to be studied in the future for a more comprehensive understanding. Several of them are listed as follows: effect of hydrogen bond strength on thermal transport along polymer chains; role of hydrogen bonds when heat flow is perpendicular to the interfaces in bundled nanostructures; effect of hydrogen bonds on thermal transport when heat is parallel to the interfaces between dissimilar materials; and effect of hydrogen bonds when the filler materials are randomly oriented in polymer nanocomposites. Insights from all these studies may guide the engineering of advanced hydrogen-bonded materials for desired thermal properties.

APPENDICES

APPENDIX A

SUPPLEMENTAL MATERIAL OF CHAPTER 2

A.1 Structure

This study is focused on poly-A β-sheet because according to experiment, the β-sheet is an important component of *N. Clavipes* spider silk [Figure A.1(a)]. The atomistic structure of poly-A β-sheet was build based on previous work that simulates the mechanical response of poly-A β-sheets [1]. Our β-sheet models were verified by visualization with the Visual Molecular Dynamics (VMD) package [2]. A snapshot from VMD [Figure A.1(b)] shows that hydrogen bonds (red lines) are spontaneously formed in the equilibrated β-sheet structure.

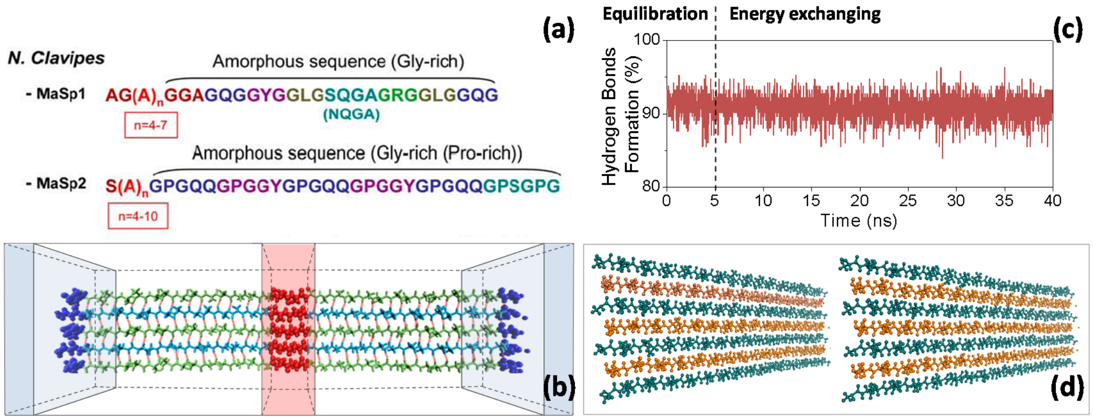
(a)
N. Clavipes
Amorphous sequence (Gly-rich)
- MaSp1
AG(A)nGGAGQGGYGGLGSQGAGRGGLGGQG
(NQGA)
n=4-7
Amorphous sequence (Gly-rich (Pro-rich))
- MaSp2
S(A)nGPGQQGPGGYGPGQQGPGGYGPGQQGPSGPG
n=4-10
(b)
Equilibration
Energy exchanging
(c)
Hydrogen Bonds Formation (%)
100
90
80
0
5
10
15
20
25
30
35
40
Time (ns)
(d)

Figure A.1. **(a)** The protein sequence of MaSp1 and MaSp2 *N. Clavipes* spider silk [3]. **(b)** A snapshot of the simulation model from VMD. **(c)** Percentage of hydrogen bond formation versus simulation time. **(d)** Structural comparison for a β-sheet before and after energy exchange.

To demonstrate the stability of hydrogen bonds in our models, Figure A.1(c) plots the percentage of hydrogen bond formation versus simulation time. The rate of hydrogen bond formation is calculated by taking a ratio between the number of hydrogen bonds at any time instant and the number of hydrogen bonds that could be formed in the ideal condition. Results show that the percentage of hydrogen bond formation remains ~91% during the equilibration and the energy exchange procedures. VMD snapshots in Figure A.1(d) denote that the structure does not change much in energy exchange. The insensitivity of protein structure to energy exchange is due to the very careful procedure we followed when performing the research. The frequency of energy exchange was fine-tuned for all jobs such that the temperature difference between the two ends of the protein is about 30±2 K. The temperature difference is small enough to avoid protein denaturation at high temperatures [4]. It is also large enough to overcome thermal perturbation such that smooth temperature profiles could be obtained.

We note that molecular dynamics simulation does not require the identification of hydrogen bonds. However, we need to identify hydrogen bonds in the visualization and analysis processes, e.g. Figure A.1(b,c). Although there are several different geometric definitions of hydrogen bonds available [5, 6], we employed a widely adopted criterion [7] wherein the distance between the donor (D) and the acceptor (A) is less than 3.5 Angstrom, and the angle of ADH is less than 30 degree (H represents the hydrogen atom). Using different criteria could give slightly different numbers of hydrogen bonds. However, this would not affect any simulation result because molecular dynamics simulation does not involve the identification of hydrogen bonds. This would not significantly affect visualization and analysis [e.g. Figure A.1(b,c)] either because the physics is not changed.

A.2 Determination of Unit Cell Size

Stress state plays a key role in thermal transport [8-10]. In the present work, we attempted to make the model under a free stress state. We also attempted to make it not floppy in the length direction so that there was no transverse expansion and oscillation. The model generated this way enabled us to focus on the intrinsic effects of hydrogen bonding on thermal transport.

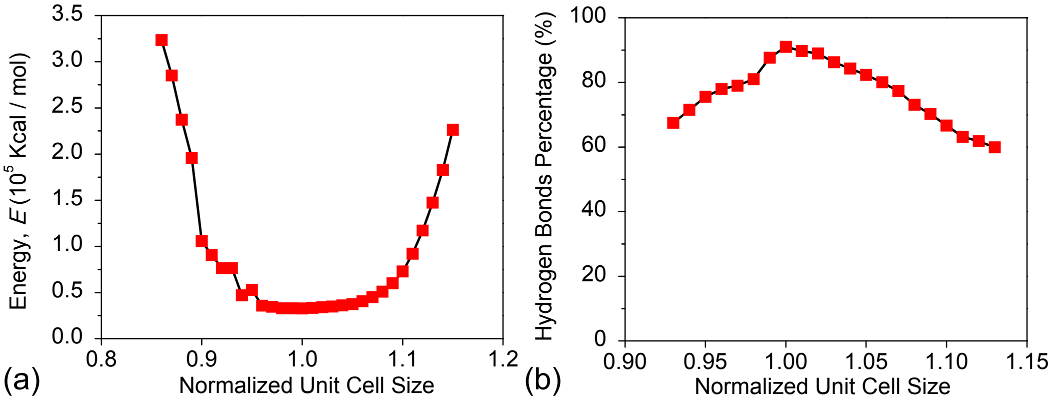

Figure A.2. Variations of (a) system potential energy and (b) number of hydrogen bonds with respect to unit cell size along the length direction. The horizontal axes are normalized by the currently adopted unit cell size, 0.396 nm per residue. When the normalized unit cell size is larger than 1, the β-strands are stressed under tension. When the normalized unit cell size is smaller than 1, the β-strands are sloppy leading to transverse expansion.

The desired model was generated by choosing an appropriate unit cell size in the length direction. Theoretically, when the unit cell size is too small, the transverse expansion would happen. This will (1) break some of the hydrogen bonds, and (2) increase potential energy due to forced bending of the β-sheet. Similarly, when the unit cell size is too large, the β-sheet would be stressed, increasing potential energy and breaking some of the hydrogen bonds.

Therefore, at the "appropriate" unit cell size, system potential energy should minimize, and the number of hydrogen bonds should maximize. Figure A.2 shows the variations of potential energy and the number of hydrogen bond as functions of the unit cell size along the length direction. To be clear, the unit cell size is normalized by the size adopted for this research, 0.396 nm per residue. It is shown that potential energy minimizes and the number of hydrogen bond maximizes at the chosen unit cell size. This demonstrates that the structures adopted in this research are free from significant stress and transverse expansion. This is also evidenced by the snapshots shown in Figure A.1(b,d) where no transverse expansion is observed.

A.3 Determination of Area

Thermal conductivity calculation involves a critical parameter – area. The determination of the area (or thickness) of low-dimensional materials (e.g. graphene and carbon nanotube) has been an active research topic for several years. Many previous papers studying the thermal properties of graphene have used the thickness of 0.335 nm [11, 12]. This represents a common approach to obtain the thickness of graphene − consider graphene as a uniform slab in graphite and adopt the interlayer spacing in graphite as the thickness of graphene. There are also several other ways to determine the graphene thickness, but most of them give consistent results [13].

For β-strands, we adopted an approach similar to that commonly used for graphene. First, a block of β-strands (Figure A.3b) was generated and equilibrated for 20 ns. Snapshots were generated every 10ps during the last 10 ns simulation. Each snapshot gave a "lattice" formed by the interior 25 β-strands (Figure A.3c). Lattice parameters were then averaged to achieve the area associated with each β-strand. Averaging over the 1000 snapshots led to a value of 0.236 nm^2, which was used in all the thermal conductivity calculations presented in this work.

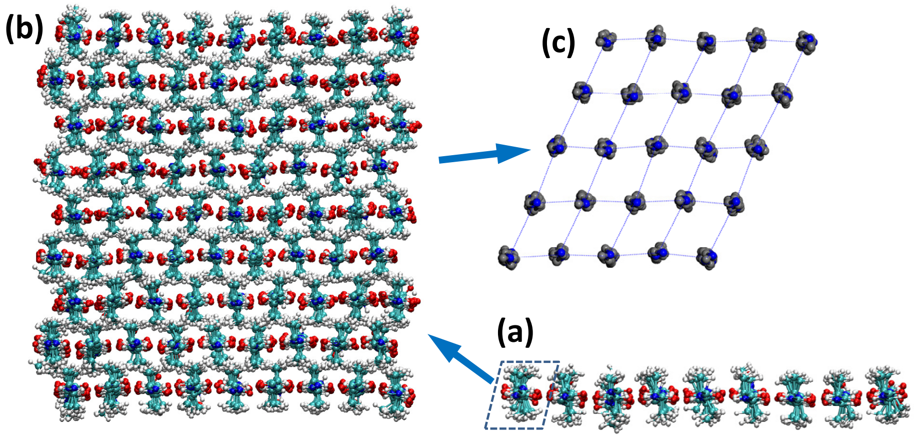

Figure A.3. Determination of the area associated with each β-strand: (a) a β-sheet consisting of 9 β-strands; (b) a block of β-strands (9 layers of 9-strand β-sheets, totaling 81 β-strands); (c) The "lattice" formed by the interior 5x5 β-strands. The area associated with each β-strand is an average over the 25 β-strands during a 10 ns simulation.

A.4 Representative Temperature Profile and Determination of d*T*/d*x*

Thermal conductivity calculation also involves another critical parameter, i.e. d*T*/d*x*, which should be determined by molecular simulations under the Muller-Plathe framework. Figure A.4 shows the variation of temperature along the length direction of an A16-7-1 β-sheet. The β-sheet was divided into 16 slabs for evaluating temperature. The curve is nonlinear. Previous applications of the Muller-Plathe method [14-19] suggested using the relatively linear region in the curve to evaluate d*T*/d*x*. In this work, only the temperatures for slabs 5~13 were used to fit d*T*/d*x*.

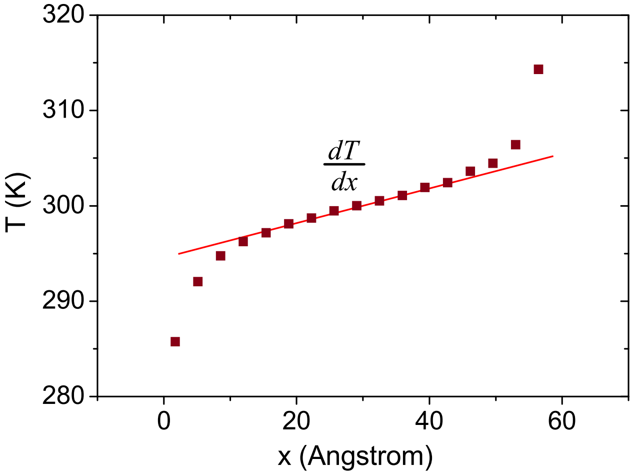

Figure A.4. Determination of d*T*/d*x*. The temperature profile is along the length direction.

A.5 Phonon Density of States (DOS) and Partial DOS Profiles for Representative β-Sheet Structures

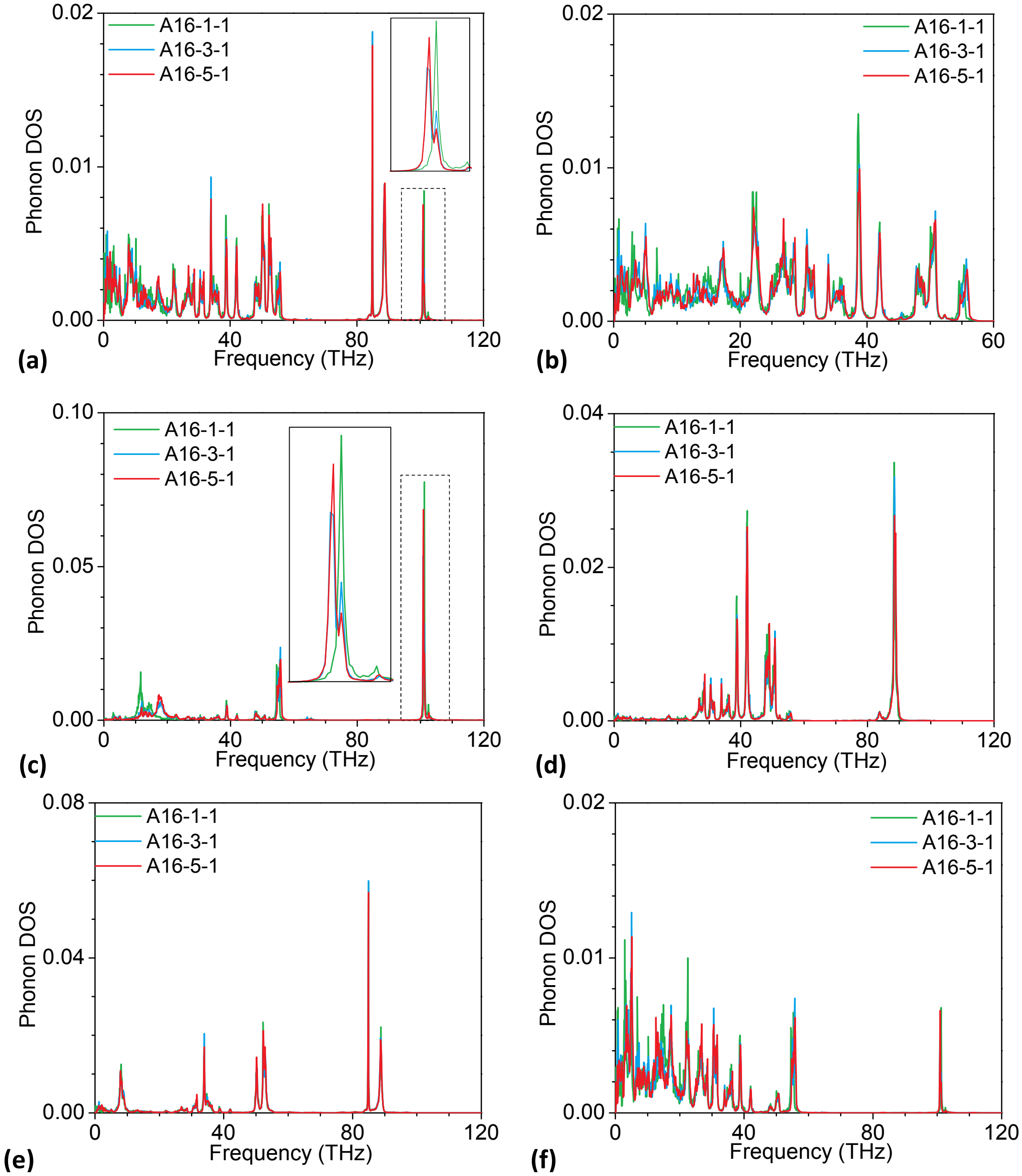

Figure A.5. (a) Phonon DOS profiles of three antiparallel β-sheet structures (A16-1-1, A16-3-1, and A16-5-1). Partial phonon DOS projected on (b) backbone atoms, (c) H atoms (hydrogen atoms bonded to nitrogen atoms), (d) HA atoms (hydrogen atoms bonded to α-carbon atoms), (e) HB atoms (hydrogen atoms of methyl groups), and (f) nitrogen atoms (denoted by N). (a) and (b) show that phonon spectra of A16-3-1 and A16-5-1 are close to each other but different from that of A16-1-1. The inset of (c) shows that frequency of phonons corresponding to the vibration of H atoms shifts from 101.2 to 100.8 THz due to hydrogen bonding. (d) and (e) demonstrate that primary phonon modes of HA and HB have the frequency of 88.6 and 84.8 THz, respectively. (f) shows a blue shift in the frequency of the phonon mode of N atoms in low-frequency regime, from A16-1-1 to A16-3-1 and A16-5-1.

REFERENCES

1. S. B. Xiao, W. Stacklies, M. Cetinkaya, B. Markert and F. Grater, *Biophys J*, 2009, **96**, 3997-4005.

2. W. Humphrey, A. Dalke and K. Schulten, *J. Mol. Graphics*, 1996, **14**, 33-38.

3. T. Lefèvre, M.-E. Rousseau and M. Pézolet, *Biophys J*, 2007, **92**, 2885-2895.

4. D. Paschek and A. E. Garcia, *Phys Rev Lett*, 2004, **93**, 238105.

5. T. Steiner, Angewandte Chemie International Edition, 2002, **41**, 48-76.

6. R. Taylor, O. Kennard and W. Versichel, *Acta Crystallogr. Sect. B-Struct. Commun.*, 1984, **40**, 280-288.

7. A. Luzar and D. Chandler, *Nature*, 1996, **379**, 55-57.

8. J. Zhang, X. He, L. Yang, G. Wu, J. Sha, C. Hou, C. Yin, A. Pan, Z. Li and Y. Liu, *Sensors*, 2013, **13**, 9388-9395.

9. W. Ning, X. Lanqing, W. Hui-Qiong and Z. Jin-Cheng, *Nanotechnology*, 2011, **22**, 105705.

10. K. Jung, M. Cho and M. Zhou, *Journal of Applied Physics*, 2012, **112**, 083522.

11. J. Hu, X. Ruan and Y. P. Chen, *Nano Letters*, 2009, **9**, 2730-2735.

12. Y. Ni, Y. Chalopin and S. Volz, *Applied Physics Letters*, 2013, **103**, 141905.

13. W. Philipp, V. I. Viktoria, J. R. Mark, R. B. Patrick and P. E. Christopher, *Journal of Physics: Condensed Matter*, 2013, **25**, 155302.

14. E. Lussetti, T. Terao and F. Müller-Plathe, *The Journal of Physical Chemistry B*, 2007, **111**, 11516-11523.

15. T. Terao, E. Lussetti and F. Müller-Plathe, *Physical Review E*, 2007, **75**, 057701.

16. E. Rossinsky and F. Müller-Plathe, *The Journal of Chemical Physics*, 2009, **130**, 134905.

17. E. A. Algaer, M. Alaghemandi, M. C. Böhm and F. Müller-Plathe, *The Journal of Physical Chemistry A*, 2009, **113**, 11487-11494.

18. N. Boris, W. Taku and R. P. Simon, *Journal of Physics: Condensed Matter*, 2009, **21**, 084219.

19. P. K. Schelling, S. R. Phillpot and P. Keblinski, *Physical Review B*, 2002, **65**, 144306.

APPENDIX B

SUPPLEMENTAL MATERIAL OF CHAPTER 3

B.1 Structure

The atomistic structures of the β-sheets were build based on previous work simulating the mechanical response of β-sheets [1]. Our models were verified by visualization with the Visual Molecular Dynamics (VMD) package [2]. A snapshot from VMD [Figure B.1(a)] shows that hydrogen bonds (red lines) are spontaneously formed in the equilibrated β-sheet structure.

To demonstrate the stability of hydrogen bonds in our models, Figure B.1(b) plots the percentage of hydrogen bond formation versus simulation time. The percentage of hydrogen bond formation was calculated by taking a ratio between the number of hydrogen bonds at any time instant and the number of hydrogen bonds that could be formed in the ideal condition. Results show that the percentage of hydrogen bond formation remains ~91% during the equilibration and velocity swapping procedures. VMD snapshots in Figure B.1(c) show that the structure does not change much in velocity swapping.

The insensitivity of protein structure to velocity swapping is due to the very careful procedure we followed when performing the simulations. The frequency of temperature swap was fine-tuned for all jobs such that the temperature difference between the two ends of the protein is about 30±2 K. The temperature difference is small enough to avoid protein denaturation at high temperatures [3]. It is also large enough to overcome thermal perturbation such that smooth temperature profiles could be obtained.

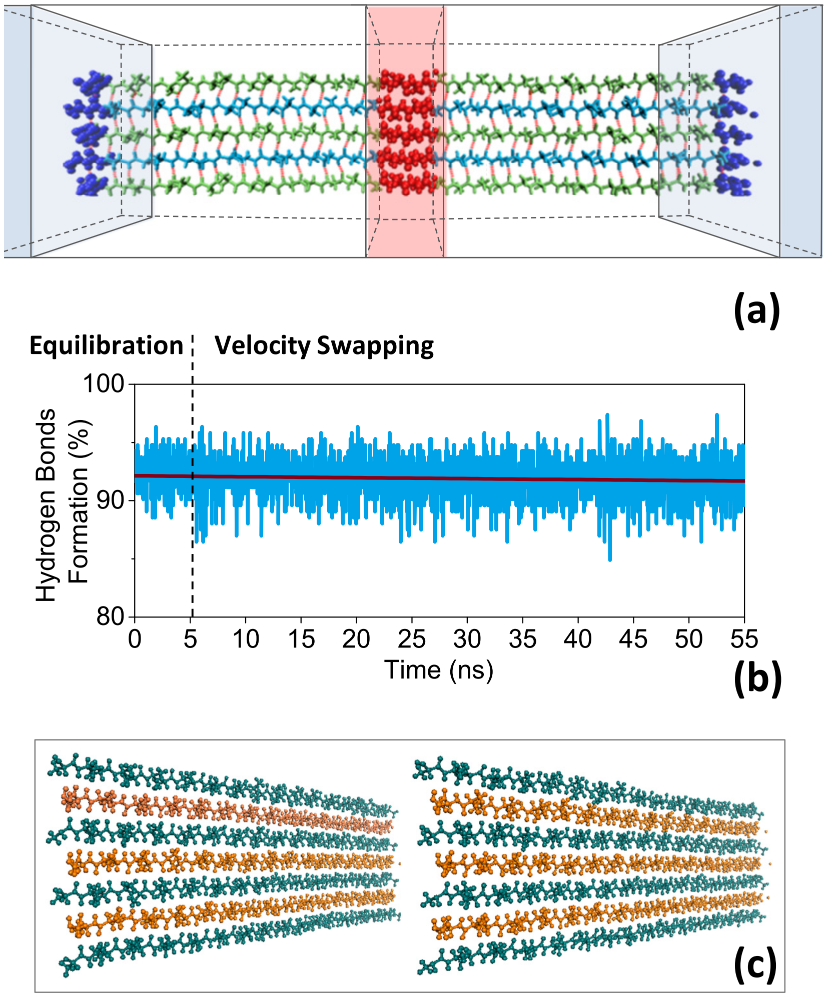

Figure B.1. (a) A snapshot of the simulation model from VMD. (b) Percentage of hydrogen bond formation versus simulation time. (c) Structural comparison for a β-sheet before and after velocity swapping.

B.2 Identification of Hydrogen Bonds

Molecular dynamics simulation does not require the identification of hydrogen bonds. However, we need to identify hydrogen bonds in the visualization and analysis processes, e.g. Figure B.1(a,b). Although there are several different geometric definitions of hydrogen bonds available [4, 5], we employed the default criteria in VMD [6]:

"A hydrogen bond is formed between an atom with a hydrogen bonded to it (the donor, D) and another atom (the acceptor, A) provided that the distance D-A is less than the cut-off distance (default 3.5 Angstroms) and the angle D-H-A is less than the cut-off angle (default 30 degrees)."

We note that, using different criteria could give slightly different numbers of hydrogen bonds. However, this would not affect any simulation result because molecular dynamics simulation does not involve the identification of hydrogen bonds. This would not significantly affect visualization and analysis [e.g. Figure B.1(a,b)] either because the physics is not changed.

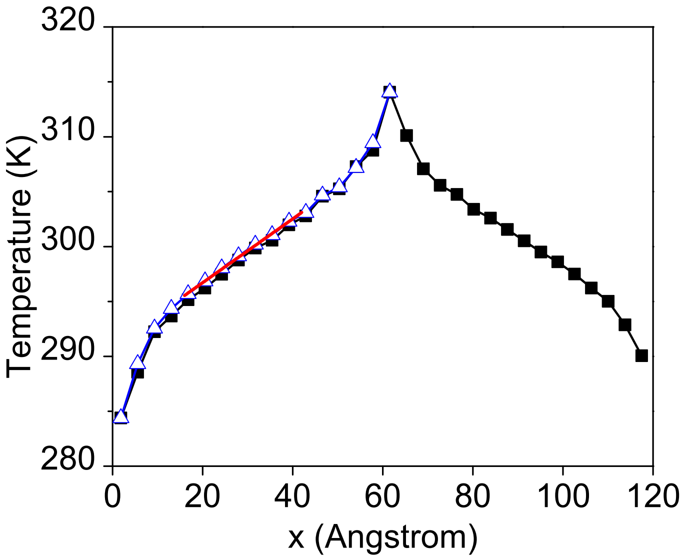

Figure B.2. Temperature profile along the length of a β-sheet

B.3 Calculation of Thermal Conductivity

To calculate thermal conductivity, we adopted the reverse non-equilibrium molecular dynamics method developed by Muller-Plathe [7, 8] which generates a heat flux by a velocity swapping algorithm. Each non-equilibrium molecular dynamics simulation led to a temperature profile similar to that shown in Figure B.2. The temperature profile is nonlinear due to the perturbation caused by the artificial velocity swapping. An average was taken between the temperature profiles to the left and right of the heat source. Line regression of the linear portion of the temperature profile was then calculated to obtain the temperature gradient. On the other hand, the induced heat flux was evaluated by $J = \Delta E / 2tA$, where t denotes the time interval between two swaps, ΔE is the averaged kinetic energy transferred per swap, A is the cross-sectional area of the material, and the coefficient “2” reflects the two symmetric heat transport paths from the hot slab to the cold slab. The value of A was calculated based on the chain-averaged cross-sectional area in the multilayer nanocrystals. Finally by Fourier’s law, thermal conductivity was calculated by $\kappa = -J / \frac{dT}{dx}$, where $\frac{dT}{dx}$ is the temperature gradient along the x-direction.

REFERENCES

1. S. B. Xiao, W. Stacklies, M. Cetinkaya, B. Markert and F. Grater, *Biophys J*, 2009, **96**, 3997-4005.

2. W. Humphrey, A. Dalke and K. Schulten, *J. Mol. Graphics*, 1996, **14**, 33-38.

3. D. Paschek and A. E. Garcia, *Phys Rev Lett*, 2004, **93**, 238105.

4. T. Steiner, Angewandte Chemie International Edition, 2002, **41**, 48-76.

5. R. Taylor, O. Kennard and W. Versichel, *Acta Crystallogr. Sect. B-Struct. Commun.*, 1984, **40**, 280-288.

6. M. Seifert, A. H. R. Koch, F. Deubel, T. Simmet, L. H. Hess, M. Stutzmann, R. Jordan, J. A. Garrido and I. D. Sharp, *Chem. Mater.*, 2013, **25**, 466-470.

7. F. Muller-Plathe, *J Chem Phys*, 1997, **106**, 6082-6085.

8. M. M. Zhang, E. Lussetti, L. E. S. de Souza and F. Muller-Plathe, *J Phys Chem B*, 2005, **109**, 15060-15067.

APPENDIX C

SUPPLEMENTAL MATERIAL OF CHAPTER 4

C.1 OPLSAA Force Field

We used OPLSAA force field[1, 2] to describe interatomic interactions for nylon nanocrystals. The total potential energy comprises non-bonded potential, bond stretching potential, angle bending potential, and torsional potential. Table C.1 provides the non-bonded Lennard-Jones 12-6 potential parameters and charges of all atom types in nylon. The inset of Table C.1 illustrates the atom types of nylon 4. The geometric mixing rule is used to evaluate the non-bonded parameters between different atom types, i.e. $\varepsilon_{ij} = (\varepsilon_{ii} * \varepsilon_{jj})^{0.5}$ and $\sigma_{ij} =(\sigma_{ii} * \sigma_{jj})^{0.5}$. Potential parameters for bond, angle, and dihedral are shown in Table C.2-4, respectively.

Table C.1. Non-bonded potential parameters for all atom types of nylon

Atom type	q (e$^-$)	ε (kcal· mol^{-1})	σ (Å)
C	0.500	0.105	3.750
CT	0.080	0.066	3.500
CT1	-0.120	0.066	3.500
H	0.300	0.000	0.000
HC	0.060	0.030	2.500
N	-0.500	0.170	3.250
O	-0.500	0.210	2.960

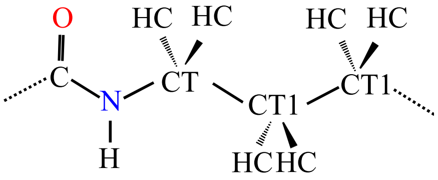

Table C.2. Bond stretching potential parameters for all bond types of nylon

Bond type	k (kcal · mol^{-1} · Å^{-2})	R_0 (Å^2)
C-CT1	317.00	1.522
C-N	490.00	1.335
C-O	570.00	1.229
CT-CT1	268.00	1.529
CT-HC	340.00	1.090
CT-N	337.00	1.449
CT1-CT1	268.00	1.529
CT1-HC	340.00	1.090
H-N	434.00	1.010

Table C.3. Angle bending potential parameters for all angle types of nylon

Angle type	k_θ (kcal· mol^{-1}·radian^{-2})	θ (degree)
C-CT1-CT1	63.00	111.10
C-CT1-HC	35.00	109.50
C-N-CT	50.00	121.90
C-N-H	35.00	119.80
CT-CT1-CT1	58.35	112.70
CT-CT1-HC	37.50	110.70
CT-N-H	38.00	118.40
CT1-C-N	70.00	116.60
CT1-C-O	80.00	120.40
CT1-CT-HC	37.50	110.70
CT1-CT-N	80.00	109.70
CT1-CT1-HC	37.50	110.70
HC-CT-HC	33.00	107.80
HC-CT-N	35.00	109.50
HC-CT1-HC	33.00	107.80
N-C-O	80.00	122.90

Table C.4. Torsional potential parameters for all dihedral types of nylon

Dihedral type	V_1 (kcal· mol^{-1})	V_2 (kcal· mol^{-1})	V_3 (kcal· mol^{-1})	V_4 (kcal· mol^{-1})
C-CT1-CT1-CT	-2.060	-0.313	0.315	0.000
C-CT1-CT1-HC	0.000	0.000	-0.100	0.000
CT-CT1-CT1-HC	0.000	0.000	0.300	0.000
CT1-C-N-CT	2.300	6.089	0.000	0.000
CT1-C-N-H	0.000	4.900	0.000	0.000
CT1-CT-N-C	0.000	0.462	0.000	0.000
CT1-CT-N-H	0.000	0.000	0.000	0.000
HC-CT-CT1-CT1	0.000	0.000	0.300	0.000
HC-CT-CT1-HC	0.000	0.000	0.300	0.000
HC-CT-N-C	0.000	0.000	0.000	0.000
HC-CT-N-H	0.000	0.000	0.000	0.000
HC-CT1-CT1-HC	0.000	0.000	0.300	0.000
N-C-CT1-CT1	1.173	0.189	-1.200	0.000
N-C-CT1-HC	0.000	0.000	0.000	0.000
N-CT-CT1-CT1	0.845	-0.962	0.713	0.000
N-CT-CT1-HC	0.000	0.000	0.464	0.000
O-C-CT1-CT1	0.000	0.000	0.000	0.000
O-C-CT1-HC	0.000	0.000	0.000	0.000
O-C-N-CT	0.000	6.089	0.000	0.000
O-C-N-H	0.000	4.900	0.000	0.000

C.2 Effects of Torsional Disorder on Thermal Conduction

We chose the single-chain nylon 4 and the 2×1 nanofiber as two examples to demonstrate the effects of torsional disorder on thermal conduction. The torsional disorder was controlled by adjusting the dihedral potential in the OPLSAA force field. In the case with full dihedral potential, the torsional motion of polymer segments is restricted leading to more ordered chain structures. When the dihedral potential is neglected, however, the structures are more disordered. Evidence can be found in Figure C.1(a), which shows less deviated dihedrals when the computation includes the dihedral potential. Figure C.1(b) further establishes the correlation between structural order and thermal conductivity. For both the single-chain and 2×1 nylon 4, thermal conductivity is found to be higher when the dihedral potential is considered (i.e. when the structure is more ordered). The most significant contribution of the present paper is to provide a feasible means to confine the torsional disorder by hydrogen bonds for improved thermal conductivities.

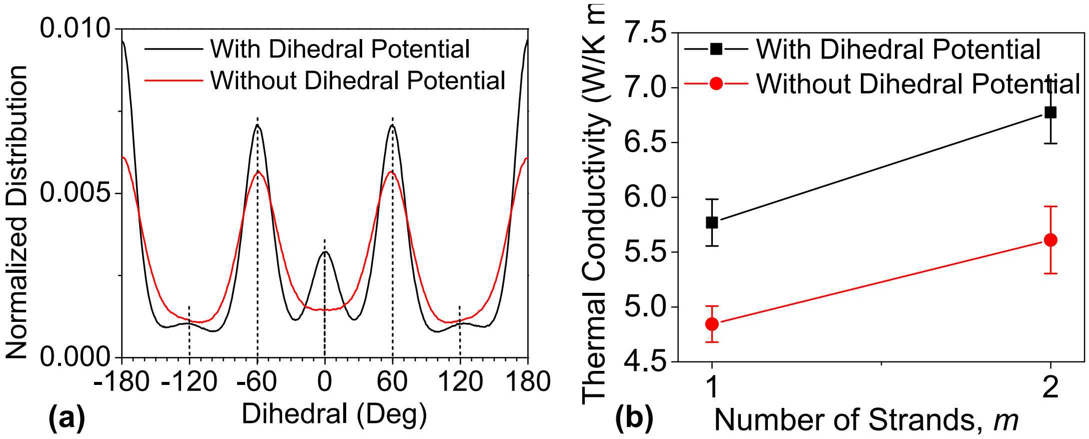

Figure C.1. (a) Dihedral distributions of nylon4-20-1-1 computed with and without considering the dihedral potential in the force field. (b) Thermal conductivities of nylon4-20-1-1 and nylon4-20-2-1 computed with and without the dihedral potential.

C.3 Normalized Distributions of 12 Types of Dihedrals in Nylon2-20-*m*-1

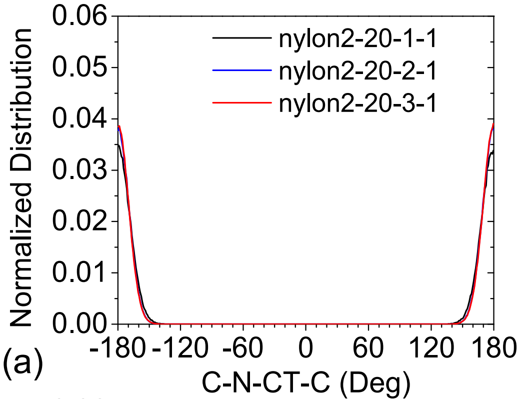

(a)

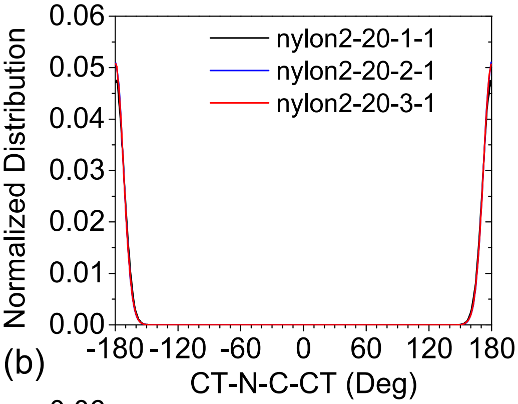

(b)

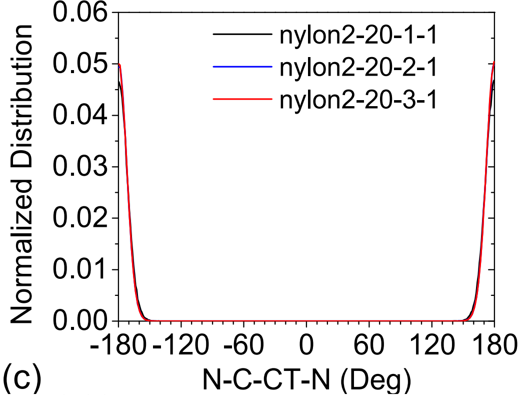

(c)

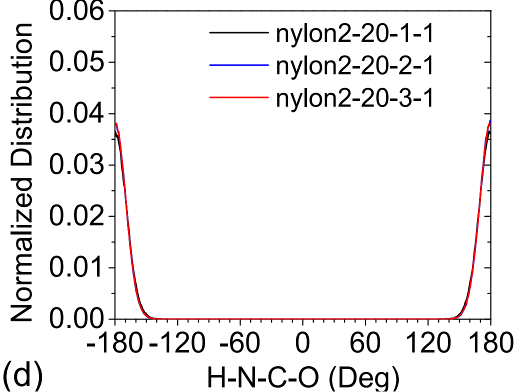

(d)

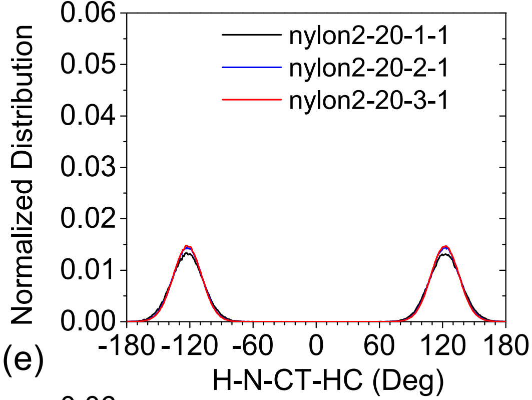

(e)

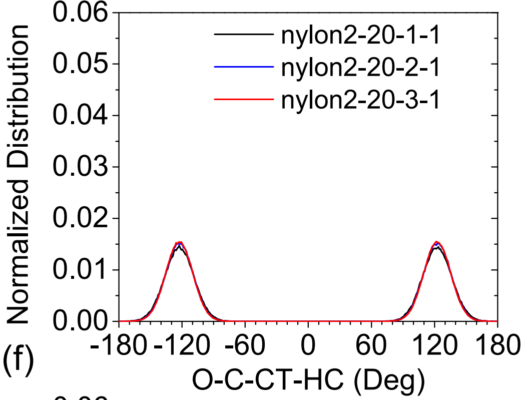

(f)

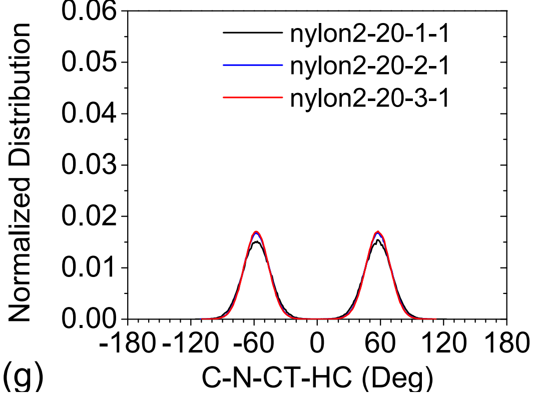

(g)

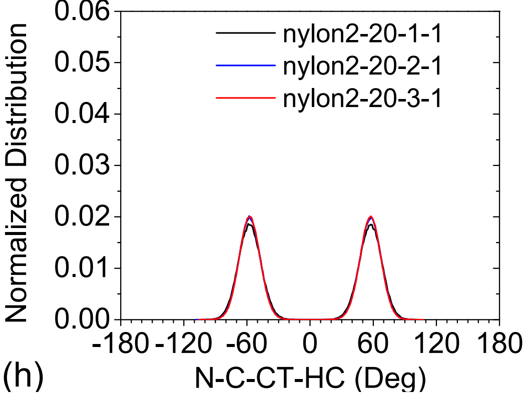

(h)

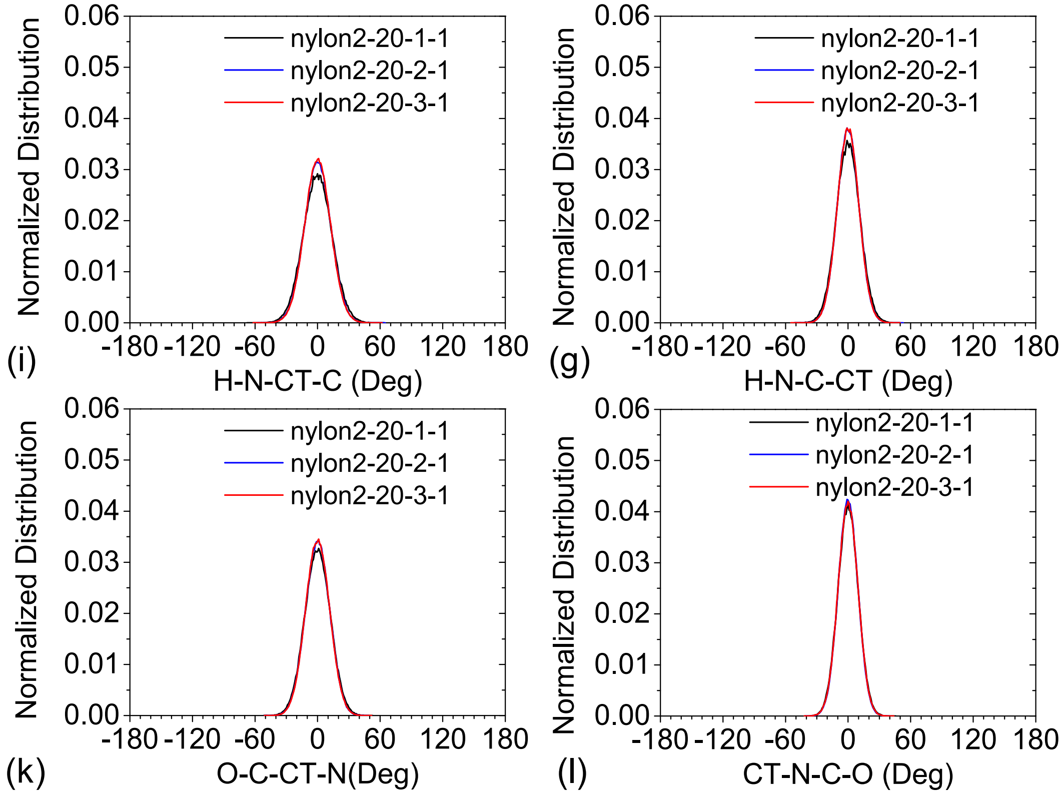

Figure C.2. Normalized distribution of dihedrals.

C.4 Time Histories of 12 Types of Dihedrals in Nylon2-20-*m*-1

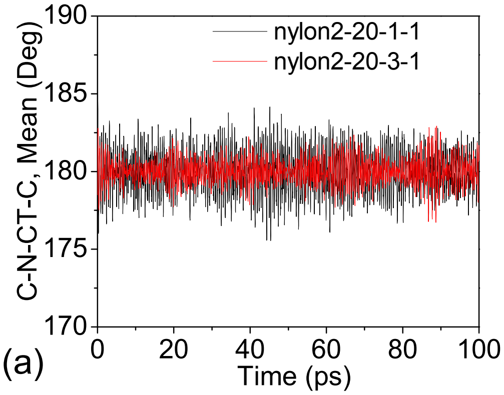

(a)

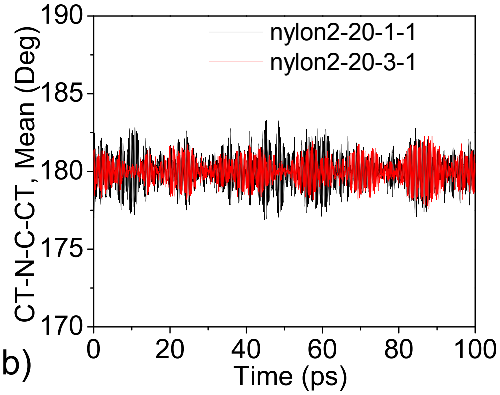

(b)

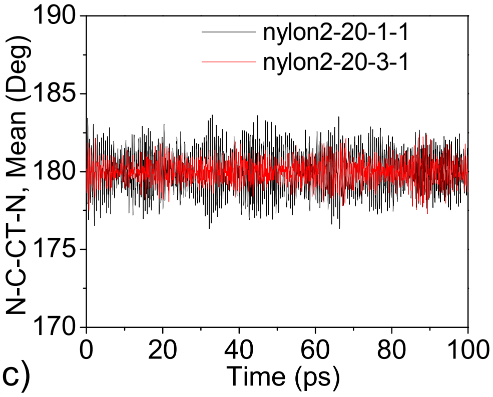

(c)

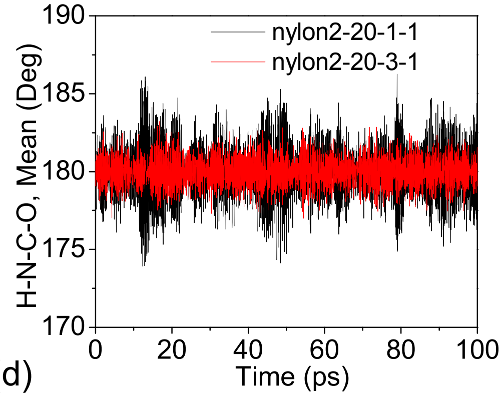

(d)

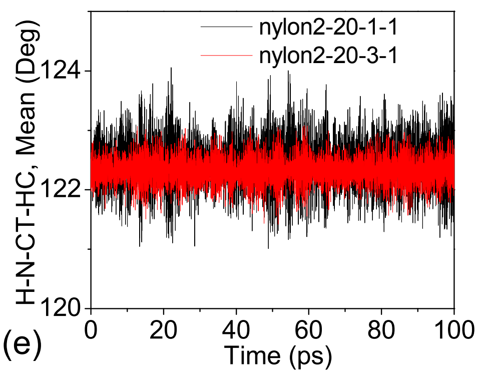

(e)

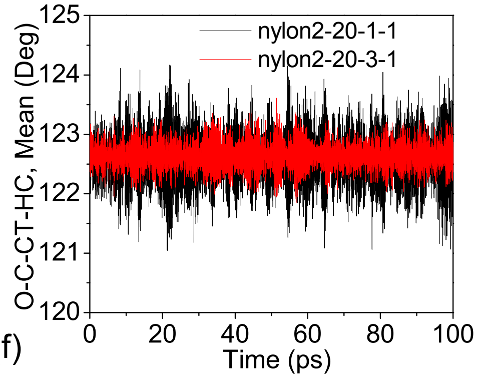

(f)

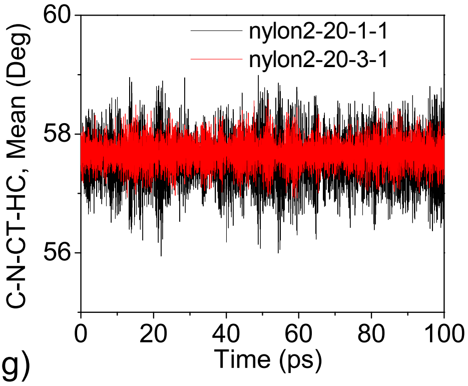

(g)

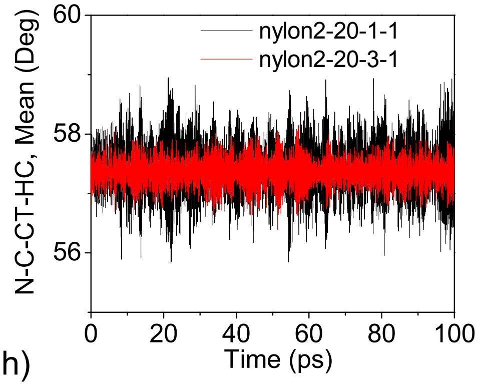

(h)

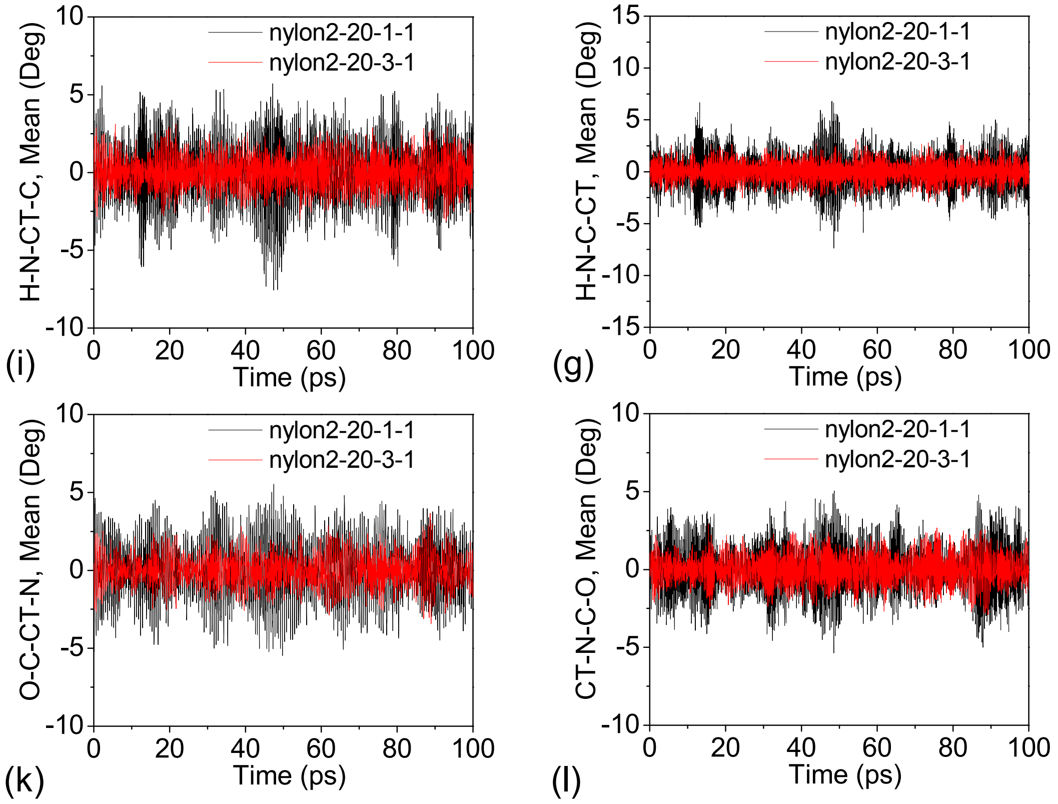

Figure C.3. Mean value of dihedral angles versus time.

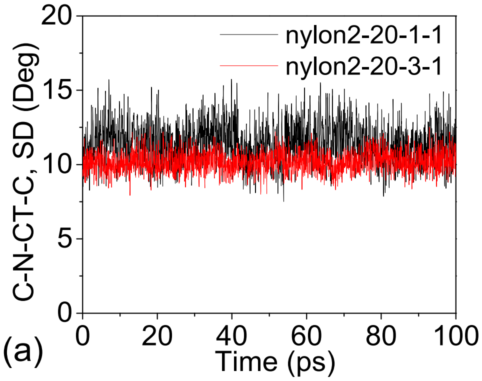
C-N-CT-C, SD (Deg)
0
5
10
15
20
0
20
40
60
80
100
Time (ps)
nylon2-20-1-1
nylon2-20-3-1

(a)

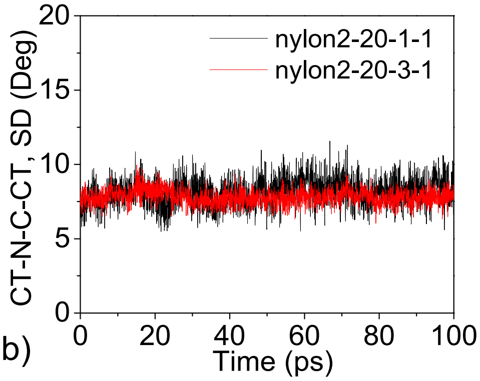
CT-N-C-CT, SD (Deg)
0
5
10
15
20
0
20
40
60
80
100
Time (ps)
nylon2-20-1-1
nylon2-20-3-1

(b)

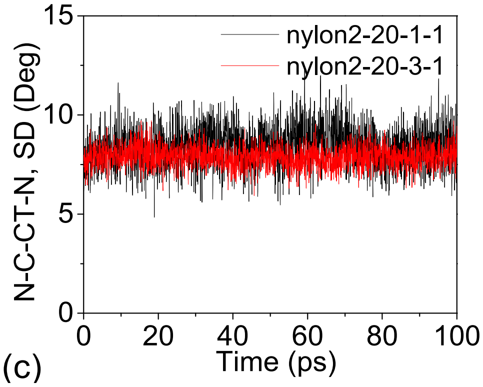
N-C-CT-N, SD (Deg)
0
5
10
15
0
20
40
60
80
100
Time (ps)
nylon2-20-1-1
nylon2-20-3-1

(c)

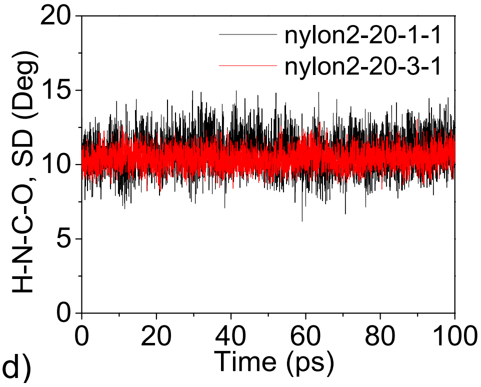
H-N-C-O, SD (Deg)
0
5
10
15
20
0
20
40
60
80
100
Time (ps)
nylon2-20-1-1
nylon2-20-3-1

(d)

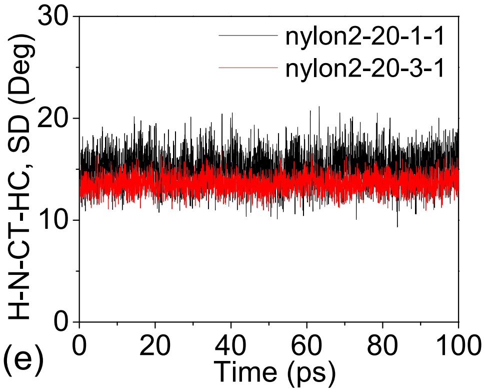
H-N-CT-HC, SD (Deg)
0
10
20
30
0
20
40
60
80
100
Time (ps)
nylon2-20-1-1
nylon2-20-3-1

(e)

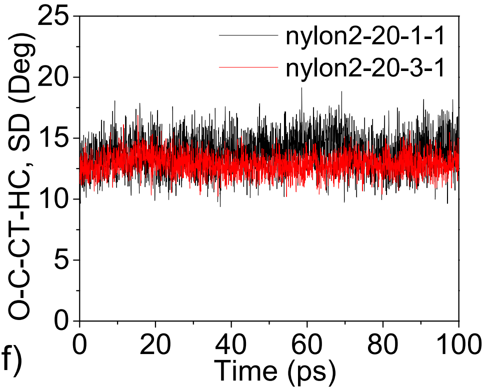
O-C-CT-HC, SD (Deg)
0
5
10
15
20
25
0
20
40
60
80
100
Time (ps)
nylon2-20-1-1
nylon2-20-3-1

(f)

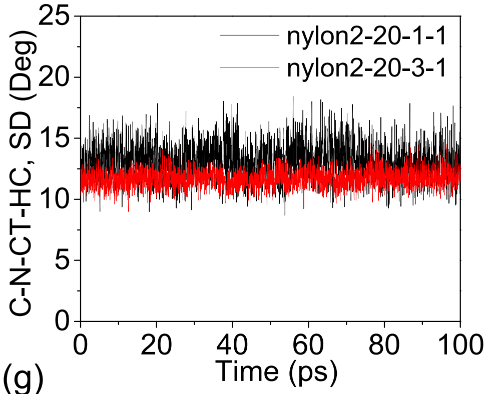
C-N-CT-HC, SD (Deg)
0
5
10
15
20
25
0
20
40
60
80
100
Time (ps)
nylon2-20-1-1
nylon2-20-3-1

(g)

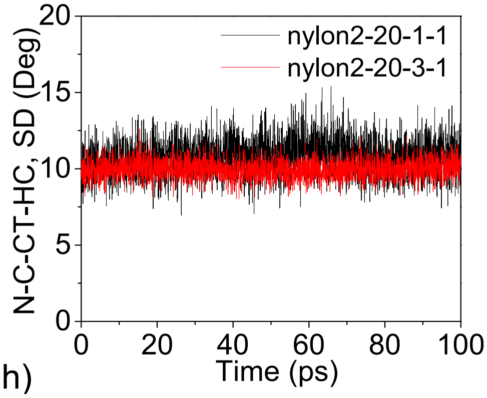
N-C-CT-HC, SD (Deg)
0
5
10
15
20
0
20
40
60
80
100
Time (ps)
nylon2-20-1-1
nylon2-20-3-1

(h)

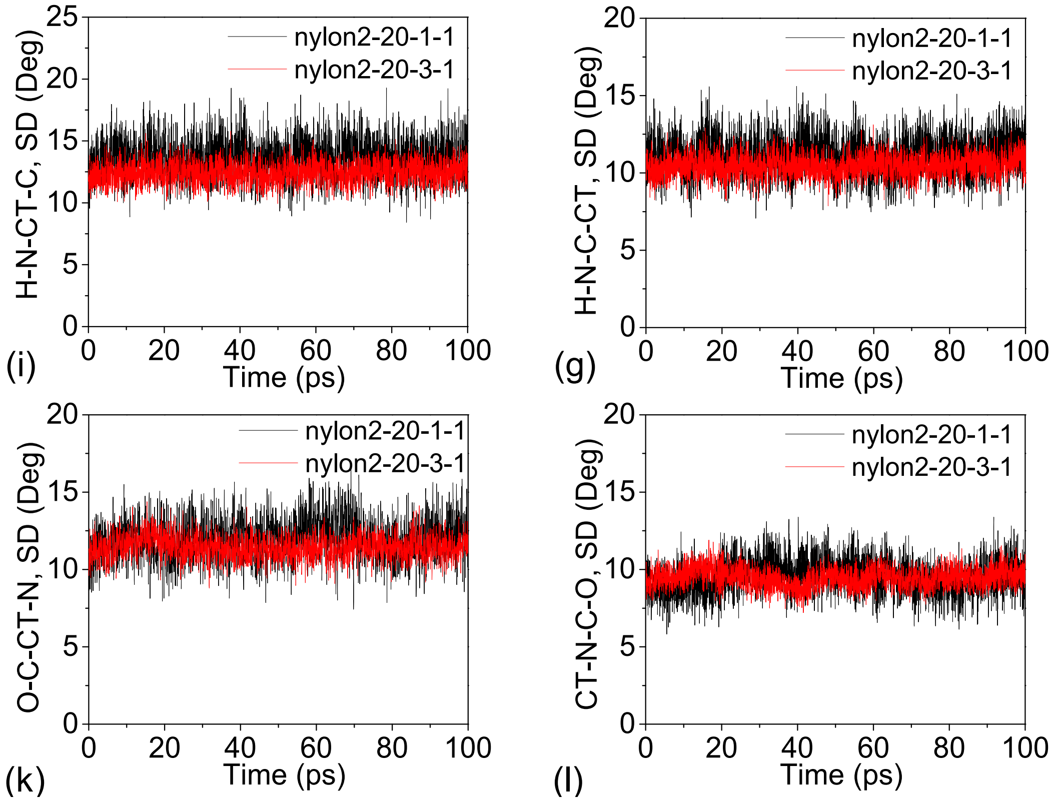

Figure C.4. Standard deviation of dihedral angles versus time.

REFERENCES

1. M. L. P. Price, D. Ostrovsky and W. L. Jorgensen, *J Comput Chem*, 2001, **22**, 1340-1352.

2. W. L. Jorgensen, D. S. Maxwell and J. TiradoRives, *J Am Chem Soc*, 1996, **118**, 11225-11236.

APPENDIX D

SUPPORTING INFORMATION OF CHAPTER 5

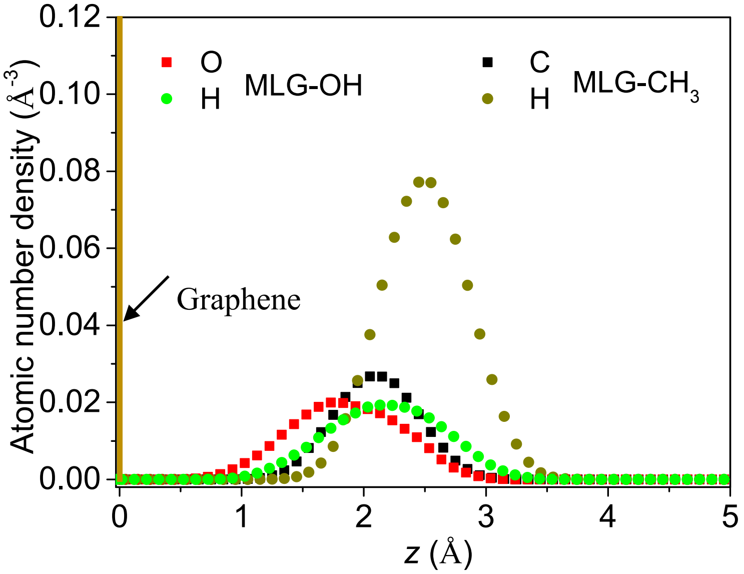

Figure D.1. Atomic number density of the atoms of different types in the functional groups in MLG-OH and MLG-CH$_3$. The graphene is positioned at $z = 0$.

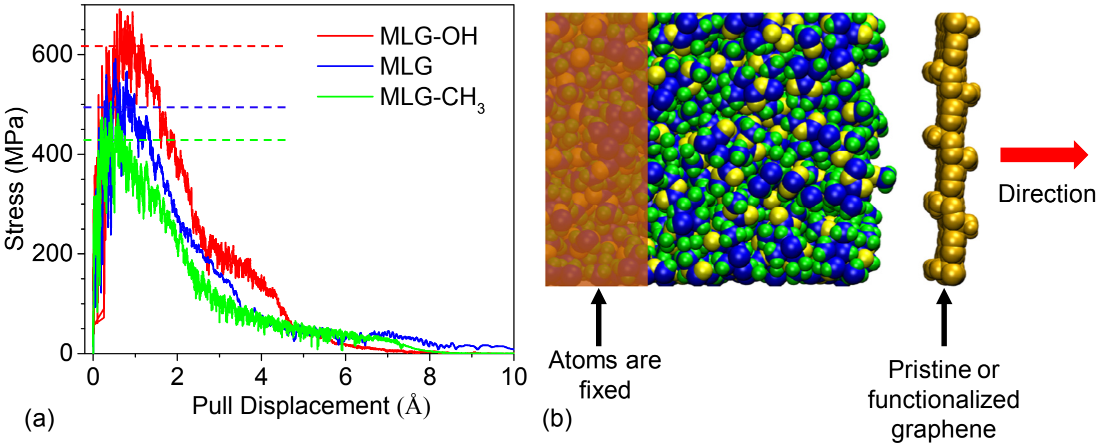

Figure D.2. (a) Interfacial normal stress versus the displacement of the filler material with respect to PMMA in MLG, MLG-OH, and MLG-CH3. Zero displacement corresponds to the equilibrium position. The dashed lines indicate the corresponding interfacial strengths. (b) Schematic illustration of the interfacial strength simulation setup. The left part of PMMA was fixed and the red arrow shows the direction of pulling the graphene or functionalized graphene. Periodic boundary conditions were applied in the transverse directions perpendicular to the pulling direction. The results were obtained by averaging the simulation results from five runs with randomized initial atomic velocities at 300 K.

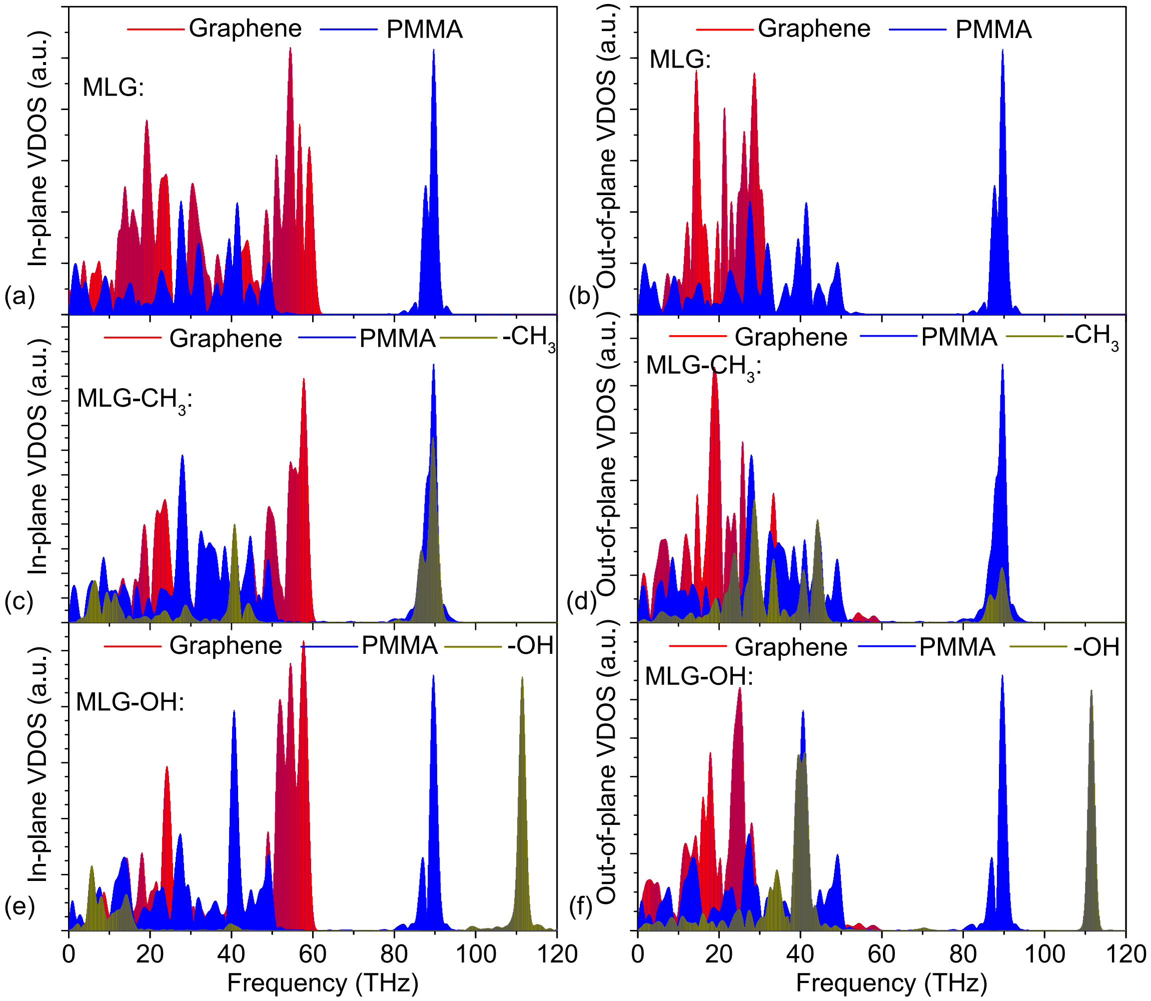

Figure D.3. In-plane and out-of-plane vibrational density of states (VDOS) of different components in three material systems: (a) in-plane and (b) out-of-plane VDOS for MLG, (c) in-plane and (d) out-of-plane VDOS for MLG-CH_3, and (e) in-plane and (f) out-of-plane VDOS for MLG-OH.

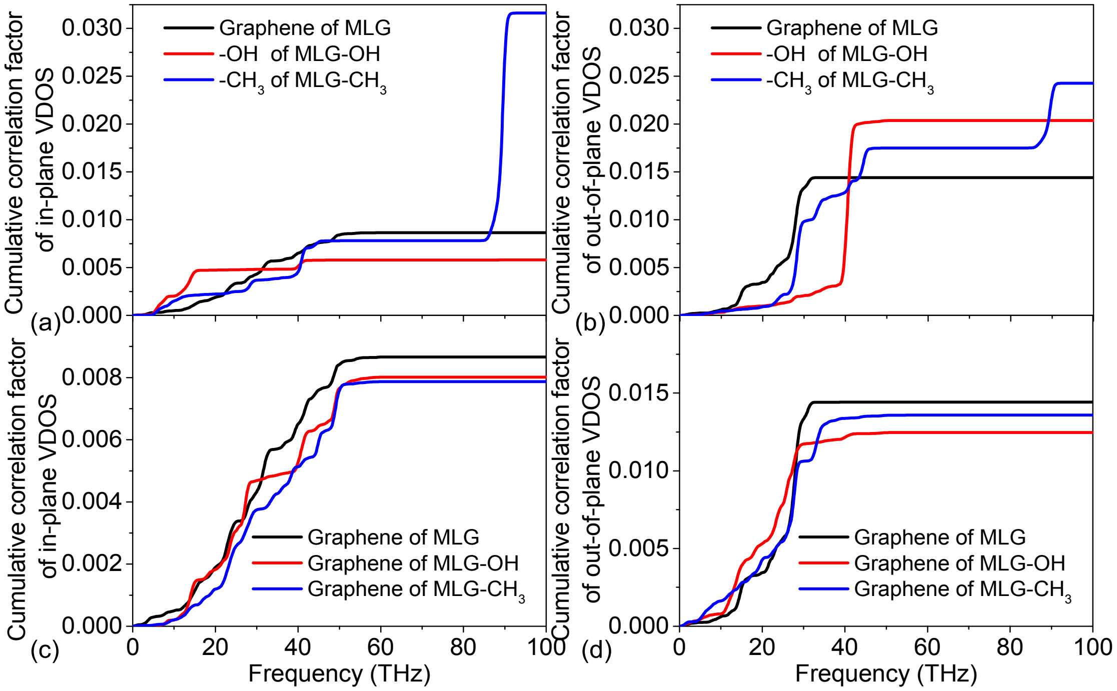

Figure D.4. In-plane and out-of-plane cumulative correlation factors between PMMA and different components of the filler materials: (a) in-plane and (b) out-of-plane cumulative correlation factors between the graphene and PMMA in MLG, between the hydroxyl groups and PMMA in MLG-OH, and between the methyl groups and PMMA in MLG-CH$_3$; (c) in-plane and (d) out-of-plane cumulative correlation factors between the *sp*^{2} carbon atoms in graphene and PMMA in MLG, MLG-OH, and MLG-CH$_3$.

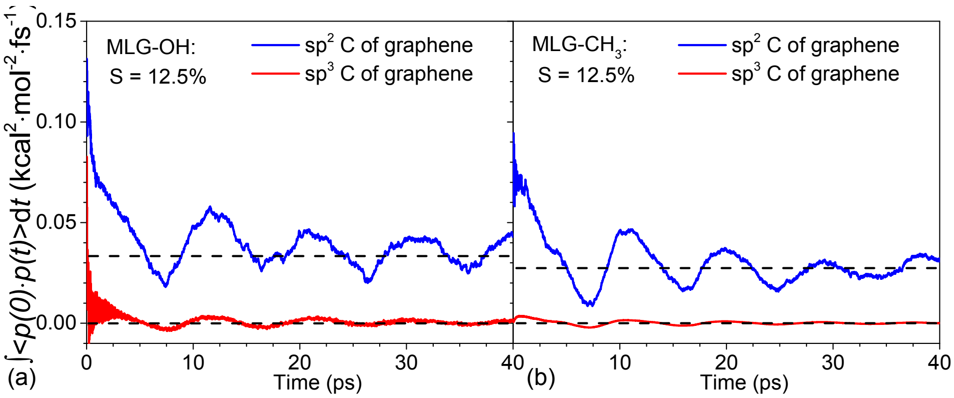

Figure D.5. The integrated autocorrelation of interfacial heat power between PMMA and the *sp*^{2} and *sp*^{3} carbon atoms of the functionalized graphene in MLG-OH (left) and MLG-CH$_3$ (right).

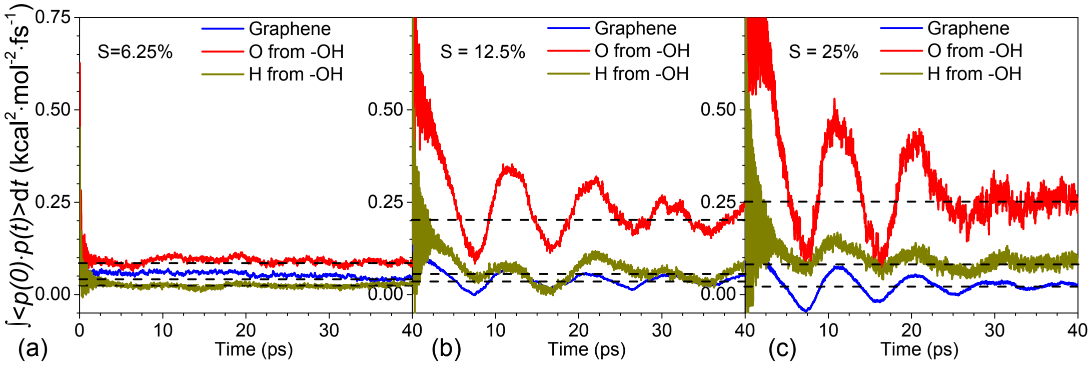

Figure D.6. The integrated autocorrelation of interfacial heat power between three components of the hydroxyl-functionalized graphene (i.e. sp^2 carbon atoms, and the oxygen and hydrogen atoms from the hydroxyl groups) and PMMA in MLG-OH at three degrees of functionalization (*S*): (a) 6.25%, (b) 12.5%, and (c) 25%. The dashed lines approximate the converged values.

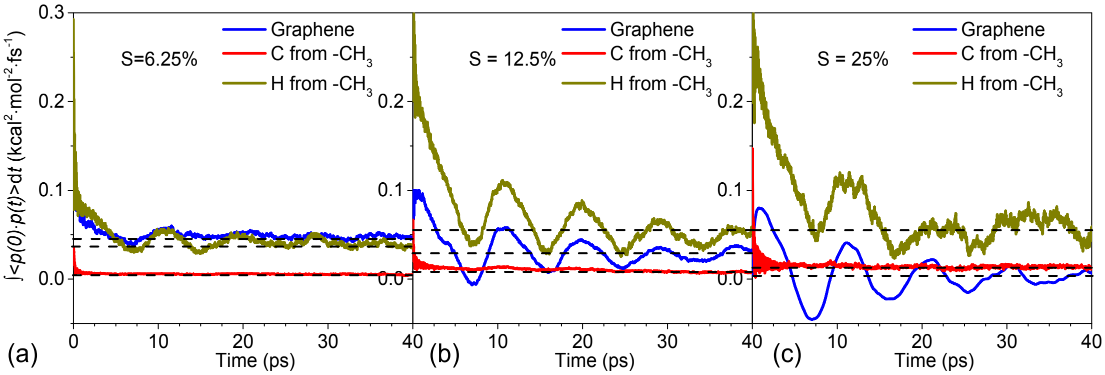

Figure D.7. The integrated autocorrelation of interfacial heat power between three components of the methyl-functionalized graphene (i.e. sp^2 carbon atoms, and the carbon and hydrogen atoms from the methyl groups) and PMMA in MLG-CH3 at three degrees of functionalization (*S*): (a) 6.25%, (b) 12.5%, and (c) 25%. The dashed lines approximate the converged values.

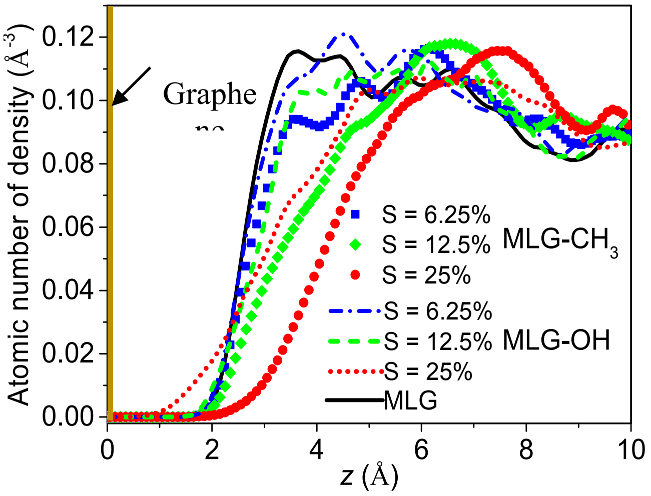

Figure D.8. Atomic number density of PMMA in MLG, and MLG-CH3 and MLG-OH with different degrees of functionalization (*S*). The graphene is positioned at *z* = 0.

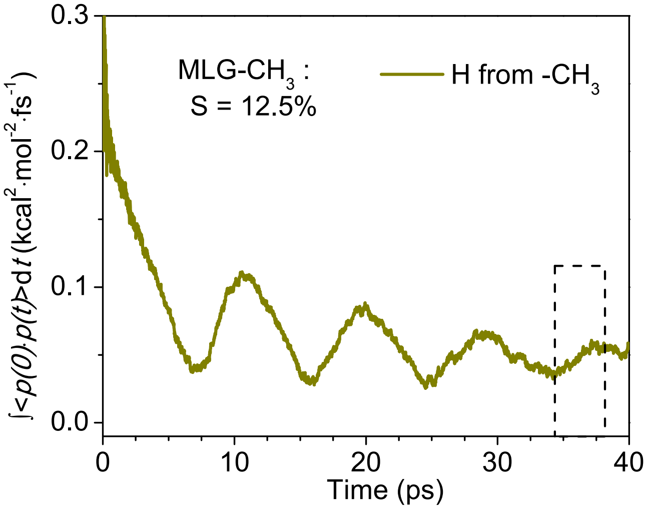

Figure D.9. Illustration of how the converged integrated autocorrelation of interfacial heat power is calculated. The converged value is approximated by the mean value of all data points in the last half period of oscillation as shown in the dashed box. The error is estimated by the difference between the maximum value and the mean value in in the dashed box.

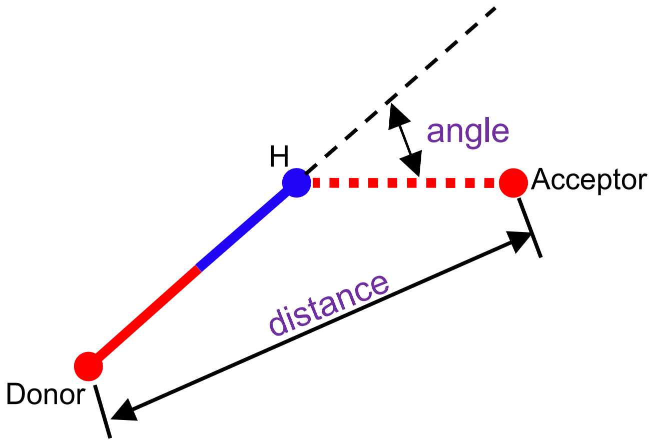
H
angle
Acceptor
distance
Donor

Figure D.10. Schematic representation of a hydrogen bond. The geometric criterion employed to identify hydrogen bonds is based on: (1) the distance between the hydrogen bond donor (D) and acceptor (A), and (2) the angle of D-H-A.

APPENDIX E

SUPPORTING INFORMATION OF CHAPTER 6

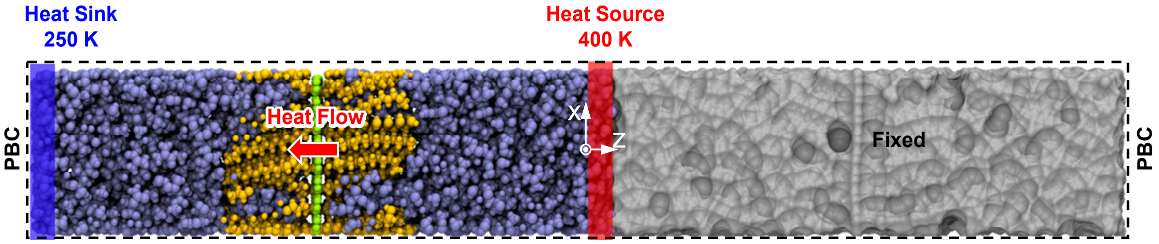
Heat Sink
250 K
Heat Source
400 K
Heat Flow
X
Z
Fixed
PBC
PBC

Figure E.1. A molecular dynamics simulation system to evaluate interfacial thermal conductance by nonequilibrium molecular dynamics method. Blue, orange, and green spheres: poly-(methyl methacrylate) (PMMA), polyethylene, and graphene. Atoms in the gray region are fixed. The temperature of the heat source and the heat sink was set to be 400 K and 250 K, respectively. Periodic boundary conditions (PBC) were applied in all three directions.

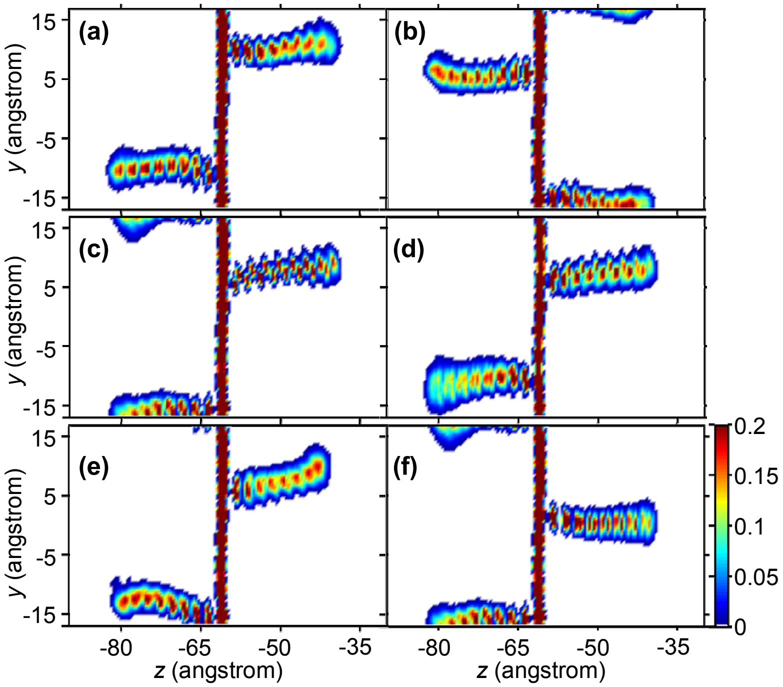

Figure E.2. Atomic number density distributions of graphene and two functional polyethylene chains for G32PE8. Two polyethylene chains are chosen randomly from G32PE8 in (a-f) with a comparable distance of grafting points with that of G1PE8.

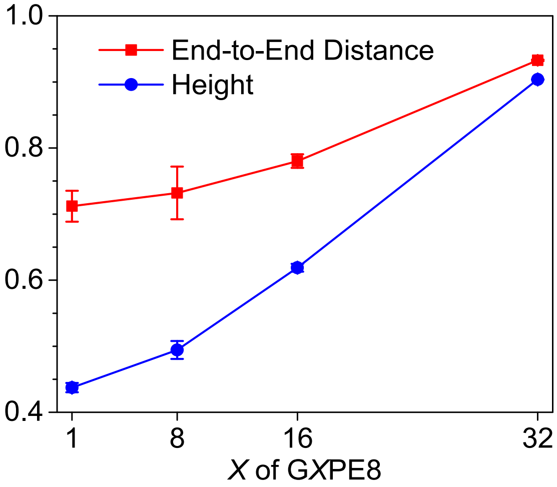

Figure E.3. Normalized end-to-end length and height of PE chains versus the number of PE chains in GXPE8 (8 repeat units). Actual lengths and heights are normalized by the length of fully extended PE chains. The normalized length quantifies the extent to which PE chains are stretched. In addition to this stretching ratio, the normalized height also present the angle of chain with respect to the surface.

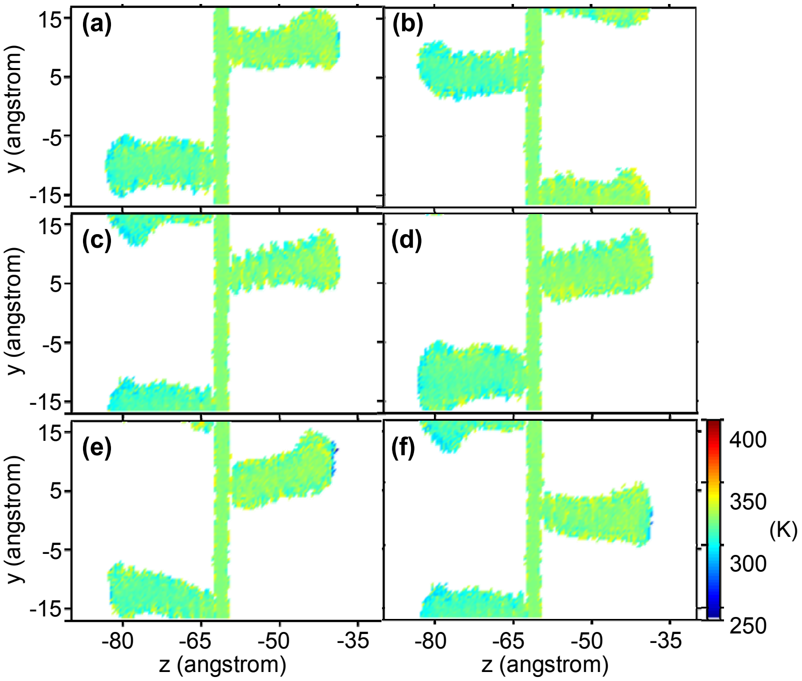

Figure E.4. Temperature contours of graphene and two functional polyethylene chains for G32PE8. Two polyethylene chains are chosen randomly from G32PE8 in (a-f) with a comparable distance of grafting points with that of G1PE8.

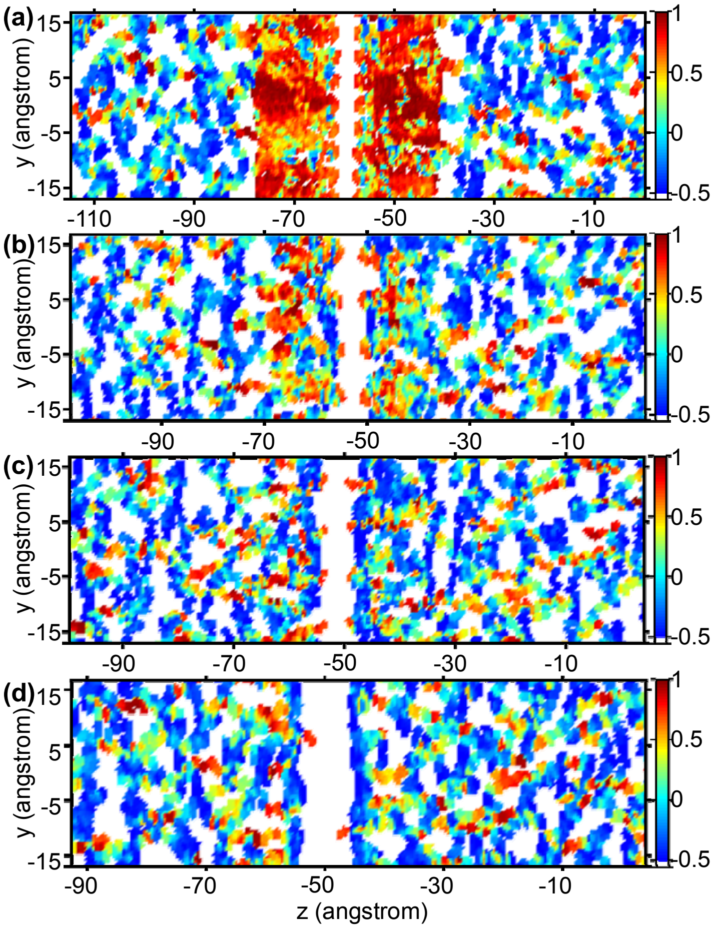

Figure E.5. Local Herman's orientation factors of main chains of polyethylene molecules and PMMA matrix for (a) G32PE8, (b) G16PE8, (c) G8PE8, and (d) G1PE8, respectively.

APPENDIX F

SUPPORTING INFORMATION OF CHAPTER 7

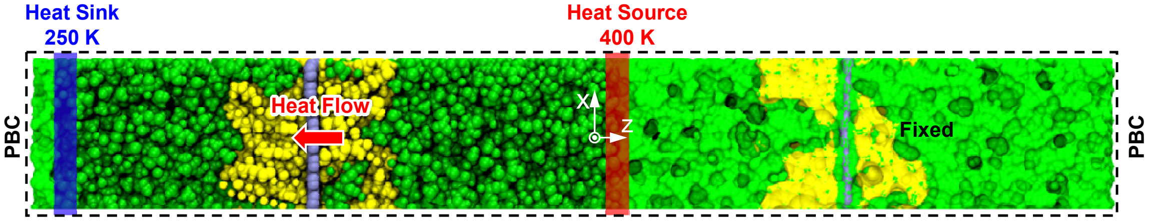

Fig. F.1. A system setup for nonequilibrium molecular dynamics simulations (NEMD). Green, yellow, and blue spheres: poly-(methyl methacrylate) (PMMA), polyvinyl alcohol (PVA), and graphene. Atoms in the frozen region were fixed. Temperature of the heat source and the heat sink were fixed to be 400 K and 250 K, respectively. Periodic boundary conditions (PBC) were applied in all three directions.

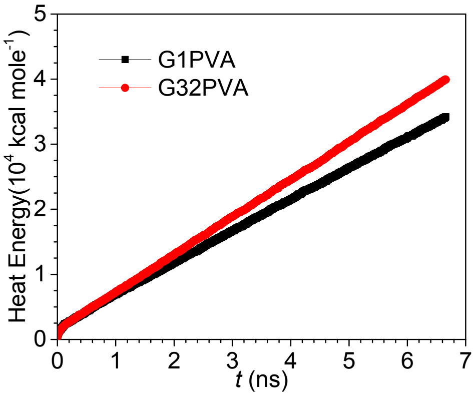

Fig. F.2. Heat energy added to the heat source by the Langevin thermostat versus time in NEMD.

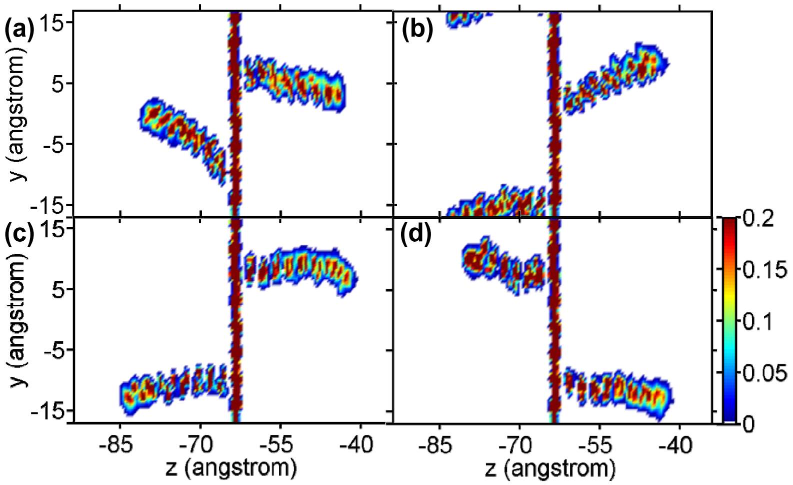

Fig. F.3. Contour plots of the atomic number density of graphene and a pair of PVA chains chosen from G32PVA. Two PVA chains in (a)-(d) were randomly chosen such that the distance between their grafting points is comparable to that of G1PVA.

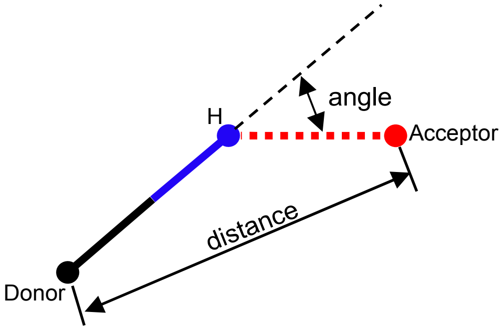

Fig. F.4. Geometric criterion to identify a hydrogen bond: (1) the distance between hydrogen bond donor and acceptor; (2) the angle between the vector donor-H and H-acceptor.

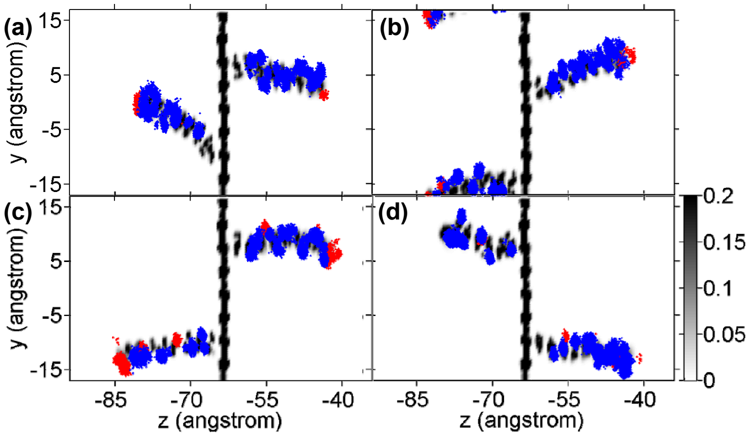

Fig. F.5. Plots of hydrogen bonds formed with a pair of PVA chains of G32PVA. Atomic number density is shown by gray colors. Red dots stand for the hydrogen bonds between PVA and PMMA while blue dots represent those between PVA chains.

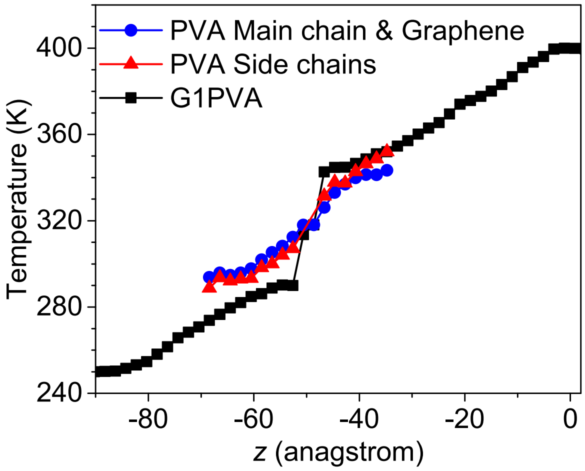

Fig. F.6. Temperature profiles of G1PVA from NEMD.

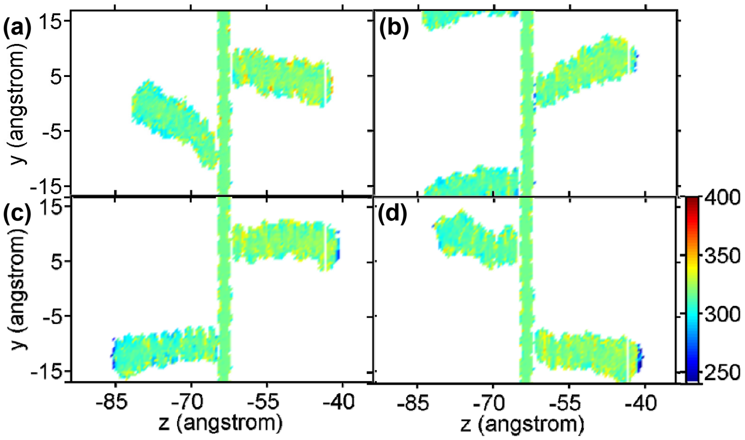

Fig. F.7. Temperature contours of graphene and a pair of PVA chains of G32PVA. Two PVA chains in (a)-(d) were randomly chosen such that the distance of grafting points is comparable to that of G1PVA.

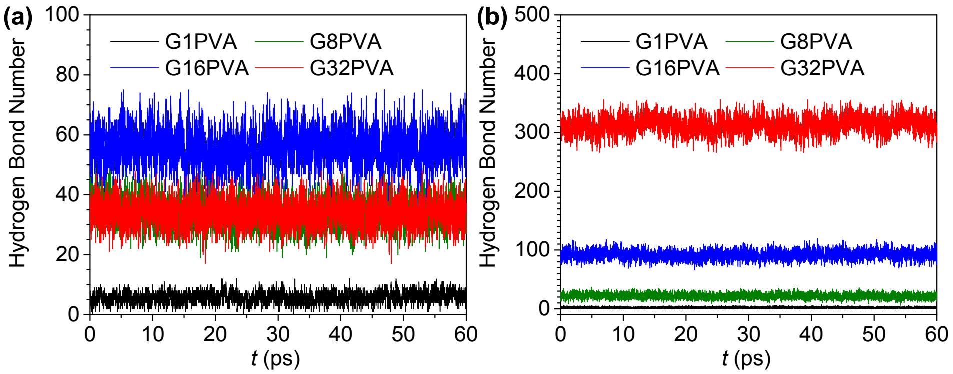

Fig. F.8. Hydrogen bonds of G*X*PVA (a) between PVA and PMMA and (b) within PVA.

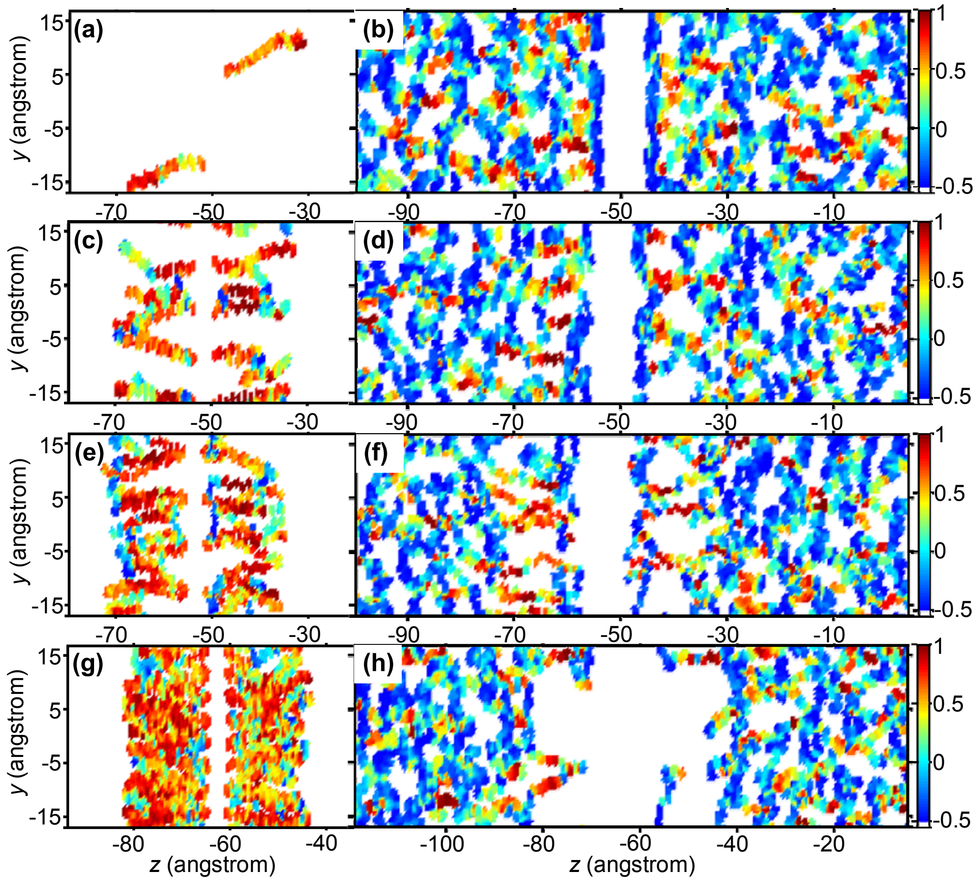

Fig. F.9. Local Herman's orientation factor of main chains in G*X*PVA. (a), (c), (e), and (g) are factors of PVA and (b), (d), (f), and (h) are factors of PMMA with *X* of 1, 8, 16, and 32, respectively.

CURRICULUM VITAE

LIN ZHANG

Education

- **Ph.D.** in **Mechanical Engineering**

  Utah State University, Logan, UT, August 2017 (expected)

  — Dissertation: Facilitation of Nanoscale Thermal Transport by Hydrogen Bonds

  — Advisor: Dr. Ling Liu

- **M.S.** in **Engineering Mechanics**

  Harbin Institute of Technology, Harbin, China, July 2009

  — Thesis: Progressive Failure Analysis of Laminated Composite Materials

  — Advisor: Dr. Linzhi Wu

- **B.S.** in **Engineering Mechanics**

  Harbin Institute of Technology, Harbin, China, July 2006

  — Thesis: Design for Deployable and Morphing Structures

  — Advisor: Dr. Jinsong Leng

Book Chapters

- L. Liu, **L. Zhang**. Nanofluidics in Graphene-Based Material Systems, ***Graphene Science Handbook: Mechanical and Chemical Properties***, CRC Press, 2016.

Journal Publications

- **L. Zhang**, L. Liu. Enhanced Interfacial Thermal Transport of Graphene/Polymer Nanocomposites Via Hierarchically Hydrogen-Bonded Molecular Heat Spreader. Under review.
- **L. Zhang**, L. Liu. Polymeric Self-Assembled Monolayers Anomalously Improve Thermal Transport Across Graphene/Polymer Interfaces. Accepted by ***ACS Applied Materials & Interfaces.***
- **L. Zhang**, Z. T. Bai, L. Liu. Exceptional Thermal Conductance across Hydrogen-Bonded Graphene/Polymer Interfaces. ***Advanced Materials Interfaces***, 2016. (**Inside Front Cover**)
- **L. Zhang**, Z. T. Bai, H. Ban, L. Liu. Effects of the Amino Acid Sequence on Thermal Conduction Through Beta-Sheet Crystals of Natural Silk Protein. ***Phys Chem Chem Phys***, 2015, 17, 29007-29013.
- **L. Zhang**, M. Ruesch, X. Zhang, Z. T. Bai, L. Liu. Tuning Thermal Conductivity of Crystalline Polymer Nanofibers by Interchain Hydrogen Bonding. ***RSC Adv***, 2015, 5, 87981-87986.
- **L. Zhang,** T. L. Chen, H. Ban, L. Liu. Hydrogen Bonding-Assisted Thermal Conduction in Beta-Sheet Crystals of Spider Silk Protein. ***Nanoscale***, 2014, 6, 7786-7791.
- Z. T. Bai, **L. Zhang**, L. Liu. Effects of Ion Beam Orientation on Defect Generation in Graphene. Under Review.

- Z. T. Bai, **L. Zhang**, H. Li, L. Liu. Nanopore Creation in Graphene by Ion Beam Irradiation: Geometry, Quality, and Efficiency. ***ACS Applied Materials & Interfaces**,* 2016, 8, 24803-24809.
- Z. T. Bai, **L. Zhang**, L. Liu. Improving Low-Energy Boron/Nitrogen Ion Implantation in Graphene by Ion Bombardment at Oblique Angles. ***Nanoscale***, 2016, 8, 8761-8772.
- Z. T. Bai, **L. Zhang**, L. Liu. Bombarding Graphene with Oxygen Ions: Combining Effects of Incident Angle and Ion Energy to Control Defect Generation. ***J Phys Chem C***, 2015, 119, 26793-26802.
- M. Yang, D. W. Xu, L. H. Jiang, **L. Zhang**, D. Dustin, R. Lund, L. Liu, H. Dong. Filamentous Supramolecular Peptide-Drug Conjugates as Highly Efficient Drug Delivery Vehicles. ***Chem Commun**,* 2014, 50, 4827-4830.
- L. Liu, **L. Zhang**, Z. G. Sun, G. Xi. Graphene Nanoribbon-Guided Fluid Channel: A Fast Transporter of Nanofluids. ***Nanoscale**,* 2012, 4, 6279-6283.
- L. Liu, **L. Zhang**, J. Lua. Branched Carbon Nanotube Reinforcements for Improved Strength of Polyethylene Nanocomposites. ***Appl Phys Lett**,* 2012, 101.
- **L. Zhang**, C. Z. Gao, J. F. Wu. Harmonic Finite Element Analysis Based on Large Mass Method, ***Semiconductor Technology***, 2011, 36, 402-405. **(In Chinese)**

- K. J. Li, **L. Zhang**, D. A. Dixon, T. M. Klein. Undulating Topography of HfO_2 Thin Films Deposited in a Mesoscale Reactor Using Hafnium (IV) Tert Butoxide. ***AICHE J,*** 2011, 57, 2989-2996.

- W. Liang, G. Zhao, L. Wu, H. Yu, M. Li, **L. Zhang**. Sample-Size Effects on the Compression Behavior of a Ni-Based Amorphous Alloy. ***Int J Mod Phys B*****,** 2009, 23, 1324-1330.

Conference Papers

- B. Xie, **L. Zhang**, L. Liu. Stress Propagation in a Hierarchical Energy Dissipating Composite Based on NPSL, ***IMECE 2015,*** Nov. 13-19, 2015, Houston, Texas, USA.

Conference Posters

- **L. Zhang**, L. Liu, H. Dong. Molecular Mechanisms Governing the Solubility of Peptide-Based Supramolecular Drug-Delivery Vehicles, *NanoUtah 2014*, Oct. 12-15, 2014, Salt Lake City, UT, USA.

Conference Presentations

Presenter $^+$

- **L. Zhang**$^+$, L. Liu. Exceptional Interfacial Thermal Conductance across Hydrogen-Bonded Graphene/Polymer Interfaces, *IMECE 2016*, Nov. 11-17, 2016, Phoenix, Arizona, USA.

- **L. Zhang$^+$,** L. Liu. Improving Interfacial Thermal Conductance between Graphene and Polymer via Hierarchical Heat Spreaders, *IMECE 2016*, Nov. 11-17, 2016, Phoenix, Arizona, USA.
- **L. Zhang$^+$**, L. Liu. Parametric Studies of Hydrogen Bonding Effect on Heat Transfer in Nanostructured Materials, *IMECE 2015*, Nov. 13-19, 2015, Houston, Texas, USA.
- **L. Zhang$^+$**, L. Liu. Hydrogen Bonding Effect on Thermal Transport in Single Crystalline Polymers, *IMECE 2015*, Nov. 13-19, 2015, Houston, Texas, USA.
- B. Xie, **L. Zhang$^+$**, L. Liu. Stress Propagation in a Hierarchical Energy Dissipating Composite Based on NPSL, *IMECE 2015*, Nov. 13-19, 2015, Houston, Texas, USA.
- L. Liu, **L. Zhang$^+$**. Multiscale Simulation to Understand Failure of Cladding Tubes with Hybrids, *IMECE 2015*, Nov. 13-19, 2015, Houston, Texas, USA.
- **L. Zhang$^+$**, L. Liu. Mechanics of Filamentous Supramolecular Peptide-Drug Conjugates, *IMECE 2015*, Nov. 13-19, 2015, Houston, Texas, USA.
- **L. Zhang$^+$**, L. Liu. Thermal Conduction in Silk Beta-Sheet Crystals, *IMECE 2014*, Nov. 14-20, 2014, Montreal, Canada.
- L. Liu, **L. Zhang$^+$**. Simulation of Composites Incorporating Structured Nanoreinforcements, *IMECE 2014*, Nov. 14-20, 2014, Montreal, Canada.

- **L. Zhang**$^+$, L. Liu. Molecular Mechanisms Governing the Solubility of Self-Assembled Filamentous Drug Delivery Vehicles, *IMECE 2014*, Nov. 14-20, 2014, Montreal, Canada.
- **L. Zhang**$^+$, Liu, L. Thermal Transport in Beta-Sheet Crystalline of Spider Silk and Silkworm Silk, *USU Graduate Research Symposium 2014*, April. 10, 2014, Logan, Utah, USA.
- **L. Zhang**$^+$**,** L. Liu. Hydrogen Bonding-Assisted Thermal Conduction in Beta-Sheet Crystals of Spider Silk Protein, *IMECE 2013*, Nov. 15-21, 2013, San Diego, CA, USA.

Awards and Grants

- Professional Education Course Scholarship, MIT, 2017
- Outstanding Graduate Student Scholar, College of Engineering, USU, 2017
- Graduate Research and Creative Opportunities Grant (GRCO), USU, 2016
- Dissertation Fellowship, Office of Research and Graduate Studies, USU, 2016
- Outstanding Graduate Researcher, Dept. of Mechanical and Aerospace Engineering, USU, 2016
- Graduate Student Travel Awards, Office of Research and Graduate Studies, USU, 2014, 2015, 2016
- Graduate Student Travel Grants, College of Engineering, USU, 2014, 2015
- First Class Graduate Fellowships, Harbin Institute Technology, China, 2007 – 2009

People's Scholarships, Harbin Institute Technology, China, 2002 – 2006

Positions Held

- **Graduate Research Assistant**

  — MAE Department, Utah State University, Logan, UT

  05/2017 – Present

  05/2013 – 12/2016

  — Center for Composite Materials & Structures, Harbin Institute of Technology, Harbin, China

  07/2007 – 07/2009

  08/2005 – 07/2006

- **Research Engineer**

  — The 13rd Research Institute, China Electronics Technology Group Co. Shijiazhuang, China

  07/2009 – 08/2011

- **Graduate Teaching Assistant**

  — MAE Department, Utah State University, Logan, UT

  01/2017 – 05/2017 Engineering Numerical Methods

  01/2013 – 05/2013 Material Science

  Kinematics

08/2012 – 12/2012 Design for Manufacturability

Continuum Mechanics and Elasticity

— Center for Composite Materials & Structures, Harbin Institute of Technology, Harbin, China

08/2006 – 07/2007 Mechanics of Composites

Outreach

Lecturer of Engineering State, 2014 – 2017

Tutor of Native American STEM Mentorship Program, 2016

Professional Memberships

ASME – Since 2013